

https://dspace.org/

Extension of the incremental hole-drilling technique for residual stress measurement

Smit, Teubes Christiaan

2021

https://hdl.handle.net/10539/33385

Downloaded from a DSpace repository. https://dspace.org/

Extension of the Incremental Hole-Drilling Technique for Residual Stress Measurement

Teubes Christiaan Smit

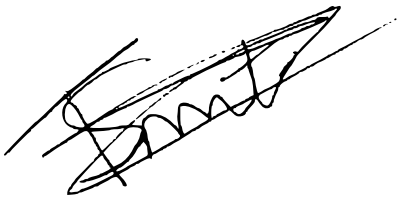
A thesis submitted to the Faculty of Engineering and the Built Environment, University of the Witwatersrand, Johannesburg, in fulfilment of the requirements for the degree of Doctor of Philosophy.

Johannesburg, August 2021

Declaration

I declare that this thesis is my own, unaided work, except where otherwise acknowledged. It is being submitted for the degree of Doctor of Philosophy at the University of the Witwatersrand, Johannesburg. It has not been submitted before for any degree or examination at any other university.

Signed this 3rd day of August 2021



Teubes Christiaan Smit

For my parents

Acknowledgements

I would like to thank Professor Robert Reid for his supervision, support, encouragement and extensive efforts during the course of this research project, and with regard to the journal publications related to this work.

I would also like to thank my girlfriend, Elaine, and my parents, Barbara and Francois, for all their love, support and encouragement during this research project. My siblings for their support and encouragement. And a special thanks to my nephews, Franco and Elan, for bringing me so much joy over the past few years.

Abstract

Incremental hole-drilling (IHD) is one of the most widely used residual stress measurement techniques as it is practical to implement, low cost, semi-destructive and yields reliable and accurate results. The unit pulse integral computational method is used extensively with IHD and can be used to determine residual stress distributions in almost any material type. IHD has a standardised test procedure for isotropic materials which includes the use of Tikhonov regularization with the integral method to smooth the calculated stress distribution and remove noise artefacts. However, the use of Tikhonov regularization with the integral method has not been extended to fibre reinforced plastic (FRP) laminates. Therefore, the integral methods currently employed in FRP laminates are sensitive to measurement errors which can result in large stress uncertainties. Existing variations of the integral method are also not able to measure discontinuous residual stress distributions in complex angle ply laminates that may have steep stress gradients through a single ply, while maintaining tolerance to measurement errors and high depth resolution. Series expansion is an alternative computational method that was first introduced with IHD in isotropic materials in 1981. However, for 40 years it has seldom been used, due to the suspected issues around instability at higher orders. Series expansion has the potential to overcome some shortcomings of the integral method, particularly in FRP laminates, as it is less sensitive to noise in the experimental data or to single erroneous measurements due to least-squares curve fitting in the inverse solution.

The primary aim of this thesis is to address limitations of IHD in FRP laminates by extending the use of separate series expansion to IHD for the measurement of residual stress distributions in laminates of arbitrary construction, and to extend the use of Tikhonov regularization with the integral method to cross-ply laminates. The discontinuous nature of residual stresses in FRP laminates at changes in fibre orientation, coupled with the typically small thickness of individual plies, means that the residual stress distribution within each ply orientation has low complexity and can, therefore, be well approximated by separate series expansion stress distributions of low order that are less susceptible to numerical instability. The least-squares inverse solution allows the amplitudes of each term in the series to be determined simultaneously in each ply, and consequently the residual stress distributions to be completely defined. Separate series expansion can be applied to laminates with any number of plies, orientated in any direction, or in any layered composite material where stress discontinuities

exist. A method to incorporate Tikhonov regularization with the integral method in cross-ply laminates is developed and it is demonstrated that regularization significantly reduces error sensitivity of the stress distribution while maintaining high depth resolution such that stress variation within a single ply can be captured correctly.

The secondary aim of this thesis is to demonstrate that series expansion is indeed a viable computational alternative to measure highly non-uniform residual stress distributions in isotropic materials. The use of finer depth increments and a means to select an appropriate series order have resolved issues around instability. A physical characteristic of IHD is that near-surface stress measurements are susceptible to large uncertainties, independent of the stress computation method used. Therefore, near-surface X-ray diffraction (XRD) measurements are commonly used to complement IHD results in isotropic materials and fully define the through-thickness stress distribution. To overcome this limitation of IHD, novel approaches to combine residual stress measurements from XRD and IHD into a single least-squares or regularized solution using series expansion and the integral method, respectively, is presented and demonstrated. These approaches allow XRD measurements to be incorporated into IHD results which showed strong correlation with standard series expansion and regularized integral methods and greatly reduced stress uncertainty near the surface. By incorporating XRD results into IHD, the advantages of both measurement techniques can be exploited while minimising the effects of their shortcomings.

Published Work

Aspects of this thesis have been published in the following references:

- T.C. Smit, R.G. Reid. Residual Stress Measurement in Composite Laminates using Incremental Hole-Drilling with Power Series. *Experimental Mechanics*, 58(8):1221–1235, 2018. DOI: 10.1007/s11340-018-0403-6.

  Contribution of authors:

  Contribution of candidate (T.C. Smit): Development of solution method, experimental testing, development of all FE models and software for results extraction/processing. Write-up of article and generation of all figures and tables.

  Contribution of supervisor (R.G. Reid): Suggested the topic, suggested and conceptualized the research problem, formulation of the problem, discussion as work progressed, proofreading of article and suggesting improvements.

- T.C. Smit, R.G. Reid. Tikhonov Regularization with Incremental Hole-Drilling and the Integral Method in Cross-Ply Composite Laminates. *Experimental Mechanics*, 60(8):1135–1148, 2020. DOI: 10.1007/s11340-020-00629-x.

  Contribution of authors:

  Contribution of candidate (T.C. Smit): Suggested and conceptualized the research problem, formulation of the problem and development of solution method, experimental testing, development of all FE models and software for results extraction/processing. Write-up of article and generation of all figures and tables.

  Contribution of supervisor (R.G. Reid): Discussion as work progressed, proofreading of article and suggesting improvements.

- T.C. Smit, R.G. Reid. Use of Power Series Expansion for Residual Stress determination by the Incremental Hole-Drilling Technique. *Experimental Mechanics*, 60(9):1301–1314, 2020. DOI: 10.1007/s11340-020-00642-0.

  Contribution of authors:

  Contribution of candidate (T.C. Smit): Conceptualized the research problem, formulation of the problem and development of solution method, experimental testing, development of all FE models and software for results extraction/processing. Write-up of article and generation of all figures and tables.

  Contribution of supervisor (R.G. Reid): Discussion as work progressed, proofreading of article and suggesting improvements.

- T.C. Smit, R.G. Reid. A Method to Combine Residual Stress Measurements from XRD and IHD using Series Expansion. *Experimental Mechanics*, 61(6):1029-1043, 2021. DOI: 10.1007/s11340-021-00719-4.

  Contribution of authors:

  Contribution of candidate (T.C. Smit): Development of solution method, experimental testing, development of all FE models and software for results extraction/processing. Write-up of article and generation of all figures and tables.

  Contribution of supervisor (R.G. Reid): Suggestion and conceptualization of the research problem, formulation of the problem, discussion as work progressed, proofreading of article and suggesting improvements.

Contents

Declaration i

Acknowledgements iii

Abstract iv

Published Work vi

Contents viii

List of Figures xiii

List of Tables xvii

List of Acronyms xix

Nomenclature xx

1 Introduction 1

2 Literature Survey 6

2.1 Non-destructive Diffraction Techniques 6

2.1.1 X-ray Diffraction 6

2.2 Relaxation Techniques 8

2.2.1 Incremental Slitting (Crack Compliance) 10

2.2.2 Incremental Hole-Drilling 12

2.2.2.1 Integral Method 14

2.2.2.2 Series Expansion Method 19

2.2.2.3 Incremental Hole-Drilling in Composite Materials 20

2.3 Gaps in Literature and Opportunities for Improvements and Extensions to IHD . . . 23

3 Research Questions **27**

4 Objectives **28**

5 Residual Stress Measurement in FRP Laminates with Series Expansion **29**

5.1 Introduction 30

5.2 Separate Series Expansion 31

5.3 Demonstration of Procedure 36

5.3.1 Experimental 38

5.3.2 Computational 42

5.3.3 Propagation of Uncertainties 46

5.3.4 Monte Carlo Simulation 53

5.3.5 Order Selection 56

5.4 Results and Discussion 59

5.5 Conclusions 64

5.6 Contribution to Knowledge 64

6 Tikhonov Regularization with the Integral Method in Cross-Ply Composite Laminates 65

6.1 Introduction . . . 66

6.2 Computational Methods . . . 67

6.2.1 Fully Coupled Integral Method . . . 67

6.2.2 Tikhonov Regularization . . . 68

6.3 Demonstration of Procedure . . . 71

6.3.1 Experimental . . . 71

6.3.2 Computational . . . 74

6.3.3 Propagation of Uncertainties . . . 78

6.4 Results and Discussion . . . 80

6.5 Conclusions . . . 88

6.6 Contribution to Knowledge . . . 88

7 Use of Power Series Expansion for Residual Stress Measurement in Isotropic Materials 89

7.1 Introduction . . . 90

7.2 Computational Methods . . . 91

7.2.1 Series Expansion in Isotropic Materials . . . 91

7.2.2 Zuccarello Approach . . . 92

7.3 Demonstration of Procedure . . . 93

7.3.1 Experimental . . . 93

7.3.2 Computational . . . 95

7.3.3 Propagation of Uncertainties . . . 100

7.3.4 Series Expansion Order Selection . . . 102

7.4 Results and Discussion . . . 104

7.5 Conclusions . . . 108

7.6 Contribution to Knowledge . . . 109

7.7 Acknowledgements . . . 109

8 Methods to Combine Residual Stress Measurements from XRD with IHD 110

8.1 Introduction . . . 111

8.2 Theoretical . . . 112

8.2.1 Imposition of Constraints on the Series Expansion Method . . . 112

8.2.2 Imposition of Constraints on the Regularized Integral Method . . . 115

8.3 Demonstration of Procedure . . . 117

8.3.1 Experimental . . . 117

8.3.1.1 Specimen and LSP . . . 117

8.3.1.2 XRD . . . 118

8.3.1.3 IHD . . . 118

8.3.2 Computational . . . 119

8.3.3 Propagation of Uncertainties . . . 120

8.3.4 Selection of Series Order . . . 121

8.4 Results and Discussion . . . 124

8.5 Conclusions . . . 133

8.6 Contribution to Knowledge . . . 133

8.7 Acknowledgements . . . 133

9 Conclusions 134

10 Recommendations and Future Work **137**

References **139**

List of Figures

2.1 Physical interpretation of matrix $\bar{\mathbf{A}}$ coefficients for the integral method 15

2.2 Current state of prominent residual stress measurement techniques 23

2.3 Envisioned extension of the IHD technique 26

5.1 Schematic strain variation with depth 32

5.2 Applied eigenstrain and resultant stress distribution 34

5.3 Methodology for residual stress measurement using IHD with separate series expansion 37

5.4 $[0_2/+45/-45]_s$ specimen and configuration of the 1.5/350M RY61 rosette 40

5.5 Strain variation with depth in the x, y and 45° gauge directions 41

5.6 Top view of mesh around the hole including the strain gauge grid locations 42

5.7 Section through the mesh thickness 43

5.8 Strain variation in the x-direction at a quarter thickness hole depth and the strain gauge grid locations 44

5.9 Determination of interpolated calibration coefficients from FE data 45

5.10 Least-squares fits to 45° strain measurements using (1, 1, 1) and (4, 4, 4) order combinations 45

5.11 Methodology for uncertainty estimation using Monte Carlo simulation 47

5.12 Least-squares curve fits to Monte Carlo strains in x-direction 53

5.13 Least-squares curve fits to Monte Carlo strain in y-direction 54

5.14 Least-squares curve fits to Monte Carlo strain in 45° direction 54

5.15 σ_x Monte Carlo stress distributions and associated uncertainties obtained using the (2, 2, 0) combination of series orders 55

5.16 σ_y Monte Carlo stress distributions and associated uncertainties obtained using the (2, 2, 0) combination of series orders 55

5.17 τ_{xy} Monte Carlo stress distributions and associated uncertainties obtained using the (2, 2, 0) combination of series orders 56

5.18 Overlap of the uncertainty bounds in σ_x for the twenty fits most converged to the (2, 2, 0) combination 58

5.19 Overlap of the uncertainty bounds in σ_y for the twenty fits most converged to the (2, 2, 0) combination 58

5.20 Overlap of the uncertainty bounds in τ_{xy} for the twenty fits most converged to the (2, 2, 0) combination 59

5.21 Least-squares curve fits to experimental strain data with associated uncertainties using the (2, 2, 0) combination of series orders 60

5.22 Stress distributions and associated uncertainties obtained using the (2, 2, 0) combination of series orders 60

6.1 x and y offset of the hole 72

6.2 Strain variation with depth in the x, y and $45°$ gauge directions 73

6.3 Initial and erroneous spline interpolations for each strain direction 73

6.4 Mesh around the hole and stress variation due to an applied unit stress in the x-direction at 0.41 mm hole depth 75

6.5 Biharmonic surface spline to calculate nodal displacements around the perimeter of each grid 75

6.6 Hole offset correction during biharmonic spline interpolation 77

6.7 Identification of zero depth position 79

6.8 Regularized fits to experimental strain data 81

6.9 Axial stress distributions and associated uncertainties obtained using integral methods 82

6.10 Transverse stress distributions and associated uncertainties obtained using integral methods 82

6.11 Stress distributions and associated uncertainties obtained using regularized integral and series expansion methods 83

6.12 Maximum transverse stress on hole bottom 86

6.13 Location of the critical transverse stress 87

7.1 Strain variation with depth in the x, y and 45° gauge directions 94

7.2 Top view of mesh around the hole including the strain gauge grid locations 96

7.3 Section through the mesh thickness 97

7.4 Strain variation in the x-direction at 0.5 mm hole depth and strain gauge grid locations 97

7.5 Determination of interpolated calibration coefficients from FE data 99

7.6 Least-squares fits to strain data in the x-direction using 2^{nd} and 6^{th} order series . . . 99

7.7 Overlap of the uncertainty bounds in σ_x for 0^{th} to 14^{th} order series 103

7.8 Overlap of the uncertainty bounds in σ_x for converged and 14^{th} order series 103

7.9 Least-squares curve fits to experimental strain data with associated uncertainties . . . 105

7.10 Stress distributions and associated uncertainties obtained using the 6^{th} order series . . 105

7.11 σ_x distributions and associated uncertainties of each method 106

7.12 σ_y distributions and associated uncertainties of each method 106

8.1 Strain variation with depth in the x, y and 45° strain gauge directions 118

8.2 σ_x distribution generated by 2^{nd} order eigenstrain in the x-direction, including the strain gauge grid locations 119

8.3 Constrained least-squares fits to strain data in the x-direction using 4^{th}, 6^{th}, 9^{th} and 10^{th} order series 121

8.4 Least-squares fits to strain data in the x-direction using 4^{th} and 8^{th} order series 122

8.5 Overlap of the uncertainty bounds in σ_x for 2^{nd} to 15^{th} order series 123

8.6 Variation and convergence of total RMS stress uncertainty for 2^{nd} to 15^{th} order series 123

8.7 Least-squares fits to the experimental strain data using the constrained 9^{th} order series 124

8.8 Stress distributions and associated uncertainties obtained using the constrained 9^{th} order series 125

8.9 Location of maximum von Mises stress during material removal 126

8.10 Variation of the maximum von Mises stress during material removal 126

8.11 σ_x distributions and associated uncertainties of each method 127

8.12 σ_y distributions and associated uncertainties of each method 128

8.13 σ_x uncertainty distributions for varying magnitudes of XRD uncertainty 130

8.14 σ_x distributions and associated uncertainties of each method 131

8.15 σ_y distributions and associated uncertainties of each method 131

List of Tables

5.1 Orthotropic lamina properties 38

5.2 Properties of each strain gauge grid of the 1.5/350M RY61 rosette 40

5.3 Uncertainty sources and their assigned probability density functions 46

5.4 Breakdown of RMS uncertainty in stress arising from each uncertainty source, x_i . . 61

6.1 Uncertainty sources and their assigned probability density functions 78

6.2 Breakdown of RMS uncertainty in stress arising from each uncertainty source, x_i . . 84

6.3 Effect of additional strain data points past the midplane 85

6.4 Effect of additional strain data points past the midplane on RMS Uncertainty in the 90° ply 85

7.1 Mechanical properties and chemical composition of aluminium alloy 7075-T651 . . 93

7.2 Laser specifications and LSP parameters 93

7.3 Uncertainty sources and their assigned probability density functions 100

7.4 Breakdown of RMS uncertainty in stress arising from each uncertainty source, x_i . . 107

8.1 Uncertainty sources and their assigned probability density functions 120

8.2 Breakdown of RMS uncertainty in stress arising from each uncertainty source, x_i . . 128

8.3 Breakdown of RMS uncertainty in stress resulting from reducing only the uncertainty in XRD results 129

8.4 Breakdown of RMS uncertainty in stress arising from each uncertainty source, x_i . . 132

List of Acronyms

AM	Additive Manufacturing
CLT	Classical Lamination Theory
CTE	Coefficient of Thermal Expansion
DIC	Digital Image Correlation
EAC	Environmentally Assisted Cracking
EDM	Electrical Discharge Machining
FE	Finite Element
FRP	Fibre Reinforced Plastic
GFRP	Glass Fibre Reinforced Plastic
IHD	Incremental Hole-Drilling
JCGM	Joint Committee for Guides in Metrology
KKT	Karush-Kuhn-Tucker
LRM	Layer Removal Method
LSP	Laser Shock Peening
ND	Neutron Diffraction
PC	Polycarbonate
PEEK	Polyetheretherketone
PET	Polyethylene Terephthalate
POM-C	Polyacetal Copolymer
RMS	Root Mean Square
SCC	Stress Corrosion Cracking
SLM	Selective Laser Melting
SP	Shot Peening
XEC	X-ray Elastic Constants
XRD	X-ray Diffraction

Nomenclature

a	Calibration constant for the integral method
$\mathbf{a}$	Amplitude vector for series expansion
$\bar{\mathbf{A}}$	Equi-biaxial calibration matrix for the integral method
$\bar{\mathbf{A}}_{(Zucc)}$	Equi-biaxial calibration matrix for the Zuccarello approach
b	Calibration constant for the integral method
$\mathbf{B}$	Constraint matrix for the constrained regularized integral method
$\bar{\mathbf{B}}$	Shear calibration matrix for the integral method
$\bar{\mathbf{B}}_{(Zucc)}$	Shear calibration matrix for the Zuccarello approach
c	Calibration constant for the integral or series expansion method
$\mathbf{C}$	Calibration matrix for series expansion or integral method
$\mathbf{C}_x$	Decoupled x-direction calibration matrix for the integral method
$\bar{\mathbf{C}}$	Longitudinal calibration matrix
$\hat{\mathbf{C}}$	Transverse calibration matrix
$\mathbf{d}$	Vector containing magnitude and/or slope constraints
E	Young's modulus
E_1	Young's modulus of lamina in fibre direction
E_2	Young's modulus of lamina transverse to fibre direction
E_3	Young's modulus of lamina transverse to fibre direction
E_x	Young's modulus in axial direction
E_y	Young's modulus in transverse direction
g	Strain gauge location
G	Shear modulus
G_{12}	In-plane shear modulus of lamina
G_{13}	In-plane shear modulus of lamina
G_{23}	Out-of-plane shear modulus of lamina
i	Hole depth increment
j	Ply orientation to which eigenstrain is applied
K_t	Transverse sensitivity coefficient
$\mathbf{L}$	Tri-diagonal 'second derivative' matrix for Tikhonov regularization

m	Nodal position in the through-thickness direction
$\mathbf{m}$	Vector containing magnitude constraints for series expansion
n	Order of the temperature variation used to apply eigenstrain; Number of depth increments
p	Component of stress in series expansion stress matrix
$\mathbf{p}$	Isotropic (equi-biaxial) strain vector
p_{rms}	RMS of the misfit vectors
p_{std}	Standard errors of the combination strain
$\mathbf{q}$	45° shear strain vector
$\mathbf{Q}$	Constraint matrix for constrained series expansion
$\mathbf{t}$	x-y shear strain vector
s	Component of eigenstrain
$\mathbf{s}$	Vector containing slope constraints for series expansion
$\mathbf{S}$	Stress matrix for series expansion
V_f	Volume fraction of the fibres within a lamina
V_m	Volume fraction of the matrix within a lamina
W	Final hole depth
z_0	Zero depth
z_i	Incremental depth
α	Regularization factor
α_p	Regularization factor for isotropic (equi-biaxial) stress
α_q	Regularization factor for 45° shear stress
α_t	Regularization factor for x-y shear stress
α_x	Coefficient of thermal expansion in the x-direction; Regularization factor for stress in the x-direction
α_{xy}	Coefficient of thermal expansion in the in-plane shear direction
α_y	Coefficient of thermal expansion in the y-direction
ϵ	Strain
ϵ_{45°	45° strain
ϵ_m	Indicated experimental strain
$\boldsymbol{\epsilon}_{meas}$	Experimental strain vector
ϵ_{noise}	Experimental noise
ϵ_r	Radial strain
ϵ_x	Axial strain
ϵ_y	Transverse strain
ν	Poisson's ratio
ν_0	The Poisson's ratio of the material on which the manufacturer's gauge factor was measured
ν_{12}	Poisson's ratio of unidirectional lamina. Primary strain in direction 1,

	Poisson's strain in direction 2 of material coordinate system
ν_{13}	Poisson's ratio of unidirectional lamina. Primary strain in direction 1, Poisson's strain in direction 3 of material coordinate system
ν_{23}	Poisson's ratio of unidirectional lamina. Primary strain in direction 2, Poisson's strain in direction 3 of material coordinate system
σ_1	Stress in fibre direction
σ_2	Stress transverse to fibre direction
$\boldsymbol{\sigma}_p$	Isotropic (equi-biaxial) stress vector
$\boldsymbol{\sigma}_q$	45° shear stress vector
$\boldsymbol{\sigma}_{res}$	Residual stress vector
$\boldsymbol{\sigma}_t$	x-y shear stress vector
σ_x	Axial stress in the global coordinate system
$\boldsymbol{\sigma}_{XRD}$	Vector containing XRD stress measurements
σ_y	Transverse stress in the global coordinate system
σ_z	Stress normal to the surface
τ_{12}	In-plane shear stress in material coordinate system
τ_{xy}	In-plane shear stress in global coordinate system
θ_1	Total misalignment during tensile testing of a 0° laminate
θ_2	Total misalignment during tensile testing of a 90° laminate
θ_3	Total misalignment during tensile testing $\pm$45° laminate
θ_{0° ply	Misalignment of 0° plies of hole-drilling specimen
θ_{45° ply	Misalignment of +45° plies of hole-drilling specimen
θ_{-45° ply	Misalignment of -45° plies of hole-drilling specimen
θ_{90° ply	Misalignment of 90° plies of hole-drilling specimen
θ_{coupon}	Fibre misalignment of tensile testing coupons
θ_{grips}	Misalignment of specimen in grips of tensile testing machine
θ_{SG_h}	Misalignment of strain gauge during hole-drilling
θ_{SG_t}	Misalignment of strain gauge during tensile testing

1 Introduction

Many engineering materials, such as fibre reinforced plastic (FRP) laminates and selective laser melted (SLM) additively manufactured (AM) components, develop residual stresses during production or undergo surface treatment, such as laser shock peening (LSP) to induce beneficial residual stress. The combination of processing parameters used during production or surface treatment impact the form and magnitude of the residual stress distribution in these parts. Therefore, it is important that these stress distributions can be accurately measured to allow optimisation of processing parameters.

FRP composite materials are widely used in the automotive, marine and aerospace industries because of their excellent strength-to-weight ratios and corrosion resistance. FRP laminates undergo complex temperature and pressure cycles during production [1], where many thermal processes and chemical reactions occur within the laminate. Residual stresses are generated due to factors such as the differences in the coefficients of thermal expansion (CTE) of the fibres and the resin system, differences in the mechanical properties arising from variations in fibre orientation between plies, tool-part interaction and cure shrinkage of the resin [1, 2]. Tool-part interaction occurs when a laminate with a low CTE is cured on a tool with a much higher CTE. Steel and aluminium tools have much higher CTE than FRP parts, and tend to elongate the parts as they heat up. In-plane stresses can arise through the thickness and, as a result, cause bending when the stresses are released. Cure shrinkage is a chemical effect that takes place during curing when the polymer volume decreases and can lead to high levels of residual stress. The majority of the residual stresses are generated during cooling from the final hold temperature. Thermal and resin shrinkage induced stresses can subsequently cause distortion and premature cracking of the composite [3]. Other mechanisms that may cause residual stresses in FRP laminates are; moisture, ageing, elevated post-cure temperature, fluctuation of material properties on the microscopic scale, free surfaces, differences in fibre-volume fraction and non-uniform curing. The residual stress distribution depends on aspects such as the laminate configuration, the cure-cycle used and the material properties of each ply. Due to changes in the latter with respect to the global coordinate system, FRP laminates develop residual stresses that are discontinuous at interfaces between plies of different orientation [4, 5].

The residual stresses that develop in FRP components may introduce fibre waviness or micro-buckling [5], that reduce the overall strength and quality of these parts [6]. Fibre waviness develops during the

manufacturing process of a FRP composite structure when the fibres are subjected to compressive axial loads from thermal residual stresses. Since the matrix cannot provide any transverse support, the fibres are deformed (micro-buckling) and fibre waviness is developed. Transverse cracking may develop in regions where tensile residual stresses initiate microcracks at pre-existing imperfections such as voids and flaws in the fibre-matrix bond [7]. Such cracks can develop even in the absence of a applied mechanical loading [8]. These cracks may propagate into the matrix or through the fibre-matrix interface and promote environmentally assisted cracking (EAC) by providing a means for the corrosive media to reach the reinforcing fibres. Microcracks may grow into transverse ply cracks that form initiation points for delamination of the plies within the laminate [6] and eventually failure of the laminate. More importantly, they can cause premature failure under cyclic loading conditions [5]. The rate of crack propagation is directly associated with the crack tip stress intensity [9], and therefore this type of failure always occurs in regions of tensile stress [10–12].

Apart from the creation of transverse cracks, the difference between the residual stresses in the 0° and 90° plies in cross-ply laminates can also lead to delamination [6], resulting in the gradual loss of stiffness and strength. Another mechanism that causes delamination is the free edge effect, which also leads to matrix cracking. Delamination at free edges is associated with high interlaminar stresses, which are developed due to the discontinuity of properties at the free edges. Delamination may also occur around any geometric stress concentration, for example around holes, cut-outs and general changes in section, which considerably reduces the load-carrying capability of the composite component [5]. Interlaminar failure of FRP materials is characterised by gradual propagation of the delamination, which finally leads to loss of stiffness and strength of the structure. Residual stresses in FRP laminates often result in dimensional changes and warpage when fabricated on flat tooling [13]. Warpage or dimensional instability may be the result of two mechanisms: non-uniform temperature distribution or cooling, and tool-part interaction. Tool-part interaction can contribute significantly to warpage, especially for thin laminates.

The residual stresses in FRP laminates can be high and can have a significant influence on the mechanical performance of the laminate [6]. The stiffness, strength and life of a FRP component can be reduced due to the negative effects caused by residual stresses such as matrix microcracking, interface debonding and warping [14]. To determine the actual stress within a FRP component subjected to external loading, the residual stresses within the component must be included. Therefore, it is essential that the residual stresses can be determined so that designers can estimate their influence on the mechanical properties of a part. If residual stresses are not included during the design of a component they can cause failure under fatigue loading prior to the useful design life of the part [15, 16]. Consequently, large safety factors are often employed in the design of composite parts, leading to over-weight and over-designed components.

The adverse effects of residual stresses within FRP components have led to studies focused on the reduction of these stresses during the manufacturing process. White and Hahn [17] investigated the

effect of the cure cycle on the resulting residual stresses, and demonstrated that the residual stresses could be minimised by reducing the cure and post-cure temperatures, and increasing the cooling time. Although optimisation of the manufacturing process can reduce the residual stresses within FRP components to some extent, these stresses still need to be taken into account when determining the overall stress state of these components. A number of analytical models have been developed to predict the residual stress state within FRP components [18, 19]. These models, however, require knowledge of parameters that govern the formation of the residual stresses such as those that are dependent on the properties of the constituent materials. For instance, the cure shrinkage of the resin is required, which is dependent on the quantity of accelerator and catalyst, as well as the ambient temperature during initial cure [18]. In addition to this, certain models require cure kinetics parameters [19, 20], which are determined by measuring the state of cure and cure rate simultaneously [21]. Even if these parameters could be easily determined, a certain level of inaccuracy in the residual stresses can be expected because of the inability to precisely model non-linear effects such as the visco-elasticity of the resin [6].

The most popular technique to estimate residual stress in FRP laminates is to measure the curvature of asymmetrical cross-ply laminates which are known to develop curvature after processing. The magnitude of residual stress within the laminate is directly related to the curvature. These methods are based on classical lamination theory (CLT) and the elastic [22–24] or visco-elastic [25–27] response of the laminate during the cooling stage. Although this method is practical, it does not enable the stress distribution through the thickness of a particular ply to be determined. Neither can it be applied to symmetrical laminates since the resulting part will be flat after production, as the in-plane strains are balanced about the neutral axis of the part. The most effective procedure for determining the residual stress state within FRP components is to measure them directly. Measurement of the residual stresses is important since it allows the overall stress state to be determined, and thus enables the design of safer and more efficient FRP components. The calculated residual stresses can also be used to validate and promote the development of improved models for the prediction of residual stresses within these structures.

Residual stresses in metallic components arise during manufacturing processes as a result of plastic deformation, non-uniform temperature changes and phase changes. The residual stresses affect the mechanical and metallurgical properties such as fatigue life [28] and resistance to stress corrosion cracking (SCC), crack initiation and propagation [29] and wear [30]. Surface treatment techniques such as LSP and shot peening (SP) are used extensively in metallic components to induce beneficial compressive residual stress near and at the surface that can improve these mechanical and metallurgical properties since the preferred site for initiation of fatigue cracks is often free surfaces.

LSP irradiates an object with high intensity laser pulses (in the order of nano-seconds) that ionizes the metal surface into plasma. The plasma is confined by a transparent medium [31] such that the high pressure generated is transferred through the metallic object via shockwaves. These shockwaves

exceed the dynamic yield strength of the material [32] and cause plastic deformation at the surface and up to a depth of around 1 mm which affect the properties and microstructure of the material [33]. The elastic response of the remaining material generates a beneficial compressive residual stress near the surface and typically up to 1 mm depth. The shape and depth of the induced residual stress distribution depend on the LSP processing parameters [34, 35], surface condition of the material [36], and the geometry and thickness of the specimen [37]. Sacrificial absorbent coatings are often employed to prevent melting, laser ablation [31, 33] and surface damage due to direct laser/material interaction, thereby ensuring that a mechanical cold-working process is applied.

Compressive residual stress induced by LSP is typically greater in magnitude and reaches a greater depth than conventional SP [38, 39] and with less surface roughness [40]. Early development of LSP focussed on increasing resistance to crack propagation to improve fatigue life [33, 41, 42]. LSP can result in greater fatigue life improvement compared to SP due to the greater depth and magnitude of LSP-induced compressive residual stresses [37, 41, 43]. Application of either LSP or SP increases the surface roughness compared to that of the baseline material which can provide additional crack initiation sites and reduce fatigue and fretting fatigue life [44], and resistance to wear [45] and corrosion [46]. The surface condition of the target material and the processing parameters of the surface treatment technique influence the resulting surface roughness [40]. Due to the deeper layer of compressive residual stress of LSP, the surface roughness can be reduced down to similar levels as that of the baseline material with significantly less relaxation of the compressive stresses than in the case of SP.

During LSP treatment the material undergoes high strain rates of $10^6 \cdot s^{-1}$ [47] due to plastic deformation that result in microstructural changes [44] and grain refinement [30] near the surface. The refined microstructure can lead to improved material properties such as surface hardness [48] which translate to greater fatigue strength [41], tensile strength [49] and wear resistance [30]. LSP-induced compressive residual stresses combined with the refined microstructure and enhanced mechanical properties has shown significant improvement in fretting fatigue life of contacting surface [50] and resistance to SCC [51]. The microstructural features are dependent on the LSP processing parameters [44] and number of impacts [43] (which result in further plastic deformation and subsequent grain refinement). However, defects such as microcracks [52], craters, holes, solidified droplets [53], mild indentations [52] and internal cracking [54] have also been observed depending on the target material and LSP processing parameters. Internal rupture of components has also been reported due to over-processing [55]. Therefore, LPS processing parameters must be carefully selected and optimised to avoid the introduction of defects into the material.

LSP has been applied to a wide range of materials including titanium alloys [35, 44, 50], aluminium alloys [31, 40] and various grades of steel [32]. LSP has many potential applications such as in the aerospace industry to treat components ranging from turbine blades, rotor components and gear shafts for example and has advantages over SP for treating components with features such as fastener holes

in aircraft skin panels. Geometric features such as fillets and notches are difficult to treat using SP, but can be treated using LSP [56]. LSP can be applied to thin sections, however, the effect of tensile stresses must be carefully considered to avoid distortion of the component [56]. Distortion can be minimised by applying LSP to both sides of the component since the reflected tensile stresses cancel out [57]. This approach is commonly used in gas turbine compressor blade applications [55, 57] such as increasing the durability of a turbine blade leading edge to guard against foreign object damage [58, 59]. LSP has been applied to turbofan engines in military and commercial aircraft [60] such as the F-16, F/A-18, F-22, B-2, Airbus A320, Boeing 777, Boeing 787 and Gulfstream 650 to mitigate fatigue failures.

Optimising the LSP processing parameters for a specific application is complex since an effective LPS process depends on the combined effects of the laser specification, numerous LSP parameters, target material, specimen geometry, as well as the properties of the transparent confinement medium and sacrificial absorbent layer. Selecting the most appropriate laser system type and LSP process parameters such as wavelength, pulse frequency, energy per shot, spot shape, spot size and power intensity is paramount to achieving the desired outcome in a particular application. The parameter selection can be optimised by extensive experimental work and numerical simulation since no standardised LSP processing parameters exist at present. An important measure of the effectiveness of the LSP process is the resulting compressive residual stress distribution. The residual stress distribution induced by LSP can be challenging to measure accurately since it usually exhibits a steep gradient near the surface and a local minimum within the first 0.4 mm from the surface. After maximum compression is reached, the stress distribution tends towards tensile at around 1 mm depth (depending on material, LSP parameters and specimen thickness) so that the complete through-thickness stress remains in equilibrium. Although there are numerous residual stress measurement techniques, some discrepancy usually exists between techniques in quantifying the residual stress distribution, especially at the surface. Use of modelling and simulation of the LSP process can greatly reduce the experimental cost of investigating all the parametric combinations [35]. Many investigations have been conducted, for example, the laser-material interactions to predict the induced residual stress distribution [61, 62] and surface deformation [63]. The numerical models have shown good agreement with experimental measurements, especially for thick sections but further work and validation of numerical models are still required to fully determine the effects of LSP processing parameters. It is, therefore, important to be able to accurately measure the LSP-induced residual stress distribution so that the process parameters can be optimised for a particular application.

The detrimental effects of residual stresses, and techniques that can impose beneficial residual stress in advanced materials are critical to many present and future industries. Therefore, it is of paramount importance that accurate, affordable, accessible and reliable residual stress measurements techniques are further improved and developed.

2 Literature Survey

Many different non-destructive, semi-destructive and destructive techniques exist to measure residual stresses, each with varying degrees of complexity, accuracy, material applicability and implementation difficulty. In any residual stress measurement, it is essential to estimate the uncertainty if the significance of the measurement is to be assessed. This section reviews some of the most common and widely used residual stress measurement techniques, that are relevant to this thesis, and assesses each method's suitability to measure residual stresses in FRP laminates and LSP-induced stresses in isotropic materials.

2.1 Non-destructive Diffraction Techniques

Diffraction techniques are non-destructive and are used for the identification and quantification of the constituents of crystalline structures. Diffraction patterns are obtained when an object with crystalline structure is irradiated by particles such as X-ray photons, neutrons or electrons. The basic principle of diffraction techniques is based on Bragg's Law [64], which defines the relationship between the angle of the incident radiation, the wavelength of the radiation and the crystal lattice geometry of the irradiated object.

2.1.1 X-ray Diffraction

X-ray Diffraction (XRD) is a near-surface measurement technique that can be used to determine the residual stress from the strain and associated X-ray elastic constants (XEC) in a crystal lattice [65]. XRD measurements are made using the plane stress assumption where the stress normal to the surface is zero [66]. High energy X-rays, which penetrate a small distance below the surface, are used to irradiate a specimen. Crystal lattice planes diffract the X-rays according to Bragg's Law and detectors record the intensity of the diffracted rays at different angular positions as they rotate around the specimen. A widely used method is the $\sin^2\psi$ approach [67] where the lattice spacing is measured for a range of ψ tilts. Lattice spacing is plotted against $\sin^2\psi$ and the stress is determined from

the slope of a linear or elliptical least-squares fit to the data. The technique is limited to crystalline materials, ideally with small grain sizes. Large grain sizes can adversely affect the XRD measurement since fewer grains within the irradiated volume contribute to the diffraction peak. This results in lower peak intensities and reduced accuracy in location of the peaks [66]. The texture of the material is also important since it can cause large variation in diffraction peak intensity between ψ tilts. This effect can be mitigated somewhat by using appropriate ψ tilts and by oscillation in ψ by typically $\pm 2^{\circ}$ such that grains over a larger area contribute to the measurement [66]. Since X-rays penetrate some depth into the specimen, the measured strain and residual stress is essentially an average over the penetration depth of a few microns below the surface. The surface roughness of the sample should, therefore, clearly be smaller than the penetration depth [68].

The penetration depth depends on various parameters such as the linear absorption coefficient of the material, ψ tilt, diffraction peak intensities and Bragg reflection angle [65]. Soft X-rays are most commonly used, which have a penetration depth of up to 50 µm depending on the material under investigation [69]. For aluminium alloys the penetration depth is up to 20-30 µm [70]. Hard X-rays from synchrotron sources, however, have greater penetration [26]. A synchrotron is a circular electron accelerator that uses extremely powerful magnetic fields to maintain the particles on a closed path. As the electrons pass through these various magnetic fields, extremely bright and high energy light is produced. By channelling specific wavelengths of light off the main beam, several experimental workstations can be set up to conduct a diverse number of experiments including X-ray wavelengths for residual stress measurements in crystalline materials. These X-rays have a penetration depth of as much as 145 µm when interacting with aluminium alloys [71], however, access to this type of equipment can be difficult to obtain. If measurement of a residual stress profile beneath the surface layer is required, successive XRD measurements with material removal by electro-polishing between measurements is necessary [66, 72].

Residual stress measurements from XRD can be prone to relatively high uncertainty since the technique is sensitive to small variations in the crystal lattice [65, 69] and to errors arising from the possible difficulty in determining the position of the diffraction peak [66], operator skill, uncertainty in alignment and equipment calibration. Therefore, a robust experimental technique is required to minimise the effect of various measurement uncertainty sources [73]. A thorough uncertainty estimation for XRD is difficult since many uncertainty sources are non-quantifiable [66]. The main XRD uncertainty sources have been investigated by inter-laboratory comparisons [74] with 16 participating laboratories using 21 different XRD instruments. The largest sources of measurement uncertainty were found to be associated with the peak fitting software and the operator. Total measurement uncertainty in the region of ± 20 MPa is common [69, 75]. XRD has been widely used to measure LSP-induced residual stress distributions in metals [35, 43, 46, 76].

Since this technique requires that the material be crystalline [69], its application to FRP components is limited. Researchers have, however, addressed this issue by adding small metallic filler particles

[77–79], roughly the same size as the diameter of a single fibre, into the resin before curing the FRP component. Nickel and aluminium powder are commonly used due to their small particle size (≈5 µm and ≈3 µm, respectively) which causes minimal disruption of the fibres in the laminate [80]. The residual stresses within these particles are measured during X-ray diffraction. A supplementary experiment is required to relate the strain in these particles to that of the surrounding laminate [81]. The full three-dimensional strain tensor can be determined from this technique, and hence the full stress tensor. While metallic particles can be added to the resin when components are manufactured for the purpose of residual stress measurement, it is not done during general manufacturing of FRP laminates which prevents residual stress measurements in existing FRP components or those manufactured by a 3rd party. The small penetration depth of XRD cannot be easily overcome with successive layer removal in the case of composite laminates since layer removal will lead to increasing curvature of the remaining asymmetric laminate and strain release due to the removal of material which would need to be included in all subsequent residual stress calculations. Therefore, this technique is unsuitable for general residual stress measurement in FRP laminates.

2.2 Relaxation Techniques

The use of relaxation techniques is usually required in the case of FRP laminates since non-destructive residual stress measurement techniques such as XRD and neutron diffraction (ND) have highly restricted application, or cannot be applied due to lack of crystallinity [82] . Relaxation techniques are also extensively used to measure residual stresses in crystalline components since these techniques usually allow more affordable and accessible measurement of through-thickness residual stress distributions. Relaxation techniques involve the measurement of deformations arising from the removal of stressed material [83]. The deformations, which are typically measured in the form of displacements or strains, are used to calculate the residual stresses that existed in the material prior to its removal. Commonly used techniques include layer removal [84], slitting (crack compliance) [85] and hole-drilling [86]. Irrespective of the technique used, relating measured deformations to the residual stresses creates a computational challenge [87] since the stresses are calculated at a different location from where the deformation measurements are taken and the displacement field around the removed material may be non-uniform. Additionally, all stress components throughout the volume of removed material affect the measured deformation in the adjacent material. The relaxation techniques all differ in their material removal geometry and deformation measurement location, but the resulting integral equations that govern the relationship between the residual stresses that existed in the removed material and the measured deformations are similar [87].

Calculation of the residual stresses from the integral equations consists of two separate steps, namely the forward and inverse solutions [85, 87]. In the forward solution, the deformations as a function

of depth of material removed, or the 'calibration coefficients', are determined for known through-thickness stress distributions. This can be done using a fracture mechanics approach or finite element (FE) calculations [88–91]. The inverse solution makes use of the calibration coefficients, obtained from the forward solution, to determine the residual stresses that most closely approximate the measured deformation response. The use of FE calculations to determine the calibration coefficients allows greater flexibility in the specimen shape, material properties, and experimental procedure than if only analytically calculated factors are used [92]. This has led to the development of computational techniques such as the unit pulse integral method and series expansion [93].

The most commonly used computational technique is the unit pulse integral method, where the through-thickness stress distributions utilised to determine the calibration coefficients are unit pulses of uniform stress that are assumed to be released with each increment in cut or hole depth [85, 93]. The inverse solution of the integral method produces a strain fit that exactly matches the measured data, since the number of unknown coefficients is equal to the number of material removal depths [94]. This causes the approach to be sensitive to measurement errors [95, 96] which places severe demands on the experimental deformation measurement technique, as well as the accuracy of the results obtained from the FE calculations [97]. Second derivative Tikhonov regularisation [98], which adds continuity to the minimisation function, is often utilised to smooth the resulting residual stress distribution and remove noise artefacts by allowing a misfit between the calculated strain data and the measured strain data. It requires an iterative process to determine the optimal degree of regularization that should be applied [87]. The Morozov Discrepancy Principle [98] can be used to determine the optimal degree of regularization such that the RMS of the misfit equals the standard error in the strain measurement. Tikhonov regularization in its standard form cannot be used for discontinuous stress distributions in layered composite materials [99].

Series expansion is an alternative approach, where it is assumed that the residual stresses are expandable into continuous stress distributions defined by a series of functions [92]. Series expansion has the advantage that the inverse solution employs a least-squares approach, where a best fit of the calibration coefficients to the measured data allows the amplitudes of each term in the series to be determined simultaneously, and consequently, the residual stress distributions to be completely defined [85, 88]. Since the strain fit is not constrained to pass through all the experimentally measured data, this method is inherently tolerant of small measurement errors [94]. The least-squares approach is particularly effective when the number of deformation measurements is considerably greater than the number of unknown amplitude coefficients [94], which can be achieved through the use of small material removal increments. Prime and Hill [94] made use of Monte Carlo simulation [100] to demonstrate that when series expansion is used, the uncertainties associated with the inability of the chosen series to exactly fit the measured strain variation are important and must be considered alongside the usual errors in the measured data. If this source of uncertainty is ignored, a conventional uncertainty estimate is generally non-conservative, sometimes by more than an order of magnitude.

Series expansion residual stress measurements are susceptible to high uncertainties near the surface and towards the bottom of material removal due to the series being less constrained at their ends.

The most common technique used in the forward solution of series expansion is to apply surface pressure series, either power or Legendre, to the wall of the cut. Since a stress is applied directly, boundary conditions must be carefully considered to ensure self-equilibrium. Legendre functions are the most commonly used since they automatically satisfy the self-equilibrium requirement [101–103] for orders greater than 1, however, power series expansion [93, 104] has also been employed. A limitation of the standard method is that it is not suitable for discontinuous residual stress distributions as in layered composite materials [99]. Alternatively, series expansion of initial strain, or eigenstrain, distributions can be used in the forward solution of the incremental slitting and hole-drilling techniques [105–111]. Eigenstrain distributions give rise to residual stresses due to the redistribution of mechanical strain throughout the thickness of the specimen. The resultant stress distribution is inherently self-equilibrating regardless of the eigenstrain distribution used since no external force or moment is applied. Eigenstrain distributions described by Legendre series require a finer mesh to adequately represent the increasing number of turning points in the Legendre series. Power series on the other hand can be represented by a much coarser mesh which reduces the computational requirement for FE calculations.

2.2.1 Incremental Slitting (Crack Compliance)

The incremental slitting technique was initially developed by Vaidyanathan and Finnie [112] in 1971, and requires a slit to be incrementally deepened through the thickness of a component containing residual stresses. The release of these stresses alters the state of stress within the remaining component, which must always satisfy force equilibrium. The removal of stressed material results in measurable deformation of the component. These deformations can be used to determine the residual stresses released by each depth increment of the slot, allowing the through-thickness residual stress distribution to be obtained. Strain gauges are most commonly used to measure the deformation caused by incremental slitting, although optical techniques like Moiré interferometry [113] and digital image correlation (DIC) [114] have also been used. To enable through-thickness measurement, strain gauges are bonded on the back face of the specimen directly below the cut and aligned normal to the cut plane. Sometimes a second strain gauge is bonded on the top face, in close proximity to the cut, that allows for increased resolution of the surface residual stresses [85]. The strain response of the gauge on the top face saturates relatively quickly, thereby preventing its sole use to determine the through-thickness residual stresses.

Wire electrical discharge machining (EDM) is the preferred method of cutting [85] since it is a non-contact method and does not introduce significant cutting stresses. The application of wire EDM to FRP laminates is limited since these materials are poor conductors. Mechanical machining of the slot,

such as sawing [115, 116] and the use of milling cutters [102, 117], has also been utilised, however, these methods introduce significant cutting stresses which can affect the strain response of the top face gauges, thereby producing erroneous near-surface stresses [85]. Fortunately, the strain gauges bonded to the back face are not significantly affected by additional cutting stresses, and accurate results can be obtained provided that thermal effects associated with the cutting process are accounted for [85]. A slot extended up to 95% through the thickness of a component can produce accurate results. Beyond this depth, however, difficulties arise with regard to supporting the mass of the free ends of the component, which greatly affects the strain response [87]. Additionally, the finite length of the strain gauges also influences the measured strain response as the depth of cut approaches the specimen thickness [87].

The slitting technique has been used to measure LSP-induced residual stresses in metals [118–120] and residual stress variations within individual deposit layers of SLM AM Ti-6Al-4V specimens with layer thickness of 500 µm [121]. The incremental slitting technique has also been used to measure the residual stresses within layered components [122–124] and metal matrix composites [109], but has seen less application to FRP laminates [4, 115, 116, 125]. Power series expansion has been applied to discontinuous stress profiles with the incremental slitting technique by utilising separate series expansions for each material layer [4, 115, 124]. Residual shear stresses in FRP laminates are usually more important than in isotropic materials since significant shear stresses are more likely to exist in FRP laminates due to their heterogeneous composition [125]. While slitting focusses on determination of the residual stress component normal to the slit face, the slitting process also releases two in-plane and out-of-plane shear stress components which influence the measured strains [125]. Shokrieh and Akbari [125] investigated the effect of residual shear stresses on the measured strains in carbon/epoxy and glass/epoxy laminates as well as a steel specimen using FE calculations. The strain distribution on the top and back surfaces due to relaxation of shear stresses was compared with the strain distribution due to the residual stresses normal to the cut. It was found that the shear stresses have a negligible effect on the measured strains on the back surface of the specimen, but an appreciable effect on the top surface strain measurement that cannot be ignored. A method was also presented to separate the effects of normal and shear stress components using strain gauges on both sides of the slit on the top surface. This method also allows strains due to the in-plane and out-of-plane shear stresses to be isolated from each other, which could allow calculation of residual shear stress distributions using slitting.

Residual normal and shear stresses can be determined simultaneously from a single strain gauge when using eigenstrain distributions in the forward solution. Prime and Hill [109] illustrated successful application of this method to determine residual stress distributions in a metal-matrix composite using a strain gauge on the top surface of the specimen. Large out-of-plane shear stresses were measured, but the in-plane shear stress was assumed to be zero or have negligible effect on the experimental strains. Ekbote et al. [126] used series expansion of continuous eigenstrains to determine the discontinuous

residual stress distribution in multi-layered ceramics. This is possible since continuous eigenstrains in the forward solution generate discontinuous stress distributions due to changes in material properties. However, this does not ensure that a good fit to experimental strain data of layered composite materials can be obtained in the inverse solution since the strain release in these materials can exhibit sharp turning points or slope discontinuities that cannot be well approximated by continuous eigenstrain functions.

The integral method has also been used with slitting in composite materials, however, since standard Tikhonov regularization cannot be applied to layered composite materials, regularization must either be applied separately to each material layer [99] or regularization must be adapted to allow for discontinuities at the interfaces between changes in material [127]. Akbari et al. [99] used unit pulses of uniform stress and Tikhonov regularisation to measure the hoop stress distribution in a [90/±45/90] carbon/epoxy filament-wound ring. An axial slit was incrementally deepened from the outer surface of the ring, and the resulting circumferential strain response was measured directly below the cut. These authors utilised FE calculations to determine the calibration coefficients and demonstrated the effectiveness of Tikhonov regularisation in stabilising the residual stress distribution obtained using unit pulses. Tikhonov regularization combined with Morozov Discrepancy Principle was applied separately to each ply orientation of the carbon/epoxy ring. To achieve this, the effects of residual stresses in upper plies on measured strains in lower plies were initially removed prior to computing the stresses within each ply orientation. Prime and Crane [127] demonstrated that Tikhonov regularization can be applied directly when dealing with stress discontinuities in layered materials with the slitting technique. The second derivative regularization matrix was adapted such that continuity across the interface between layers is not enforced, thereby allowing regularization to be applied to discontinuous stress distributions.

The effect of residual shear stresses on the released strain can, however, be large in angle-ply and complex FRP laminates when using the incremental slitting technique. Although the effect has been investigated by Shokrieh and Akbari [125], it is unclear whether the in-plane residual shear stress within FRP laminates can be accurately measured using this approach.

2.2.2 Incremental Hole-Drilling

The hole-drilling technique was first introduced by Mathar [128] to determine uniform through-thickness residual stress in homogeneous isotropic materials. Soete [129] was the first to introduce the use of strain gauges for hole-drilling measurements, whereby the hole is drilled through the centre of the rosette into the material. This approach greatly improved measurement accuracy and reliability. The modern approach is to introduce a blind hole of progressively increasing depth, and is termed the incremental hole-drilling (IHD) technique [130]. IHD is one of the most widely used relaxation techniques [72, 131] because it is practical to implement [82], low cost [132] and yields reliable and

accurate results. Another advantage of IHD is that it is only semi-destructive, unlike other relaxation techniques. Real structures often require holes to be drilled and so the hole introduced by IHD for residual stress measurement, if suitably located, does not necessarily result in the destruction of the part. IHD has a standardised test procedure, ASTM E837-13a [86], for isotropic materials using the unit pulse integral method. The method of determining the through-thickness variation of all three in-plane stress components is based on the assumptions that the stress component normal to the surface is negligible, and that no significant residual stress is induced by the IHD process.

During IHD, strains are measured as stressed material is incrementally removed from the hole. The strain release on the measurement surface quickly becomes insensitive to the removal of stressed material as the hole depth increases, as indicated by Saint-Venant's Principle, and diminishes significantly once the depth of the hole surpasses half the diameter [82]. To overcome this physical limitation, an accurate and robust experimental procedure is essential for the quality of the measurement. The positioning of the hole relative to the centre of the strain gauge rosette is of crucial importance and is a commonly recognised problem with the strain gauge rosette method that can have a significant effect on the calculated residual stress distribution as the measured strains are sensitive to hole-eccentricity errors (i.e. the error due to the hole not being drilled exactly in the centre of the rosette) [5, 82]. Consequently, special strain gauge rosettes are specified in the ASTM standard that improve the accuracy of gauge alignment. Generally, the mean diameter of the strain gauge rosette is between two to four times the hole diameter, making the region covered by the rosette large in comparison to the released strain field [5], limiting the sensitivity of the method somewhat. Optical techniques such as Moiré interferometry [133–135] and Electronic Speckle Pattern Interferometry [136–139], as well as DIC [140] have also been used to measure the deformation response due to hole-drilling in isotropic materials. IHD calibration coefficients can be determined experimentally [141], numerically using FE calculations [89–92] or analytically [142, 143]. Factors determined using FE calculations are generally more consistent than those determined experimentally [82]. The coefficients depend on the material properties, strain gauge rosette geometry, as well as the hole geometry, position, diameter and depth [144]. A detailed approach to estimate the uncertainty in stress measurement is not included in the ASTM standard, but is of utmost importance to evaluate the applicability of any IHD computational method. Numerous investigations have been conducted that propose approaches to estimate the stress uncertainty and define the main sources of uncertainty. Notable recent studies include the works of Peral et al. [145], Richter and Müller [146], and Scafidi et al. [132].

The stress concentration around the hole may induce localised yielding if the residual stress is similar in magnitude to the yield strength of the specimen material, which can introduce significant errors [86, 147]. Experimental and analytical studies have been conducted [148] that found that errors arising from localised yielding are negligible if the residual stress is below 70% of the yield strength of the specimen material. However, when the residual stress exceeds this limit, errors of 10% to 30% (and greater) have been reported. According to the ASTM standard, acceptable results can be obtained

if residual stresses are below 80% of the yield strength when the specimen thickness is greater than the mean diameter of the strain gauge rosette. This limit may be insufficient for highly non-uniform stress distributions due to the successive calculation nature of the integral method which means that any errors due to plasticity effects near the surface will propagate through the depth of the calculated stresses [147]. In this case, a limit of 60% of the yield strength is more appropriate [149]. A plasticity correction factor has been proposed by Beghini et al. [150] and its use has been extended by Nobre et al. [147] for the case of non-uniform stress distributions induced by surface treatment, where the yield strength of the surface treated layers is also incorporated.

Several drilling techniques have been investigated for IHD and the most common technique involves the use of carbide burs or end mills driven by a high-speed air turbine or electric motor rotating at 20 000 to 400 000 rpm [151] to reduce drilling induced stresses. This technique is suitable for all but the hardest isotropic materials. Low-speed drilling using a drill-press or power hand-drill is discouraged because the technique has the tendency to create machining-induced residual stresses at the hole boundary [152]. Zero depth detection is essential for any hole-drilling residual stress measurement, and can be a significant source of stress uncertainty [132, 145]. For metals and other conductive materials it is possible to use an electrical contact technique that identifies the contact between the end mill and the surface of the specimen when the electrical connection occurs.

2.2.2.1 Integral Method

The unit pulse integral method is the most widely used computational method for IHD. The method is well known and fully documented in the ASTM standard. When a through hole is drilled into stressed material at the centre of a rosette, Kirsch's ideal plate model allows the radial strain release on the measurement surface to be related to the relieved uniform stress distribution by equation (2.1). Equation (2.1) forms the basis for residual stress calculation procedures in isotropic materials [153], where $c = 2b$.

$$\epsilon_r = a\,(\sigma_x + \sigma_y) + b\,(\sigma_x - \sigma_y)\cos 2\theta + c \cdot \tau_{xy} \sin 2\theta \tag{2.1}$$

The calibration constants, a and b, that are used to relate the measured strain response to the released residual stresses must be found. The unit pulse integral method is a derivation of the uniform stress calculation procedure, where equation (2.1) is rewritten in vector-matrix form. The stresses, σ and τ, become vectors of the residual stresses contained within the incremental hole depths. The strain, ϵ, becomes a vector of strains measured on the surface of the specimen for the incremental hole depths. The strain release is due to the residual stresses in each hole depth increment and due to hole geometry changes [130]. The calibration constants a and b become matrices, $\bar{\mathbf{A}}$ and $\bar{\mathbf{B}}$, relating the various stresses and strains. The $\bar{\mathbf{A}}$ and $\bar{\mathbf{B}}$ matrices can be determined by FE calculations for the release of equi-biaxial and shear stress, respectively. When determining the calibration coefficients

in the forward solution, it is assumed that unit pulses of uniform stress exist at each incremental hole depth as the depth of the hole is increased [86, 93]. A physical representation of the coefficients of matrix $\bar{\mathbf{A}}$ is shown in Figure 2.1 [153]. Coefficient a_{43} represents the combination strain resulting from a unit equi-biaxial stress within the third increment of a hole four increments deep. The resulting calibration matrix is lower triangular since only stresses that exist within the hole contribute to the measured strains [154], and the magnitude of the diagonal elements is small which reduces the matrix determinants to almost zero. The calibration matrix of the unit pulse integral method is numerically ill-conditioned, with a large condition number, and is therefore prone to high error sensitivity [82].

The sensitivity to strain measurement errors depends on the distribution of the material removal depths [155, 156] and can increase with an increasing number of depth increments [93, 157], and also with the use of regular depth increments [155, 156]. This sensitivity can be reduced by limiting the number of depth increments used in the calculation [93, 155]. This approach is not always possible, however, when a steep stress gradients exists since the stress in each increment is considered constant [130] and many depth increments are required to represent a rapidly varying stress field adequately as a sequence of uniform stresses. The numerical conditioning of $\bar{\mathbf{A}}$ and $\bar{\mathbf{B}}$ is strongly related to their diagonal elements and Zuccarello [155] has shown that the conditioning can be optimised by ensuring that the diagonal elements of $\bar{\mathbf{A}}$ and $\bar{\mathbf{B}}$ are constant in magnitude. This results in lower sensitivity to measurement errors and consequently reduced stress uncertainty. This approach requires progressively increasing incremental depths with an accompanying loss of resolution, however.

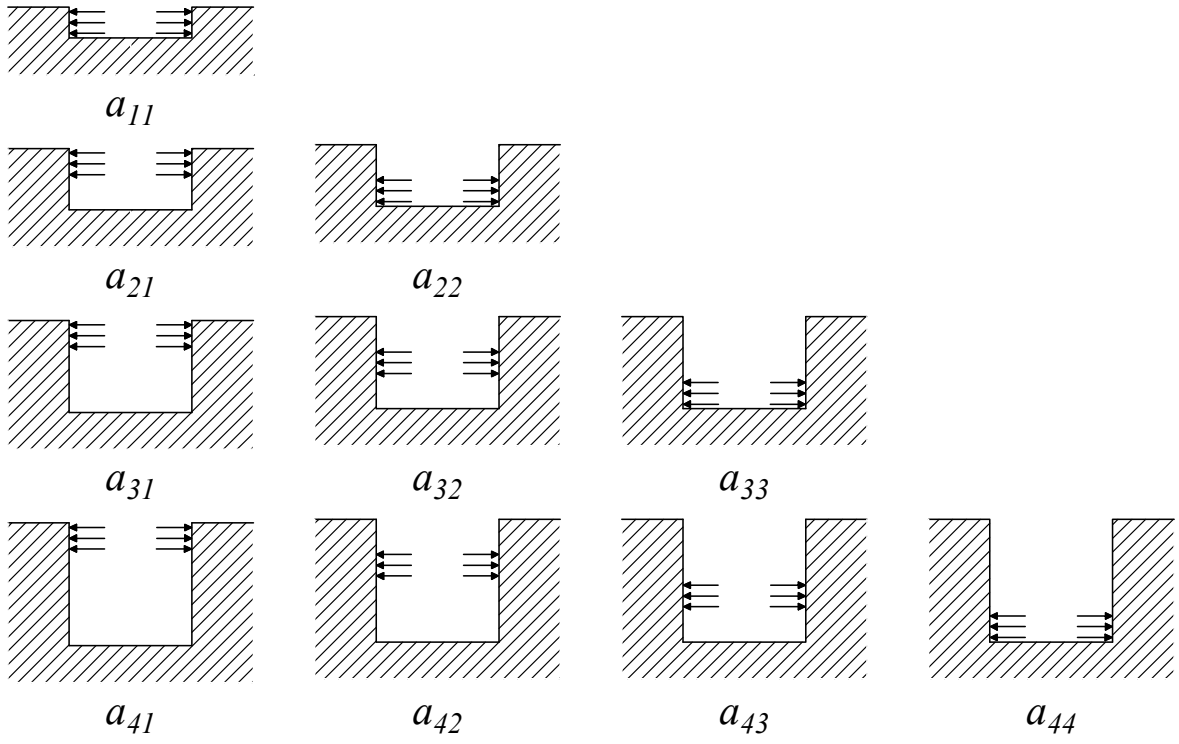


Figure 2.1: Physical interpretation of matrix $\bar{\mathbf{A}}$ coefficients for the integral method

Tikhonov regularization [98] is usually employed with the integral method and IHD in isotropic materials to reduce the sensitivity to measurement errors without sacrificing depth resolution. Small depth increments can be used with Tikhonov regularization to capture a steeply varying stress distribution, which therefore allows the residual stress distribution to be fully defined with minimal uncertainty. When combined with Tikhonov regularization, the assumption of unit pulses does not have a substantial detrimental effect when making many small depth increments and identifying the stress depth at the mid-step depth. The continuity characteristics of the regularized integral solution also allow the interior data to be extrapolated to the surface and, with modern fine-increment drilling, the distance to be extrapolated is small. By the same principle as the inability of series expansion to exactly match the measured strain data [94], the misfit that is allowed by Tikhonov regularization must also be included in any uncertainty estimation for the unit pulse integral method. The extent of regularization must be carefully considered, however, as it can distort the calculated stresses [86].

The ASTM E837-13a standard provides calibration tables for twenty uniform depth increments for a number strain gauge rosette types, and includes the use of Tikhonov regularization. Calibration matrices $\bar{\mathbf{A}}$ and $\bar{\mathbf{B}}$ relate the various stresses and strains according to equations (2.2)-(2.4):

$$\bar{\mathbf{A}}\,\boldsymbol{\sigma}_p = \frac{E}{1+\nu}\,\mathbf{p} \tag{2.2}$$

$$\bar{\mathbf{B}}\,\boldsymbol{\sigma}_q = E\,\mathbf{q} \tag{2.3}$$

$$\bar{\mathbf{B}}\,\boldsymbol{\sigma}_t = E\,\mathbf{t} \tag{2.4}$$

where $\boldsymbol{\sigma}_p$ is the isotropic (equi-biaxial) stress, $\boldsymbol{\sigma}_q$ is the 45° shear stress, $\boldsymbol{\sigma}_t$ is the x-y shear stress and $\mathbf{p}$, $\mathbf{q}$ and $\mathbf{t}$ are combination strain vectors. The Cartesian stresses at each depth increment can be found from $\boldsymbol{\sigma}_p$, $\boldsymbol{\sigma}_q$ and $\boldsymbol{\sigma}_t$ [86].

Using twenty uniform depth increments can lead to high error sensitivity and Tikhonov regularization is employed by using the tri-diagonal 'second derivative' matrix, $\mathbf{L}$, in the form:

$$\mathbf{L} = \begin{bmatrix} 0 & 0 & & & \\ -1 & 2 & -1 & & \\ & -1 & 2 & -1 & \\ & & -1 & 2 & -1 \\ & & & 0 & 0 \end{bmatrix} \tag{2.5}$$

where the number of rows is equal to the number of hole depth increments used.

Equations (2.2)-(2.4) are adjusted to implement Tikhonov second derivative regularization:

$$\left(\bar{\mathbf{A}}^T\,\bar{\mathbf{A}} + \alpha_p\,\mathbf{L}^T\,\mathbf{L}\right)\boldsymbol{\sigma}_p = \frac{E}{1+\nu}\,\bar{\mathbf{A}}^T\,\mathbf{p} \tag{2.6}$$

$$\left(\bar{\mathbf{B}}^T\,\bar{\mathbf{B}} + \alpha_q\,\mathbf{L}^T\,\mathbf{L}\right)\boldsymbol{\sigma}_q = E\,\bar{\mathbf{B}}^T\,\mathbf{q} \tag{2.7}$$

$$\left(\bar{\mathbf{B}}^T\,\bar{\mathbf{B}} + \alpha_t\,\mathbf{L}^T\,\mathbf{L}\right)\boldsymbol{\sigma}_t = E\,\bar{\mathbf{B}}^T\,\mathbf{t} \tag{2.8}$$

Regularization has the effect of smoothing the stress results. The factors α_p, α_q and α_t control the amount of regularization that is applied. Zero values for the factors yield the unregularized results. Positive values of the factors smooth the results progressively as larger factors are chosen. Insufficient regularization leads to excessive uncertainty in the calculated stress results, while excessive regularization distorts the stress results. Optimal regularization is required to balance these two tendencies. The ASTM standard suggests small regularization factors in the range 10^{-4} to 10^{-6}. The regularized strains that correspond to the calculated stresses ($\boldsymbol{\sigma}_p$, $\boldsymbol{\sigma}_q$ and $\boldsymbol{\sigma}_t$) using equation (2.6)-(2.8) do not exactly match the experimental combination strains ($\mathbf{p}$, $\mathbf{q}$ and $\mathbf{t}$). The extent of regularization applied can be determined by adjusting each regularization factor using equation (2.9) until the RMS of the misfit vectors, equation (2.10), are within 5% of the standard errors of the combination strains. A convenient method to estimate standard errors is to separate slowly and rapidly varying features in the measured strains by evaluating a least-squares parabola through successive sets of four adjacent combination strain data points [87]. The local misfit norm of the least-squares fit is used to estimate the standard error using equation (2.11). Shown only for $\mathbf{p}$, but similarly for $\mathbf{q}$ and $\mathbf{t}$. The method described in the ASTM standard is essentially the same as the Morozov Discrepancy Principle even though not directly stated as such. Since the estimate of standard errors is not exact, it may be necessary to adjust the amount of regularization applied if noise artefacts remain, or if distortion of the stress solution occurs [87].

$$(\alpha_p)_{new} = \frac{{p_{std}}^2}{{p_{rms}}^2} (\alpha_p)_{old} \tag{2.9}$$

$${p_{rms}}^2 = \frac{1}{n} \sum_{j=1}^{n} (p_{misfit})_j^2 \tag{2.10}$$

$${p_{std}}^2 = \sum_{j=1}^{n-3} \frac{(p_j - 3p_{j+1} + 3p_{j+2} - p_{j+3})^2}{20\,(n-3)} \tag{2.11}$$

where n is the number of depth increments.

Calibration coefficients provided in ASTM E837-13a have several limitations regarding their use, such as those related with the thickness of the specimen and allowable hole diameter ranges for a specific rosette. According to ASTM E837-13a, non-uniform residual stresses can only be determined in specimens of greater thickness than the mean diameter of the strain gage rosette used. To make use of calibration coefficients provided in ASTM E837-13a to measure residual stress distributions in thinner samples, correction functions must be employed such as proposed by Held et al. [158] and Nobre et al. [76]. Schajer [159] recently reduced the bulk calibration data for IHD residual stress measurement with the integral method to a two-variable polynomial formulation to extend the application of the IHD integral method and further increase ease of implementation. The polynomial formulation comprises 15 numerical coefficients and provides calibration data with average accuracy within 1%, with occasional outliers reaching around 2%. Calibration coefficients for finite thickness or 'thin' specimens are also included. The latest version of the ASTM standard, ASTM E837-20, has been updated in accordance with the work of Schajer [159]. When IHD is applied to isotropic

materials, small variations in hole diameter (from the 2 mm nominal diameter specified in the ASTM) can be corrected by adjusting all calibration coefficients by a factor of $(D/2)^2$ [93]. However, this correction can only be applied to a finite deviation from the nominal 2 mm diameter. A range of 1.88 mm to 2.12 mm is suggested in the ASTM standard for application of the correction factor.

Significant work has been done to extend the use of the integral method with IHD to nearly all applications and to correct common errors such as hole bottom fillet radius and hole eccentricity. Hole-drilling experiments are usually carried out with specific end mills, such as inverted cone mills, to create flat hole-bottoms. The reason for this is simply to achieve the best possible match between the FE models used to obtain the calibration coefficients, and the physical hole-drilling experiments. However, even with specialised end mills, a small hole-bottom fillet radius is usually present. To include hole-bottom fillet radius in the FE model would require a significantly more detailed mesh and severely affect computational time which is not practical at present. It is not currently possible to account for the hole-bottom fillet radius when measuring highly non-uniform stresses [145]. Calibration coefficients determined by FE calculations according to the real blind hole geometry have been investigated for uniform stress distributions [160] and have been found to have an appreciable effect on the measured stresses, especially in the first few hole depth increments. Hole eccentricity is a commonly recognised problem with the strain gauge rosette method and can have a significant effect on the calculated residual stress distribution. Correction for hole eccentricity in isotropic materials is available [161–163], but these corrections cannot be directly applied to layered composite materials. This effect can be somewhat mitigated by the use of a 6 element strain gauge rosette, but it cannot be fully compensated for by this alone because of the complex strain field around the hole.

IHD with the integral method has been widely used to measure the residual stress distribution in isotropic materials [164–166], including shot peening [167] and LSP-induced residual stresses [76, 168] in aluminium, with good correlation to XRD measurements. However, the IHD method is susceptible to large stress uncertainties near the surface primarily due to uncertainty in establishing the the zero depth datum of the measured strain data. IHD with the integral method has also been used to measure residual stress distributions in SLM AM Ti-6Al-4V specimens [121] where reasonable correlation with incremental slitting measurements was found.

2.2.2.2 Series Expansion Method

Schajer [92] initially proposed the use of series expansion with IHD for isotropic materials in 1981 by applying power series stress distributions to the wall of the hole. However, application of this approach has been limited due to possible numerical instabilities arising from the use of series orders greater than 1 that can increase the uncertainty in stress or distort the stress solution [92, 115]. Higher order Legendre series have, however, been successfully used with the slitting technique [4, 94, 109, 124].

While Schajer [92, 169] found numerical instabilities for series orders greater than 1, only a limited number of depth increments were used that may have prevented the full benefits of series expansion with IHD from being realised. Schajer only used 6 depth increments of 100 μm in 1981 [92] and only 4 depth increments in 1988 [93], presumably due to the experimental and computational limits of the time. With this limited number of strain measurements, higher order terms are not of much use, and can easily become unstable. Successful use of series expansion requires convergence to a solution as the series order is increased, and before instability dominates. However, due to the discontinuous nature of the stress results at lower orders, large changes occur between each stress distribution in the sequence which gives the appearance of instability at low orders. Nobre et al. [149] used four IHD computational methods, including first order power series expansion and the unit pulse integral method, to measure rapidly varying SP-induced residual stress distributions in five different grades of steel specimens. IHD stress measurements were compared to XRD measurements combined with electrolytic layer removal technique to achieve residual stress depth profiles. First order series expansion was unable to satisfactorily describe the rapid near-surface stress variation and local minimum of the SP-induced stress distribution. A significantly higher series order would be required to describe such a stress distribution.

A limitation of the standard series expansion method is that it is only suitable for continuous stress distributions. Continuous eigenstate functions can be used in the case of discontinuous stress distributions such as those in layered composite materials, however, the abrupt changes in material properties at the interfaces between material types can result in sharp turning points or slope discontinuities in the strain measurements at these interfaces. This type of strain distribution is difficult to describe using a least-squares curve fit of a single series, even at very high orders, which prevents the use of standard series expansion.

2.2.2.3 Incremental Hole-Drilling in Composite Materials

Application of IHD in composite materials and FRP laminates has not been as frequent as in isotropic materials, especially in complex angle-ply laminates. In isotropic materials, the relationship between residual stresses and measured strains in each depth increment has a trigonometric form that allows the number of calibration coefficients to be decreased from nine to three in the case of through-hole drilling to facilitate the calculation of uniform residual stresses. The first extension of the through-hole drilling technique for the measurement of uniform residual stresses in orthotropic materials was presented by Bert and Thompson [170]. Thereafter, Lake et al. [141] proposed a residual stress calculation procedure for orthotropic materials using three calibration coefficients based on equation (2.1), for which c is independent of a and b. However, Schajer and Yang [144] showed that the displacements around a hole in a stressed orthotropic plate do not have such a simple form, which can lead to erroneous results. Subsequently, Schajer and Yang, based on Smith's work [171], proposed a procedure to determine uniform through-thickness residual stress distributions in orthotropic materials using nine calibration coefficients. However, the elastic properties of FRP laminates can change suddenly from ply to ply. Therefore this approach cannot be used with cross-ply or angle-ply laminates because of the discontinuities in stress that exist at the interfaces between plies of different orientations. Pagliaro and Zuccarello [172] extended this technique to determine discontinuous residual stress distributions in symmetric cross-ply and angle-ply laminates. In this work, the stresses were assumed constant in each ply. Ghasemi et al. [173] made the same assumption and used the integral method to determine the residual stresses in symmetric and asymmetric cross-ply composite laminates, as well as symmetric quasi-isotropic laminates. The calculated residual stresses compared favourably with theoretical calculations. Sicot et al. [90] adapted Lake's model [141] for IHD where the redistribution of stresses after each increment are taken into account. The principal stresses in each depth increment are related to the measured strains by three calibration coefficients. This method was used to determine the through-thickness residual stress distributions in unidirectional and cross-ply laminates using unit pulses. Gong et al. [174] further refined the method of Sicot et al. [90] to remove mathematical approximations and subsequently investigated its use to measure variations in residual stress distributions between simple FRP laminates of $[0_2/\theta_2]_s$ construction.

Most recent studies deal with the residual stresses determination in unidirectional, cross-ply and simple laminates with various propositions, however, work on residual stress measurement in complex laminate configurations (for example, $[\pm\theta]$ angle-ply laminates and quasi-isotropic laminates) is extremely limited. Akbari et al. [157] extended the method proposed by Schajer and Yang [144] to IHD measurement of non-uniform residual stresses in FRP laminates using nine calibration coefficients to represent each stress application depth for each depth increment. This fully coupled unit pulse integral method, considering all three stress and strain directions simultaneously, was implemented to measure the residual stress distribution in a filament wound carbon/epoxy ring of [90/±45/90] construction. These researchers found that the hoop stress varied significantly through the thickness of

each ply. The stress distributions obtained from this method compared reasonably well with regularized slitting measurements [99], and the stress gradient through the thickness of each ply could be measured. However, this method is still susceptible to computational error sensitivity and error amplification. The number of drilling increments was limited to reduce sensitivity to strain measurement errors [93, 155], thereby increasing stability of the stress solution since regularization could not be applied. Limiting the number of depth increments to reduce error sensitivity is common practice, however, this approach is limited if a rapidly varying residual stress distribution exists, since the calculated stress in each incremental depth is considered constant. Distortion of stress results can consequently occur due to averaging effects if the depth increments become too large.

In the case of isotropic materials, many depth increments can be used with Tikhonov regularization to reduce sensitivity to strain measurement errors. The residual stress can be decoupled into equi-biaxial and shear components due to the trigonometric relationship between residual stress distributions and released strains [93], which allows separate application of Tikhonov regularization to the decoupled residual stress distributions. Such a decoupling is not possible in orthotropic materials since the relationship between residual stresses and released strains does not have a trigonometric form [157]. Therefore, Tikhonov regularization has not been successfully implemented with IHD in composite materials or FRP laminates and the integral methods currently employed remain sensitive to measurement errors.

Although the hole-drilling technique is a suitable residual stress measurement method for FRP laminates, there are experimental factors that can also limit the application of the through-hole or IHD techniques in these materials. The measured strain data depends on the drilling and translational speeds [5], and these need to be optimised for each experiment. Drilling speed in composite laminates is an important subject that would appear as yet to be unresolved. Valentini et al. [175] demonstrated the need for low speed electric drilling to avoid melting in unfilled thermoplastic polymers; polyacetal copolymer (POM-C), polycarbonate (PC), polyetheretherketone (PEEK) and polyethylene terephthalate (PET). However, that work does not deal with FRP laminates made with thermosets, which are quite different. Nobre et al. [176, 177], on the other hand, found that high speed drilling is suitable in FRP laminates made with thermosets, provided that slow feed rates and small depth increments are used to reduce heating effects. Zero depth detection is essential for any hole-drilling residual stress measurement, and can be a significant source of stress uncertainty. For metals and other conductive materials it is possible to use an electrical contact technique that identifies the contact between the end mill and the surface of the specimen when the electrical connection occurs. However, this approach is limited with FRP laminates since these materials are poor conductors.

Since the sensitivity of the strain response diminishes significantly once the depth of the hole surpasses about half the diameter [82], IHD can only be used to measure the through-thickness residual stresses in thin FRP laminates. Small variations in hole diameter in FRP laminates cannot simply be corrected by the $(D/D_0)^2$ ratio. The relationship between the hole diameter and that of the strain

gauge rosette directly affects the sensitivity of IHD. The maximum sensitivity is obtained for a hole diameter equal to the diameter of the rosette. The maximum diameter of the hole is, however, limited by the presence of a plastic zone around the hole [89]. At the same time, it is problematic if the diameter of the rosette is significantly greater than the hole diameter due to sensitivity loss as the gauges move further away from the edge of the hole. Correct application of IHD requires optimisation of the relationship between the hole diameter and that of the strain gauge rosette. Sicot and Gong [89] performed tests on cross-ply $[0_4/90_4]_s$ FRP laminates to investigate the optimum relative position of the hole and the strain gauge rosette. Two ratios were defined: $\delta = R_t/R_j$ and $\lambda = R_t/R_{xj}$. Where R_t is the hole radius, R_j the inner radius of the rosette and R_{xj} the centre radius of the rosette. The authors concluded that the ratio δ affects the stability and magnitude of the calculated residual stress and that usable results are only obtained when δ is between 0.3 and 0.5. Furthermore, the ratio, λ, does not have any significant influence on the calculated residual stress, implying that the geometry of the gauge does not play an important role. Corrections for hole eccentricity in isotropic materials [161, 178] is also not directly applicable to IHD in FRP laminates.

The IHD plasticity requirement for metals to ensure that the residual stress is lower than about 60% - 80% of the yield strength is not applicable when dealing with FRP laminates. Yielding normally does not occur in FRP laminates in the same sense as in metals [179]. While the matrix material can exhibit plastic behaviour, failure of the laminate is dominated by the high strain concentration in the matrix. The primary failure modes are tensile matrix failure and fibre debonding [180]. Stress concentrations arising from fibres, interfacial bond flaws and inhomogeneities such as voids and regions of high fibre volume fraction serve as the originators for the development of microcracks [7]. Under increasing load, microcracks can serve as catalysts for further damage and macrocracks [7], eventually causing failure. Unidirectional laminates with tensile loading transverse to the fibres typically fail through cracking parallel to the fibres [181]. As a consequence, fracture parallel to the fibres being the dominant failure mode, the issue of plasticity correction factors is not relevant to FRP laminates, and instead this concern is replaced by the impact of transverse fracture. Similar to localised yielding in isotropic materials, FRP laminates can be susceptible to transverse fracture at the hole. The transverse strength of a glass fibre reinforced plastic (GFRP) lamina is low, around 35 MPa [182]. It is worth noting at this point that the transverse strength should not be considered an intrinsic property of a composite lamina [183]. It is strongly affected by the restraints provided by adjacent plies in the laminate [183]. Effectively, adjacent plies constrain the strains within the lamina and hence prevent premature cracking. As a consequence, the behaviour of a lamina within a laminate is quite different to that of a unidirectional laminate [183]. This also makes it difficult to get representative measurements of the strength transverse to the fibres when within a laminate. While transverse fracture in internal plies might be prevented by the restraint provided by the transverse fibres of adjacent plies, as reported by Flaggs and Kural [183], such restraint does not exist on the upper surface. The possibility of transverse cracking has been reported by Akbari et al. [157], although no physical evidence of cracking was found when investigated under a microscope.

2.3 Gaps in Literature and Opportunities for Improvements and Extensions to IHD

The current state of prominent residual stress measurement techniques is shown in Figure 2.2. While residual stress measurement in nearly any material type can be achieved by one or another existing technique, IHD offers the advantages of being affordable, accessible, practical and allows accurate measurement of all in-plane stress components simultaneously. IHD with the integral method is used extensively and can readily define the residual stress distribution in almost any material type. It has a standardised test procedure for isotropic materials which includes the use of Tikhonov regularization to smooth the calculated stress distribution and remove noise artefacts.

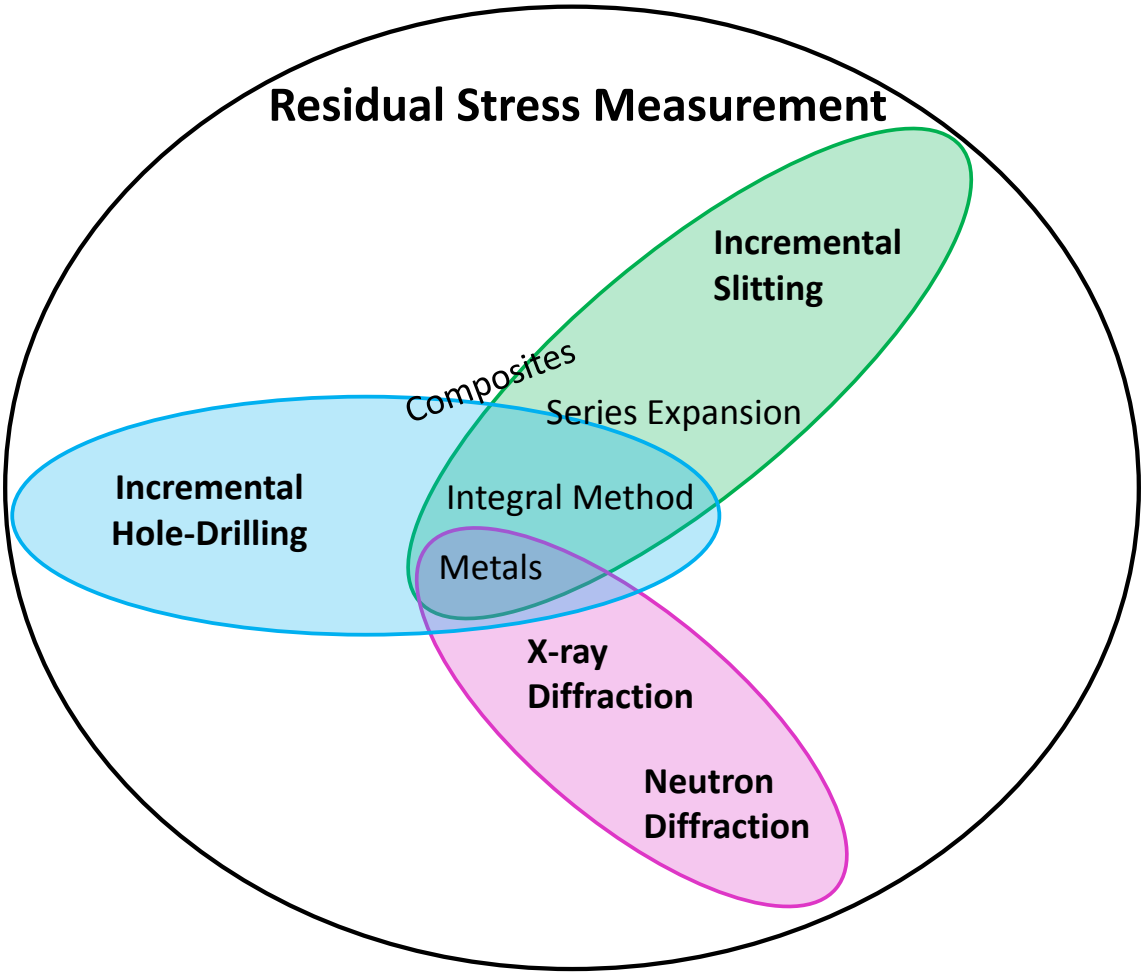


Figure 2.2: Current state of prominent residual stress measurement techniques

The unit pulse integral method with IHD appears effective in composite materials and can be used to measure the in-plane residual stress distributions within angle-ply FRP laminates, however, it requires regulated depth increments to ensure that the stress discontinuities at the interfaces between plies of different orientations can be correctly captured. Additionally, if a steep stress gradient exists within a material type or ply orientation, many depth increments are required to approximate the stress gradient as a sequence of uniform stresses. These approaches have the potential to increase the sensitivity to measurement errors when using pulse functions, however, because the sensitivity can increase with both the number of material removal increments [4, 93, 157] and the use of regular depth increments [155, 156]. Distortion of stress results can occur due to averaging effects if the depth increments become too large. Sensitivity to measurement errors cannot be reduced through application of Tikhonov regularization since it has not been extended to layered composite materials with IHD. Therefore, existing integral methods for IHD have somewhat limited utility and tolerance to measurement errors in layered composite materials for the complex case of measuring discontinuous residual stress distributions where a steep gradient within a single layer may exist. Steep stress gradients can occur within a single ply orientation of a FRP laminate due to tool/part interactions at the surface of a laminate, for example. Currently, no computational method exists for IHD that can simultaneously measure all in-plane residual stress components of complex angle-ply laminates with steep stress gradients through a single ply that is also tolerant to measurement errors and has high depth resolution. Series expansion is an alternative computational method that has seldom been used due to the suspected issues around instability at higher series orders, but has the potential to resolve the limitations of IHD in layered composite materials as it is inherently tolerant to noise in the experimental data or to single erroneous measurements due to least-squares curve fitting in the inverse solution.

Although issues around instability of series expansion has been reported in isotropic materials, the situation may be less problematic in composites materials such as FRP laminates. The discontinuous nature of the residual stresses at changes in fibre orientation, coupled with the typically small thickness of individual plies, means that the residual stress distribution within each ply orientation has low complexity and can, therefore, be well approximated by stress distributions of low order that are less susceptible to numerical instability. Use of separate series in each ply orientation of a FRP laminate could allow much closer representation of strain distributions with discontinuities in slope at interfaces between plies of different orientation and considerably improve the least-squares fit to the experimental strain data.

Tikhonov regularization cannot be applied directly to FRP laminates since there is no trigonometric relationship between residual stresses and released strains. However, the use of IHD with the regularized integral method in FRP laminates would allow measurement of detailed stress distributions with reduced uncertainty and increased tolerance to experimental noise compared to existing integral solutions, and it would be computationally less expensive and more familiar to implement than series

expansion. If the contribution to strain in a particular direction is mostly due to stress in that direction, such as in the case of cross-ply FRP laminates, Tikhonov regularization could potentially be applied separately to each measurement direction, similar to how regularization has been applied to composite materials with the slitting technique. However, with IHD the fully coupled integral method would still need to be applied after regularization to ensure that all in-plane components of stress and strain are incorporated correctly.

The regularized integral method is widely used to measure stress distributions with steep gradients and sharp turning points in isotropic materials, however, it can still be susceptible to larger stress uncertainties or distortion of the stress results depending on the amount of regularization applied. Series expansion has been applied with IHD in isotropic materials but the use of low orders due to issues around instability in the solution has severely limited its use. The foundational work of Schajer was limited by the computational resources of the time and a finer mesh in the forward solution would allow more accurate determination of calibration coefficients for the higher series order terms. The use of fine-increment drilling would provide sufficient experimental strain data points to achieve a robust least-squares fit using higher order series. These adjustments, together with a means to select an appropriate series order have the potential to overcome the reported shortcomings of series expansion in isotropic materials. If series expansion can remain stable up to high enough series orders it could provide an alternative for measuring rapidly varying stress distributions in isotropic materials with potentially reduced uncertainty in calculated stress compared to the regularized integral method due to its inherent tolerance to measurement errors.

An intrinsic characteristic of the IHD technique is that it is susceptible to large stress uncertainties near the surface and XRD measurements are commonly used to complement IHD measurements in isotropic materials to fully define a through-thickness stress distribution. However, the two techniques have never been combined into a single solution. Guo et al. [131] recently identified combining residual stress measurement techniques as an existing opportunity in residual stress measurement. By combining different techniques, the advantages of both techniques can be exploited while minimising the effects of their shortcomings. If constraints can be imposed on the inverse problem of IHD, it would allow incorporation of other residual stress measurements within a single solution such that inherent characteristics of IHD that lead to large uncertainty in stress measurement can be suppressed somewhat.

The primary aim of this thesis is to extend the use of IHD with both the series expansion and regularized integral methods to layered composite materials to reduce sensitivity to measurement errors and improve depth resolution. The secondary aim of this thesis is to use series expansion with IHD to measure complex stress distributions in isotropic materials with reduced uncertainty and incorporate other residual stress measurements, such as XRD, into the IHD solution. Robust uncertainty estimation of calculated stresses is usually lacking from IHD investigations, especially in FRP laminates, and so the performance of existing methods is not fully quantified. A comprehensive and robust uncertainty estimation methodology must therefore be developed so that the significance of the residual stress measurement can be assessed, and informed comparisons made between established and developing methods. The envisioned contribution of this thesis is to extend the application of the IHD technique as shown in Figure 2.3.

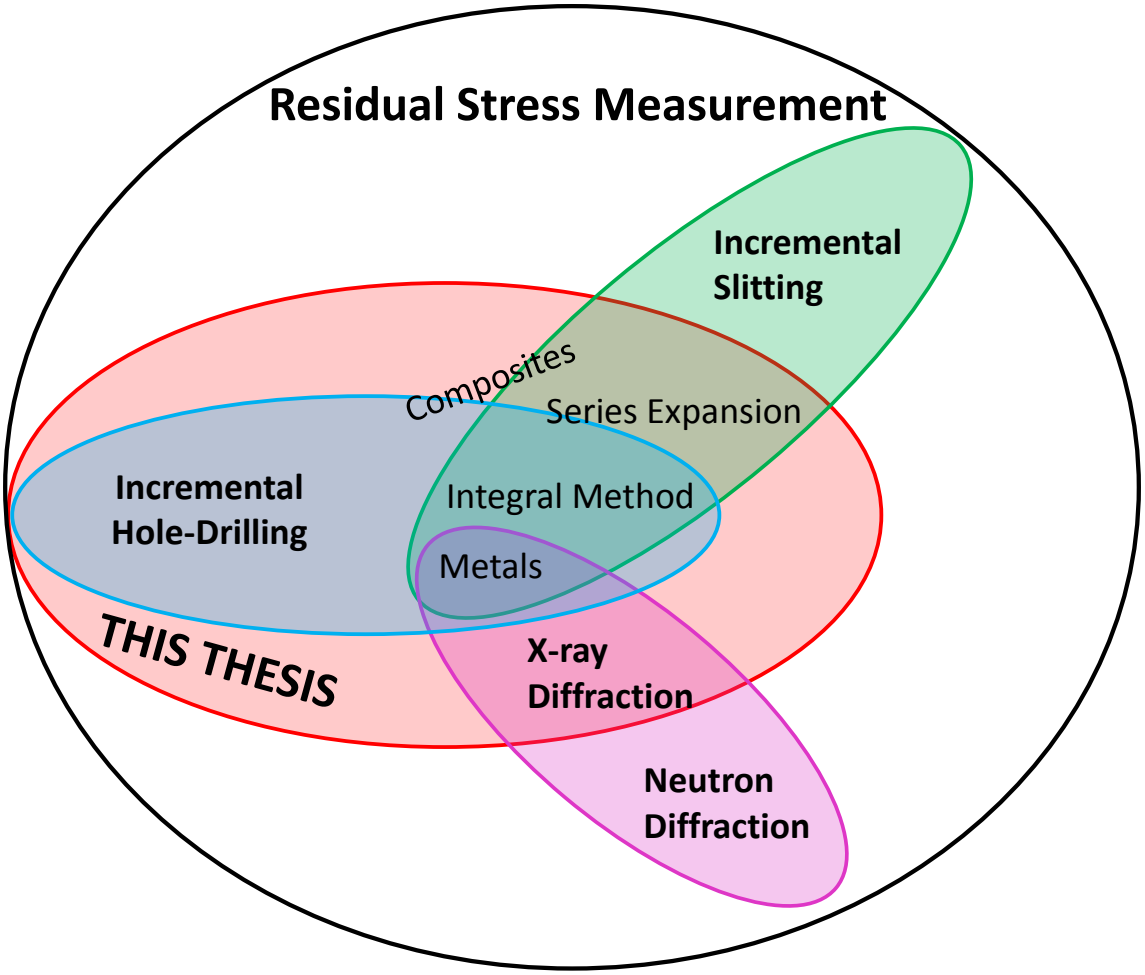


Figure 2.3: Envisioned extension of the IHD technique

3 Research Questions

- IHD is an excellent option for general residual stress measurement, however, it requires further refinement to be truly applicable to layered composite materials such as FRP laminates. Series expansion applied separately to different layers of a composite material has been employed with the slitting technique. Can this approach be successfully extended to IHD to measure all in-plane discontinuous residual stress distributions in a FRP laminate of arbitrary construction?
- Tikhonov regularization has become a mainstay of IHD in isotropic materials with the integral method. It has been successfully used with slitting in composite materials. Can Tikhonov regularization be extended to IHD in cross-ply FRP laminates, considering the complex strain field around the hole, the orthotropic nature of each ply orientation and the discontinuous nature of the through thickness residual stress distribution?
- Does series expansion truly become unstable at orders greater than 1 when applied with IHD to measure residual stress distributions in isotropic materials? If it remains stable beyond first order, can it be used as an alternative to the regularized integral method, especially for measurement of rapidly varying stress fields?
- Can constraints be imposed on IHD solutions to enable the incorporation of residual stress measurements from different techniques into that of IHD to reduce the effect of inherent characteristics of IHD that lead to large uncertainty in stress measurement, such as near the surface?

4 Objectives

The objectives of this work are to extend the use of existing computational methods and to develop new computational methods for IHD to overcome current limitations of IHD residual stress measurement, especially in composite materials. These methods must:

- Be capable of measuring discontinuous stress distributions in composite materials.
- Be capable of measuring highly non-uniform stress distributions in isotropic materials.
- Be versatile enough to allow the imposition of constraints to represent certain physical phenomenon or constraints to known residual stresses through the thickness of the specimen.
- Be more tolerant to noise in experimental strain measurements and other uncertainties and/or achieve greater depth resolution than existing methods.

Achieving these objectives will allow the residual stresses within nearly all material types to be measured using IHD and will also address some issues surrounding the current applications of IHD. Secondary objectives of this work are therefore to:

- Extend the use of separate series expansion to IHD to enable measurement of all in-plane components of discontinuous residual stress distributions within any layered composite material.
- Extend the use of Tikhonov regularization with the unit pulse integral method to cross-ply FRP laminates using IHD.
- Investigate the use of series expansion to determine a rapidly varying residual stress distribution in an isotropic material.
- Use XRD measurements to constrain IHD residual stress measurements near the surface, thereby obtaining full depth IHD stress measurements with reduced uncertainty near the surface.
- Develop a comprehensive and robust means to accurately assess the effects of experimental and computational uncertainties on the calculated residual stress distribution of IHD.

5 Residual Stress Measurement in FRP Laminates with Series Expansion

This chapter presents and demonstrates the use of series expansion with IHD to overcome the limitations of existing computational methods in FRP laminates of arbitrary construction. Power series expansion of eigenstrain is applied to each ply orientation separately in the forward solution to calculate the necessary calibration coefficients at each incremental depth. This ensures that a good fit to the measured strain data can be achieved and the discontinuities in the residual stresses at ply interfaces can be correctly captured. The inverse solution employs a least-squares approach, where a best fit of the calibration coefficients to the measured strain data allows the amplitudes of each term in the eigenstrain series to be determined simultaneously in each ply, and consequently fully define the residual stress distributions of a complex FRP laminate using IHD with series expansion. The residual stress distributions determined from this method are continuous across each ply and discontinuous at the interfaces between plies of different orientation. A comprehensive and robust means of estimating uncertainties in the residual stress distributions is developed using Monte Carlo simulation. Because of the use of least-squares curve fitting, the inverse solution is somewhat insensitive to noise in the experimental data or to single erroneous measurements. The method is also robust against uncertainties in all other input data. The order of the least-squares fit to the experimental data is increased until the residual stress distribution is found from that combination of series orders in the different ply orientations that has the lowest RMS uncertainty, selected only from those combinations that have converged. The method is not limited in its use, allowing the analysis of FRP laminates with any number of plies, orientated in any direction, or any composite material or application where a discontinuity in stress exists through the depth. The method is demonstrated on a GFRP laminate of $[0_2/+45/-45]_s$ *construction.*

This chapter has been adapted and extended from: **T.C. Smit**, R.G. Reid. Residual Stress Measurement in Composite Laminates using Incremental Hole-Drilling with Power Series. *Experimental Mechanics*, 2018, Springer Nature. The published article is available at https://doi.org/10.1007/s11340-018-0403-6. Licensed permission to reuse this content can be found in Appendix I: Springer Nature License Agreements.

5.1 Introduction

IHD with the integral method has been extensively used to measure residual stress distributions in FRP laminates and other layered composite materials. However, most of the existing variations of the integral method are unable to deal satisfactorily with FRP laminates of arbitrary construction or where steep stress gradients exist within a single ply orientation, and all variations are sensitive to small measurement errors. Depth resolution is usually sacrificed by reducing the number of depth increments used in the inverse solution in an attempt to limit the sensitivity to measurement errors. This approach has its limitations, however, and can remove the ability to capture steep stress gradients within a single ply orientation such as those that can occur at the surface of a laminate due to tool/part interactions. Limiting the number of depth increments can significantly reduce stress uncertainty but it can also distort the stress results due to the successive calculation nature of the integral method and averaging effects if the depth increments become too large. This is especially true for complex laminates with numerous ply orientations.

A robust uncertainty analysis is usually lacking from IHD investigation in FRP laminates and since Tikhonov regularization cannot be applied, as in isotropic materials, the residual stresses obtained may yield unacceptably large uncertainty in calculated stresses. IHD strain measurements in GFRP laminates are generally smaller in magnitude than in the case of isotropic materials where surface treatment such as LSP has been used for example. In addition, temperature compensation and drilling induced stresses are significant factors in FRP laminates due to heating of the low thermal conductivity material. Therefore, strain measurement errors can be much larger in terms of percentage when drilling in GFRP laminates which can severely affect the accuracy and uncertainty of the residual stress measurement.

The series expansion method is an alternative that can overcome this limitation of IHD in FRP laminates due to its use of least-squares error minimisation in the inverse solution. The residual stresses in FRP laminates are discontinuous at interfaces between ply orientations which can result in sharp turning points in the experimental strain distributions at these interfaces. This type of strain distribution is difficult to describe using a least-squares curve fit of a single series, even at very high orders, which prevents the use of standard series expansion. To combat this, a separate series expansion method is employed, where the laminate is divided into different regions defined by ply orientation such that lower order series can be used within each ply orientation to better represent the experimental strain distribution and prevent numerical instability and large uncertainty in the stress solution.

5.2 Separate Series Expansion

The series expansion method to determine the through-thickness variation in all three in-plane components of the residual stress is based on the following assumptions. The material is elastic, orthotropic within a single ply, and the stress component perpendicular to the surface (σ_z) is negligible. It is also assumed that removal of material does not induce significant residual stresses in the remaining laminate.

If one considers the residual stress component in the x-direction, where the variation with depth from the surface is $\sigma_x(z)$, the unknown stress distribution is assumed to be expandable into the stress distributions, s_{jn}, arising from unit power series of eigenstrain of order n in all three in-plane components with undetermined coefficients a_{jn}; $j = x, y, xy$ and $n = 0, 1, 2, \ldots$ such that [92]:

$$\begin{aligned}\sigma_x(z) = {} & a_{x0}s_{x0}(z) + a_{x1}s_{x1}(z) + a_{x2}s_{x2}(z) + \ldots \\ & + a_{y0}s_{y0}(z) + a_{y1}s_{y1}(z) + a_{y2}s_{y2}(z) + \ldots \\ & + a_{xy0}s_{xy0}(z) + a_{xy1}s_{xy1}(z) + a_{xy2}s_{xy2}(z) + \ldots\end{aligned} \tag{5.1}$$

where z is the depth from the surface.

As a hole is incrementally introduced into the laminate, the change in strain at each measurement location on the surface is measured relative to the undrilled laminate. The measured strains are affected by the relaxation of the x, y and in-plane shear components of the residual stress. As the hole depth increases, the strain response in the x-direction, $\epsilon_x(z)$, at a particular location can be written as:

$$\begin{aligned}\epsilon_x(z) = {} & a_{x0}c_{x0}(z) + a_{x1}c_{x1}(z) + a_{x2}c_{x2}(z) + \ldots \\ & + a_{y0}c_{y0}(z) + a_{y1}c_{y1}(z) + a_{y2}c_{y2}(z) + \ldots \\ & + a_{xy0}c_{xy0}(z) + a_{xy1}c_{xy1}(z) + a_{xy2}c_{xy2}(z) + \ldots\end{aligned} \tag{5.2}$$

where the calibration coefficient, $c_{jn}(z)$, is the strain response in the x-direction at the measurement location due to the j component of eigenstrain of order n.

The power series amplitudes, a_{jn}, can be determined by a least-squares minimisation of error between the measured strains and that calculated using equation (5.2). The residual stress distribution can subsequently be determined from equation (5.1). In vector-matrix form, and considering all components of stress and strain, equations (5.1) and (5.2) can be expressed as equations (5.3) and (5.4) respectively. These equations and all subsequent equations in this thesis are presented in a format where matrices are denoted by boldface upper-case characters, vectors are denoted by boldface lower-case characters and scalars are denoted by standard typeface.

$$\boldsymbol{\sigma} = \mathbf{S}\,\mathbf{a} \tag{5.3}$$

$$\boldsymbol{\epsilon} = \mathbf{C}\,\mathbf{a} \tag{5.4}$$

High orders of power series expansion are required if experimental strains vary abruptly or exhibit sharp turning points. For example, if the standard power series expansion method is applied to a laminate with an IHD strain variation as presented in Figure 5.1, such high order series would be required to achieve a reasonable fit to the strain data that instabilities could dominate and distort the residual stress distribution. Additionally, such high series orders would be sensitive to measurement errors and result in large stress uncertainties, which prevents this approach.

The adapted series expansion method is to divide the material into multiple through-thickness regions, as presented in Figure 5.1, such that multiple separate series of lower order can be used to achieve a good fit to the strain data. The material properties in FRP laminates vary abruptly at the interfaces between plies of different material type or orientation and the IHD strains can therefore have turning points or sharp changes in slope at the depth of such interfaces. This provides a convenient means for defining the regions to which series expansion can be separately applied. Within each of these regions a higher order power series expansion yields a better fit to the strain data, but a certain order is reached where the benefits of an improved fit are outweighed by the inherent instability associated with a higher order series. Convergence of the calculated residual stress distributions, as the series order increases, and the magnitude of the associated uncertainty bounds can be used to determine the most appropriate order within each region.

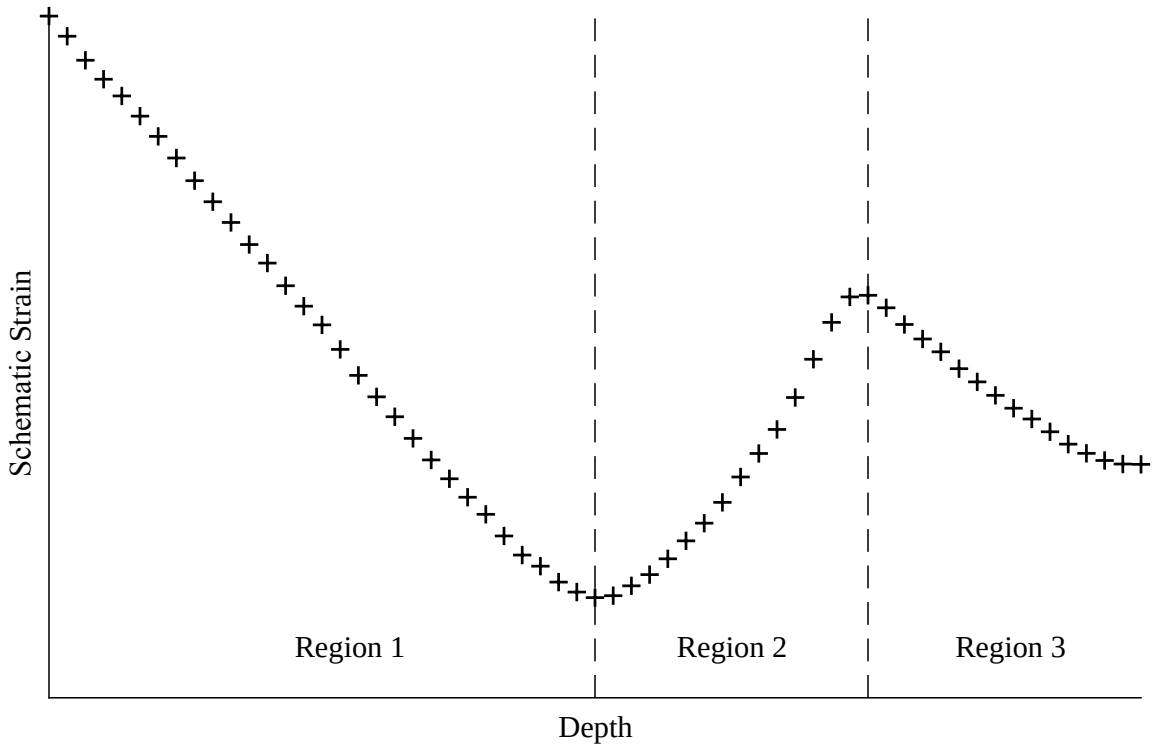


Figure 5.1: Schematic strain variation with depth

In the forward solution, the response of the laminate to through-thickness stress distributions defined by power series functions is evaluated using the FE method. The stress distributions are generated by applying separate eigenstrain distributions in each of the three in-plane strain components to each set of plies having particular material properties when observed in the global (x, y) coordinate system. Differences in material properties from one ply to the next could arise from changes in material type or, more commonly, from changes in ply orientation within a FRP laminate of constant material type as presented in this chapter.

Eigenstrain is applied by the use of through-thickness temperature variations, defined by functions with a range of [-1, 1], in conjunction with dummy coefficients of thermal expansion in each of the desired directions; α_x, α_y and α_{xy}. The use of temperature variation to apply eigenstrain and the use of functions with a range of [-1, 1] are out of convenience and not necessity. The temperature variations are defined by power series functions according to equations (5.5) and (5.6) for even and odd orders respectively, where z is the normalised perpendicular position with respect to the midplane, i.e. z has a value of 1 on the top surface and -1 on the bottom surface of the laminate. Power series functions ranging from 0^{th} to 4^{th} order are used in this chapter.

$$T_{even}(z) = 2z^n - 1 \tag{5.5}$$

$$T_{odd}(z) = z^n \tag{5.6}$$

Eigenstrain in any of the three in-plane strain components causes a mechanical strain redistribution throughout the thickness of the laminate and, in turn, a through-thickness stress distribution in all the in-plane stress components. The use of eigenstrain to generate the through-thickness stress distributions maintains force and moment equilibrium in the laminate as a whole. The temperature functions are applied to each and every ply orientation separately by assigning a CTE of 1 to the ply orientation of interest and 0 to the remaining ply orientations. It is important to note that although the eigenstrain is applied to each ply orientation independently, it generates a stress distribution through the entire thickness of the laminate, i.e. in all remaining ply orientations. For illustrative purposes, the balanced stress distribution in the x-direction of a $[0_2/90_2]_s$ laminate, produced by a 2^{nd} order eigenstrain in the x-direction applied to the 90° plies is presented in Figure 5.2 up to the midplane. When material is removed from a ply to which no eigenstrain is directly applied, there are still stresses that are released and a change in strain is observed at the strain gauge locations. These released strains define a corresponding calibration coefficient and must be included in the analysis. This also applies to the stress distributions that result from eigenstrain in other directions. The total released strain variation in the x-direction, for instance, within a particular ply orientation thus also has terms associated with eigenstrain applied to other ply orientations and also those applied in the y-direction and in-plane shear. Therefore, calibration coefficients need to be determined for each strain gauge location for every applied eigenstrain, regardless of direction, at each incremental depth. The calibration coefficients are unique for a particular laminate configuration and set of experimental parameters (length and position of strain gauges, hole diameter, depth of each increment, etc.).

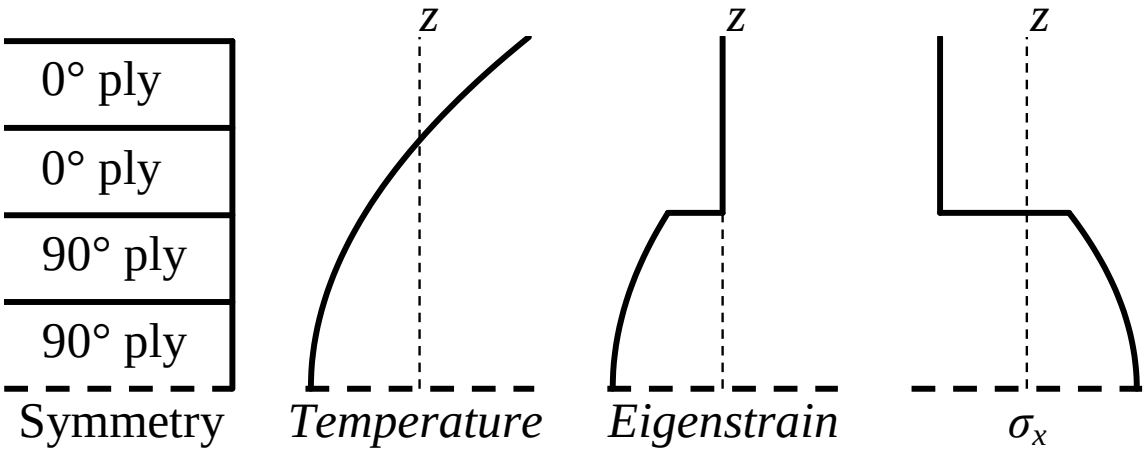


Figure 5.2: Applied eigenstrain and resultant stress distribution

In the case of a rectangular strain gauge rosette, the longitudinal strain at the x, y and 45° strain gauge locations are calculated at each incremental depth within the FE model. The strain release at each depth increment for each applied eigenstrain distribution, relative to the undrilled laminate, is used to construct the calibration matrix, $\mathbf{C}$, in the following form:

$$\mathbf{C} = \begin{bmatrix} C_{1_{x_0x_0}} & \dots & C_{1_{x_0y_0}} & \dots & C_{1_{x_0xy_0}} & \dots & C_{1_{x_{js_n}}} \\ C_{1_{y_0x_0}} & \dots & C_{1_{y_0y_0}} & \dots & C_{1_{y_0xy_0}} & \dots & C_{1_{y_{js_n}}} \\ C_{1_{45_0x_0}} & \dots & C_{1_{45_0y_0}} & \dots & C_{1_{45_0xy_0}} & \dots & C_{1_{45_{js_n}}} \\ \vdots & \dots & \vdots & \dots & \vdots & \dots & \vdots \\ C_{i_{g_0x_0}} & \dots & C_{i_{g_0y_0}} & \dots & C_{i_{g_0xy_0}} & \dots & C_{i_{g_{js_n}}} \end{bmatrix} \tag{5.7}$$

where C_{igjsn} is the released strain due to the presence of the hole, i is the hole depth increment, g is the strain gauge location, j is the ply orientation to which eigenstrain is applied, s is the component of eigenstrain, and n is the order of the temperature variation used to apply eigenstrain.

The through-thickness far-field stress distributions arising from the applied eigenstrain functions are used to create a stress matrix, $\mathbf{S}$, in the following form:

$$\mathbf{S} = \begin{bmatrix} S_{1_{x_0x_0}} & \dots & S_{1_{x_0y_0}} & \dots & S_{1_{x_0xy_0}} & \dots & S_{1_{x_{js_n}}} \\ S_{1_{y_0x_0}} & \dots & S_{1_{y_0y_0}} & \dots & S_{1_{y_0xy_0}} & \dots & S_{1_{y_{js_n}}} \\ S_{1_{xy_0x_0}} & \dots & S_{1_{xy_0y_0}} & \dots & S_{1_{xy_0xy_0}} & \dots & S_{1_{xy_{js_n}}} \\ \vdots & \dots & \vdots & \dots & \vdots & \dots & \vdots \\ S_{m_{p_0x_0}} & \dots & S_{m_{p_0y_0}} & \dots & S_{m_{p_0xy_0}} & \dots & S_{m_{p_{js_n}}} \end{bmatrix} \tag{5.8}$$

where m is the nodal position in the through-thickness direction, starting at 1 on the top surface and increasing with depth. Nodes shared by elements in the through-thickness direction have two stresses associated with them, one from each element, which allows discontinuities in stress to be captured. The component of stress is denoted by p and j, s and n have the same meaning as in equation (5.7).

The experimental strains are assembled into a strain vector, $\boldsymbol{\epsilon}_{meas}$, in the following form:

$$\boldsymbol{\epsilon}_{meas} = \begin{Bmatrix} \epsilon_{1_x} \\ \epsilon_{1_y} \\ \epsilon_{1_{45^\circ}} \\ \vdots \\ \epsilon_{i_g} \end{Bmatrix} \tag{5.9}$$

where i and g have the same meaning as in equation (5.7).

The matrix of calibration coefficients is used with the experimental strain vector in the inverse solution to determine the amplitude vector, $\mathbf{a}$, by manipulating equation (5.4) into the form presented in equation (5.10).

$$\begin{aligned} \boldsymbol{\epsilon}_{meas} &= \mathbf{C}\,\mathbf{a} \\ \mathbf{C}^T\boldsymbol{\epsilon}_{meas} &= \mathbf{C}^T\mathbf{C}\,\mathbf{a} \\ \mathbf{a} &= \left(\mathbf{C}^T\mathbf{C}\right)^{-1}\mathbf{C}^T\boldsymbol{\epsilon}_{meas} \end{aligned} \tag{5.10}$$

where $\mathbf{a}$ is the unique set of amplitudes of the applied unit eigenstrains that best matches the experimental strain response, in the form:

$$\mathbf{a} = \begin{Bmatrix} a_{0_{x_0}} \\ a_{0_{x_1}} \\ \vdots \\ a_{j_{s_n}} \end{Bmatrix} \tag{5.11}$$

where j, s and n have the same meaning as in equation (5.7).

The calculated amplitude vector is used with stress matrix, $\mathbf{S}$, to determine the though-thickness residual stress distribution vector, $\boldsymbol{\sigma}_{res}$, for the laminate using equation (5.3), which is presented in vector-matrix form:

$$\boldsymbol{\sigma}_{res} = \mathbf{S}\,\mathbf{a} \tag{5.12}$$

Since all coefficients of the amplitude vector, and subsequently the residual stress distributions, are solved using a least-squares fit to the experimental strain data, the method is inherently insensitive to noise in the strain measurements. To achieve a robust least-squares fit, the number of terms in $\boldsymbol{\epsilon}_{meas}$ must be significantly greater than in the amplitude vector [94]. Therefore, it is beneficial to use small experimental depth increments to obtain a large strain data set.

At this point, the issue of correcting for transverse sensitivity of the gauges needs to be discussed. Usually, the experimental strain measurements in vector $\boldsymbol{\epsilon}_{meas}$ would be corrected for transverse sensitivity, but because the strain field is not uniform around the hole, the standard method of correction [184] is inaccurate and an alternative approach is required. The approach followed in this work is to leave the strains measured by the gauges as uncorrected, and instead modify the calibration coefficients determined from FE calculations. In essence, the uncorrected strain measurements are matched

using calibration coefficients that are adjusted so that they reflect the strains that would be measured experimentally if transverse sensitivity correction was to be ignored. An entirely new set of calibration coefficients corresponding to transverse strain is therefore required. The transverse calibration coefficients are a direct match for the longitudinal calibration coefficients and are readily obtained because all the necessary data is available from the FE analysis required to obtain the longitudinal calibration coefficients. Each term, C_{igjsn}, in the matrix of calibration coefficients now corresponds to the change in strain that would be measured if transverse sensitivity correction was not accounted for. The matrix of 'uncorrected' calibration coefficients can be determined from the calibration coefficients in the longitudinal and transverse directions according to equation (5.13), which is found by manipulation of the standard transverse sensitivity equations given in [184]. The uncorrected calibration matrix found using FE calculations is then used with the uncorrected experimental strains to determine the coefficients of the amplitude vector using equation (5.10). The complete residual stress distribution is found using equation (5.12).

$$C_{igjsn} = \frac{\bar{C}_{igjsn} + \hat{C}_{igjsn} \times K_{tp}}{1 - \nu_0 K_{tp}} \tag{5.13}$$

where $\bar{C}_{igjsn}$ and $\hat{C}_{igjsn}$ are the corresponding terms of the longitudinal and transverse calibration matrices, respectively, K_{tp} is the transverse sensitivity coefficient of the particular strain gauge of the rosette and ν_0 is the the Poisson's ratio of the material on which the manufacturer's gauge factor was measured.

5.3 Demonstration of Procedure

The flow chart shown in Figure 5.3 describes the entire residual stress measurement process using IHD with separate series expansion. Each element of the flow chart will be discussed in greater detail in the following sections.

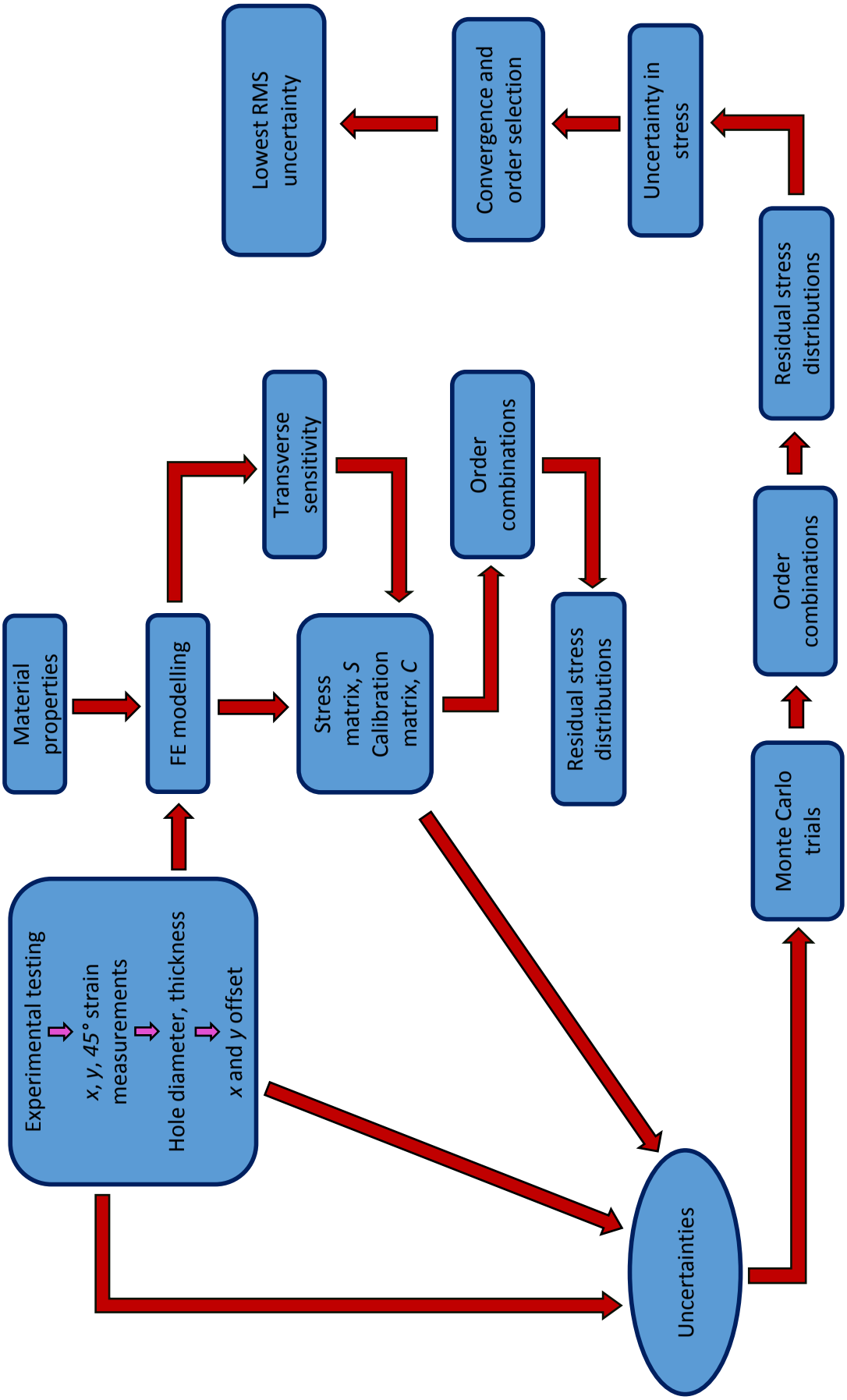


Figure 5.3: Methodology for residual stress measurement using IHD with separate series expansion

5.3.1 Experimental

The method outlined thus far is demonstrated using a GFRP laminate manufactured from E-glass/epoxy. Aerospace grade prepreg material ($V_f \approx 60\%$, ply thickness ≈ 200 µm) was supplied by c-m-p gmbh with manufacturer's code T-GE-1 250/635 CP002. The use of aerospace grade prepreg material ensures uniform fibre density and spreading which results in layers of uniform thickness. The laminate configuration used was $[0_2/+45/-45]_s$ with fibre alignment being carefully controlled during lay-up. The plate had dimensions 400 mm $\times$ 400 mm and was cured between two steel plates of the same dimensions and 0.9 mm thickness. The laminate was debulked at 85°C before being cured at 6 bar and 120°C for 3 hours. The cured plate of 1.57 mm thickness had smooth surfaces on both sides, no noticeable voids and no apparent curvature. The primary in-plane elastic properties of the composite material were determined in accordance with the ASTM D 3039 [185] and ASTM D 3518 [186] standards and are listed in Table 5.1.

Table 5.1: Orthotropic lamina properties

Longitudinal modulus, E_1 (MPa)	38154
Transverse modulus, E_2 (MPa)	10747
Shear modulus, G_{12} (MPa)	3712
Poisson's ratio, ν_{12}	0.3113
Poisson's ratio, ν_{23}	0.4124

The hydrostatic approximation was used to estimate the value of ν_{23}, with the required bulk modulus estimated using the concentric cylinder assemblage model presented by Hill [187]. The properties of the lamina are transversely isotropic in the material coordinate system and so the material properties transverse to the fibre direction are all identical as given in equation (5.14). The remaining Poisson's ratio terms are found from the reciprocal relations of equation (5.15) and the shear modulus, G_{23}, is obtained using equation (5.16).

$$E_2 = E_3 \qquad G_{12} = G_{13} \qquad \nu_{12} = \nu_{13} \tag{5.14}$$

$$E_1\nu_{21} = E_2\nu_{12} \qquad E_1\nu_{31} = E_3\nu_{13} \qquad E_3\nu_{23} = E_2\nu_{32} \tag{5.15}$$

$$G_{23} = \frac{E_2}{2\,(1+\nu_{23})} \tag{5.16}$$

The test specimen had dimensions of 120 mm $\times$ 60 mm to allow three holes to be drilled with 30 mm clearance from any edge or neighbouring hole. Minimum allowable dimensions were assessed using FE modelling to ensure that no edge effects were present at the hole location in the centre of the plate, or at the strain gauge locations. It was determined that a specimen with a minimum radial distance of 7.5 mm, from the centre of the hole to any edge, is essentially free from any edge effects.

This distance was evaluated using both the released strains and stresses at various depth increments, as well as the stresses generated by the applied eigenstrain distributions without the presence of the hole. It was found that the strain measurements were the crucial factor in determination of the minimum allowable distance since the strains are measured some distance from the hole at the strain gauge locations closer to the edge of the plate. If another hole is present, the stress concentration around it will also take 7.5 mm to dissipate. Therefore, the distance required between the centres of neighbouring holes has to be doubled to 15 mm. This is the most conservative approach since the effect of a neighbouring hole is less severe than a free edge, however, the conservative distance of 15 mm between holes required from the free edge assessment is already less than what could practically be achieved experimentally due to the size of the IHD rosette and the experimental set-up. Therefore, there was no need to further investigate the optimal distance between neighbouring holes since it would be impossible to do experimentally. The test specimens were made significantly larger than determined from the free edge assessment for practical reasons and since material availability was not a concern. The specimen was laid flat on a surface and drilled, no other constraints were applied to avoid introducing additional mounting stresses. The specimen is not cut into individual smaller specimens prior to drilling such that it has significant inertia and so does not move during drilling. Movement of the specimen during drilling remained a concern, however, therefore each hole was investigated to confirm that it was cylindrical and thoroughly inspected for any signs of movement during testing. Good repeatability in strain measurements has been found using this approach. The experimental strain variation between tests were within the measurement uncertainty considered in this chapter, therefore, only a single experimental strain data set is presented in the following sections.

HBM foil strain gauge rosettes of type 1.5/350M RY61 with six strain gauge grids were used for the IHD experiments. The six grids of the 1.5/350M RY61 rosette are positioned in two rectangular configurations, situated symmetrically across both the x and y axes as shown in Figure 5.4. The opposing grids are connected to one another during manufacture such that the measured strain is the average of the two grids, thereby somewhat compensating for hole eccentricity errors. Details of the 1.5/350M RY61 rosette are listed in Table 5.2. Strain gauges with a resistance of 350 Ω were used to reduce heating effects on the low-conductivity material. A gauge excitation voltage of 1.5 V was selected to achieve the desired sensitivity whilst keeping the power consumed by the gauge as low as possible. Temperature compensation was employed by connecting each active gauge of the rosette with a dummy gauge (of the same type, attached to the same material) in a quarter bridge configuration to a National Instruments data acquisition system equipped with a SCXI-1520 strain gauge card. Additionally, IHD was performed in the basement of the laboratory where temperature fluctuations are minimal over the experimental testing period of approximately 35 minutes.

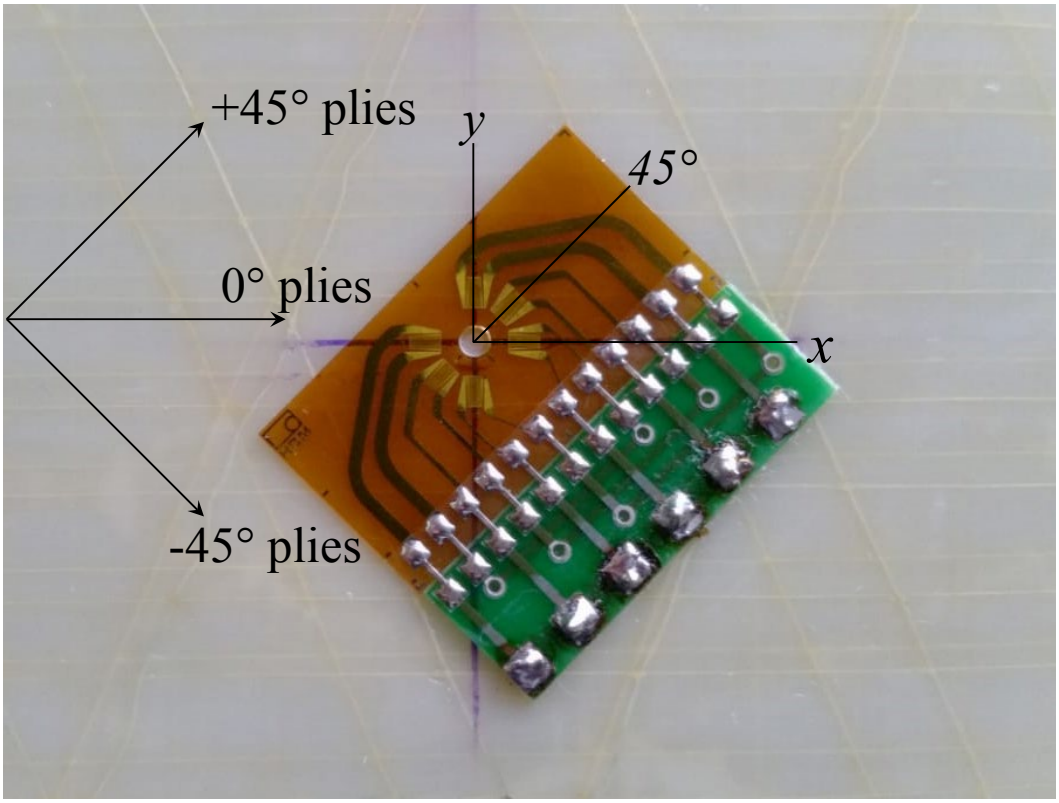


Figure 5.4: $[0_2/+45/-45]_s$ specimen and configuration of the 1.5/350M RY61 rosette

Table 5.2: Properties of each strain gauge grid of the 1.5/350M RY61 rosette

	Strain gauge grid		
Property	a (0°)	b (45°)	c (90°)
Nominal resistance (Ω)	350 ± 0.35%	350 ± 0.35%	350 ± 0.35%
Gauge factor	1.86 ± 1.5 %	1.83 ± 1.5 %	1.86 ± 1.5 %
ν_0	0.285 ± 3 %	0.285 ± 3 %	0.285 ± 3 %
Transverse sensitivity	2.2% ± 0.1 %	2.6% ± 0.1 %	2.2% ± 0.1 %

A Sint Technology Restan MTS 3000 with a pneumatic turbine, which achieves drilling speeds of approximately 300 000 rpm, was used to perform the incremental drilling. Valentini et al. [175] found that high speed drilling is not suitable in unfilled thermoplastic polymeric materials due to localised melting and can induce significant residual stresses. However, high speed drilling in thermoset FRP laminates, such as the material used in this chapter, has been investigated by Nobre et al. [176, 177] and found to yield acceptable results, provided that heating effects are kept minimal. The depth increment was set to ≈13 µm ($1/60^{th}$ of the final hole depth of 0.785 mm) to reduce the introduction of heat into the specimen as far as possible. The feed rate of the MTS 3000 was set to 0.2 mm/min. Drilling alignment was controlled to ensure that drilling occurred perpendicular to the surface of the laminate, and in the centre on the strain gauge rosette. A stepper motor controls the incremental

drilling to a resolution of up to 1 µm, resulting in good reproducibility. The hole diameter and position of the hole can be determined with a resolution of 10 µm using the built-in microscope and dial gauges of the MTS 3000. A tungsten carbide inverted cone end mill of 1.40 mm diameter was used to cut the hole that had final diameter of 1.59 mm. The ratio between the hole radius and the inner radius of the strain gauge was found to be 0.44, which is in accordance with the recommendations of Sicot et al. [89].

As a consequence of the symmetric lay-up, incremental hole-drilling was conducted up to the mid-plane only. The small depth increments also mean that 60 measurements were used to populate the experimental strain vector, $\boldsymbol{\epsilon}_{meas}$, that allowed a robust least-squares fit. Strain readings were taken 25 seconds after each drilling increment to allow for all thermal effects to dissipate and for steady state conditions to resume. Ten strain readings were taken over 5 seconds and averaged to reduce the effects of noise. The experimentally measured variation in strain release with depth at the x, y and 45° strain gauge locations is presented in Figure 5.5.

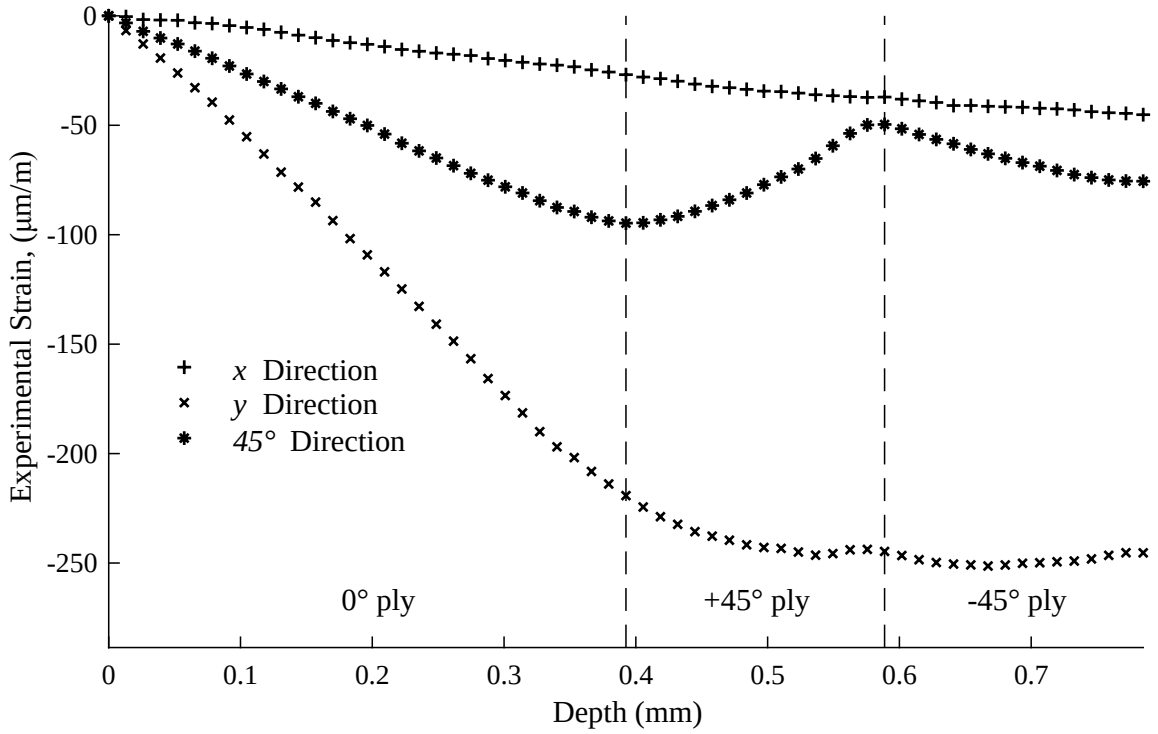


Figure 5.5: Strain variation with depth in the x, y and 45° gauge directions

5.3.2 Computational

The calibration coefficients were calculated using MSC Nastran FE analysis. The GFRP laminate was modelled using HEX20 type 3D elements with 32 elements through the thickness, 4 per ply. It would be beneficial to increase the number of elements through the thickness of each ply, but the increase in computational time cannot be justified at present. Increasing the number of elements per ply must be accompanied by a reduction of element size in the x-y plane to ensure that the element aspect ratios remain within acceptable bounds. Therefore, to double the number of elements per ply to 8, for example, requires a mesh that has 8 times as many nodes and, as tested, requires approximately 30 times the computational time. This issue is exacerbated by the inclusion of various uncertainties that require computation of additional FE models. A mesh independence study was conducted to ensure that acceptable accuracy was achieved while minimising the computational time required. Elements were assigned orthotropic material properties according to the ply orientation they represent. The hole diameter measured during IHD was used in the FE model. The $[0_2/+45/\text{-}45]_s$ laminate is not symmetric about the x-z or y-z plane and must therefore be modelled in its entirety. The mesh around the hole, including the strain gauge grid locations (highlighted), is presented in Figure 5.6. The grid locations and sizes are included to facilitate determination of the matrix of calibration coefficients. Layers of elements representing the hole were incrementally removed to simulate the increasing depth of the hole. A section through the mesh is presented in Figure 5.7.

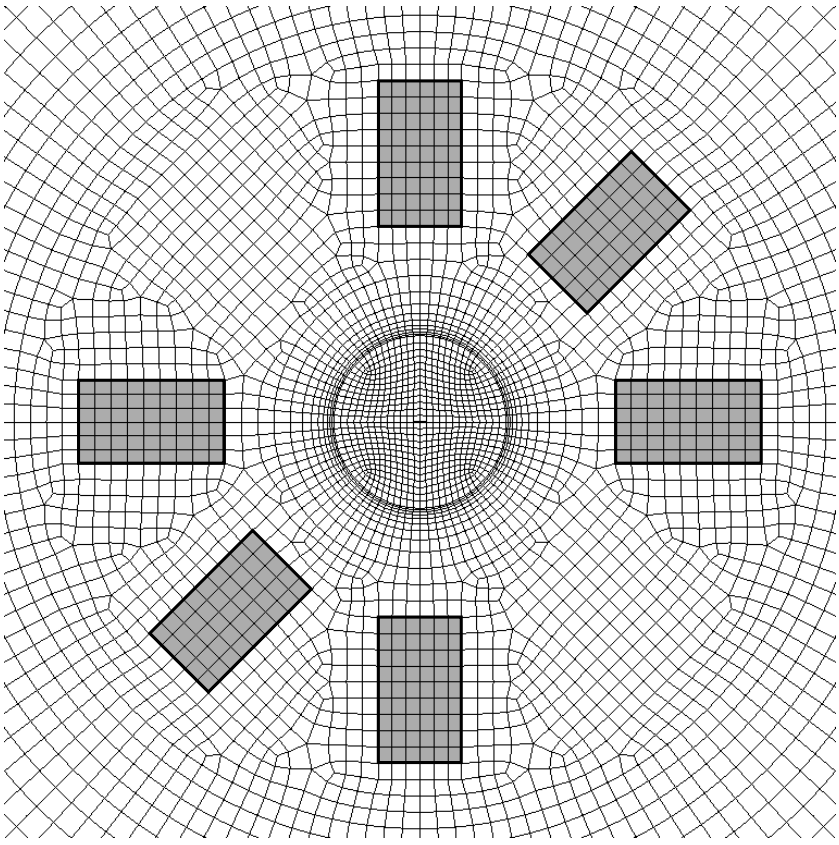


Figure 5.6: Top view of mesh around the hole including the strain gauge grid locations

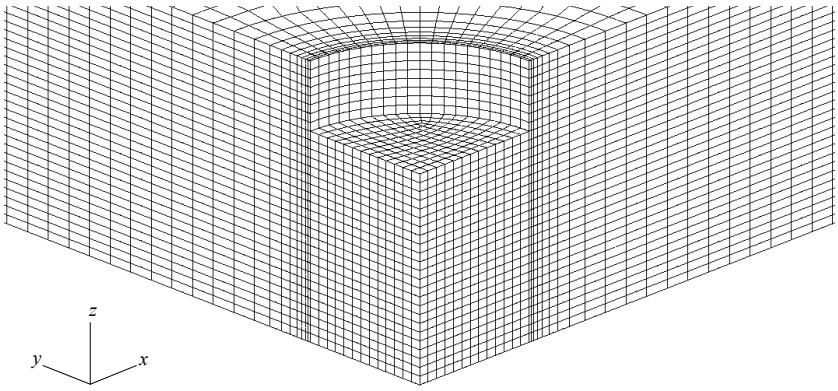


Figure 5.7: Section through the mesh thickness

Eigenstrains were applied to plies of a particular orientation by assigning a CTE of unity to these plies and a CTE of zero to all other plies, and then subjecting the entire laminate to a through-thickness temperature variation corresponding to a particular order of power series. Since all applied loads are self-equilibrating, the boundary conditions were simply those required to prevent rigid body motion. There are many different ways to apply eigenstrain, and the use of temperature variation with a dummy CTE is just one such way which is straightforward to do in Nastran. Shear thermal strains were applied by assigning a dummy CTE in the global shear direction, this is possible by using the MAT9 material card of Nastran which allows α_{xy} to be specified and used for this purpose. The effect of shear strains are significantly lower for 0° and 90° plies of a cross-ply laminate, for example, and it may be possible to neglect the shear contribution if ply misalignment is not considered in the analysis. However, if a 45° ply orientation is included in the lay-up then the shear component cannot be neglected without introducing significant errors into the solution.

The application of the various eigenstrain distributions in the FE model yielded strain distributions around the hole for each incremental depth. For illustrative purposes, the strain variation in the x-direction due to a 2$^{\text{nd}}$ order eigenstrain in the x-direction applied to the 0° plies at a quarter thickness hole depth is presented in Figure 5.8. The longitudinal and transverse strain released at every drilling increment, resulting from every eigenstrain was calculated at each strain gauge location on the top surface using the displacement summation method introduced by Schajer [188]. These strains were used to populate the longitudinal and transverse calibration matrices, $\bar{\mathbf{C}}$ and $\hat{\mathbf{C}}$ respectively. The longitudinal strain was determined as the difference in average nodal displacement, in the gauge length direction, along the lines defining the inner and outer edges of each gauge grid, divided by the length of the grid. The transverse strain at each gauge was calculated similarly but referenced to the transverse direction.

The vertical dimensions of $\boldsymbol{\epsilon}_{meas}$, $\bar{\mathbf{C}}$ and $\hat{\mathbf{C}}$ must agree to allow the use of equation (5.10). Therefore, the 16 depth increments of the FE model had to be used to find the coefficients of $\bar{\mathbf{C}}$ and $\hat{\mathbf{C}}$ for the 60 experimental depth increments. The strain release vs. depth relationships obtained from the

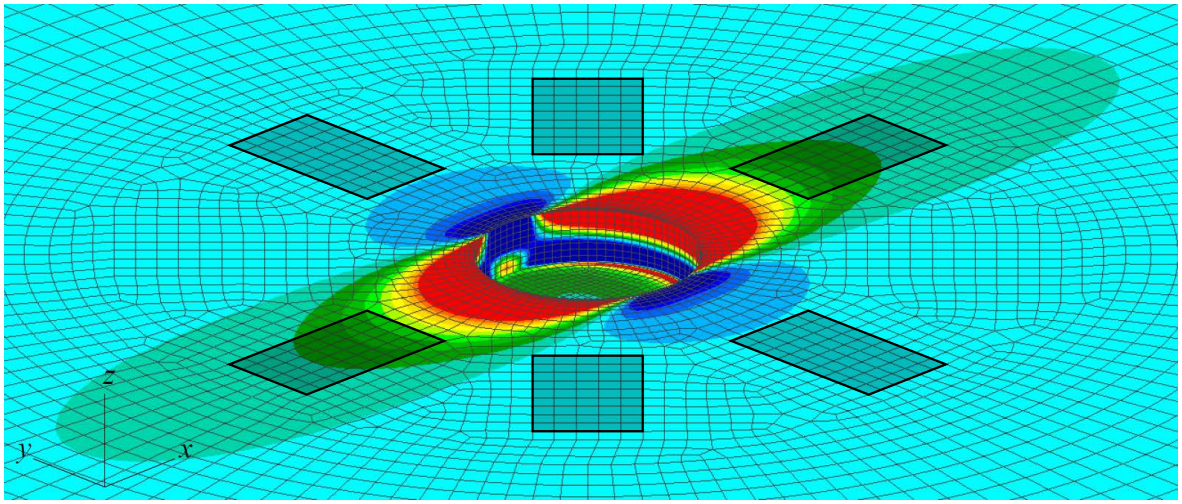


Figure 5.8: Strain variation in the x-direction at a quarter thickness hole depth and the strain gauge grid locations

FE calculations follow smooth variations, with discontinuities at the interfaces between different ply orientations. A separate spline was fitted to the calculated FE strain data within each ply orientation to allow an increase in the number of calculated strain readings per ply from 4 up to 15 through interpolation. This was done for the calculated strain data at the x, y and 45° gauge locations arising from all eigenstrain distributions, i.e. $g \times j \times s \times n$ curves were generated. This procedure is presented in Figure 5.9 for the calculated longitudinal strain in the x-direction resulting from a 2$^{\text{nd}}$ order eigenstrain in the x-direction, applied to the 0° ply orientation.

Although it is entirely possible to use a separate series order for each component of eigenstrain in each ply orientation, for the sake of simplicity and illustration, the same order series was used for all three components of eigenstrain within a particular ply orientation. Therefore, for the current laminate and for series orders ranging from 0$^{\text{th}}$ order to 4$^{\text{th}}$ order in each ply orientation, there are a total of 125 possible combinations of series expansion orders. The total number of possible combinations is found from the number of series orders considered in each ply orientation raised to the power of the number of ply orientations in the laminate, therefore, 5^3 in this case. To enable concise discussion, the abbreviation (n_0, n_{+45}, n_{-45}) is used where each value of n refers to the maximum order of the series expansion and the subscript refers to the ply orientation. This allows (1, 2, 3) to refer to the combination of 1$^{\text{st}}$, 2$^{\text{nd}}$ and 3$^{\text{rd}}$ order series expansion in the 0°, +45° and -45° plies, respectively. Combinations of higher order series have the ability to better fit the experimental strain data as can be seen in Figure 5.10 for the 45° strain gauge, where (1, 1, 1) and (4, 4, 4) order combinations are fitted to the experimental strain data. Combinations of higher order series can be more sensitive to measurement errors, however, that can lead to instability and greater uncertainty in the residual stresses. A thorough understanding of how uncertainty propagates through the analysis is therefore required.

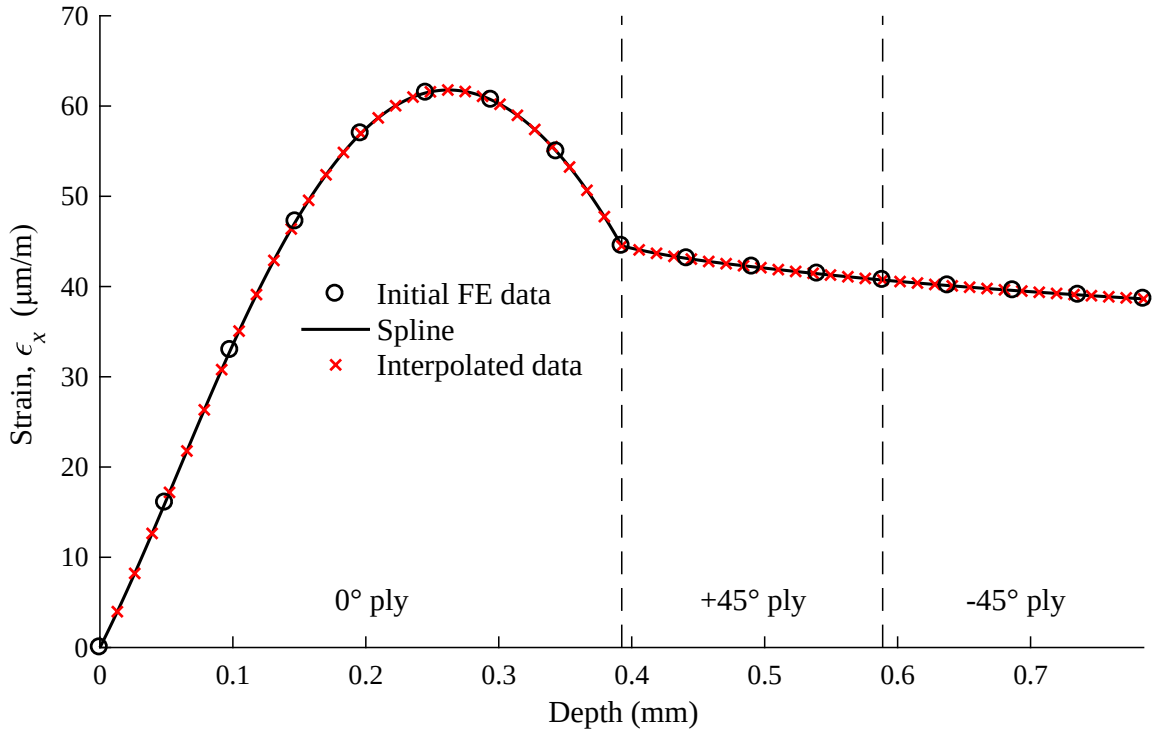


Figure 5.9: Determination of interpolated calibration coefficients from FE data

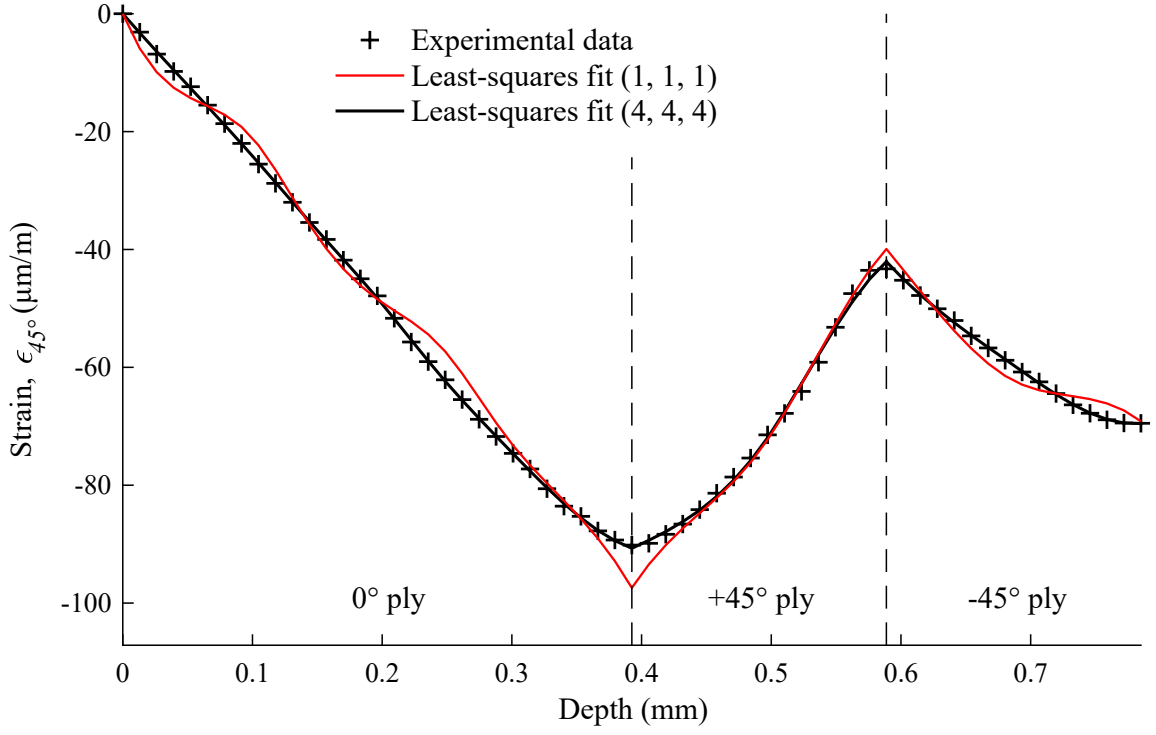


Figure 5.10: Least-squares fits to 45° strain measurements using (1, 1, 1) and (4, 4, 4) order combinations

5.3.3 Propagation of Uncertainties

The uncertainty in the residual stress distributions cannot be found directly using the law of propagation of uncertainty because the relationship between the measured strains and the stress is unknown and so the partial derivative terms cannot be found in a straightforward manner. The uncertainty in the stress distribution is instead estimated through the use of Monte Carlo simulation as per JCGM 101:2008 (Joint Committee for Guides in Metrology) [100]. The uncertainty sources and their assigned probability density functions considered in the Monte Carlo simulation are provided in Table 5.3. Ten thousand trials were simulated for each combination of series orders. Uncertainties in this chapter can be divided into those that affect the strain vector, $\boldsymbol{\epsilon}_{meas}$, and those that affect the calibration and stress matrices, $\mathbf{C}$ and $\mathbf{S}$. The flow chart shown in Figure 5.11 describes the experimental and computational uncertainty sources considered in the Monte Carlo simulation. Each element of the flow chart will be discussed in greater detail in the following section.

Table 5.3: Uncertainty sources and their assigned probability density functions

x_i	Description	$p(x_i)$	Type	Nominal value, uncertainty
E_1	Longitudinal modulus	Normal	B	38154 MPa, 2.0%
E_2	Transverse modulus	Normal	B	10747 MPa, 2.2%
G_{12}	Shear modulus	Normal	B	3712 MPa, 2.6%
ν_{12}	Poisson's ratio	Normal	B	0.3113, 2.1%
ν_{23}	Poisson's ratio	Normal	B	0.4124, 5%
z_i	Incremental depths	Rectangular	B	13 µm, 0.5 µm
z_0	Zero depth	Rectangular	B	0 µm, 13 µm
ϵ_m	Indicated experimental strain	Normal	B	Figure 5.5, 1.6%
ϵ_{noise}	Experimental noise	Normal	A	Figure 5.5, 0.61 µm
K_{t_x}	Transverse sensitivity for gauge 1	Normal	B	2.2%, 0.1%
$K_{t_{45^\circ}}$	Transverse sensitivity for gauge 2	Normal	B	2.6%, 0.1%
K_{t_y}	Transverse sensitivity for gauge 3	Normal	B	2.2%, 0.1%
ν_0	Poisson's ratio of the material on which gauge factor was measured	Normal	B	0.285, 3%
θ_{SG_t}	Misalignment of strain gauge on tensile testing coupon	Normal	B	0, 1°
θ_{coupon}	Fibre misalignment of tensile testing coupons	Normal	B	0, 0.5°
θ_{grips}	Misalignment of coupon in grips of tensile testing machine	Normal	B	0, 1°
θ_{SG_h}	Misalignment of strain gauge during hole-drilling	Normal	B	0, 1°
$\theta_{0^\circ\text{ply}}$	Misalignment of 0° plies of hole-drilling specimen	Normal	B	0, 0.5°
$\theta_{45^\circ ply}$	Misalignment of +45° plies of hole-drilling specimen	Normal	B	0, 0.5°
$\theta_{-45^\circ ply}$	Misalignment of -45° plies of hole-drilling specimen	Normal	B	0, 0.5°
FE	Finite element calculations	Normal	B	0, 2%

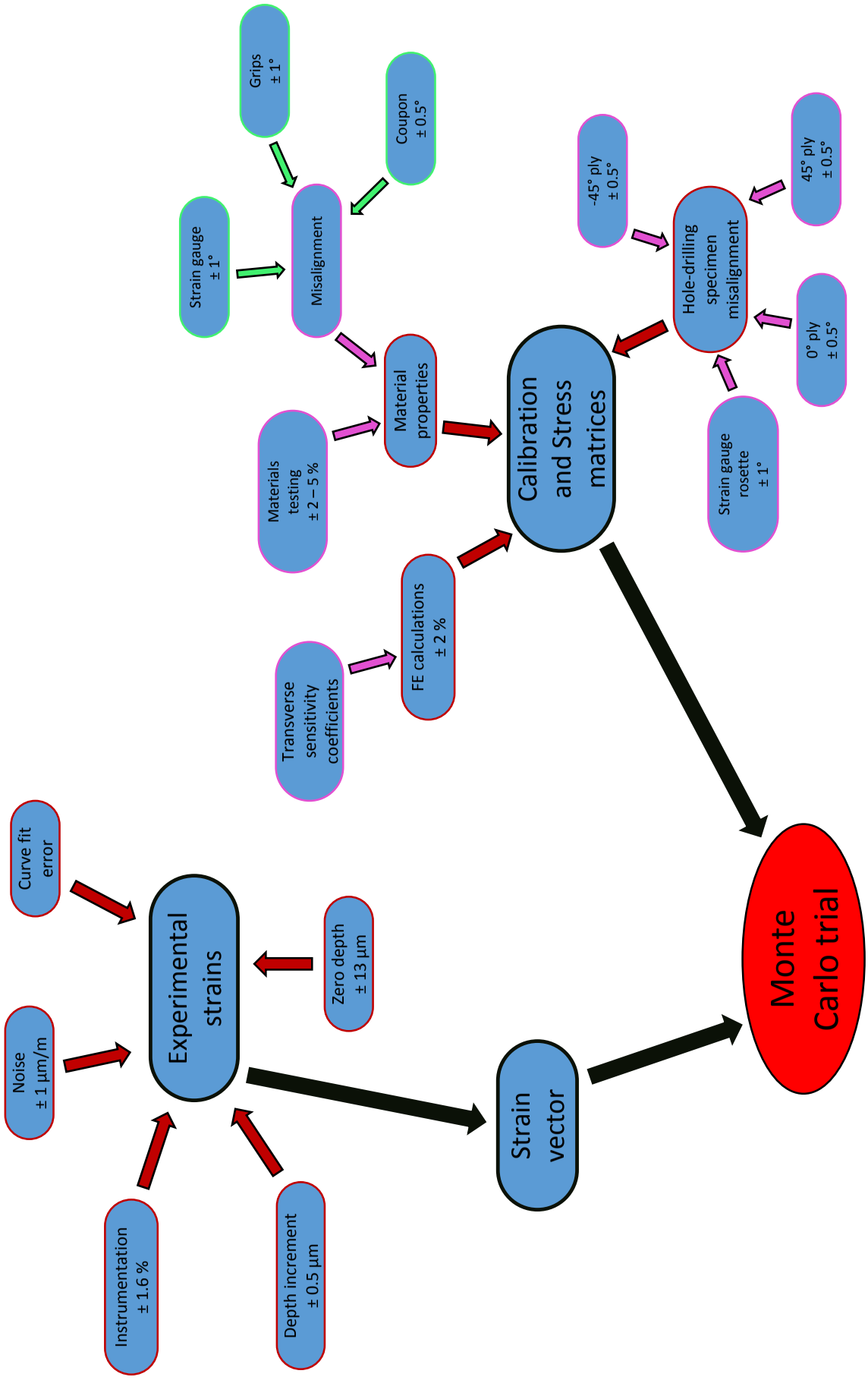


Figure 5.11: Methodology for uncertainty estimation using Monte Carlo simulation

Uncertainties in the experimental strain data are discussed first. Uncertainty propagation in the indicated strain measurements, ϵ_m, is calculated using the law of propagation of uncertainty as per JCGM 100:2008 [189]. Uncertainty in the measurement of the experimental strains arose through inaccuracies in instrumentation such as strain gauges and data acquisition and from uncertainty in the average temperature during the test. The inherent noise uncertainty in the strain gauge and data acquisition system was quantified by recording strain data over a 30 minute period and calculating a standard deviation from the large data set.

Zero depth detection is essential for any hole-drilling residual stress measurement and can be a significant source of stress uncertainty. It is not possible to use the electrical contact technique for GFRP laminates to identify the contact between the end mill and the surface of the specimen. Since many data points are required for series expansion, the incremental depth between each datum is small (≈13 μm). The approach used in this chapter was to start the drilling process slightly above the specimen. No relaxation response occurs while the end mill is in the air or within the thickness of the strain gauge and so the measured response is simply the scatter associated with measurement noise. Manufacture of a angle-ply GFRP laminate induces residual stress near the surface, and therefore some elastic response must occur when the end mill starts to penetrate into the specimen. After the IHD experiment, the strain variations were investigated and shifted along the x-axis to find the most likely position of the surface. The discontinuity at the interface between ply orientations was used to aid the determination of the zero depth position. Using this approach, it would not be known if the first measured response occurred as the end mill was just making contact with the specimen or whether the end mill was a full depth increment into the specimen when the data was recorded. The depth uncertainty would therefore be one half of the depth increment, or ≈6.5 μm. It is, however, possible that the end mill could slightly penetrate into the specimen and the associated elastic response would be so small that it could get lost in the scatter of the preceding data points. This would mean that the first datum point would be missed. In this case, the uncertainty would need to be increased. To be conservative, it was assumed that a full depth increment into the specimen could be missed, and so the zero depth uncertainty was doubled to ≈13 μm. The MTS 3000 hole-drilling machine has a depth resolution of 1 μm and therefore the uncertainty associated with each incremental depth was taken as one half of this depth resolution. Each depth increment is allowed to vary independently within a rectangular probability density function between [-0.5 μm, 0.5 μm].

The experimental strains of each Monte Carlo trial were first adjusted for the uncertainty associated with strain measurement instrumentation. All experimental strain measurements were made using the same instrumentation, therefore they are considered fully correlated and were all varied using the same random variable. The experimental depths were independently adjusted for the uncertainty in each individual depth increment, and all adjusted for the uncertainty in zero depth position. Spline interpolation was used to determine the strain data used in each Monte Carlo trial, referenced to the zero depth of that trial, at the depth increments inherent to the $\mathbf{C}$ matrix. Some additional uncertainty

was introduced by the use of spline interpolation, but this uncertainty is negligible in comparison with the uncertainty associated with the depth position of each increment. Each interpolated strain component was then independently adjusted for measurement noise. Finally, the uncertainty arising from the inability of the particular combination of series orders under consideration to exactly match the strain data is included. This misfit uncertainty is calculated as the standard deviation between the experimentally measured strains and the least-squares fit within each ply orientation.

The calibration and stress matrices are affected by uncertainty in the material properties and in the orientation of each ply. Uncertainty in each experimentally measured material property is calculated using the law of propagation of uncertainty as per JCGM 100:2008 [189]. Uncertainty in these measurements arose through inaccuracies in instrumentation such as strain gauges, data acquisition, micrometers and from uncertainty in the average temperature during materials testing. These uncertainties, however, do not include the effects of misalignment during material testing since they are not linearly related to the uncertainty in material properties. There are three possible sources of misalignment; misalignment of the plies within the material test coupons, misalignment of the strain gauges on the coupons and misalignment of the coupons in the tensile testing machine. While the orientation of the epoxy prepreg material used in the investigation could be readily identified, and great care was taken in cutting the material at the appropriate angles, some misalignment must have been present. This misalignment will have been small, however, because the effects of even small angular variations are quite noticeable over the scale of the laminates manufactured. This misalignment was conservatively estimated to have a standard deviation of 0.5°. It is also possible that the strain gauge rosette was misaligned relative to the laminate coordinate system. In this case, the laminate coordinate system is aligned with the fibres on the top ply which are clearly visible under the correct lighting conditions. This means that it is possible to align the gauges very accurately with the fibres. Small misalignments must nonetheless exist. A conservative standard deviation in gauge misalignment of 1° was assumed. It is also possible that the test coupons were misaligned in the grips of the tensile testing machine. Again, care was taken in placing the coupons in the grips but some misalignment must have occurred. A conservative value of 1° was assumed for this misalignment as well. Because the effects of misalignment are not linearly related to the angular misalignment, uncertainty due to these effects was considered within the Monte Carlo simulation. This means that the effective uncertainty in each material property is greater than that given in Table 5.3.

Within each Monte Carlo trial, the material properties are first individually adjusted for the effects of measurement uncertainty in their determination. The effects of all the possible sources of misalignment during materials testing on the material properties are then incorporated. The experimentally obtained material properties were determined from three different tensile tests. E_x and ν_{xy} were determined from tensile testing of a 0° unidirectional laminate, E_y was determined from tensile testing of a 90° unidirectional laminate, and G_{xy} was determined from tensile testing of a $\pm 45°$ laminate.

The total misalignment of each tensile test is given by:

$$\begin{aligned}\theta_1 &= \theta_{SGt_1} + \theta_{coupon_1} + \theta_{grips_1}\\ \theta_2 &= \theta_{SGt_2} + \theta_{coupon_2} + \theta_{grips_2}\\ \theta_3 &= \theta_{SGt_3} + \theta_{coupon_3} + \theta_{grips_3}\end{aligned} \tag{5.17}$$

where θ_1, θ_2 and θ_3 is the total misalignment during tensile testing of a 0°, 90° and ±45° laminate, respectively.

The relationship between the misaligned properties and the material properties in the *1,2* coordinate system of the laminate is given in vector-matrix form by:

$$\begin{Bmatrix} 1/E_x \\ 1/E_y \\ \nu_{xy}/E_x \\ 1/G_{xy} \end{Bmatrix} = \begin{bmatrix} {c_1}^4 & {s_1}^4 & -2{s_1}^2{c_1}^2 & {s_1}^2{c_1}^2 \\ {s_2}^4 & {c_2}^4 & -2{s_2}^2{c_2}^2 & {s_2}^2{c_2}^2 \\ -{s_1}^2{c_1}^2 & -{s_1}^2{c_1}^2 & {s_1}^4 + {c_1}^4 & {s_1}^2{c_1}^2 \\ 4{s_3}^2{c_3}^2 & 4{s_3}^2{c_3}^2 & 4{s_3}^2{c_3}^2 & -2{s_3}^2{c_3}^2 + {s_3}^4 + {c_3}^4 \end{bmatrix} \begin{Bmatrix} 1/E_1 \\ 1/E_2 \\ \nu_{12}/E_1 \\ 1/G_{12} \end{Bmatrix} \tag{5.18}$$

where $s_m = \sin\theta_m$ and $c_m = \cos\theta_m$

The material properties, in the laminate coordinate system, of each Monte Carlo trial can be found by inverting equation (5.18). The percentage variation from the original material properties can then be established. Another source of uncertainty in the calculated residual stresses is misalignment in the hole-drilling specimen. This can have two sources: misalignment of the different plies in the laminate relative to their nominal values, and misalignment of the hole-drilling strain gauge rosette relative to the laminate coordinate system. The uncertainties associated with these effects are the same as those that occurred due to misalignment in the materials testing: 0.5° and 1°, respectively. While the angular alignment of each ply can vary independently, the 0° ply became the reference coordinate system after the laminate was cured. The misalignment in the 0° ply therefore translates to relative misalignment of the +45° and -45° plies such that the actual misalignment of the +45° ply is equal to the misalignment of the 0° ply plus the misalignment of the +45° ply, similarly for the -45° ply. The rosette misalignment is added to the misalignment of all plies in the laminate. It must be noted that all layers of a particular ply orientation were treated together, i.e. those above and below the midplane were considered simultaneously. This is obviously not the most realistic or fully correct way to consider misalignment since each layer can be misaligned individually. However, to consider all layers individually would add significant FE computational cost and also some additional results processing for the Monte Carlo simulation since it adds more variables that will, therefore, likely require more than 10 000 trials to achieve repeatable stress uncertainties. Since the stress uncertainty due to misalignment is low compared to more dominant uncertainties, the increased computational cost to include misalignment of individual layers cannot be justified at present. It is expected that considering the misalignment of each individual layer would increase the total uncertainty in stress by a negligible amount.

When including the uncertainties in material properties and the uncertainties in the orientation of individual plies within the hole-drilling specimen into the Monte Carlo simulation, it is not computationally feasible to perform a new FE calculation for each trial. A more computationally efficient approach is therefore required. The changes in every term in the calibration and stress matrices are consequently determined for a 1% change in each material property, and a 1° change in each ply orientation. Due to the complex nature of the problem, each term of these matrices varies uniquely for each of these changes. Because of the use of a linear model, however, the variation in each of these terms can be scaled according to the uncertainty in each material property. In the case of angular misalignment in the hole-drilling specimen, the variation is scaled according to the square of the angular misalignment between each ply and the strain gauge rosette. For small angles, the effects of angular misalignment translate into quadratic variations in elastic constants and hence quadratic variations in the compliance and stiffness matrices. The two calibration matrices and the stress matrix within each Monte Carlo trial are then estimated using equations (5.19) to (5.21).

$$\bar{\mathbf{C}}_j = \bar{\mathbf{C}} + \sum_{i=1}^{5} r_j(x_i)u(x_i)\bar{\mathbf{C}}(x_i) + \sum_{i=6}^{8} r_j(x_i)u^2(x_i)\bar{\mathbf{C}}(x_i) \tag{5.19}$$

$$\hat{\mathbf{C}}_j = \hat{\mathbf{C}} + \sum_{i=1}^{5} r_j(x_i)u(x_i)\hat{\mathbf{C}}(x_i) + \sum_{i=6}^{8} r_j(x_i)u^2(x_i)\hat{\mathbf{C}}(x_i) \tag{5.20}$$

$$\mathbf{S} = \mathbf{S} + \sum_{i=1}^{5} r_j(x_i)u(x_i)\mathbf{S}(x_i) + \sum_{i=6}^{8} r_j(x_i)u^2(x_i)\mathbf{S}(x_i) \tag{5.21}$$

where:

$r(x_i)$ corresponds to normally distributed random numbers with standard deviations of ± 1,

$u(x_{1-5})$ correspond to uncertainties in E_1, E_2, G_{12}, ν_{12} and ν_{23}, respectively, including all material testing misalignment effects,

$u(x_{6-8})$ correspond to uncertainties in the orientation of the 0°, +45° and -45° plies of the hole-drilling specimen, including the misalignment of the hole-drilling rosette,

$\bar{\mathbf{C}}(x_{1-5})$, $\hat{\mathbf{C}}(x_{1-5})$ and $\mathbf{S}(x_{1-5})$ are the changes in the $\bar{\mathbf{C}}$, $\hat{\mathbf{C}}$ and $\mathbf{S}$ matrices, respectively, as a result of a 1% increase in E_1, E_2, G_{12}, ν_{12} and ν_{23}, respectively,

$\bar{\mathbf{C}}(x_{6-8})$, $\hat{\mathbf{C}}(x_{6-8})$ and $\mathbf{S}(x_{6-8})$ are the changes in the $\bar{\mathbf{C}}$, $\hat{\mathbf{C}}$ and $\mathbf{S}$ matrices, respectively, as a result of a 1°increase in ply orientation in each of the 0°, +45° and -45° plies, respectively,

$\bar{\mathbf{C}}$, $\hat{\mathbf{C}}$ ans $\mathbf{S}$ are the original longitudinal and transverse calibration and stress matrices, respectively, and $\bar{\mathbf{C}}_j$, $\hat{\mathbf{C}}_j$ and $\mathbf{S}_j$ are the longitudinal and transverse calibration and stress matrices, respectively, for Monte Carlo trial j.

It is important to note that the material properties are independent of each other and are therefore varied independently. A variation in a particular material property has simultaneous effects on the calibration and stress matrices and so they are varied by the same normal distribution. The same applies to variations in each ply orientation. While it must be acknowledged that this approach does not take higher order effects into account, the first order effects on the calculated stress are of a similar

magnitude to the variation in material properties. Since these are small, the higher order effects are not believed to be significant enough to justify the additional computational cost of including them.

The calculation of the two calibration matrices, $\bar{\mathbf{C}}$ and $\hat{\mathbf{C}}$, depends entirely on the FE method. Since FE models cannot completely represent all the deformations that are possible in reality, some uncertainty exists in the knowledge of these matrices. The individual terms within the calibration matrices are considered to be fully correlated and so they are all varied using the same random variable [145]. The stress matrix is similarly modified. Finally, the calibration matrix is adjusted to compensate for uncertainty in the transverse sensitivity of each gauge. Equation (5.13) which includes the transverse sensitivity coefficient of each gauge in that particular Monte Carlo trial, is used at this stage.

Uncertainties associated with hole eccentricity are not taken into account in this chapter. Hole offset from the centre of the strain gauge rosette is an extremely important consideration as any offset will affect the measured strains. To correct for hole eccentricity, either the experimental strains must be corrected or the calibration matrix must be corrected. Neither of these are easily achieved due to the composite material and the FE approach of this chapter. Any x and y offset of the hole was somewhat mitigated by the use of a 6 element strain gauge rosette, but because of the complex strain field around the hole it cannot be fully compensated for by this alone. To account for this requires correction of the calibration matrices based on the x and y offset of the hole. The hole offset in the x and y directions was minimised by meticulous experimental technique to ensure that the hole coincided with the centre of the strain gauge as accurately as possible by the use of the microscope and micrometers of the MTS 3000. Hole eccentricity was measured after drilling and found to be close to zero, and so any uncertainties due to this parameter are judged to be small in comparison with the uncertainties that are considered and therefore is not included in the analysis. For the same reason, the effects of hole diameter variation are also ignored because the FE model is based on the measured hole diameter.

The inverted cone end mill used to drill the hole during IHD results in a hole bottom that is not perfectly flat. The effect of the hole-bottom fillet radius on the calculated residual stresses has been investigated by several authors in isotropic materials [160, 161, 190] and has been found to have an appreciable affect on the measured stresses, especially in the first few hole depth increments. However, proposed corrections to calibration coefficients do not extend to FRP laminates. To include the effect of the hole-bottom fillet radius in this analysis would require direct inclusion of the hole-bottom fillet radius in the FE model, which would be computationally impractical in this case. The uncertainties associated with hole-bottom fillet radius were therefore not taken into account.

Once the strain vector, $\boldsymbol{\epsilon}_{meas}$, calibration matrix, $\mathbf{C}$, and the stress matrix, $\mathbf{S}$, are determined for each Monte Carlo trial, the residual stress distribution is determined using equations (5.10) and (5.12). The uncertainties in the stress distribution of each order combination are determined by evaluating

the standard deviation in calculated stress at the nominal depth of each $\boldsymbol{\sigma_{res}}$ datum across the ten thousand trials used in the Monte Carlo simulation.

5.3.4 Monte Carlo Simulation

Every possible combination of series order was tested using Monte Carlo simulation such that each combination produced ten thousand curve fits. Such fits to the Monte Carlo strain data are shown in Figures 5.12 to 5.14 for an order combination of (2, 2, 0). To improve the clarity of these figures, only data for one hundred Monte Carlo trials are presented. Ten thousand curve fits allowed ten thousand residual stress distributions to be calculated, these are presented in Figures 5.15 to 5.17, again showing the data for only one hundred Monte Carlo trials. The uncertainties in all figures of this thesis correspond to ± 2 standard deviations, unless stated otherwise.

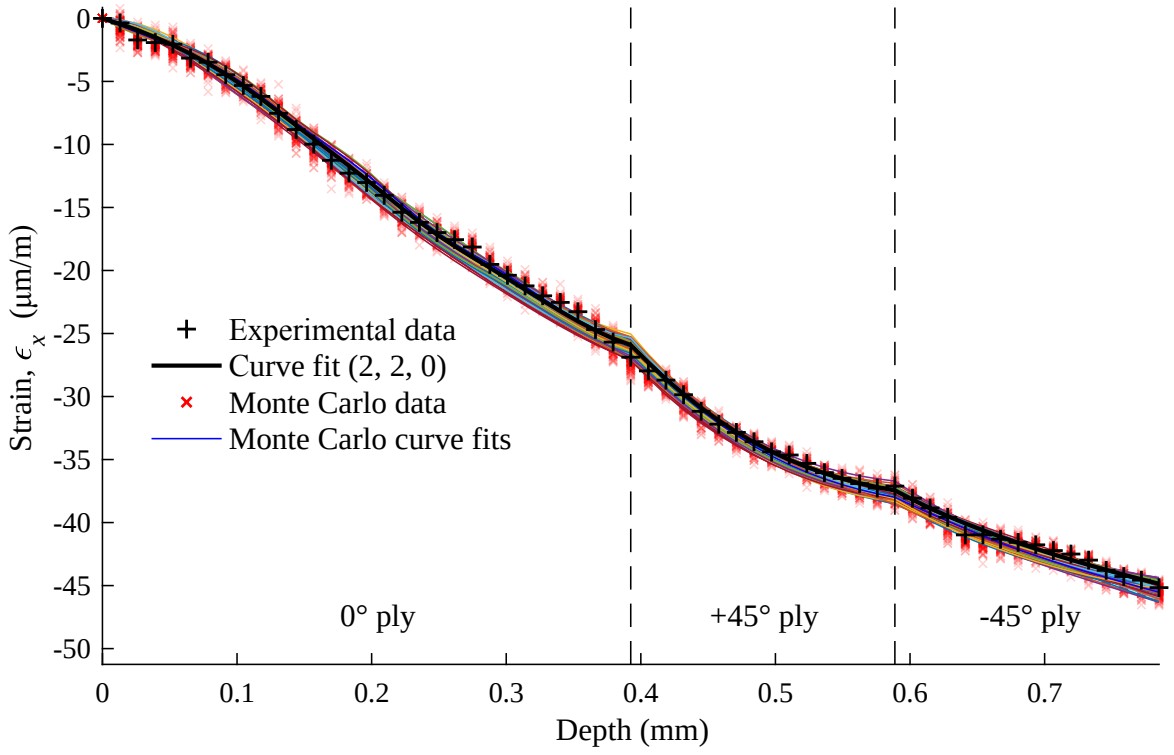


Figure 5.12: Least-squares curve fits to Monte Carlo strains in x-direction

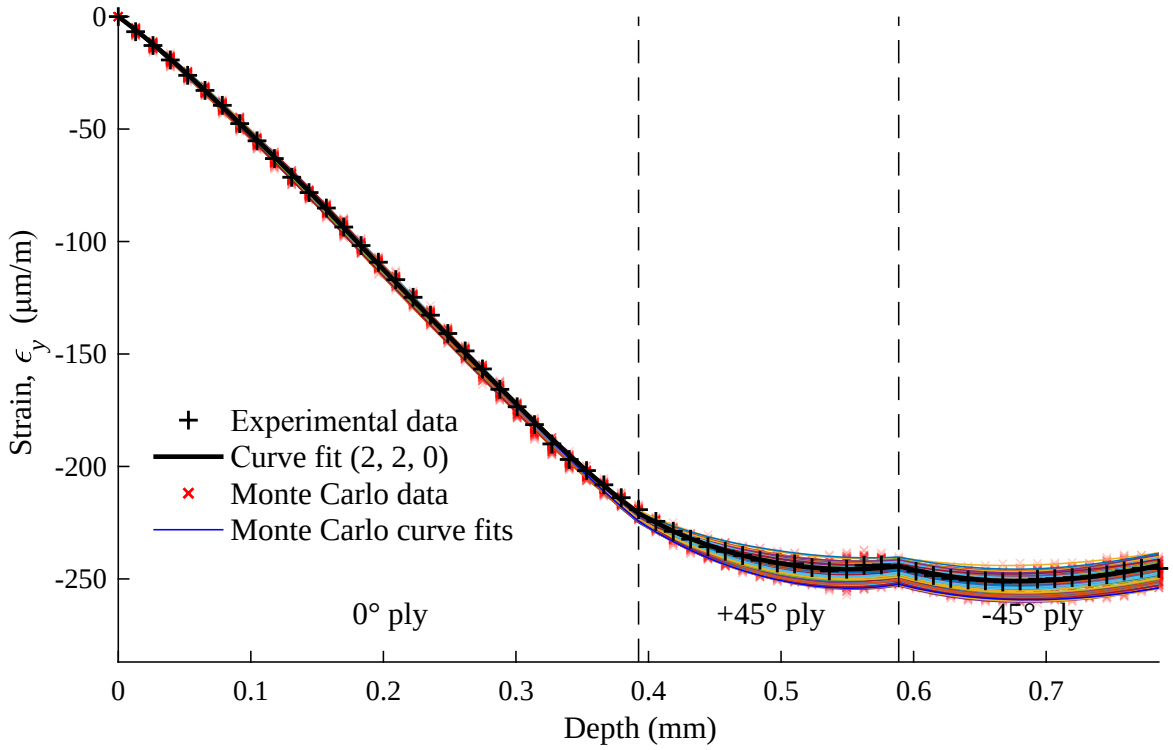


Figure 5.13: Least-squares curve fits to Monte Carlo strain in y-direction

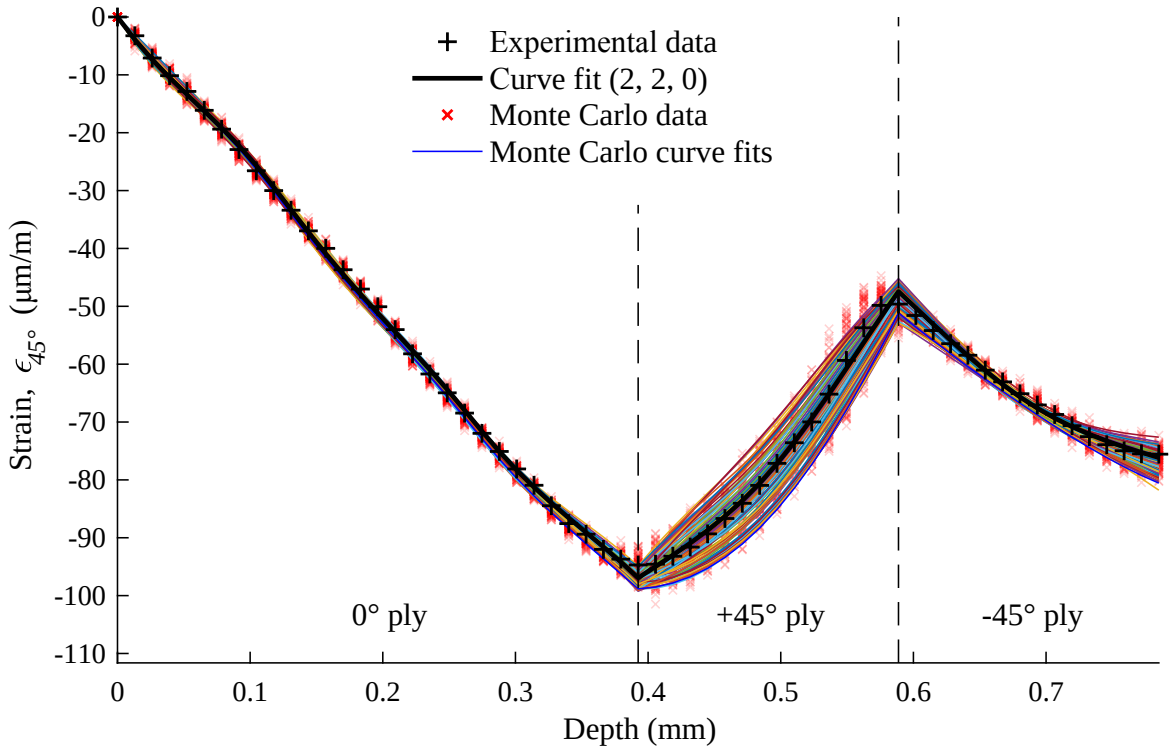


Figure 5.14: Least-squares curve fits to Monte Carlo strain in 45° direction

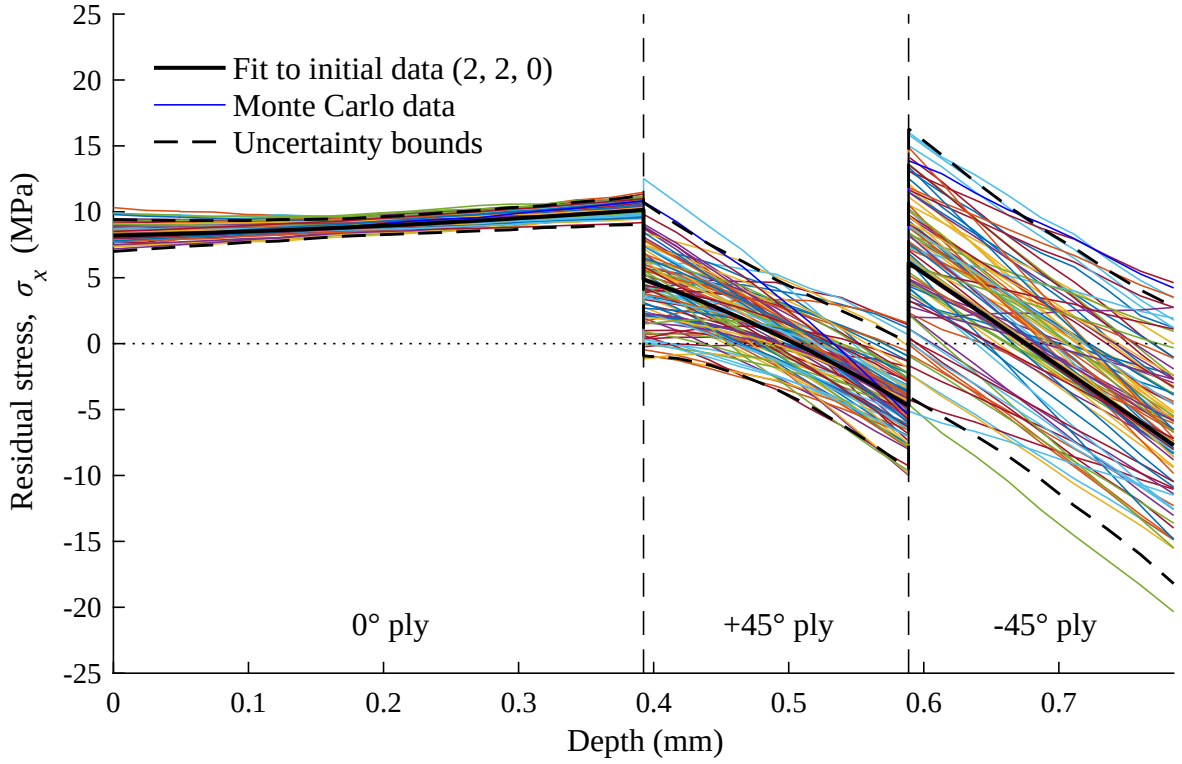


Figure 5.15: σ_x Monte Carlo stress distributions and associated uncertainties obtained using the (2, 2, 0) combination of series orders

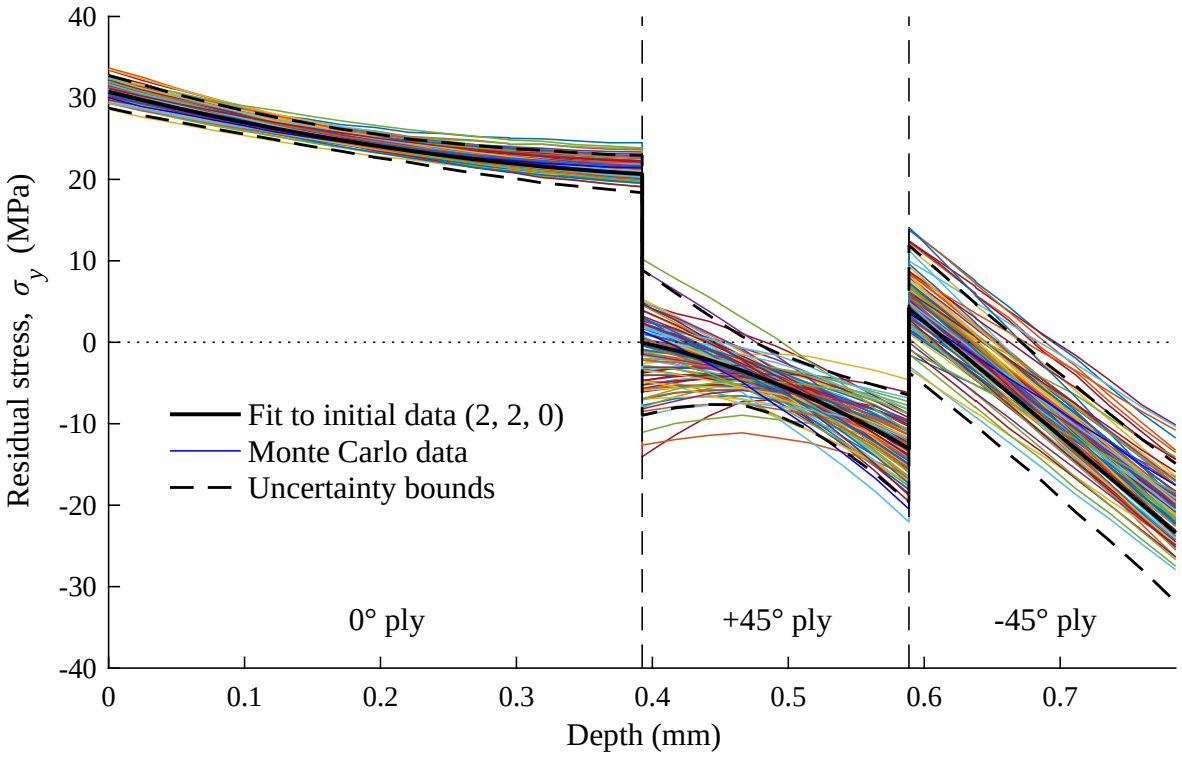


Figure 5.16: σ_y Monte Carlo stress distributions and associated uncertainties obtained using the (2, 2, 0) combination of series orders

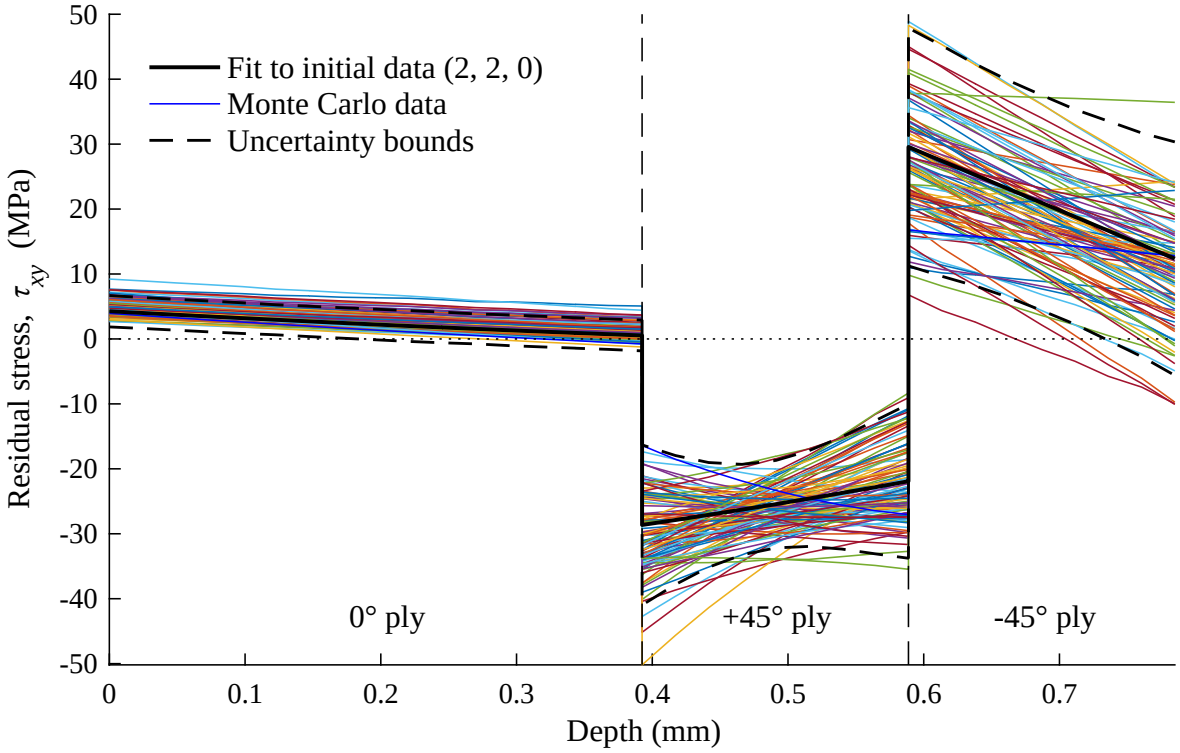


Figure 5.17: τ_{xy} Monte Carlo stress distributions and associated uncertainties obtained using the (2, 2, 0) combination of series orders

5.3.5 Order Selection

While the experimental, computational and uncertainty propagation methods used in this chapter allow the residual stress distribution and its uncertainty to be determined, the issue remains as to which combination of series orders provides the best approximation of the true residual stress from the experimental data. All combinations of series orders have the ability to solve the inverse problem, and describe the experimental strain distributions to some degree. The approach used in this work is to select the combination of series orders with the lowest RMS uncertainty from those combinations that have converged. The size of the uncertainty bounds and the convergence of every combination of series orders must therefore be investigated to quantitatively find the true, or most probable, residual stress distribution.

From the combinations that have converged, the (2, 2, 0) combination has the lowest RMS uncertainty and is consequently selected as the best solution for this laminate. Some combinations have lower uncertainty, but have not fully converged and so are not selected. Other combinations while fully converged, show the first signs of instability that leads to greater uncertainty, and so they too are not selected. It is important to emphasise that the order combination (2, 2, 0) refers to the order of the temperature variations applied to each ply orientation to generate eigenstrain and not simply to the order of the residual stress distribution in each ply orientation. They are different because each and

every separate eigenstrain and each component of eigenstrain has some effect on the residual stress distributions in every ply orientation.

It is interesting to observe that in the case of the (2, 2, 0) combination, the amplitude coefficients of the 1^{st} and 2^{nd} order eigenstrains in the 0° and +45° plies are only 0.063% and 0.001% of the 0^{th} order coefficient, respectively. The stress distribution of the (0, 0, 0) combination is quite different from that of the (2, 2, 0) combination, however, indicating that the higher order terms have a significant impact on the final stress result even with very small amplitude coefficients. The potential for instability in the results with several higher order terms is thus clear.

The tendency of higher order series combinations to become unstable makes them sensitive to changes in strains in the Monte Carlo simulation. This results in greater uncertainty bounds if the higher order functions are dominant within the order combination as is shown graphically in Figures 5.18 to 5.20 for the twenty most converged fits. The area between the uncertainty bounds of each fit is shaded in light grey and then superimposed. The darkest area corresponds to convergence where the uncertainty bounds of a number of order combinations agree. The light grey regions illustrate the divergence in uncertainty for order combinations where higher order functions are more dominant. This divergence continues to grow as the relative amplitude coefficients of the higher order terms increase. It is worth mentioning at this point, therefore, that the technique described in this chapter might not work well when a number of plies of the same orientation are stacked together into a thick block. In this case, the stress variation across the block might vary in a higher order fashion that would require a correspondingly high order series to match it. Instability in the resulting computational problem could prevent a valid solution from being obtained.

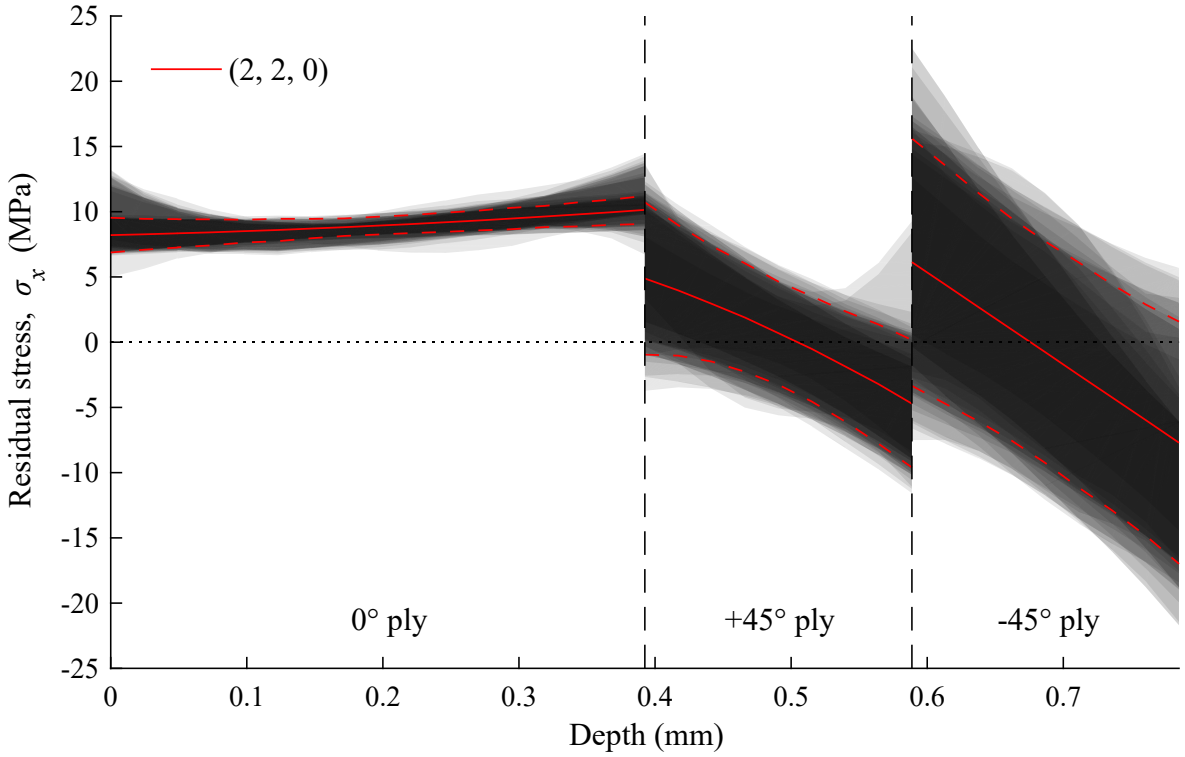


Figure 5.18: Overlap of the uncertainty bounds in σ_x for the twenty fits most converged to the (2, 2, 0) combination

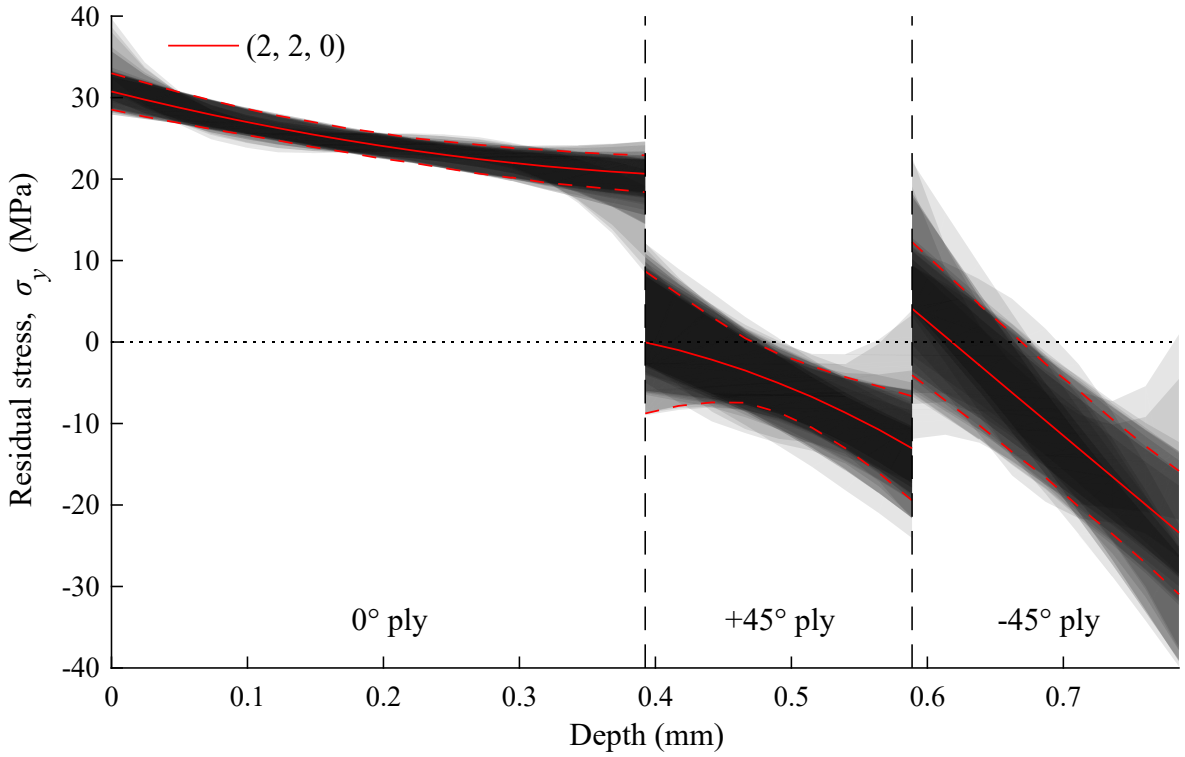


Figure 5.19: Overlap of the uncertainty bounds in σ_y for the twenty fits most converged to the (2, 2, 0) combination

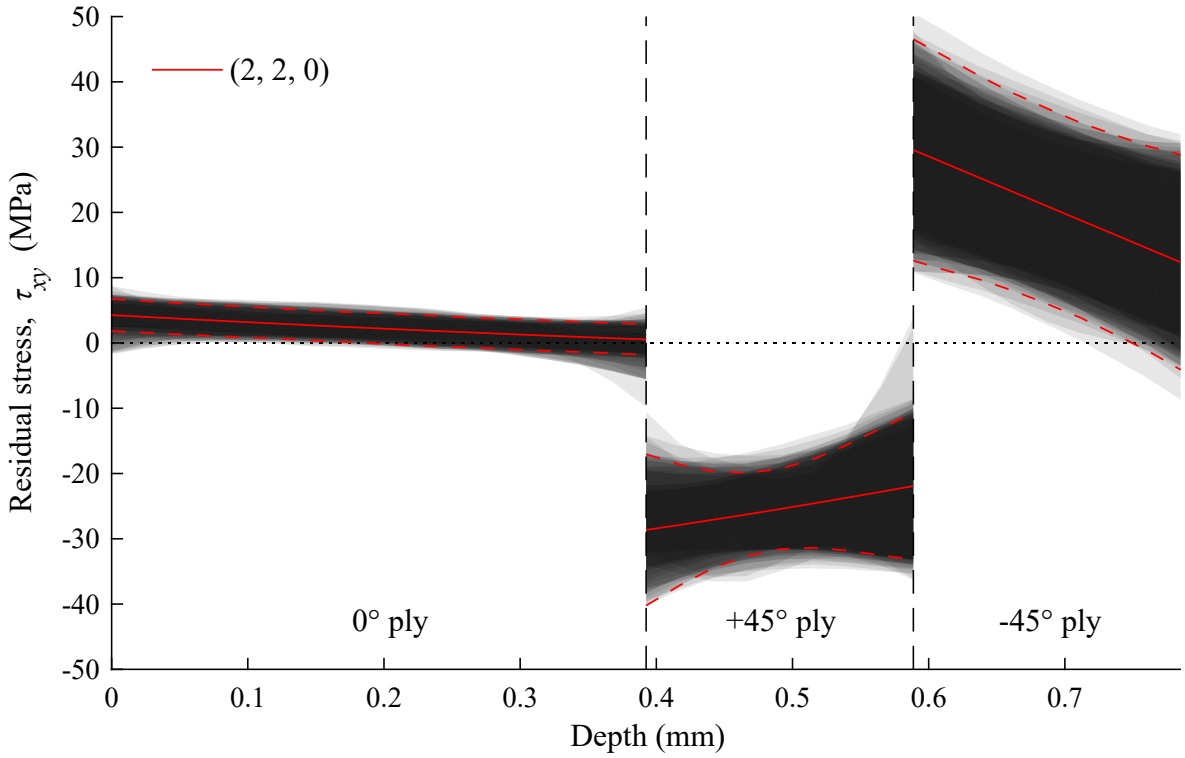


Figure 5.20: Overlap of the uncertainty bounds in τ_{xy} for the twenty fits most converged to the (2, 2, 0) combination

5.4 Results and Discussion

The least-squares fit and associated uncertainties (including that from the curve fit) of the (2, 2, 0) combination of series orders to the strain measurements obtained from the x, y and 45° gauges is shown in Figure 5.21. The stress distributions and associated uncertainties obtained using the (2, 2, 0) combination of series orders are shown in Figure 5.22. The solid line corresponds to the the mean value of the calculated residual stress for all Monte Carlo trials at each depth increment and the dashed lines are the upper and lower uncertainty bounds that correspond to ± 2 standard deviations of the Monte Carlo trials. Table 5.4 provides the RMS uncertainty in stress in the 0°, +45° and -45° plies, for each uncertainty source and also the combined uncertainty, $u(Z)$. The RMS uncertainties in stress were calculated using equation (5.22).

$$\mathrm{RMS}_{x_i} = \sqrt{\frac{\sum_{i=1}^{n}\left[\frac{\sum_{j=1}^{m}(\sigma_{ij}-\bar{\sigma}_i)^2}{m}\right]}{n}} \tag{5.22}$$

where: n is the number of depth increments within a ply orientation, and m is the total number of Monte Carlo trials,

σ_{ij} is the calculated residual stress at depth i for Monte Carlo trail j,

$\bar{\sigma}_i$ is the mean stress at depth i from all Monte Carlo trials.

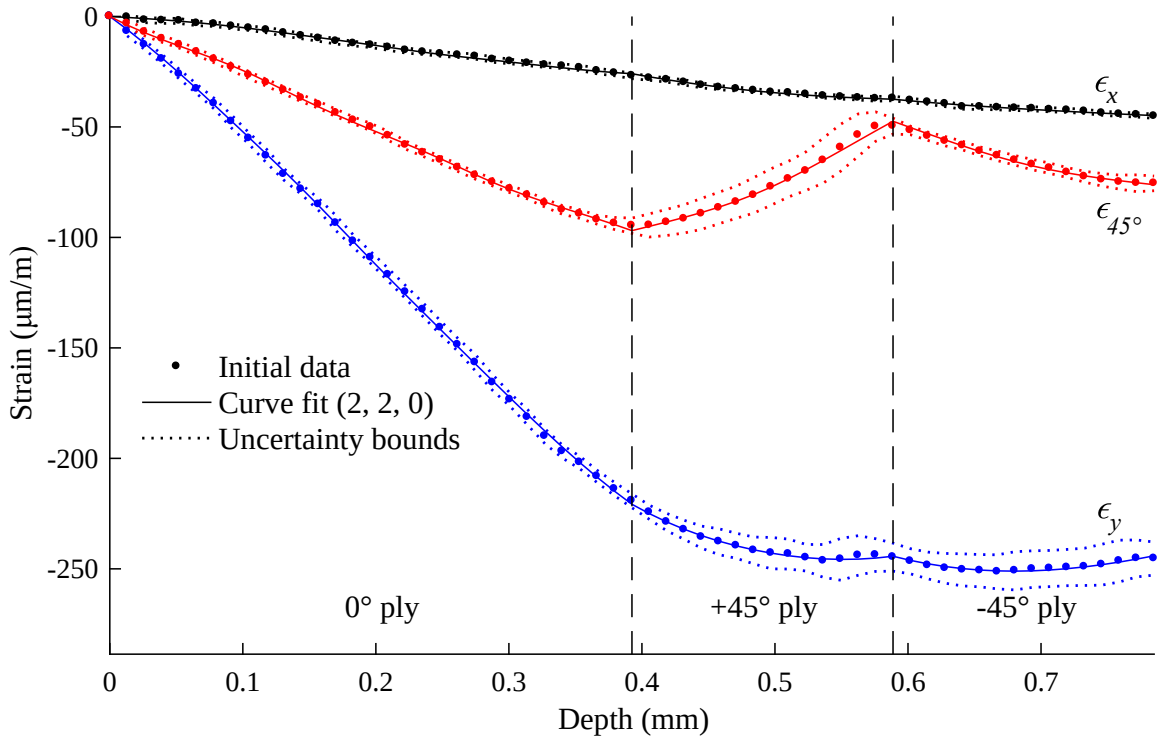


Figure 5.21: Least-squares curve fits to experimental strain data with associated uncertainties using the (2, 2, 0) combination of series orders

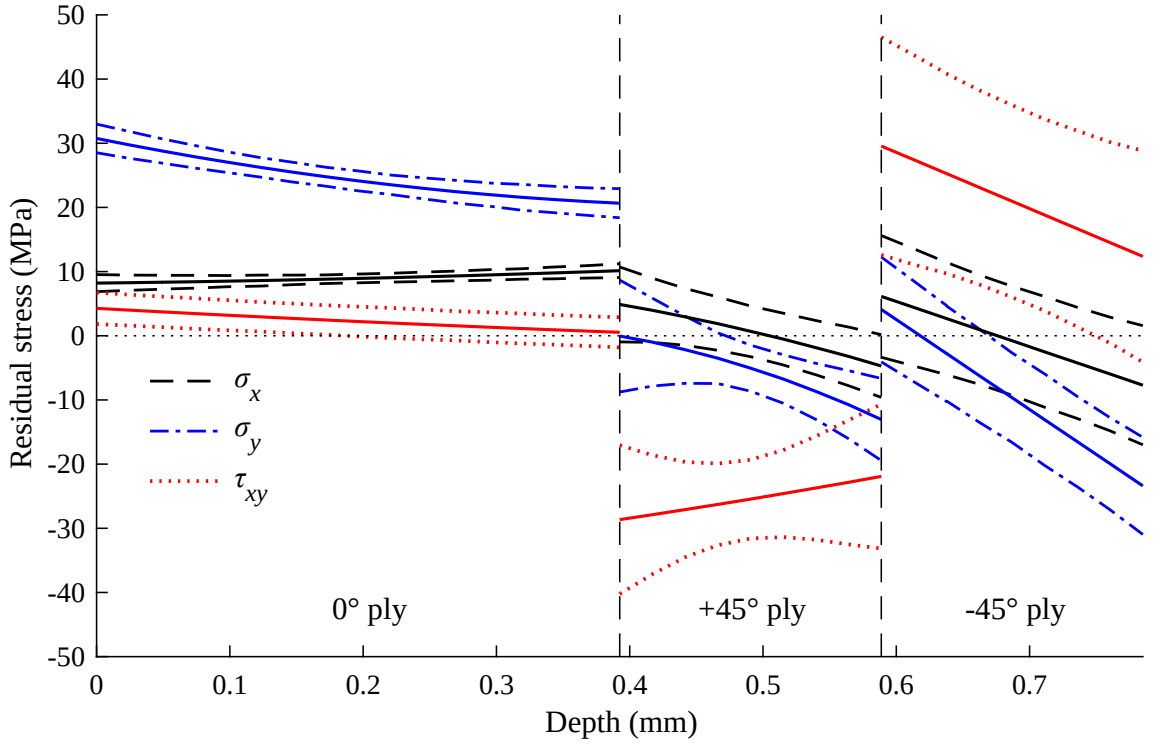


Figure 5.22: Stress distributions and associated uncertainties obtained using the (2, 2, 0) combination of series orders

Table 5.4: Breakdown of RMS uncertainty in stress arising from each uncertainty source, x_i

x_i	Contribution to $u(\sigma_x)$ [MPa]			Contribution to $u(\sigma_y)$ [MPa]			Contribution to $u(\tau_{xy})$ [MPa]		
	0° ply	45° ply	-45° ply	0° ply	45° ply	-45° ply	0° ply	45° ply	-45° ply
E_1	0.136	0.370	0.161	0.059	0.064	0.288	0.198	0.213	0.553
E_2	0.045	0.238	0.941	0.299	0.573	1.901	0.198	1.300	3.130
G_{12}	0.251	0.208	0.314	0.481	0.350	0.269	0.476	1.058	0.518
ν_{12}	0.043	0.141	0.085	0.116	0.312	0.266	0.284	0.219	1.244
ν_{23}	0.058	1.716	3.678	0.211	1.233	0.619	0.090	1.411	4.167
z_i	0.015	0.045	0.052	0.040	0.067	0.048	0.010	0.058	0.072
z_0	0.125	1.003	0.479	0.384	1.662	0.786	0.143	2.301	2.105
ϵ_m	0.039	0.017	0.017	0.109	0.037	0.051	0.011	0.110	0.099
ϵ_{noise}	0.074	0.216	0.435	0.052	0.138	0.284	0.062	0.156	0.286
K_{tp}	0.017	0.010	0.016	0.004	0.004	0.006	0.013	0.007	0.010
ν_0	0.001	0.002	0.002	0.004	0.002	0.002	0.004	0.006	0.005
θ_{SG_t}	0.019	0.085	0.043	0.021	0.051	0.036	0.023	0.042	0.144
θ_{coupon}	0.005	0.022	0.011	0.005	0.013	0.009	0.006	0.01	0.036
θ_{grips}	0.019	0.085	0.043	0.020	0.051	0.036	0.023	0.04	0.143
θ_{SG_h}	0.149	0.203	0.507	0.269	0.312	1.875	0.724	0.81	2.150
$\theta_{0^\circ\text{ply}}$	0.021	0.032	0.205	0.057	0.138	0.527	0.110	0.192	0.355
$\theta_{45^\circ\text{ply}}$	0.015	0.019	0.050	0.063	0.114	0.200	0.063	0.18	0.061
$\theta_{-45^\circ\text{ply}}$	0.010	0.016	0.169	0.011	0.027	0.336	0.046	0.024	0.286
FE	0.071	0.032	0.031	0.199	0.067	0.092	0.021	0.2	0.180
Misfit	0.094	0.495	0.878	0.129	0.523	0.851	0.165	0.713	1.128
u(Z)	0.437	2.171	4.294	0.872	2.528	3.621	1.099	3.888	7.542

As expected, the combined uncertainty, $u(Z)$, in all three stress components tends to increase from the 0° ply through the +45° ply and on to the -45° ply, or as the depth increases. This reflects the decreasing sensitivity of the relaxation strains on the upper surface of the laminate to internal stresses at increasing depths. It is also evident that the most important contributors to the uncertainty in the stress results are the zero depth, misalignment of the hole-drilling strain gauge rosette, the curve fit and the material properties E_2, G_{12}, ν_{12} and ν_{23}. The large uncertainties in stress associated with ν_{23} are ascribed to the large uncertainties in this parameter resulting from its estimation using micromechanics.

It is apparent from Figure 5.22 that the residual stress distributions in the x and y directions have similar form: the residual stress in the 0° ply is fairly constant in tension, while the stress in the +45° and -45° plies decreases through the thickness of each ply. The residual shear stress in the 0° ply is close to zero while the distributions in the +45° and -45° plies are approximately equal and opposite. A discontinuity in stress at the interfaces between plies of different orientations is also evident for all stress components, as is required. The uncertainty in stress increases near the ply interfaces which is a consequence of using a separate curve fit within each ply orientation. The fitted curves are less constrained near their ends and as a result tend to diverge from the mean, which increases the uncertainty in these regions. Instability near the endpoints of the fitted domain, using Legendre polynomials with the slitting method, has also been reported by Shokrieh et al. [4]. While it is difficult to predict the direction and variation of the x and y components of the residual stresses in this laminate, it is known that the shear stress component of the 0° ply should have zero residual stress and that the +45 and -45° plies should have opposing stresses of equal magnitude so that they are in equilibrium. Although these conditions are not perfectly satisfied, they come close to it, and equilibrium is achieved when the uncertainty in the +45° and -45° plies is considered. When the uncertainties in the x and y components are taken into consideration, they remain unbalanced by an average of about 0.6 MPa and 4.5 MPa, respectively.

The laminate is symmetrical, and so it is expected that symmetry should exist in the residual stress distribution through the thickness of the laminate. This would imply that all three stress components should have zero slope at the mid-plane. This is clearly not the case, and the source of this unexpected behaviour can be traced to the depth of the hole being too shallow to allow the actual stress distributions in this region to emerge. While the -45° ply is continuous on the deeper side of the mid-plane, the strain data do not extend beyond this point. This means that the current stress distributions are simply those of the best possible fit using the available data. If the hole depth had been extended to provide additional data on the far side of the mid-plane, it is possible that these additional data points would have changed the stress distributions in the -45° ply to allow zero slopes at the mid-plane. This might also have led to better convergence in the -45° ply than is currently observed in Figures 5.18 to 5.20. It therefore becomes apparent that the experiment should not have been terminated at the mid-plane, and drilling should have continued through the thickness of the -45° ply so that the best

estimate of the behaviour at the mid-plane could have been obtained. This might also explain the lack of equilibrium in the x and y components as this method does not enforce equilibrium in one half of the thickness only and allows for asymmetric stress distributions to be determined. Because the method is based on eigenstrain, it does, however, enforce equilibrium in the plate as a whole.

A residual stress analysis must compare the measured stresses with allowable values. Transformation of the measured stresses into the material principal coordinate system reveals that the axial stresses and in-plane shear stresses are small in comparison with the strengths of two similar materials documented by Soden et al. [182]. The transverse stresses on the upper surfaces of all plies is, however, approaching the lower of the two transverse strengths reported by these researchers. While the transverse strength of the laminate material used in this investigation is not known, it is clear that the mechanical load required to cause transverse tensile failure is significantly lower than might otherwise be expected.

Since the transverse stresses are high in comparison to the transverse strength, and since the accuracy of the hole-drilling method is clearly affected by localized transverse fracture at the hole, the effects of stress concentration must be assessed. The transverse stresses on the inner surface of the hole were consequently investigated using the FE models employed throughout this chapter. The maximum stresses are, once again, located at the upper surface of each ply, with those in the 0° ply being critical. The peak stress in the 0° ply reaches nearly 58 MPa, which is 66% higher than the lower transverse strength of 35 MPa reported by Soden et al. [182].

While transverse fracture in the internal plies might be inhibited by the transverse fibres of adjacent plies, as reported by Flaggs and Kural [183], such support does not exist on the upper surface of the 0° ply. It therefore seems probable that some transverse cracking occurred on the inner surface of the hole. The possibility of transverse cracking has also been reported by Akbari et al. [157]. It must therefore be accepted that the accuracy of the measured residual stresses results could have been affected by transverse failure. This is a very significant result that needs further investigation. As hole drilling in FRP laminates becomes more frequent, transverse failure may turn out to be as important a consideration in laminated composites as plasticity effects are in metallic structures.

5.5 Conclusions

A new method for relating experimental strains from IHD to discontinuous stress distributions has been introduced and demonstrated. It is suitable for use on FRP laminates, layered composite materials, or any other material where discontinuous stress states could exist. The method is based on the approximation of the residual stress distribution by power series expansion of separate eigenstrain functions in each material type. The unknown amplitude coefficients of each series are simultaneously determined by least-squares error minimisation which provides tolerance to measurement errors or single erroneous measurements. The method is readily implemented and allows the uncertainty bounds of all three in-plane stress components to be robustly calculated using Monte Carlo simulation. The order of the least-squares fit to the experimental data is increased until the residual stress distribution is found from that combination of series orders in the different ply orientations that has the lowest RMS uncertainty, selected only from those combinations that have converged. While the technique is not limited in its use, and allows the analysis of FRP laminates with any number of plies orientated in any direction, instability may become a problem when several plies of the same orientation are stacked together. The transverse stresses in the $[0_2/+45/-45]_s$ GFRP laminate under investigation were determined to be high enough that transverse cracking at the inner surface of the hole may have impacted on the accuracy of the measured residual stresses.

5.6 Contribution to Knowledge

- Application of IHD has been extended to composite materials and FRP laminates of any construction through the use of separate series expansion to address limitations of existing unit pulse approaches. The method can be applied to laminates with any number of plies, orientated in any direction, or in any layered material where stress discontinuities exist.
- A comprehensive and robust uncertainty estimation methodology has been developed using Monte Carlo simulation to evaluate the uncertainty in calculated residual stress distributions of IHD in FRP laminates. Contributions of a number of experimental and computation error sources to the stress measurement uncertainty was investigated to assess the separate series expansion method.
- A methodology has been developed to quantitatively select the most appropriate combination of series expansion orders to describe the residual stress distribution by investigating the convergence of uncertainty bounds and total RMS uncertainty of series order combinations.

6 Tikhonov Regularization with the Integral Method in Cross-Ply Composite Laminates

This chapter presents and demonstrates a means to apply Tikhonov regularization to the unit pulse integral method with IHD when measuring residual stress distributions in cross-ply FRP laminates. FE modelling is used to calculate the necessary calibration coefficients for unit pulses of uniform stress in all in-plane components. Tikhonov regularization is applied through simplifying approximations prior to the inverse solution with a fully coupled calibration matrix. Using this approach, Tikhonov regularization is successfully applied to cross-ply FRP laminates for the first time using IHD. Tikhonov regularization is optimised through the Morozov Discrepancy Principle to reduce the stress uncertainty, while ensuring that the stress solution is not distorted. Sixteen material removal increments are used such that the variation in residual stress within each ply can be fully defined. The calculated residual stress distribution is compared to that of the fully coupled integral method without the use of regularization and with that of the series expansion method. The effect of different numbers of drilling increments on the unregularized solution is also investigated for comparison purposes. Full uncertainty estimation and the contribution from each uncertainty source is determined using Monte Carlo simulation to facilitate a thorough comparison between all methods considered. It is found that application of Tikhonov regularization significantly improves the accuracy of the stress measurement and effectively triples the resolution compared to the unregularized integral method, and shows good agreement with the series expansion method. The method is demonstrated on a GFRP laminate of $[0_2/90_2]_s$ construction.

This chapter has been adapted and extended from: **T.C. Smit**, R.G. Reid. Tikhonov Regularization with Incremental Hole-Drilling and the Integral Method in Cross-Ply Composite Laminates. *Experimental Mechanics*, 2020, Springer Nature. The published article is available at https://doi.org/10.1007/s11340-020-00629-x. Licensed permission to reuse this content can be found in Appendix I: Springer Nature License Agreements.

6.1 Introduction

Tikhonov regularization is a powerful technique to smooth calculated stress distributions and remove noise artefacts from IHD strain measurements, thereby reducing uncertainty in calculated stress. Tikhonov regularization is used extensively and successfully with isotropic materials to reduce instability in residual stress measurements when many depth increments are used. It is widely accepted and included in the ASTM standard and it should always be applied in the case of isotropic materials. However, the use of the ASTM standard does not extend to composite materials such as FRP laminates, and Tikhonov regularization has not been applied to FRP laminates with IHD. Therefore, the existing unregularized integral methods currently employed are sensitive to measurement errors, which can result in large stress uncertainties, and require a limited number of regulated depth increments to obtain a stable solution. The chosen depth distribution can, however, adversely affect the calculated stresses.

Although the use of power series expansion with IHD has been successfully extended to layered composite materials in Chapter 5, the use of eigenstrain applied through temperature variation to generate separate series for each ply orientation, or layer with different material properties with respect to the global coordinate system, requires additional FE calculations. The inverse solution and convergence study to determine the combination of series orders that best approximates the actual residual stress distribution is also computationally more expensive than the integral method. Additionally, IHD practitioners are not as familiar with series expansion since the method has not been widely used with IHD and there are numerous subtle differences between series expansion and the widely used ASTM standard such as small experimental depth increments and results processing that relies on a robust uncertainty analysis. It is, therefore, likely that practitioners will be using the integral method for residual stress measurement with IHD in composite materials for the foreseeable future. A need therefore exists to incorporate Tikhonov regularization into the integral solution of IHD in composite materials.

Tikhonov regularization with the integral method has been successfully applied to layered materials using the slitting technique [99, 127, 191]. This was possible since the strain release with slitting is mostly due to stress normal to the cut that allows regularization to be applied, provided that discontinuities at ply interfaces are considered. In the case of IHD, the situation is more complex since all stress components effect each released strain simultaneously in a manner that cannot be described analytically at present. Tikhonov regularization can therefore not be applied directly to IHD in FRP laminates. However, Tikhonov regularization can be applied separately to each measurement direction through simplifying approximations prior to the inverse solution with a fully coupled calibration matrix provided that the contribution to strain in a particular direction is mostly due to stress in that direction, such as in the case of cross-ply FRP laminates.

6.2 Computational Methods

While three different computational methods are used in this chapter, only the regularized integral method is explained in some detail since series expansion as applied to FRP laminates is discussed in Chapter 5 and the fully coupled integral method in FRP laminates is given by Akbari et al. [157].

6.2.1 Fully Coupled Integral Method

An unknown residual stress can be determined from the integral equation relating the residual stresses, σ_{js}, and experimental strains, ϵ_{ig}, as a function of depth. The integral equation can be simplified to:

$$\epsilon_{ig} = \sum_{s=1}^{3} \sum_{j=1}^{i} c_{igjs} \sigma_{js} \tag{6.1}$$

where c_{igjs} is the measured strain at the location of strain gauge g for hole depth increment i when a unit stress is applied in the region of the j^{th} depth increment in the s component of residual stress.

Equation (6.1) can be written in vector-matrix form as equation (6.2) and an example for the first three depth increments is given by equation (6.3) [157].

$$\boldsymbol{\epsilon}_{meas} = \mathbf{C}\, \boldsymbol{\sigma}_{res} \tag{6.2}$$

$$\left\{\begin{array}{c} \epsilon_{1_x} \\ \epsilon_{1_y} \\ \epsilon_{1_{45^\circ}} \\ \hline \epsilon_{2_x} \\ \epsilon_{2_y} \\ \epsilon_{2_{45^\circ}} \\ \hline \epsilon_{3_x} \\ \epsilon_{3_y} \\ \epsilon_{3_{45^\circ}} \\ \hline \vdots \\ \epsilon_{i_g} \end{array}\right\} = \left[\begin{array}{ccc|ccc|ccc|c} C_{1111} & C_{1112} & C_{1113} & 0 & 0 & 0 & 0 & 0 & 0 & \dots \\ C_{1211} & C_{1212} & C_{1213} & 0 & 0 & 0 & 0 & 0 & 0 & \dots \\ C_{1311} & C_{1312} & C_{1313} & 0 & 0 & 0 & 0 & 0 & 0 & \dots \\ \hline C_{2111} & C_{2112} & C_{2113} & C_{2121} & C_{2122} & C_{2123} & 0 & 0 & 0 & \dots \\ C_{2211} & C_{2212} & C_{2213} & C_{2221} & C_{2222} & C_{2223} & 0 & 0 & 0 & \dots \\ C_{2311} & C_{2312} & C_{2313} & C_{2321} & C_{2322} & C_{2323} & 0 & 0 & 0 & \dots \\ \hline C_{3111} & C_{3112} & C_{3113} & C_{3121} & C_{3122} & C_{3123} & C_{3131} & C_{3132} & C_{3133} & \dots \\ C_{3211} & C_{3212} & C_{3213} & C_{3221} & C_{3222} & C_{3223} & C_{3231} & C_{3232} & C_{3233} & \dots \\ C_{3311} & C_{3312} & C_{3313} & C_{3321} & C_{3322} & C_{3323} & C_{3331} & C_{3332} & C_{3333} & \dots \\ \hline \vdots & \vdots & \vdots & \vdots & \vdots & \vdots & \vdots & \vdots & \vdots & \ddots \\ C_{ig11} & C_{ig12} & C_{ig13} & C_{ig21} & C_{ig22} & C_{ig23} & C_{ig31} & C_{ig32} & C_{ig33} & C_{igjs} \end{array}\right] \left\{\begin{array}{c} \sigma_{1_x} \\ \sigma_{1_y} \\ \tau_{1_{xy}} \\ \hline \sigma_{2_x} \\ \sigma_{2_y} \\ \tau_{2_{xy}} \\ \hline \sigma_{3_x} \\ \sigma_{3_y} \\ \tau_{3_{xy}} \\ \hline \vdots \\ \sigma_{i_s} \end{array}\right\} \tag{6.3}$$

The inverse solution of equation (6.2) determines the residual stresses from the experimental strains. Since the number of depth increments is equal to the number of unknown stresses, the strain fit produced by the inverse solution exactly matches the measured data. As a result, the fully coupled integral method can be sensitive to both measurement errors [95, 96] and inaccuracies in the results obtained from the FE calculations [97].

The number of depth increments must be carefully chosen. If the residual stress varies significantly within a ply orientation, numerous depth increments are required to represent the residual stress distribution as a sequence of uniform stresses. Zuccarello [155] has shown that the number of depth

increments should be less than ten to achieve a stable result. In light of this recommendation, four, six and eight depth increments were chosen to obtain the highest resolution in stress without instability becoming too significant. Sixteen depth increments were also considered to demonstrate the instability resulting from excessive depth increments and to subsequently investigate the effect of incorporating Tikhonov regularization. The increments have uniform depth to ensure that the discontinuities in stress at the interfaces between plies of different orientation can be captured correctly.

6.2.2 Tikhonov Regularization

Tikhonov regularization can be applied to the fully coupled integral method using equation (6.4) with a second derivative regularization matrix, $\mathbf{L}$, in the form of equation (6.3) with appropriate [-1 2 -1] pattern considering all directions simultaneously as given in equation (6.5), and accounting for the discontinuity at the interface between ply orientations. The discontinuity at the interface can be incorporated by setting the rows of the regularization matrix on either side of the interface to zero, therefore no regularization is applied at the depth increments that border the interface, or across the interface. However, this approach using equation (6.4) and (6.5) does not yield satisfactory results due to the complex relationship between residual stresses and released strains in all directions when performing IHD in FRP laminates.

$$\left(\mathbf{C}^T\,\mathbf{C} + \alpha\,\mathbf{L}^T\,\mathbf{L}\right)\boldsymbol{\sigma}_{res} = \mathbf{C}^T\,\boldsymbol{\epsilon}_{meas} \tag{6.4}$$

where α is the regularization parameter that controls the amount of regularization applied.

$$\mathbf{L} = \left[\begin{array}{ccc|ccc|ccc|ccc|c}
0 & 0 & 0 & 0 & 0 & 0 & 0 & 0 & 0 & 0 & 0 & 0 & \dots \\
0 & 0 & 0 & 0 & 0 & 0 & 0 & 0 & 0 & 0 & 0 & 0 & \dots \\
0 & 0 & 0 & 0 & 0 & 0 & 0 & 0 & 0 & 0 & 0 & 0 & \dots \\
\hline
-1 & -1 & -1 & 2 & 2 & 2 & -1 & -1 & -1 & 0 & 0 & 0 & \dots \\
-1 & -1 & -1 & 2 & 2 & 2 & -1 & -1 & -1 & 0 & 0 & 0 & \dots \\
-1 & -1 & -1 & 2 & 2 & 2 & -1 & -1 & -1 & 0 & 0 & 0 & \dots \\
\hline
0 & 0 & 0 & -1 & -1 & -1 & 2 & 2 & 2 & -1 & -1 & -1 & \dots \\
0 & 0 & 0 & -1 & -1 & -1 & 2 & 2 & 2 & -1 & -1 & -1 & \dots \\
0 & 0 & 0 & -1 & -1 & -1 & 2 & 2 & 2 & -1 & -1 & -1 & \dots \\
\hline
\vdots & \vdots & \vdots & \vdots & \vdots & \vdots & \vdots & \vdots & \vdots & \vdots & \vdots & \vdots & \ddots
\end{array}\right] \tag{6.5}$$

However, in the case of a cross-ply laminate, such as the $[0_2/90_2]_s$ GFRP laminate used in this chapter, Tikhonov regularization can be applied through the use of an approximation. Examination of the calibration matrix used in this chapter revealed that the diagonal coefficients of each 'block' in equation (6.3) are significantly greater than the other two coefficients in the same row due to Poisson's effects. Furthermore, it is expected that residual stresses in the x and y directions are similar in magnitude. Therefore, the experimental strain measured in the x and y directions at any depth increment

mostly arises from the stress released in the x and y directions, respectively, and so the calibration coefficients relating strains in a particular direction to stresses in other directions can be neglected for the purpose of regularization only. This allows the calibration matrix to be decoupled into x, y and in-plane shear components. Shown below for the x component:

$$\begin{Bmatrix} \epsilon_{1_x} \\ \epsilon_{2_x} \\ \epsilon_{2_x} \\ \vdots \end{Bmatrix} = \begin{bmatrix} C_{1111} & 0 & 0 & \dots \\ C_{2111} & C_{2121} & 0 & \dots \\ C_{3111} & C_{3121} & C_{3131} & \dots \\ \vdots & \vdots & \vdots & \ddots \end{bmatrix} \begin{Bmatrix} \sigma_{1_x} \\ \sigma_{2_x} \\ \sigma_{3_x} \\ \vdots \end{Bmatrix} \tag{6.6}$$

$$\boldsymbol{\epsilon}_x = \mathbf{C}_x \, \boldsymbol{\sigma}_x \tag{6.7}$$

Regularization must be adapted to allow for discontinuities at the interfaces between ply orientations by removing select rows from the regularization matrix. The rows on either side of the discontinuity must be set to zero to remove the smoothing across the interface between ply orientations. As an example, in the case of a $[0_2/90_2]_s$ laminate and the use of eight depth increments where the ply orientation interface lies between the 4th and 5th increment, the $\mathbf{L}$ matrix must be modified such that [127]:

$$\mathbf{L} = \left[\begin{array}{cccc|cccc} 0 & 0 & 0 & 0 & 0 & 0 & 0 & 0 \\ -1 & 2 & -1 & 0 & 0 & 0 & 0 & 0 \\ 0 & -1 & 2 & -1 & 0 & 0 & 0 & 0 \\ 0 & 0 & 0 & 0 & 0 & 0 & 0 & 0 \\ \hline 0 & 0 & 0 & 0 & 0 & 0 & 0 & 0 \\ 0 & 0 & 0 & 0 & -1 & 2 & -1 & 0 \\ 0 & 0 & 0 & 0 & 0 & -1 & 2 & -1 \\ 0 & 0 & 0 & 0 & 0 & 0 & 0 & 0 \end{array}\right], \quad \boldsymbol{\sigma} = \left\{\begin{array}{c} {\sigma_1}^{0^\circ} \\ {\sigma_2}^{0^\circ} \\ {\sigma_3}^{0^\circ} \\ {\sigma_4}^{0^\circ} \\ \hline {\sigma_5}^{90^\circ} \\ {\sigma_6}^{90^\circ} \\ {\sigma_7}^{90^\circ} \\ {\sigma_8}^{90^\circ} \end{array}\right\} \tag{6.8}$$

where the number of rows is equal to the number of hole depth increments used, and ${\sigma_i}^{0^\circ}$ refers to the stress in depth increment i in the 0° ply.

Tikhonov second-derivative regularization can then be implemented across the entire hole depth for each component of stress, shown only for the x-direction, but similarly for the y-direction and in-plane shear [ii].

$$\left(\mathbf{C}_x^T\,\mathbf{C}_x + \alpha_x\,\mathbf{L}^T\,\mathbf{L}\right)\boldsymbol{\sigma}_x = \mathbf{C}_x^T\,\boldsymbol{\epsilon}_x \tag{6.9}$$

where α_x is the regularization parameter such that $\alpha_x = 0$ indicates no regularization, and increasing positive values of α_x lead to increasing degrees of regularization.

The extent of regularization must be carefully considered. Insufficient regularization leads to excessive uncertainty in the calculated stress results, while excessive regularization distorts the stress solution. The Morozov Discrepancy Principle [98] can be used to iteratively determine an estimate of the optimal value of α_x such that the chi-squared statistic, χ^2, equals the number of depth increments. In this chapter, with 16 depth increments, the 0° and 90° plies are treated separately since the estimated standard error, e, was found to vary between ply orientations and so:

$$\chi^2 = \sum_{i=1}^{8}\left(\frac{\epsilon_i^{calc} - \epsilon_i^{meas}}{e_{0^\circ}}\right)^2 + \sum_{i=9}^{16}\left(\frac{\epsilon_i^{calc} - \epsilon_i^{meas}}{e_{90^\circ}}\right)^2 \tag{6.10}$$

where ϵ^{meas} is the measured strain data and ϵ^{calc} is the strain data corresponding to the regularized stresses, $\boldsymbol{\sigma}_x$, that can be calculated using equation (6.11):

$$\boldsymbol{\epsilon}_x^{calc} = \mathbf{C}_x\,\boldsymbol{\sigma}_x \tag{6.11}$$

The standard errors in the measured strains were determined separately for each ply orientation, which is based on the assumption that the stress profile in each ply orientation has a smooth form and that the presence of strain errors causes deviations around that smooth curve [99]. The standard error within each ply orientation, e_{0° and e_{90°, is estimated by the average local misfit norm [87] within that ply.

[ii] It is, however, entirely possible to construct an $\mathbf{L}$ matrix in the form of equation (6.5) such that only the direction of stress application effects the direction of strain measurement since this stress dominates the strain response. This has been considered and tested, but it prevents the independent variation of the regularization parameters for each direction. It would be a pity to lose this ability when the well-known approach employed in the ASTM standard has this feature. In the present case, the regularization parameters in each direction, using equation (6.9), are similar in magnitude and the regularization parameter associated with the x-direction was increased to that of the y-direction to remove leftover noise artefacts. So the stress results obtained using equation (6.4) with an appropriate $\mathbf{L}$ matrix are nearly an exact match for the current approach. This will not, however, always be the case depending on the particular laminate and the experimental strain release in each direction. It should still, however, be entirely possible to control the regularization parameter for each direction independently using equation (6.4) with an appropriate $\mathbf{L}$ matrix and a diagonal matrix containing the regularization parameters for each direction. This approach will yield exactly the same stress results as equation (6.7), but will be less familiar to other practitioners in the IHD field due to the lack of similarity to the ASTM standard, even though it would be more attractive mathematically.

It is important that the local misfit norm does not include the misfit across the ply interface. Therefore, the local misfit norm in the 0° ply is calculated from the 1st to 8th drilling increment and in the 90° ply from the 8th to 16th drilling increment using equations (6.12) and (6.13), respectively. This ensures that the standard error does not increase due to the discontinuity at the interface which would potentially allow excessive regularization and distortion of the stress results.

$$e_{0^\circ}^2 \approx \frac{1}{20 \times 5} \sum_{i=1}^{5} (\epsilon_i - 3\epsilon_{i+1} + 3\epsilon_{i+2} - \epsilon_{i+3})^2 \tag{6.12}$$

$$e_{90^\circ}^2 \approx \frac{1}{20 \times 6} \sum_{i=8}^{13} (\epsilon_i - 3\epsilon_{i+1} + 3\epsilon_{i+2} - \epsilon_{i+3})^2 \tag{6.13}$$

After applying Tikhonov regularization to the decoupled stress directions, the associated regularized strains in each direction ($\boldsymbol{\epsilon}_x^{calc}$, $\boldsymbol{\epsilon}_y^{calc}$ and $\boldsymbol{\epsilon}_{45}^{calc}$) can be combined into a full strain vector, $\boldsymbol{\epsilon}^{calc}$, in the form of equation (6.3). The regularized residual stress field is then calculated using the fully coupled calibration matrix, $\mathbf{C}$, through equation (6.2) with $\boldsymbol{\epsilon}^{calc}$. Excessive stress uncertainty, or distortion of the stress solution may necessitate adjustment of the regularization parameters.

6.3 Demonstration of Procedure

6.3.1 Experimental

A $[0_2/90_2]_s$ FRP laminate with dimensions of 400 mm × 400 mm was manufactured as described in section 5.3.1. The primary in-plane elastic properties of the composite lamina are listed in Table 5.1. A test specimen with dimensions of 75 mm × 170 mm was used for practical reasons and to allow three holes to be drilled on the single specimen without the effects of edges or neighbouring holes impacting on the results. The experimental procedure and instrumentation follows that of section 5.3.1 unless stated otherwise. The experimental strain variation between tests were within the measurement uncertainty considered in this chapter, therefore, only a single experimental strain data set is presented in the following sections. A tungsten carbide inverted cone end mill was used to drill the hole that had final diameter of 1.66 mm. The ratio between the hole radius and the inner radius of the strain gauge is 0.46 which is within the suggested limits of Sicot et al. [89]. The x and y offset of the hole from the centre of the rosette, as shown in Figure 6.1, for this experiment was measured to be 5 µm and 10 µm, respectively.

Sixty constant depth increments were used up to the midplane, and an additional six increments past the midplane. IHD was conducted beyond the midplane of the symmetric laminate to provide additional data points for series expansion based on the lessons learnt in Chapter 5. These additional data points help constrain the series near their ends where greater instability and consequently greater

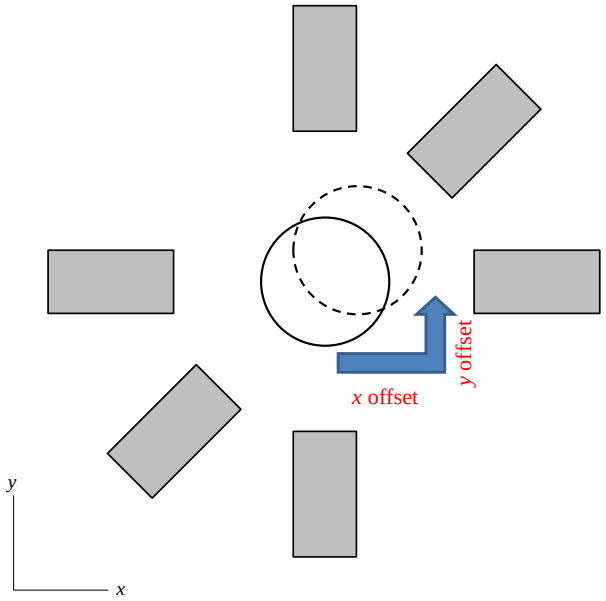


Figure 6.1: x and y offset of the hole

uncertainty in stress can occur, therefore reducing the overall uncertainty in the measured stress distribution in the 90° layer. The experimental testing period lasted approximately 40 minutes. The experimentally measured strain variations with depth at each strain gauge location are presented in Figure 6.2. Spline interpolation was used to determine the experimental strains at each of the depth increments used in the integral methods.

Some smoothing will inevitably be introduced by spline interpolation, however, the effect of this is negligible in comparison to other uncertainty sources considered. This was investigated by successively ignoring each experimental datum up to the midplane to create 60 unique 'erroneous' spline interpolations for the integral method for each strain direction. The 60 erroneous spline interpolations for each strain direction is shown over the initial spline interpolation and the strain uncertainty in Figure 6.3. The maximum variation between any datum of the erroneous curves and the initial datum was found to be 0.75 µm/m, when the turning point datum at the interface between plies was ignored. Obviously this datum is of critical importance in the case of FRP laminates, but even when ignoring it entirely the error introduced is less than the noise error of 1 µm/m considered in this chapter. The RMS of the maximum variation between the erroneous spline interpolations and the initial spline in all directions is only 0.152 µm/m. The RMS error between the erroneous spline interpolations and the initial spline at all depth increments and in all directions of the integral method is only 0.036 µm/m since the variation caused by ignoring a datum is localised. Therefore, the error introduced by the spline interpolation is negligible compared to other, larger strain uncertainties such as zero depth and noise when calculating the total strain uncertainty, and the subsequent uncertainty in residual stress, and can be safely neglected.

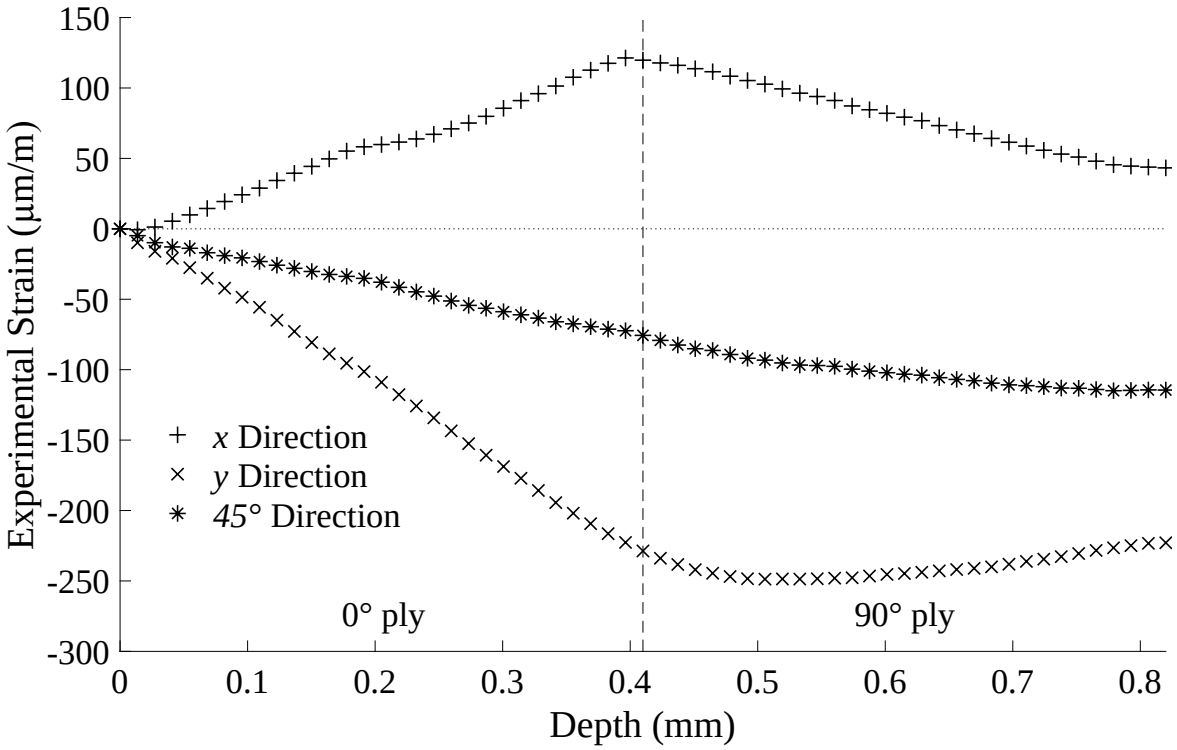


Figure 6.2: Strain variation with depth in the x, y and $45°$ gauge directions

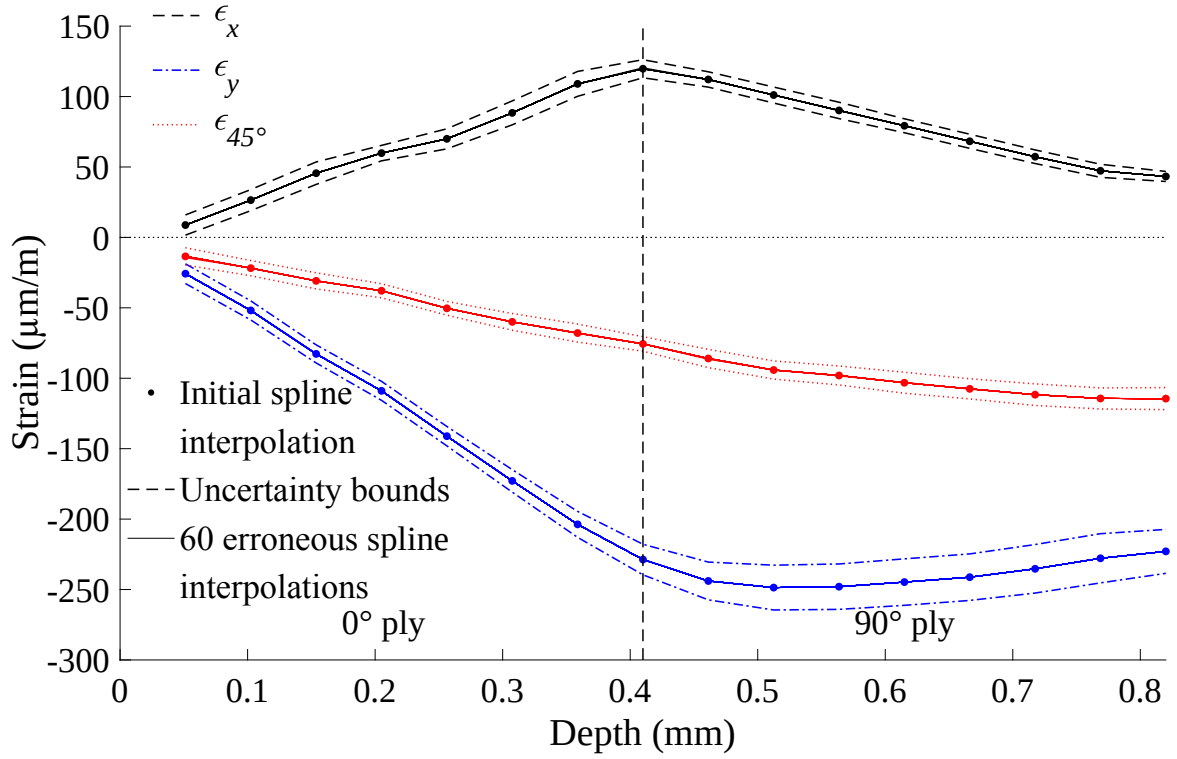


Figure 6.3: Initial and erroneous spline interpolations for each strain direction

6.3.2 Computational

MSC Nastran FE analysis was conducted as described in section 5.3.2 unless stated otherwise. In this chapter a quarter model was used due to symmetry (except for the case where a 1° misalignment between ply orientations was considered which is discussed in the next section). Symmetric and anti-symmetric boundary conditions were employed depending on the applied loading condition. The outer surfaces of the plate, including the bottom surface, were left unconstrained to represent the experimental approach taken. Only a single node was constrained in the z direction to prevent rigid body motion since all applied loads are self-equilibrating. The same FE model was used to calculate the calibration coefficients for the integral and series expansion methods to remove any variability in the results arising from FE calculations. This ensures that a reasonable comparison between the computational approaches can be achieved.

For the integral method, three load cases were considered at each depth increment, $\sigma_x = 1$, $\sigma_y = 1$ and $\tau_{xy} = 1$. Each unit stress component was applied separately, i.e. the remaining two components had magnitudes of zero in each load case. To apply each unit stress component, the equivalent radial and hoop stress distributions were applied simultaneously to the hole face according to the stress transformations [157] given in equations (6.14) and (6.15). The radial and shear stress distributions, for each load case, were applied to element faces at the appropriate depth of the inner surface of the hole using PLOAD4 cards.

$$\sigma_{rr} = \sigma_x \cos^2\theta + \sigma_y \sin^2\theta + \tau_{xy} \sin 2\theta \tag{6.14}$$

$$\tau_{r\theta} = -\frac{\sigma_x - \sigma_y}{2} \sin 2\theta + \tau_{xy} \cos 2\theta \tag{6.15}$$

The mesh around the hole is presented in Figure 6.4, and for illustrative purposes, the deformation (scaled) and stress variation due to a unit stress in the x-direction applied to the entire hole face is shown when the hole has a depth of quarter plate thickness. The strain gauge grid locations (highlighted) are not directly included in the FE model as was done in section 5.3.2. Instead, all nodal displacement data in the region of the strain gauge rosette on the top surface were calculated for each applied load as the depth of the hole was increased. A biharmonic surface spline was fitted to the nodal displacement data (Figure 6.5a) to calculate the displacements around the perimeter of each grid (Figure 6.5b) as shown in Figure 6.5. While it is easier to mesh according to the physical grid positions to get nodes directly in these positions, this approach allowed for an improved mesh with elements of higher geometric quality and also facilitates inclusion of any hole offset from the centre of the strain gauge rosette without requiring an entirely new mesh for a particular hole offset. The biharmonic surface spline approach has been compared to meshing the grids directly and the differences in calculated strain are negligible.

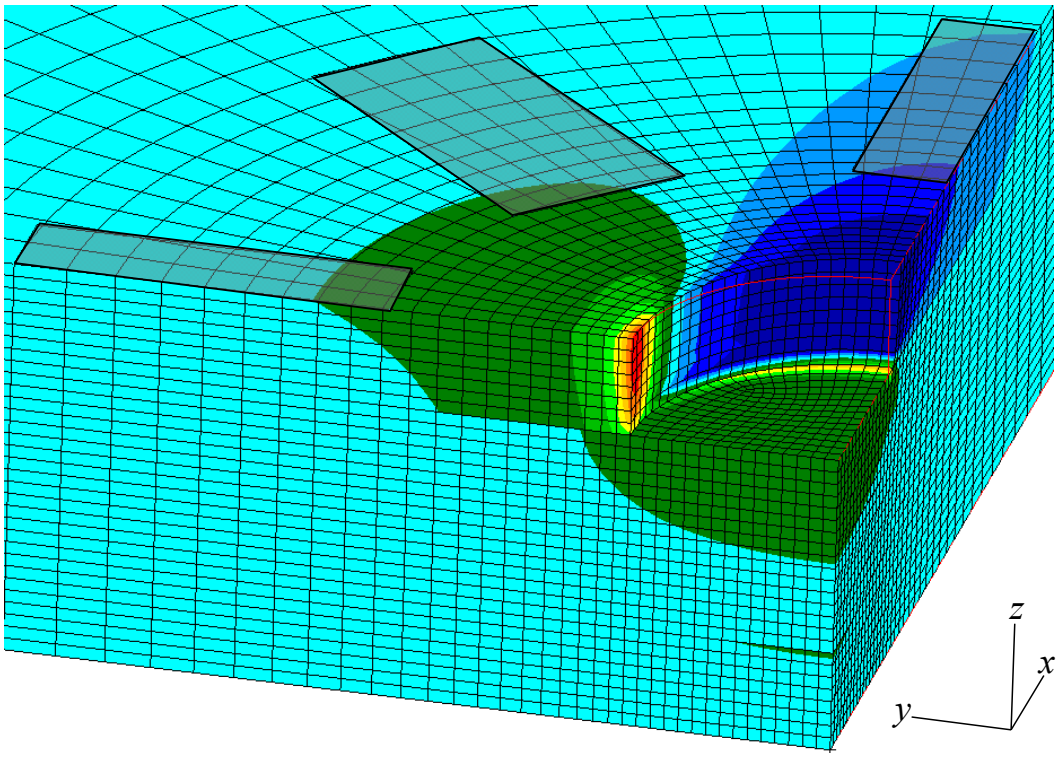
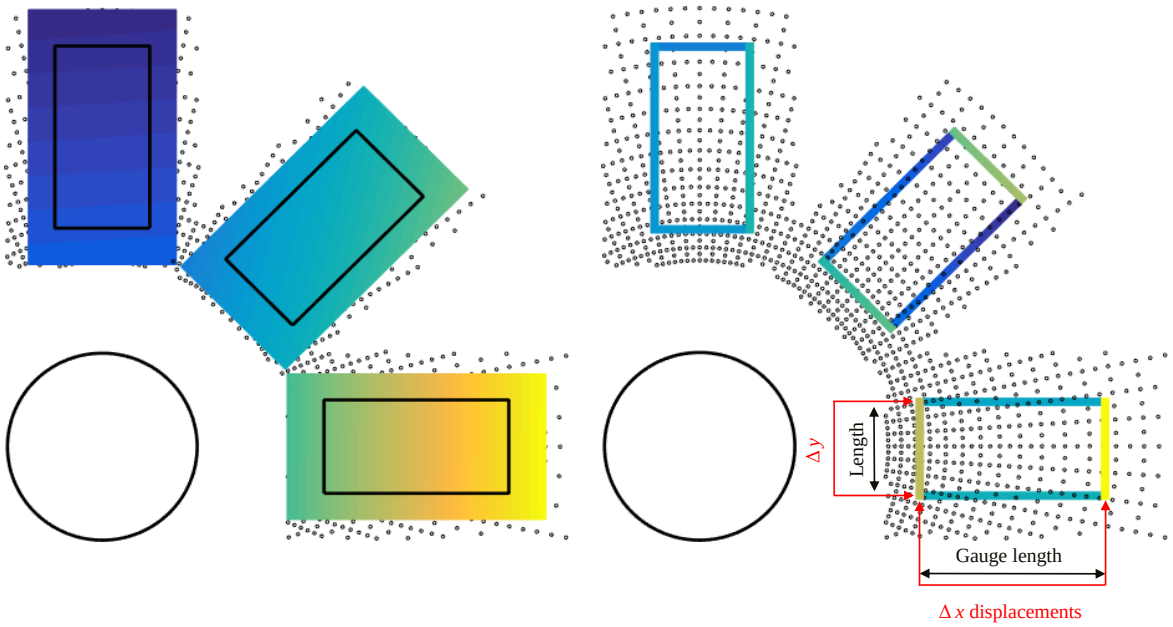


Figure 6.4: Mesh around the hole and stress variation due to an applied unit stress in the x-direction at 0.41 mm hole depth



(a) Biharmonic surface spline to nodal displacement data

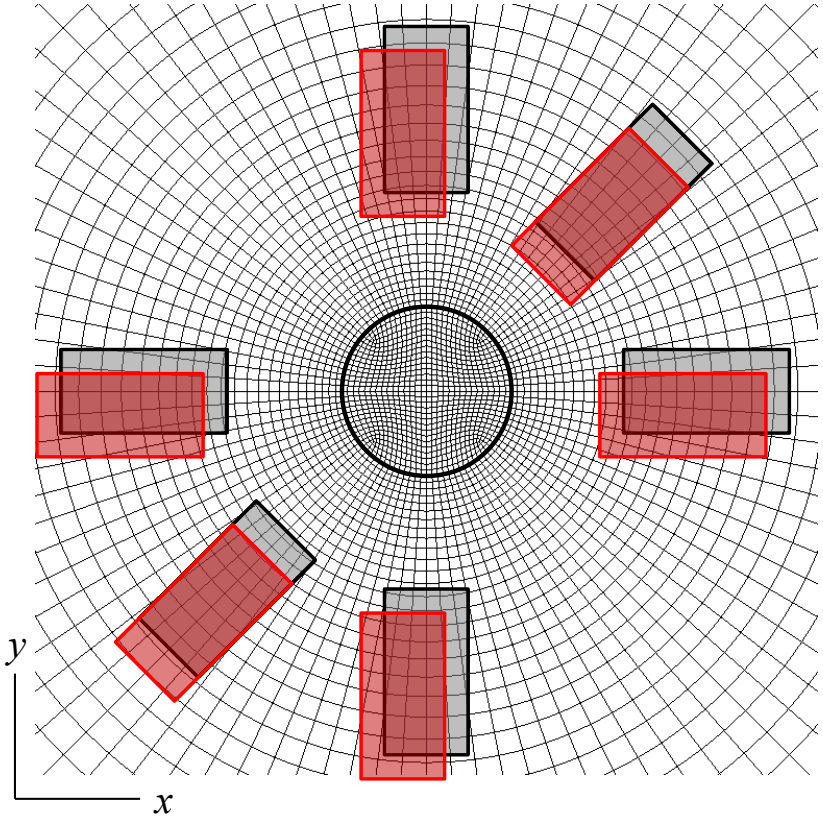
(b) Interpolated displacements around the perimeter of each grid

Figure 6.5: Biharmonic surface spline to calculate nodal displacements around the perimeter of each grid

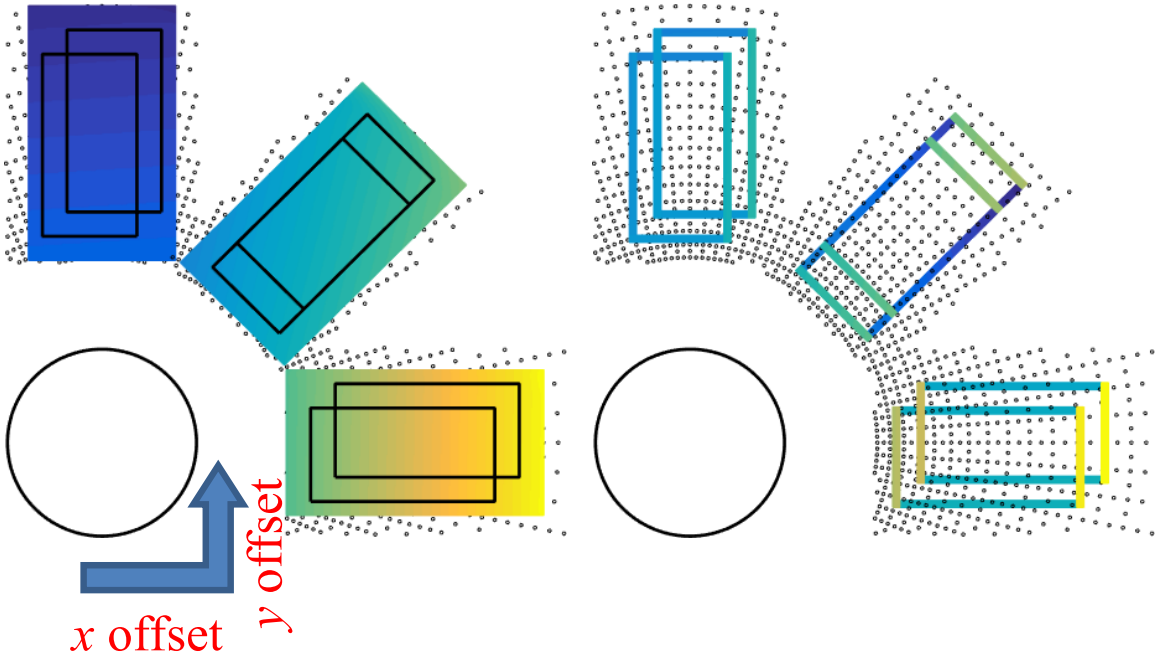
In this chapter the real position of the hole due to the hole not being drilled exactly in the centre of the rosette and the associated uncertainty in determining the position of the hole is included in the analysis. The effect of the small hole offset can be corrected by changing the position of the strain gauges with respect to the hole as shown in Figure 6.6a. These strain gauge positions are used during the biharmonic spline interpolation of the displacement data and subsequent calculation of the calibration coefficients corresponding to each grid location, as shown in Figures 6.6b and 6.6c, respectively. This process is exacerbated by the use of the 6 element rosette since any offset of the hole with respect to one rectangular half is reversed with respect to the other half of the rosette and the measured strains from each half must be averaged. Quarter model displacements were used to create full model displacements using symmetric and anti-symmetric conditions. These full model results allowed errors in hole position to be modelled by offsetting each strain gauge grid and averaging the strains at the corresponding gauges of the 6 element rosette. The longitudinal strain at each gauge location for every loading condition and drilling increment was determined using the displacement summation method introduced by Schajer [188]. The transverse strain was calculated similarly but referenced to the transverse direction. These strains were used to populate the longitudinal and transverse calibration matrices, $\bar{\mathbf{C}}$ and $\hat{\mathbf{C}}$ respectively. This process essentially eliminated any error associated with hole eccentricity.

Calibration matrices for the integral method for any depth increment distribution can be obtained from cumulative calibration coefficients [93], which were determined from the 16 step calibration matrix obtained directly from the FE results. For the series expansion approach, the calibration coefficients were calculated as described in 5.3.2.

To investigate the different computational techniques for IHD in FRP laminates, a thorough estimation of uncertainty in the residual stress distributions is required.



(a) Correction hole offset by changing the position of the strain gauges with respect to the hole



(b) Biharmonic surface spline to nodal displacement data

(c) Interpolated displacements around the perimeter of each grid

Figure 6.6: Hole offset correction during biharmonic spline interpolation

6.3.3 Propagation of Uncertainties

Uncertainty propagation was conducted as described in section 5.3.3, unless stated otherwise. Ten thousand Monte Carlo trials were simulated for each method considered in this chapter. The uncertainty sources and their assigned probability density functions considered in this chapter are provided in Table 6.1.

Table 6.1: Uncertainty sources and their assigned probability density functions

x_i	Description	$p(x_i)$	Type	Nominal value, uncertainty
E_1	Longitudinal modulus	Normal	B	38154 MPa, 2.0%
E_2	Transverse modulus	Normal	B	10747 MPa, 2.2%
G_{12}	Shear modulus	Normal	B	3712 MPa, 2.6%
ν_{12}	Poisson's ratio	Normal	B	0.3113, 2.1%
ν_{23}	Poisson's ratio	Normal	B	0.4124, 5%
z_i	Incremental depths	Rectangular	B	13 µm, 0.5 µm
z_0	Zero depth	Rectangular	B	0 µm, 14 µm
x_{offset}	Hole offset in the x-direction	Rectangular	B	5 µm, 5 µm
y_{offset}	Hole offset in the y-direction	Rectangular	B	10 µm, 5 µm
ϵ_m	Indicated experimental strain	Normal	B	Figure 6.2, 1.6%
ϵ_{noise}	Experimental noise	Normal	A	Figure 6.2, 1 µm/m
K_{t_x}	Transverse sensitivity for gauge 1	Normal	B	2.2%, 0.1%
$K_{t_{45^\circ}}$	Transverse sensitivity for gauge 2	Normal	B	2.6%, 0.1%
K_{t_y}	Transverse sensitivity for gauge 3	Normal	B	2.2%, 0.1%
ν_0	Poisson's ratio of the material on which gauge factor was measured	Normal	B	0.285, 3%
θ_{SG_t}	Misalignment of strain gauge on tensile testing coupon	Normal	B	0, 1°
θ_{coupon}	Fibre misalignment of tensile testing coupons	Normal	B	0, 0.5°
θ_{grips}	Misalignment of coupon in grips of tensile testing machine	Normal	B	0, 1°
θ_{SG_h}	Misalignment of strain gauge during hole-drilling	Normal	B	0, 1°
$\theta_{0^\circ/90^\circ}$	Misalignment of 0° and 90° plies of hole-drilling specimen	Normal	B	0, 0.5°
FE	Finite element calculations	Normal	B	0, 2%

Zero depth is of critical importance and it can, at times, be difficult to differentiate between the measurement scatter during the absence of relaxation and the first measured response. Figure 6.7 shows the experimental strain data in the y-direction after these have been shifted according to the most likely zero depth position. A linear regression though the first 7 data points (from zero to 0.082 mm) shows that there is a clear change in slope when the end mill starts to penetrate into the specimen. Since this method is not exact, a full depth increment is considered as the uncertainty in zero depth which is also shown in Figure 6.7. The discontinuity in slope at the interface between ply orientations is used as an additional check of the zero depth position by ensuring that the turning

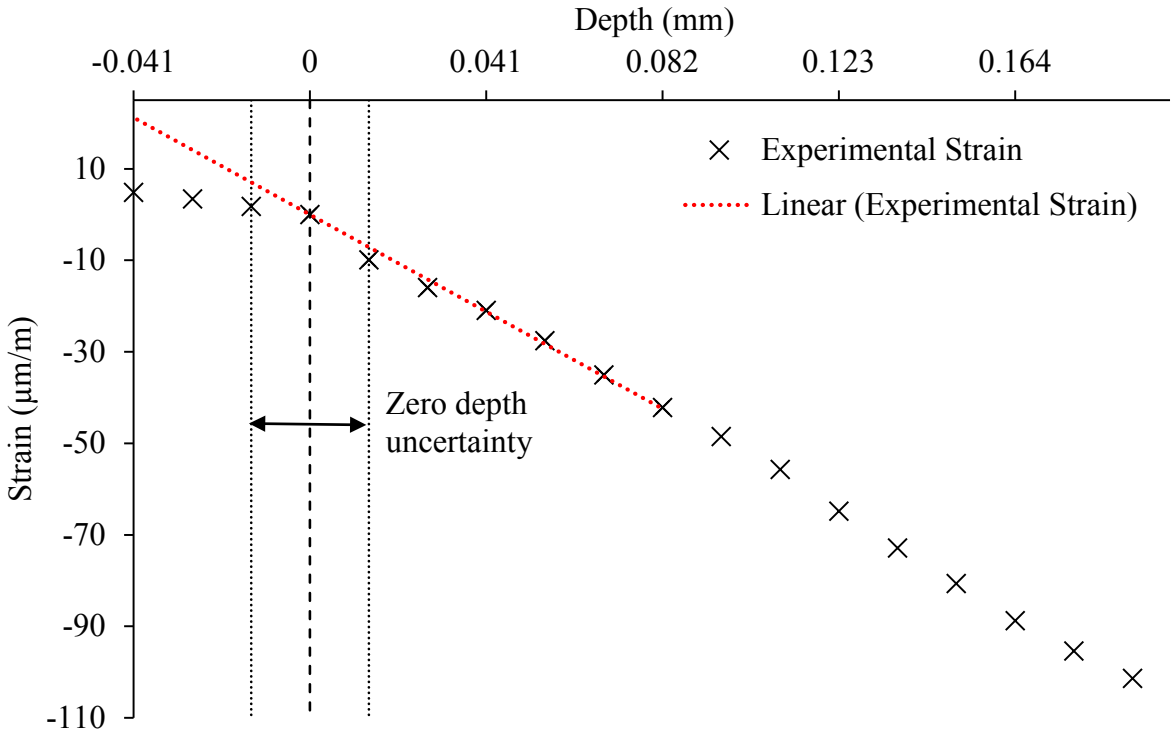


Figure 6.7: Identification of zero depth position

point in strain is within one increment of the interface between ply orientations. The position of the interface can be found with relative certainty due to the use of aerospace grade prepreg material. Although the exact position of the zero depth cannot be determined using this approach, it can at least determine this position within a single depth increment.

The regularized integral method has a certain inability to exactly match the experimental strain data that must be included in the uncertainty analysis. This uncertainty is calculated as the standard deviation of the misfit between the experimentally measured strains and those calculated using regularization within each ply orientation for the x, y and $45°$ directions. The same approach was used for the least-squares fit produced by series expansion as in section 5.3.3.

Uncertainty in material properties and angular alignment between the two ply orientations are included in each Monte Carlo trial as described in section 5.3.3. The method used in section 5.3.3 to incorporate the hole-drilling rosette misalignment when calculating the calibration matrices of each Monte Carlo trail was not fully correct. Due to the FE approach used in Chapter 5, the only option for including the hole-drilling rosette misalignment was to incorporate it into the ply misalignments. The FE approach of this chapter and biharmonic surface spline of displacement data around the hole, however, allow robust inclusion of the hole-drilling rosette misalignment along with the uncertainty associated with the measurement of the hole offset in the x and y directions in each Monte Carlo trial. The grids of the hole-drilling rosette are offset and then rotated within the displacement field around the hole to determine the the longitudinal and transverse calibration matrices of each Monte Carlo

trial. The longitudinal and transverse calibration matrices for the effect of 1% increase in material properties are similarly calculated before including the effect of material properties to find the final longitudinal and transverse calibration matrices, $\bar{\mathbf{C}}_j$, $\hat{\mathbf{C}}_j$, of Monte Carlo trial j.

The measured hole diameter was used within the FE model. To include the uncertainty associated with the measurement of the hole diameter would require additional FE models, and interpolation of each coefficient obtained from these models since no direct relationship exists between hole diameter and each coefficient. It is believed that the additional computational time required to include this uncertainty is not warranted since its effect is likely negligible when compared to other uncertainties that have been accounted for.

The residual stress field was determined for each Monte Carlo trial using equation (6.2) for the standard integral method, equations (6.9), (6.11) and (6.2) for the regularized integral method, and equations (5.10) and (5.12) for series expansion. The uncertainty in stress at each depth was determined by the standard deviation of the stress solutions from the ten thousand Monte Carlo trials.

6.4 Results and Discussion

The experimental strain measurements along with the regularized strains and associated uncertainties (including that from the misfit error) are shown in Figure 6.8 for the x, y and $45°$ strain gauge grids. The discontinuity in slope between plies of different orientation has been correctly captured. The experimental strain in the x-direction presented higher noise than in the other directions. Therefore, the regularization parameter calculated using equation (6.10) was increased to the same value as the regularization parameter associated with the y-direction to ensure that these noise artefacts were removed in the stress solution. It is evident from Figure 6.8 that this increase in regularization has not severely affected the fit to the experimental strain data. Furthermore, it was found that the misfit error was similar in magnitude to the measurement noise and excessive regularization had therefore not been applied which could have distorted the stress results. The regularization parameters found in this chapter are much smaller (10^{-12} – 10^{-11}) than the recommendations given in the ASTM standard for isotropic materials (10^{-6} – 10^{-4}). The range given in ASTM E837-13a is not applicable to FRP laminates. The main reason why the values are much lower in this case is due to the experimental strains being less smooth than in isotropic materials. Therefore, limited regularization can be applied before the misfit becomes too large and distorts the residual stress results. The drawback of the limited regularization is increased uncertainty due to some noise artefacts remaining, but this is preferable to distortion of the stress solution.

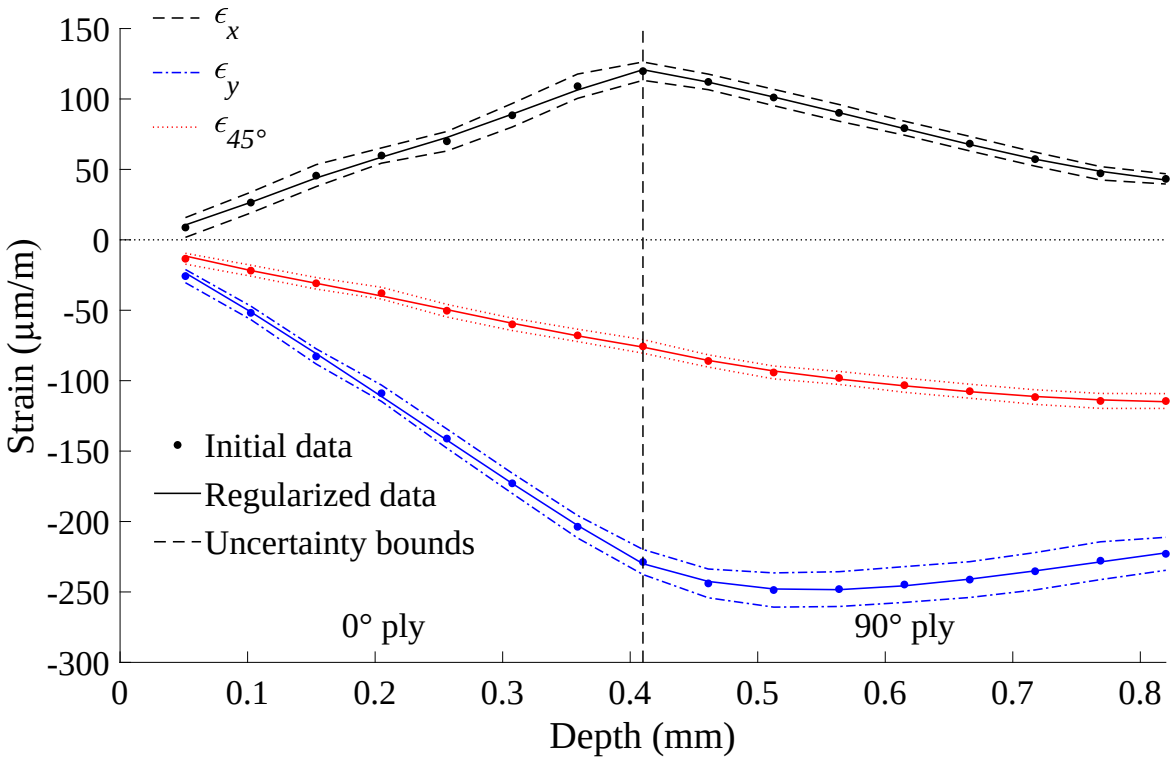


Figure 6.8: Regularized fits to experimental strain data

The stress distributions and associated uncertainties obtained using the standard and regularized integral methods are shown in Figures 6.9 and 6.10. For the standard integral method, all depth increments considered yield similar stress distributions, with increasing uncertainty as the number of depth increments increases. A lower number of depth increments yields more stable stress results, but due to averaging effects these results may be unable to properly capture rapid stress variations. Increasing the number of depth increments improves the ability to represent these stress variations but adversely affects the tolerance to measurement noise or erroneous measurements, leading to higher uncertainties in stress and somewhat erratic behaviour. In contrast to the standard method, the regularized 16 increment method produces stress results with both good resolution and low uncertainty and that match the general trend of the results obtained from the standard method.

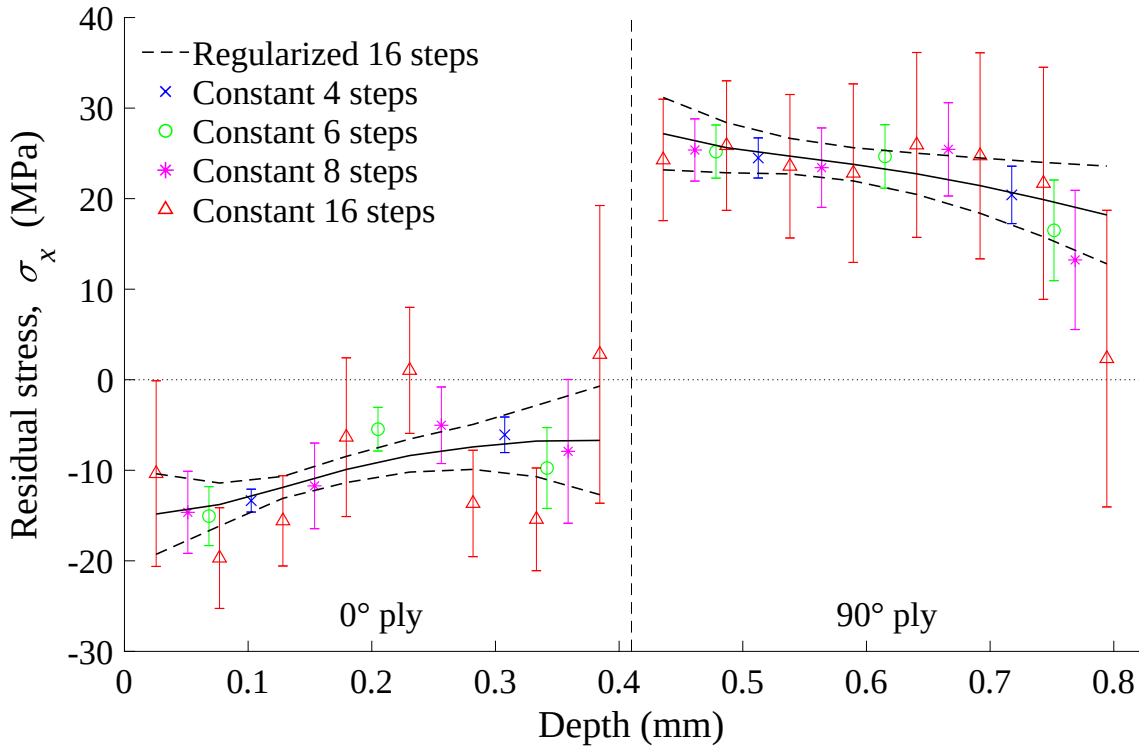


Figure 6.9: Axial stress distributions and associated uncertainties obtained using integral methods

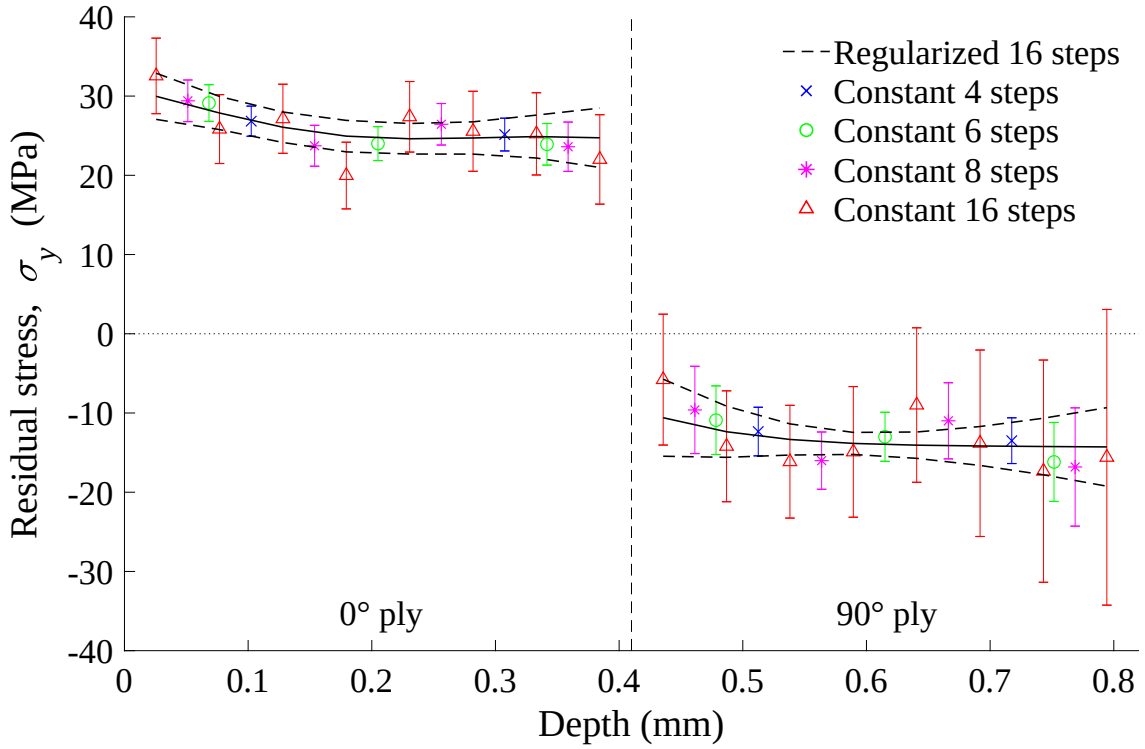


Figure 6.10: Transverse stress distributions and associated uncertainties obtained using integral methods

The residual stress distributions determined using the regularized integral method are overlaid with those determined using series expansion in Figure 6.11. It is apparent that the residual shear stress distribution is close to zero in both the 0° and 90° plies, as expected for a cross-ply laminate. A discontinuity in stress is evident for all stress components at the interfaces between plies of different orientations, as is required. The residual stress distributions compare favourably, but the uncertainty in stress is slightly lower overall in the case of the series expansion method since it has greater tolerance of experimental errors due to its use of least-squares curve fitting. Table 6.2 compares the RMS uncertainties in stress in the 0° and 90° plies for all methods considered in this chapter.

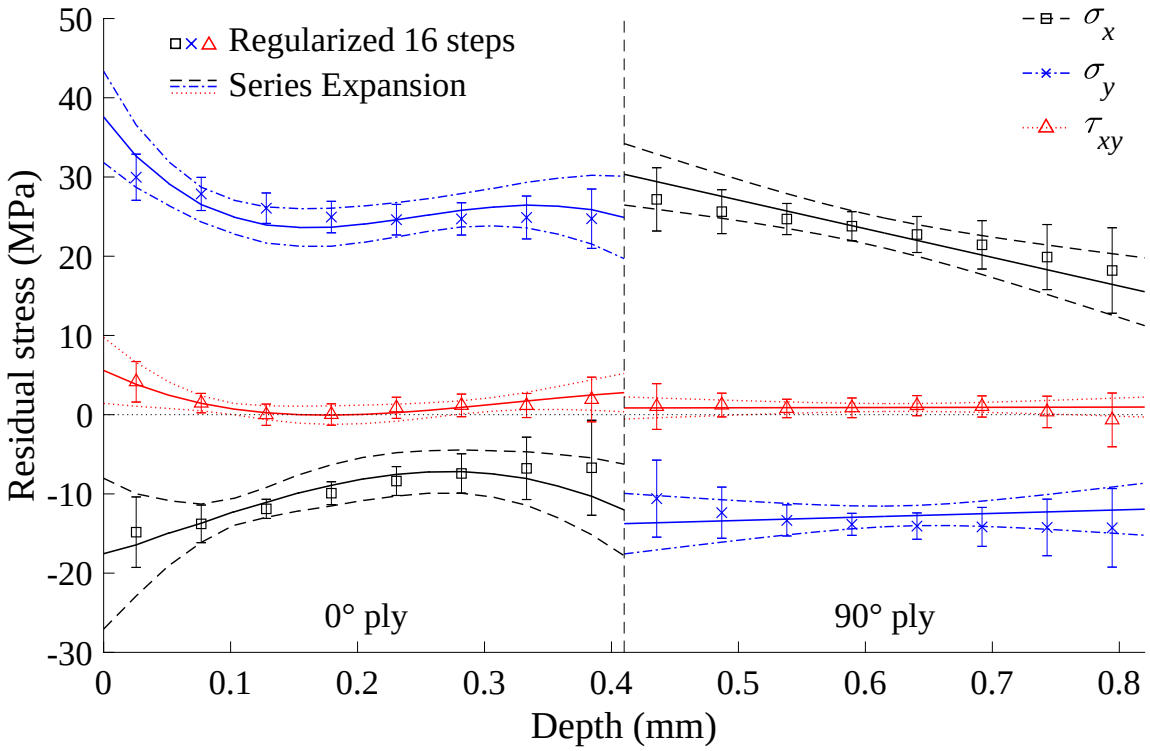


Figure 6.11: Stress distributions and associated uncertainties obtained using regularized integral and series expansion methods

Table 6.2: Breakdown of RMS uncertainty in stress arising from each uncertainty source, x_i

x_i	Contribution to $u(\sigma_x)$ [MPa]						Contribution to $u(\sigma_y)$ [MPa]						Contribution to $u(\tau_{xy})$ [MPa]					
	4 Steps	6 Steps	8 Steps	16 Steps	R 16 steps	SE	4 Steps	6 Steps	8 Steps	16 Steps	R 16 steps	SE	4 Steps	6 Steps	8 Steps	16 Steps	R 16 steps	SE
E_1	0.222	0.223	0.221	0.233	0.239	0.360	0.133	0.136	0.140	0.142	0.121	0.186	0.019	0.019	0.021	0.022	0.027	0.143
E_2	0.103	0.110	0.109	0.107	0.106	0.247	0.200	0.201	0.200	0.204	0.209	0.259	0.055	0.054	0.055	0.056	0.055	0.111
G_{12}	0.109	0.107	0.110	0.119	0.109	0.263	0.227	0.228	0.236	0.242	0.238	0.327	0.053	0.054	0.055	0.057	0.057	0.090
ν_{12}	0.024	0.026	0.027	0.030	0.028	0.523	0.033	0.032	0.033	0.034	0.034	0.236	0.012	0.012	0.012	0.013	0.012	0.236
ν_{23}	0.079	0.077	0.078	0.081	0.088	0.263	0.197	0.199	0.197	0.196	0.194	0.277	0.034	0.035	0.035	0.036	0.035	0.104
z_i	0.036	0.069	0.094	0.208	0.036	0.026	0.058	0.087	0.113	0.227	0.069	0.053	0.005	0.009	0.009	0.017	0.025	0.007
z_0	0.560	1.269	1.915	2.766	1.160	0.980	0.727	0.878	0.956	1.316	0.722	0.761	0.116	0.270	0.213	0.376	0.215	0.137
Hole offset	0.043	0.043	0.045	0.051	0.045	0.062	0.193	0.191	0.191	0.192	0.195	0.200	0.099	0.100	0.100	0.101	0.102	0.111
ϵ_m	0.278	0.280	0.277	0.290	0.285	0.290	0.329	0.331	0.332	0.334	0.335	0.326	0.019	0.021	0.024	0.028	0.034	0.023
ϵ_{noise}	0.817	1.314	1.844	4.005	0.720	0.429	0.780	1.293	1.825	4.062	0.726	0.401	0.532	0.844	1.155	2.439	0.696	0.308
K_t	0.009	0.010	0.010	0.010	0.010	0.009	0.011	0.011	0.011	0.011	0.011	0.011	0.006	0.006	0.006	0.006	0.006	0.006
ν_0	0.004	0.004	0.004	0.004	0.004	0.004	0.005	0.005	0.005	0.005	0.005	0.005	0.002	0.002	0.002	0.002	0.002	0.002
θ_{SG_t}	0.042	0.042	0.042	0.044	0.045	0.193	0.020	0.021	0.022	0.022	0.019	0.140	0.005	0.005	0.005	0.006	0.006	0.106
θ_{coupon}	0.009	0.009	0.009	0.010	0.010	0.092	0.005	0.005	0.005	0.005	0.004	0.058	0.001	0.001	0.001	0.001	0.001	0.049
θ_{grips}	0.041	0.041	0.041	0.043	0.044	0.192	0.020	0.021	0.021	0.022	0.018	0.138	0.005	0.005	0.005	0.006	0.006	0.105
θ_{SG_h}	0.010	0.013	0.016	0.022	0.018	0.017	0.010	0.012	0.014	0.018	0.015	0.033	0.113	0.114	0.113	0.114	0.115	0.111
$\theta_{0°/90°}$ *plies*	0.005	0.005	0.005	0.006	0.005	0.155	0.008	0.008	0.008	0.008	0.008	0.142	0.043	0.043	0.044	0.044	0.045	0.137
FE	0.351	0.353	0.350	0.366	0.361	0.520	0.415	0.417	0.419	0.421	0.417	0.585	0.024	0.026	0.030	0.036	0.030	0.041
Misfit	0.000	0.000	0.000	0.000	0.812	0.714	0.000	0.000	0.000	0.000	0.775	0.487	0.000	0.000	0.000	0.000	0.615	0.323
u(Z)	1.130	1.916	2.741	4.914	1.683	1.568	1.266	1.708	2.182	4.324	1.456	1.296	0.576	0.907	1.197	2.479	0.952	0.568

The largest direct contributors to uncertainties in stress are the zero depth position and noise in the experimental strains. Uncertainty due to hole offset has negligible effect on the stress uncertainty compared to the dominant uncertainty sources considered in this chapter. In the case of the integral method with 16 depth increments, regularization slightly improves the tolerance to uncertainty in the zero depth position, and greatly improves the tolerance to noise in the strain data. The uncertainty in stress associated with noise is consequently far lower than the unregularized solution. The misfit allowed by the use of Tikhonov regularization smooths the stress distribution and greatly reduces the overall uncertainty, but introduces its own considerable uncertainty into the stress results to the extent that it becomes the second largest source of uncertainty after that of the zero depth position. Overall, the regularized results have uncertainties in stress that are comparable to those obtained from six depth increments using the standard integral approach, but with nearly three times the resolution.

In the case of series expansion, the smaller error bounds on the right hand side of Figure 6.11 are mainly due to the use of additional strain data points past the midplane, but it is also partly due to a lower series order at convergence in the 90° ply orientation. The use of additional measurements past the midplane reduces the uncertainty in stress (considering all directions) at the midplane by 33.9%. The breakdown in each stress direction is given in Table 6.3. The use of additional measurements past the midplane also reduces the uncertainty in stress over the entire 90° ply orientation up to the midplane since the additional points past the midplane help stabilise the solution. The overall RMS uncertainty in stress in the 90° ply orientation reduces by 28.1% due to the use of additional data points. The breakdown in each stress direction is given in Table 6.4.

Table 6.3: Effect of additional strain data points past the midplane

	Uncertainty in stress at a depth of 0.82 mm (MPa)		
	$u(\sigma_x)$	$u(\sigma_y)$	$u(\tau_{xy})$
Measurements up to midplane only	15.48	6.3	4.28
Measurements past midplane	8.89	5.79	2.56
% Difference	42.58	8.12	40.31

Table 6.4: Effect of additional strain data points past the midplane on RMS Uncertainty in the 90° ply

	RMS Uncertainty in 90° ply (MPa)		
	$u(\sigma_x)$	$u(\sigma_y)$	$u(\tau_{xy})$
Measurements up to midplane only	8.38	4.09	2.47
Measurements past midplane	5.44	3.91	1.79
% Difference	35.14	4.26	27.58

While the axial and shear components of the residual stresses are far removed from those that result in failure of the laminate, the situation is not as clear for the transverse stress component in each ply orientation. The FE model shown in Figure 6.4 revealed that the maximum transverse stress in the 0° plies exceeds 35 MPa and 30 MPa in the 90° plies. This stress, in conjunction with the stress concentration caused by the presence of the hole, result in a peak tensile transverse stress of approximately 50 MPa in the 0° plies in the flat base of the hole as the hole depth approaches the interface with the 90° plies. Once the hole penetrates into the 90° ply these stresses drop discontinuously to much smaller values as shown in Figure 6.12. The location of the critical transverse stress is shown in Figure 6.13. It is apparent that the region of peak stress is associated with the stress concentration at the corner at the base of the hole. It is, therefore, expected that the actual stress in the laminate is slightly lower than the calculated value of 50 MPa. In reality, some small radius would exist at this corner, reducing this stress concentration somewhat, but for the purposes of this discussion a maximum transverse stress of 50 MPa is assumed.

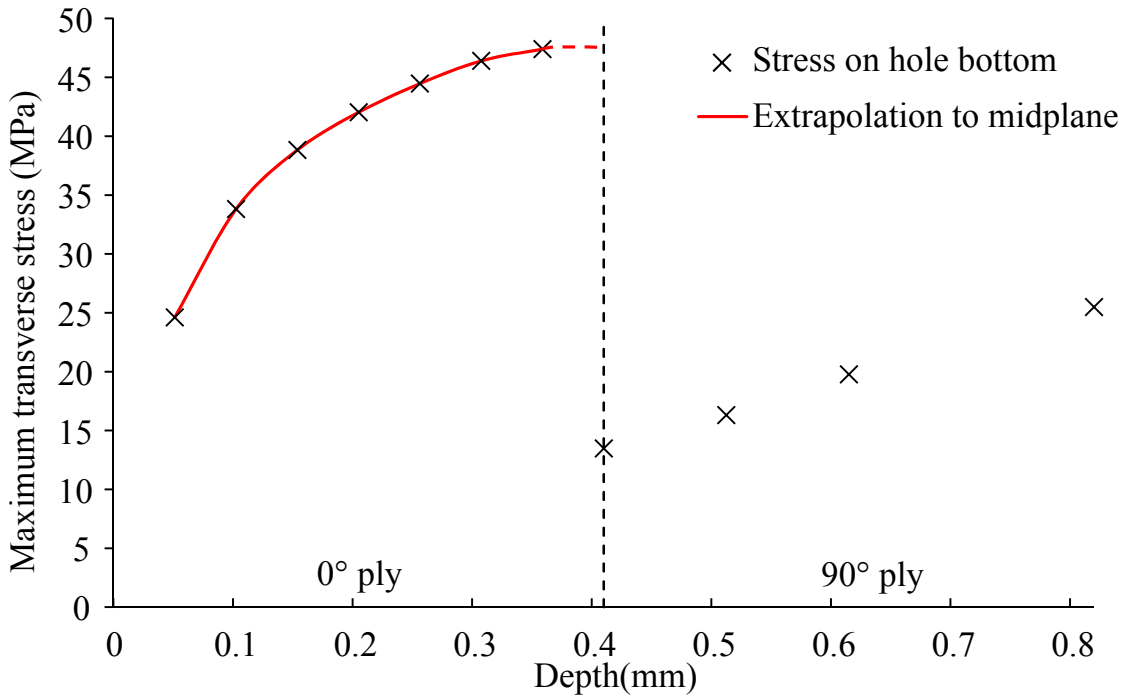


Figure 6.12: Maximum transverse stress on hole bottom

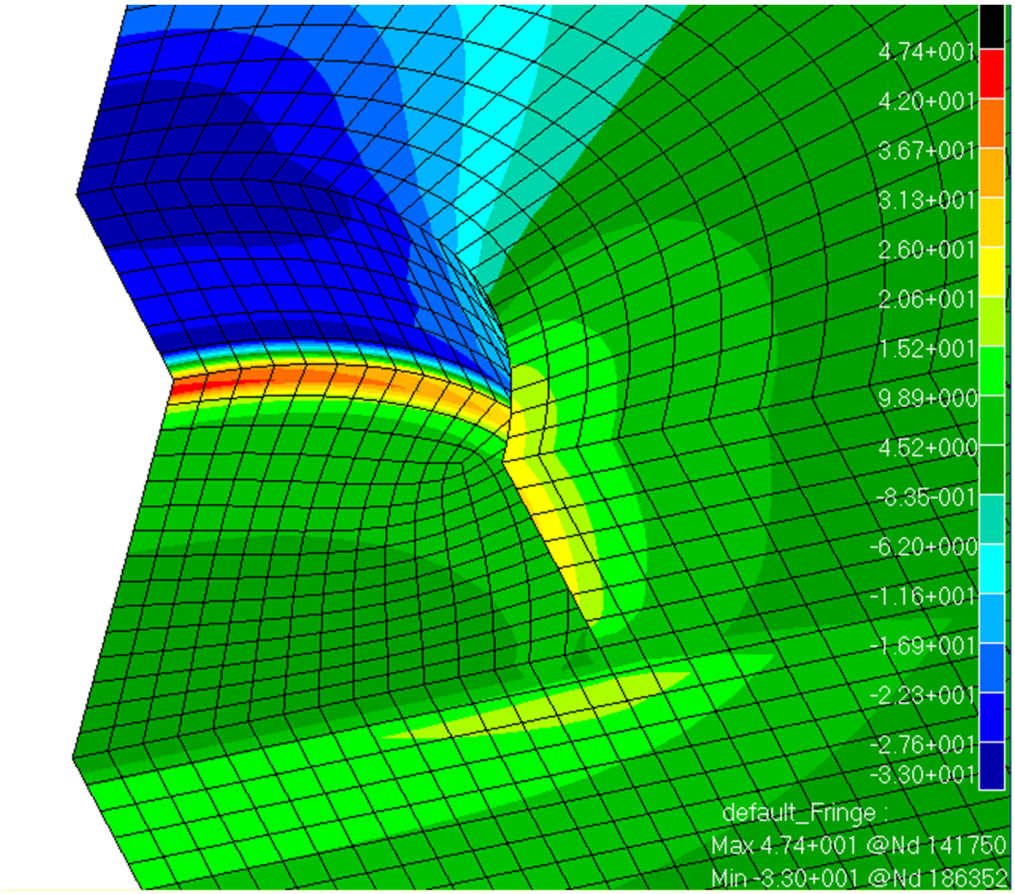


Figure 6.13: Location of the critical transverse stress

While the in-situ transverse strength of the laminate is unknown, it is clear that the peak stress is significantly higher than the transverse tensile strength of 35 MPa reported by Soden et al. [182] for unidirectional GFRP laminates. Cracking of the 0° plies in this region may, however, have been suppressed by the transverse fibres of the 90° plies in close proximity by the mechanism reported by Flaggs and Kural [183] that inhibits the extent of cracking in the transverse direction. Whether or not transverse cracking is fully inhibited or not cannot be known at this stage, however. It is also not known if the accuracy of the measured results was affected by this localized cracking at the base of the hole. While it must be acknowledged that this remains a possibility (if this is the case), however, all methods considered in this chapter would have been similarly affected and the validity of the comparison is, therefore, not compromised.

6.5 Conclusions

A comprehensive study of three different computational techniques for IHD in composite materials was performed on a $[0_2/90_2]_s$ GFRP laminate. For the first time, Tikhonov regularization with IHD was applied to a FRP laminate. Residual stress results were compared to those of the unregularized fully coupled integral method with various depth increment distributions, and with those of the series expansion method. The degree of Tikhonov regularization applied was optimised to reduce the stress uncertainty, while ensuring that the stress solution was not distorted. It was found that applying Tikhonov regularization through a simplifying approximation successfully smooths the resulting residual stress distribution and reduces stress uncertainties by removing noise artefacts from the experimental strain measurements. The uncertainty in stress associated with the regularized 16 increment integral method is similar in magnitude to that of the standard method with six depth increments, but with almost three times the depth resolution. There is good agreement in the calculated stresses of the regularized integral and series expansion computational methods and the total RMS uncertainty in stress is similar in magnitude.

6.6 Contribution to Knowledge

- The use of Tikhonov regularization with the integral method has been extended to IHD residual stress measurements in cross-ply FRP laminates or any layered material where the released strain in a particular direction is predominantly due to the residual stress in that direction. This approach greatly increases tolerance to measurement errors, without requiring a reduction in depth resolution.
- Existing computational methods for IHD in FRP laminates have been compared with robust uncertainty estimation in calculated residual stresses to highlight the effects of approaches such as limiting the number of depth increments, incorporating Tikhonov regularization and using separate series expansion. The contribution to stress measurement uncertainty was investigated for a range of common experimental and computation error sources for each method, including the effect of hole offset, to facilitate comparison of the computational methods.

7 Use of Power Series Expansion for Residual Stress Measurement in Isotropic Materials

This chapter investigates and demonstrates the use of the series expansion method with IHD to measure a rapidly varying residual stress distribution in an isotropic material. Power series expansion of eigenstrain is generated through the use of temperature variations in the forward solution to calculate the necessary calibration coefficients. Least-squares error minimisation is employed by the inverse solution to determine the amplitudes of each term in the eigenstrain series that results in a best fit to the measured strain data. These amplitudes are used along with the far-field stress distributions arising from the applied eigenstrain series to completely define the residual stress distribution. Monte Carlo simulation is used to determine robust uncertainties in the residual stress distribution that allows the series order with the lowest RMS uncertainty in stress to be selected from those series orders that have converged. The best estimate of the residual stress distribution is thereby obtained. The method is demonstrated on an aluminium alloy 7075 plate of 6 mm thickness that was subjected to laser shock peening treatment. It is shown that series expansion remains stable up to 8^{th} order and convergence to a stress solution can be found before instability dominates. The resulting stress distribution and associated uncertainties of series expansion are compared against those obtained from the regularized integral method and Zuccarello approach, including a breakdown of contribution from each uncertainty source considered. The use of series expansion reduces the RMS uncertainty in stress and is insensitive to stain measurement errors due to the least-squares approach employed by the inverse solution.

This chapter has been adapted and extended from: **T.C. Smit**, R.G. Reid. Use of Power Series Expansion for Residual Stress Determination by the Incremental Hole-Drilling Technique. *Experimental Mechanics*, 2020, Springer Nature. The published article is available at https://doi.org/10.1007/s11340-020-00642-0. Licensed permission to reuse this content can be found in Appendix I: Springer Nature License Agreements.

7.1 Introduction

IHD with the integral method is used extensively to determine residual stress distributions in isotropic materials. When used with Tikhonov regularization, the method is robust and produces accurate results with minimal uncertainty. Alternatively, an optimal hole depth distribution can be found using the method of Zuccarello to ensure the calibration matrices have constant diagonal elements, thereby improving their conditioning. If substantial measurement noise or a steep stress gradient exists, however, considerable uncertainty in, or distortion of, the calculated residual stress distribution can occur. Series expansion offers an alternative solution, but it has been reported to become unstable before meaningful accuracy can be achieved. Series expansion in isotropic materials was introduced by Schajer in 1981 [92] but possible instability beyond first order series prevented its use for highly non-uniform stress distributions. Following the successful implementation of series expansion with IHD in FRP laminates in Chapter 5, it became clear that series expansion remains stable up to higher orders. Although separate series up to only 2^{nd} order were used in Chapter 5, their amplitudes were determined in a single least-squares solution which included the effect of all series orders, in all directions, and separate application regions. Chapter 6 demonstrated that while Tikhonov regularization could be extended to cross-ply FRP laminates, series expansion still performed slightly better in terms of uncertainty and depth resolution. Considering the results obtained in Chapters 5 and 6, it is reasonable to assume that standard series expansion in isotropic materials would remain stable up to higher orders than previously reported, and it may reduce uncertainty in stress compared to the regularized integral method. It is, therefore, important to once more investigate the use of series expansion with IHD in isotropic materials.

Although the series expansion method presented in this chapter is based on the work of Schajer from 1981 [92], there are numerous subtle differences between the method employed here and that originally proposed by Schajer, even though the fundamental approach is similar. The main differences are: the work of Schajer was limited by the computational resources of the time and a much finer FE mesh is now possible, combined with the use of eigenstrain distributions to generate through-thickness stress variations instead of direct stress application to the hole surface, to more accurately determine the calibration coefficients for the higher order terms. Modern fine-increment drilling allows a large number of depth increments to be used, compared to only 6 and 4 depth increments of 100 µm used by Schajer in 1981 [92] and 1988 [93], respectively. With this limited number of strain measurements, higher order terms will not be of much use, and can easily become unstable. Least-squares solutions are particularly effective when the number of strain measurements is considerably greater than the number of unknown amplitude coefficients. Depending on the strain distribution, zeroth and first order series can result in poor fits to the strain data and the resultant stress solution may appear unusable since the difference between zeroth and first order solutions can be considerable. However, this can simply be an indication that a higher order solution is required to better represent the

actual residual stress distribution. Higher order series can be sensitive to noise in the experimental strain measurements, however, especially at the ends of the series and this may give the appearance of instability if uncertainty and convergence are not considered and compared for a number of series orders. A thorough means of assessing when to stop increasing the series order has been developed in Chapter 5 through the use of a comprehensive uncertainty analysis.

To investigate the effect of these adjustments to the series expansion method, IHD was applied to a LSP-treated aluminium alloy 7075 specimen of 6 mm thickness to access the performance of series expansion in measuring a highly non-uniform stress distribution. It is consequently necessary to compare results from other widely used approaches so that valid conclusions can be drawn. It is critical that series expansion is compared primarily to the regularized integral method as it is the accepted industry standard. As an additional comparison, the Zuccarello approach of using optimal depth distributions is used. The Zuccarello approach has the advantage of using the pure experimental strains in its calculation which negates any issues around possible stress distortion that may exist in both regularized integral and series expansion methods due to the strain mismatch resulting from regularization and least-squares curve fitting.

7.2 Computational Methods

While three different computational methods are used in this chapter, only application of series expansion of eigenstrain in isotropic materials and the Zuccarello approach [155] are explained in some detail. The standard series expansion method is explained by Schajer [92], separate series expansion method is explained in detail in Chapter 5 and the ASTM integral method [86] is well known and explained in section 2.2.2.1.

7.2.1 Series Expansion in Isotropic Materials

Series expansion of eigenstrain can be applied to isotropic materials using a similar approach to how separate series expansion is applied to FRP laminates in section 5.2. The only adjustment required is that eigenstrain distributions are only applied to a single material, which reduces the computational requirement of both the FE calculations and the inverse solution. Once the strain vector, $\boldsymbol{\epsilon}_{meas}$, calibration matrix, $\mathbf{C}$, and the stress matrix, $\mathbf{S}$, are determined, the residual stress distribution is calculated using equations (5.10) and (5.12). Residual stress distributions in isotropic materials can exhibit steep gradients, therefore, small depth increments should be used to ensure a robust least-squares fit to the experimental strains such that steep stress gradients can be correctly captured in the calculated stress distributions. The experimental strains measured during IHD in isotropic materials are generally smooth by nature without sharp turning points. However, high orders of power series

expansion may still be required to ensure a reasonable fit to the measured strain data. As the order of power series expansion is increased, the least-squares fit to the experimental data will improve, but the benefits of an improved fit will be progressively outweighed by the inherent instability associated with a higher order series. It is therefore crucial that a series order that can adequately describe the actual stress distribution is found before instabilities dominate.

7.2.2 Zuccarello Approach

The conditioning of the calibration matrices of the integral method, $\bar{\mathbf{A}}$ and $\bar{\mathbf{B}}$, can be optimised and the sensitivity to experimental strain errors minimised by ensuring that the diagonal elements of the calibration matrices are constant in magnitude. To achieve this, a non-uniform depth increment distribution must be used. Calibration matrices for any depth increment distribution can be obtained from cumulative calibration coefficients [93], which can be determined from the constant step matrices, $\bar{\mathbf{A}}$ and $\bar{\mathbf{B}}$. The non-uniform depth increment distribution that results in constant diagonal calibration coefficients can be found by iteration, following the methodology proposed by Zuccarello [155], for a particular number of depth increments or for a certain magnitude of the coefficients on the diagonal. Since biaxial stresses are dominant after the application of LSP, only the hydrostatic component, $\boldsymbol{\sigma}_p$, of the residual stress field was considered when determining the optimal depth distribution. The equi-biaxial calibration matrix for the non-uniform depth distribution is denoted as $\bar{\mathbf{A}}_{(Zucc)}$. The same depth distribution was used to determine $\bar{\mathbf{B}}_{(Zucc)}$.

The size of the first depth increment, and the corresponding first entry in $\bar{\mathbf{A}}_{(Zucc)}$, defines the magnitude of all diagonal elements of $\bar{\mathbf{A}}_{(Zucc)}$ and therefore the required depth distribution. There is scope to optimise the size of the first depth increment to find the most stable stress solution, but if this size is made too large it can lead to incorrect stress calculation when steep stress gradients exist.

7.3 Demonstration of Procedure

7.3.1 Experimental

Samples of aluminium alloy 7075-T651 were machined from a rolled plate of 15 mm thickness. The samples were reduced to a thickness of 6 mm by machining 1 mm from the top face of the plate and 8 mm from the bottom. Individual samples of 60 mm $\times$ 60 mm were then prepared. The plate thickness of 6 mm falls within the 'thick' workpiece limits prescribed by the ASTM standard. The mechanical properties and the chemical composition of aluminium alloy 7075-T651 are provided in Table 7.1 [192].

Table 7.1: Mechanical properties and chemical composition of aluminium alloy 7075-T651

Young's Modulus	Poisson's	Tensile Yield	Chemical composition Wt. (%)								
(MPa)	ratio	Strength (MPa)	Al[1]	Cr[1]	Cu[1]	Fe[2]	Mg[1]	Mn[2]	Si[2]	Ti[2]	Zn[1]
71700	0.33	503	89.3	0.23	1.6	0.5	2.5	0.3	0.4	0.2	5.6

[1] Average value

[2] Maximum value

The upper face of the machined plate underwent LSP treatment at the National Laser Centre (NLC) of the Council for Scientific and Industrial Research (CSIR) in Pretoria, South Africa, using a Quanta-Ray Pro Spectra Physics (QRPSP) Nd:YAG laser. The QRPSP laser specifications and the LSP parameters are provided in Table 7.2. An X-Y raster pattern with equidistant spot placement in the horizontal and vertical directions was used as the spot sequence strategy. A 1.5 mm spot diameter, with a spot density of 5 spots/mm^2 (70% spot overlap), was used to attain a power intensity of 1.5 GW/cm^2. LSP was applied to an area of 11.25 mm $\times$ 11.25 mm. In this work the LSP step and scan directions are represented by the x and y directions, respectively.

Table 7.2: Laser specifications and LSP parameters

QRPSP Laser Specifications						LSP Parameters		
Laser Type	Wavelength (nm)	Pulse Frequency (Hz)	Energy Range (J)	Spot Shape	Spot Size Range (mm)	Power Intensity (GW/cm^2)	Spot Diameter (mm)	Coverage (spots/mm^2)
Nd:YAG	1064	20	0.2–1	○	0.5–2.5	1.5	1.5	5

The IHD experimental procedure and instrumentation follows that of section 5.3.1 unless stated otherwise. IHD measurements were performed in the centre of the LSP area. A tungsten carbide inverted cone end mill with a 1.6 mm diameter was used to cut the hole that had a final diameter of 1.74 mm. The depth increments on the MTS Restan 3000 were set to 5 µm for the first 0.2 mm of the test to

enable inclusion of zero depth uncertainty, and 25 µm for the remainder of the test up to a depth of 1.2 mm. Drilling ceased at a depth of 1.2 mm since the region of high compressive stress resulting from LSP lies close to the surface and the sensitivity of the surface strain measurements greatly decreases beyond a depth of approximately half the hole diameter. The additional strain data points beyond 1 mm were used in the series expansion method to somewhat constrain the series at depths approaching 1 mm and so reduce the stress uncertainty in this region.

A gauge excitation voltage of 3.5 V was selected to achieve the desired sensitivity whilst keeping the power consumed by the gauge low. A 20 second delay was used after each drilling increment before strain readings were recorded to allow for all thermal effects to dissipate and for steady state conditions to resume. The experimentally measured strain variations at the x, y and $45°$ strain gauge locations are presented in Figure 7.1. Strain data are presented at depth increments of 25 µm, which correspond to the depths used to calculate the calibration matrix. The intervening strain measurements at increments of 5 µm over the first 0.2 mm of the test were omitted to improve the clarity of Figure 7.1.

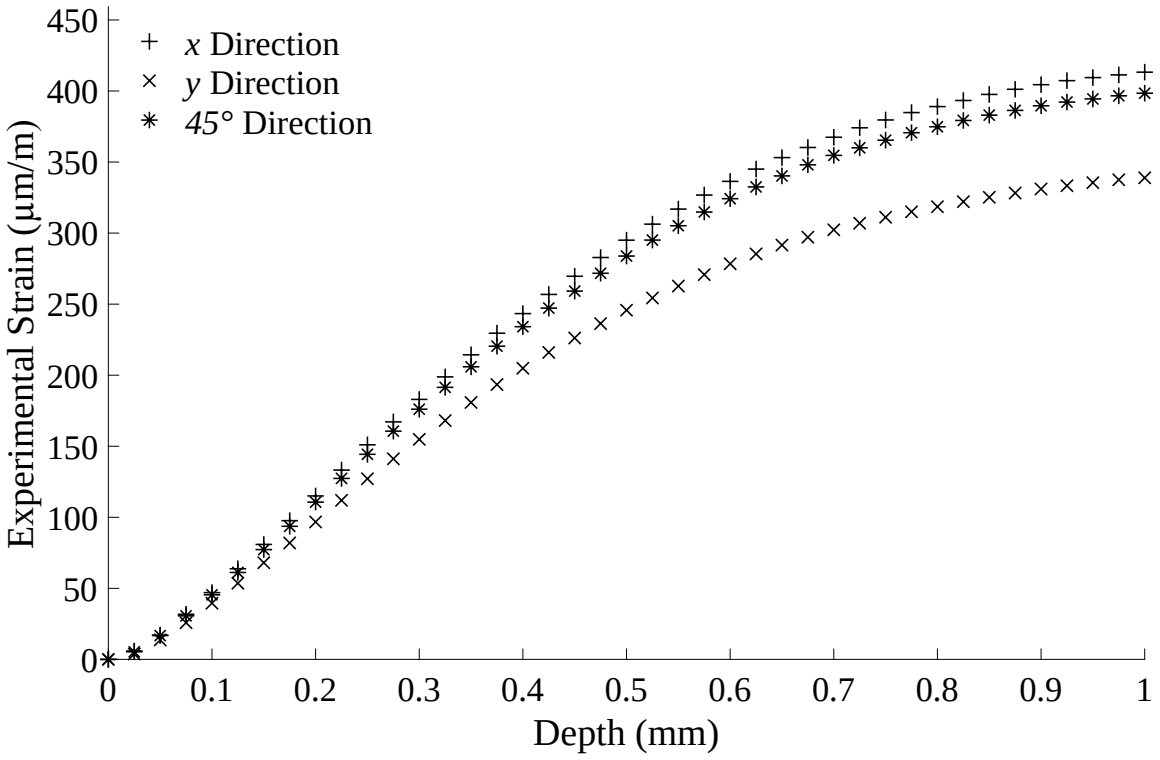


Figure 7.1: Strain variation with depth in the x, y and $45°$ gauge directions

7.3.2 Computational

The 1.5/350M RY61 strain gauge rosette used in this work has a different geometry to those specified in the ASTM standard and the hole diameter of 1.74 mm lies outside the suggested range of 1.88-2.12 mm [86]. The calibration coefficients of the integral method must, therefore, be determined using FE analysis since the ASTM calibration coefficients are not applicable in this particular case. In general, however, it is possible in principle to obtain the necessary series expansion coefficients through numerical integration of the ASTM unit pulse coefficients, provided that the plate thickness and hole diameters are within the guidelines specified by the ASTM standard. There was, however, no real benefit to be gained from integration of unit pulse coefficients in this particular case. The additional computation required to obtain the coefficients for series expansion was negligible since this merely required the inclusion of additional load cases within the FE model required to obtain the coefficients for the integral method. One benefit of the FE approach for series expansion is that the use of eigenstrain has the advantage of applying zero net force and moment. While this is not a significant benefit for a plate of 6 mm thickness, it can be beneficial in applications with smaller plate thickness. Using the same FE model and approach to calculate the calibration coefficients for both the integral and series expansion methods also removed some expected variability in the results of the two methods due to differences arising from FE calculations. This ensures that a reasonable comparison between the computational methods could be achieved.

The calibration coefficients were calculated using MSC Nastran FE analysis. The specimen was modelled using HEX8 type 3D elements. The specimen was represented by 24 elements through the first 1.2 mm from the surface, and 68 elements through the remaining thickness with linearly increasing element height towards the bottom of the plate. While the use of a 2D model would have offered benefits in terms of reduced run times and finer discretization of the *r-z* plane with a modest number of elements, the computational time requirement in this study was not a limitation. It was consequently elected to use 3D modelling as was done by Alegre et al. [193] who found very good agreement with the ASTM coefficients for the case of 'thick' samples with a coarser mesh than used in this chapter, and who found that results were practically unaffected by further mesh refinement. FE models with hole diameters of 1.70 mm, 1.75 mm and 1.80 mm were created so that any experimental hole diameter within this range could be used by interpolation. This approach also allows the uncertainty of the measured hole diameter to be included in the analysis. Due to symmetry, a quarter model was used with symmetric and anti-symmetric boundary conditions depending on the applied loading. Eigenstrain distributions for the series expansion method were applied to the FE model by means of through-thickness temperature variations defined by power series functions and dummy thermal expansion coefficients. Elements in the first 1.2 mm below the surface were assigned a coefficient of thermal expansion of unity in the x, y or in-plane shear direction and the remaining elements were assigned a coefficient of thermal expansion of zero. Each applied eigenstrain distribution results in mechanical strain redistribution that generates a through-thickness stress distribution. It is important

to note that a stress distribution was created throughout the entire thickness of the specimen even though eigenstrain was only applied to elements in the first 1.2 mm.

The mesh around the hole and position of the strain gauge grid locations (highlighted) are presented in Figure 7.2 and a section through the mesh is presented in Figure 7.3. Each applied eigenstrain distribution results in a strain distribution around the hole for each depth increment. For illustrative purposes, the strain variation in the x-direction due to a 2^{nd} order eigenstrain in the x-direction at a hole depth of 0.5 mm is presented in Figure 7.4. As in section 6.3.2, the grids were not directly included in the FE model and nodal displacement data in the region of the strain gauge grid locations was used to determine the longitudinal and transverse strain at each gauge location for every loading condition and drilling increment. The longitudinal and transverse strains at each gauge location for every drilling increment and applied eigenstrain series were used to populate the longitudinal and transverse calibration matrices, respectively. The positioning of the hole relative to the centre of the rosette was included in the analysis according to section 6.3.2. The matrix of 'uncorrected' calibration coefficients were then determined from equation (5.13).

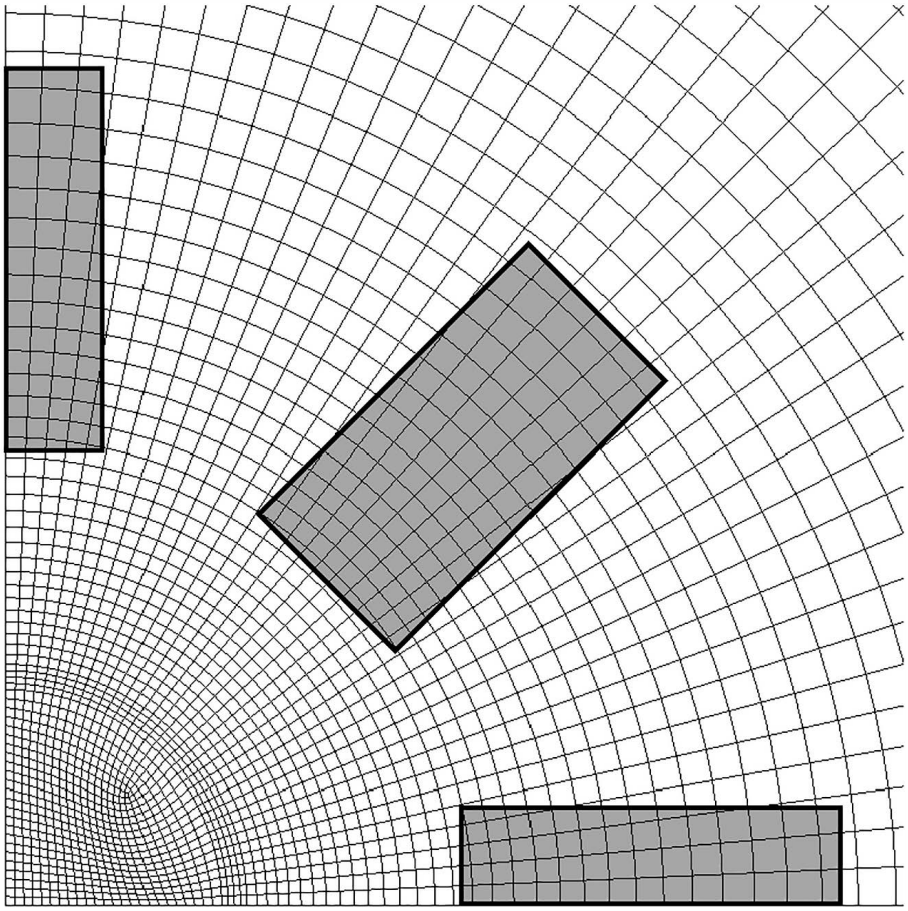


Figure 7.2: Top view of mesh around the hole including the strain gauge grid locations

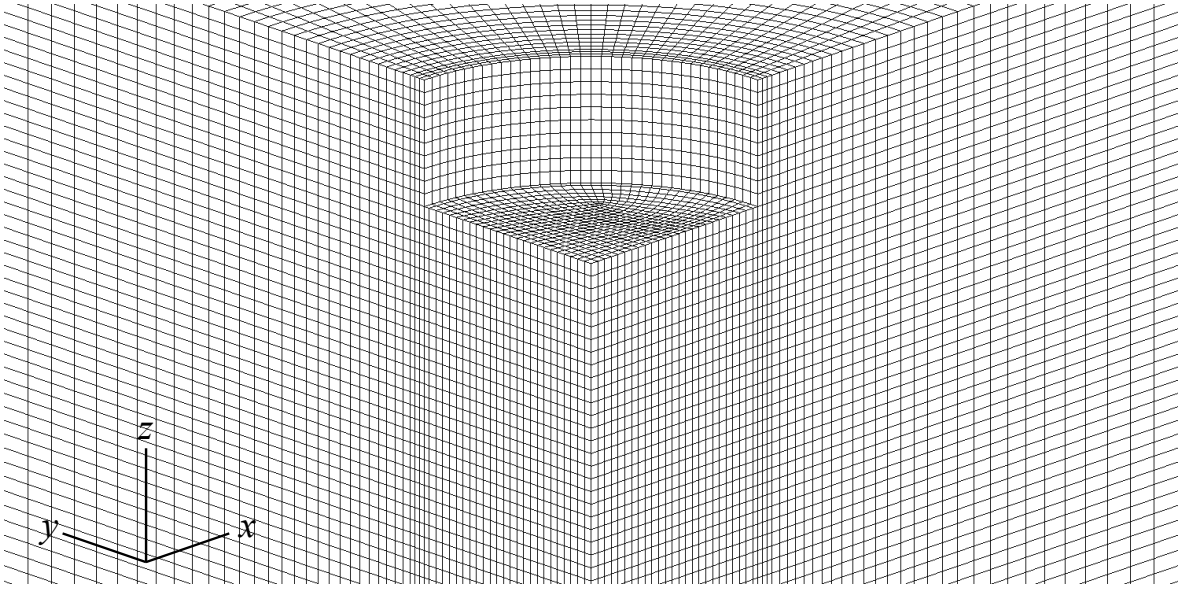


Figure 7.3: Section through the mesh thickness

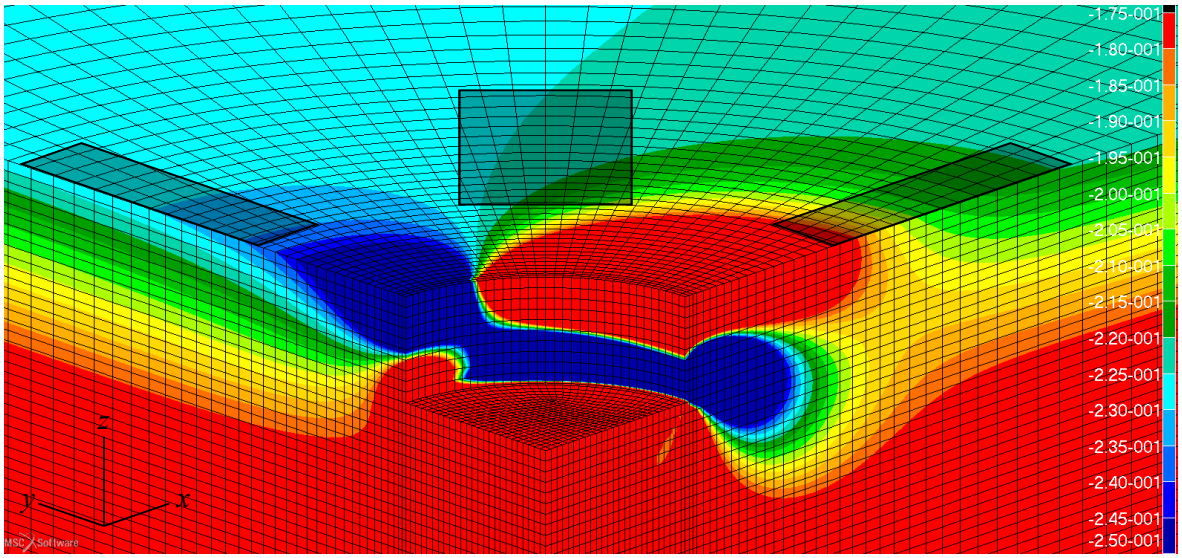


Figure 7.4: Strain variation in the x-direction at 0.5 mm hole depth and strain gauge grid locations

The necessary calibration coefficients for the integral method were determined using PLOAD4 cards to apply an equi-biaxial stress (for matrix $\bar{\mathbf{A}}$) and a pure shear stress (for matrix $\bar{\mathbf{B}}$) to the face of the hole for every loading increment at each incremental depth, as shown in Figure 2.1. To apply each of these loads, the equivalent radial and shear stress distributions were applied simultaneously to the hole face according to the following stress transformation equations [157]:

$$\sigma_x = \sigma_y = 1,\ \tau_{xy} = 0 \rightarrow \sigma_{rr} = 1,\ \tau_{r\theta} = 0 \tag{7.1}$$

$$\tau_{xy} = 1,\ \sigma_y = \sigma_x = 0 \rightarrow \sigma_{rr} = \sin 2\theta,\ \tau_{r\theta} = \cos 2\theta \tag{7.2}$$

The strains at the relevant grid locations were calculated using the same biharmonic spline approach and correction for transverse sensitivity as for series expansion. These were used to obtain the coefficients of $\bar{\mathbf{A}}$ and $\bar{\mathbf{B}}$. The $\bar{\mathbf{A}}$ and $\bar{\mathbf{B}}$ matrices obtained from the FE model were used to determine the corresponding $\bar{\mathbf{A}}_{(Zucc)}$ and $\bar{\mathbf{B}}_{(Zucc)}$ matrices for the Zuccarello approach.

The constant depth increment for the integral method with regularization was set to 50 μm up to a maximum depth of 1 mm, giving twenty constant steps as in the calibration tables of the ASTM standard. The first entry of $\bar{\mathbf{A}}$ of the standard integral method was used to determine the depth distribution that results in constant diagonal values in $\bar{\mathbf{A}}_{(Zucc)}$. Fifteen depth increments were found within 1 mm from the surface. Although this number of depth increments is greater than suggested by Zuccarello [155], the closer spacing between increments was required to correctly capture the steep stress gradient and local minimum near the surface due to LSP treatment. In the case of series expansion, the depth increment was set to 25 μm up to a maximum depth of 1.15 mm. This means that 47 depth increments, including zero depth, were used to populate the experimental strain vector, $\boldsymbol{\epsilon}_{meas}$. As in Chapter 6, the additional strain data points beyond the region of interest up to 1 mm were used to help constrain the series near their end points, where greater instability can occur, and consequently reduce uncertainty in stress.

Equation (5.10) requires that $\boldsymbol{\epsilon}_{meas}$, $\bar{\mathbf{C}}$ and $\hat{\mathbf{C}}$ follow the same depth distribution. Therefore, $\bar{\mathbf{C}}$ and $\hat{\mathbf{C}}$ must be determined for the depth increments of $\boldsymbol{\epsilon}_{meas}$. The strain vs. depth relationships obtained from the FE calculations follow smooth variations. A spline was fitted to the calculated longitudinal and transverse calibration coefficients to determine $\bar{\mathbf{C}}$ and $\hat{\mathbf{C}}$ for the depth distribution of $\boldsymbol{\epsilon}_{meas}$ through interpolation, similar to what was done in Chapter 5 in the case of separate series expansion. This procedure is presented in Figure 7.5 for the calculated longitudinal calibration coefficients corresponding to the x-direction resulting from a 2$^{\text{nd}}$ order eigenstrain in the x-direction.

For the sake of simplicity and illustration, the same order series was used for all three components of eigenstrain. It is, however, possible to use a different series orders for each component of eigenstrain. As the order of standard series expansion is increased, the least-squares fit to the experimental strain data is improved as can be seen in Figure 7.6 for the x-direction strain gauge, where 2$^{\text{nd}}$ and 6$^{\text{th}}$ order series expansion are applied, respectively. The 2$^{\text{nd}}$ order fit appears to be sufficient, but it is unable to closely fit the strain data near the surface and does not guarantee convergence to a stress solution. Therefore, higher order series are required, but the stress solution of higher order series can become unstable due to increased sensitivity to measurement errors, resulting in greater uncertainty in calculated stresses, which would negate the improved fit to the strain data. Therefore, a thorough understanding of how uncertainty propagates through the analysis is required.

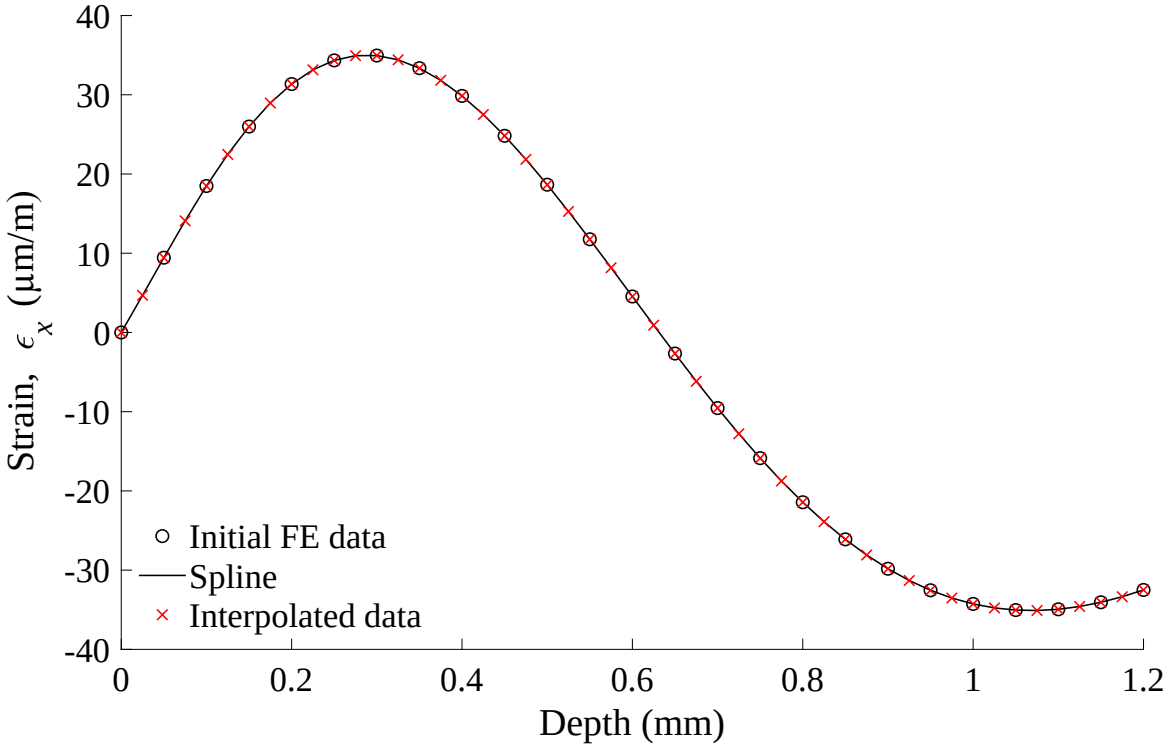


Figure 7.5: Determination of interpolated calibration coefficients from FE data

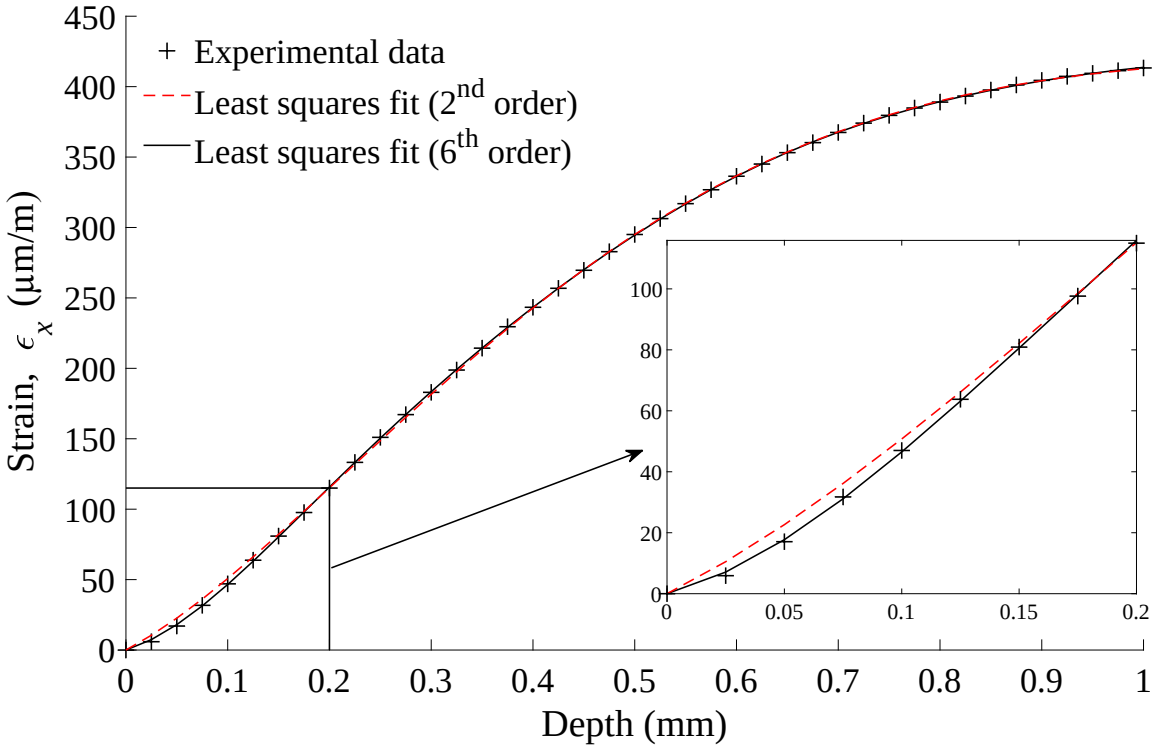


Figure 7.6: Least-squares fits to strain data in the x-direction using 2nd and 6th order series

7.3.3 Propagation of Uncertainties

Uncertainty propagation was conducted as described in sections 5.3.3 and 6.3.3 unless stated otherwise. The various experimental and computational uncertainty sources considered in this chapter are provided in Table 7.3. Ten thousand trials were simulated for each series expansion order, as well as for the regularized integral method and Zuccarello approach.

Table 7.3: Uncertainty sources and their assigned probability density functions

x_i	Description	$p(x_i)$	Type	Nominal value, uncertainty
E	Young's Modulus	Normal	B	71700 MPa, 3%
ν_{12}	Poisson's ratio	Normal	B	0.33, 3%
z_i	Incremental depths	Rectangular	B	25 µm, 0.5 µm
z_0	Zero depth	Rectangular	B	0 µm, 10 µm
HD	Hole diameter	Rectangular	B	1.74 mm, 0.005 mm
ϵ_m	Indicated experimental strain	Normal	B	Figure 7.1, 1.6%
ϵ_{noise}	Experimental noise	Normal	A	Figure 7.1, 1 µm/m
K_{tx}	Transverse sensitivity for gauge 1	Normal	B	2.2%, 0.1%
K_{t45°	Transverse sensitivity for gauge 2	Normal	B	2.6%, 0.1%
K_{ty}	Transverse sensitivity for gauge 3	Normal	B	2.2%, 0.1%
ν_0	Poisson's ratio of the material on which gauge factor was measured	Normal	B	0.285, 3%
FE	Finite element calculations	Normal	B	0, 2%

Zero depth position in aluminium can be established by using the electrical contact technique that identifies the contact between the end mill and the surface of the specimen when the electrical connection occurs. However, the approach used in section 5.3.3 was also applied here. Since LSP induces compressive residual stress near the surface, some strain response should occur when the end mill starts to penetrate into the specimen. While this method is by no means fully robust or advisable in general (since there will be no observable or an extremely small strain response if the near surface stresses are close to zero), it does allow inclusion of the uncertainty in zero depth position when calculating the residual stresses. Incorrect zero depth position can not only alter the magnitude of the first few stress measurements, but also the entire stress distribution due to the nature of the inverse solution. After the IHD experiment, the strain variations were investigated and shifted along the x-axis to find the most likely position of the surface. To be conservative, it was assumed that a datum point associated with the end mill at a full depth increment into the specimen could be missed. Additionally, the presence of surface roughness peaks from LSP or low surface stress in the specimen could impact the use of this approach. Therefore, the zero depth uncertainty in this case is taken to be two increments, or 10 µm.

Calibration matrices were found for the hole diameter of the current trial by spline interpolation of each coefficient obtained from the 1.70 mm, 1.75 mm and 1.80 mm FE models. Although it is possible to use material independent calibration and stress matrices for series expansion, which allow variations in material properties to be included directly in the stress calculation [ii], the approach of section 5.3.3 was employed here. Uncertainty in the material properties was included in the integral method within equations (2.6)-(2.8) and in the Zuccarello approach within equations (2.2)-(2.4).

Once the strain vector, $\boldsymbol{\epsilon}_{meas}$, calibration matrix, $\mathbf{C}$, and the stress matrix, $\mathbf{S}$, were determined for each trial, the stress distribution was determined using equations (5.10) and (5.12). The stress distributions for the integral and Zuccarello approaches were determined using equations (2.6)-(2.8) and equations (2.2)-(2.4), respectively.

[ii] Young's modulus, E, can easily be made independent in the analysis and simply used to scale the calculated stresses. Since eigenstrains were used to apply the stress distributions, E can simply be placed outside the stress matrix as a multiplier for the calculated residual stresses. This applies to all stress components since shear modulus, G, is proportional to E. The calibration matrix is unaffected by E since an increase in E results in higher applied stresses for the same eigenstrain, but the strain response is correspondingly reduced. The two effects both scale with E and cancel out. The situation is not as straightforward for Poisson's ratio, however. The effect of Poisson's ratio variations on the calibration and stress matrices can be included in terms of the particular Poisson's ratio used in the FE model to determine these matrices, and the Poisson's ratio of the specimen material under investigation. Poisson's ratio affects each measurement direction slightly differently and also depends on the direction of the applied stress, however, and requires the use of a correction matrix with appropriate terms to correctly scale each coefficient of the calibration and stress matrices. The relationship between Poisson's ratio and the coefficients of the calibration and stress matrices is not perfectly linear and a range needs to be defined where simple corrections can be used without introducing considerable error into the stress solution. This was also identified by Schajer [92] in the case of the integral method where less than 2% deviation was found between the Poisson's ratio correction used in the ASTM and FE calculations for a range of Poisson's ratios between 0.25 – 0.35. While it is unlikely that deviations of 2% will cause any major errors in the stress solution, this needs to be fully investigated and confirmed.

7.3.4 Series Expansion Order Selection

A practical challenge when using series expansion is the discontinuous nature of the stress results as the series order is increased. At lower orders, large changes occur between each stress distribution in the sequence. In general, however, low order series expansion should not be used. Instead, series expansion of high enough orders should be used such that the variation in stress distributions from order to order becomes negligible as the series converge. The issue of convergence therefore becomes a paramount consideration. The approach used in this chapter is to determine those series orders that have converged, and from them to select the series order with the lowest RMS uncertainty, as in section 5.3.5. Therefore, the calculated stress and uncertainty of every series order must be investigated to quantitatively determine the best estimate of the residual stress distribution.

The calculated stress and uncertainty in the x-direction for 0^{th} to 14^{th} order series is shown graphically in Figure 7.7. The corresponding figure for stress in the y-direction is similar and therefore omitted in the interest of brevity. The stress uncertainty of each series order is shaded in light grey and then superimposed. The tendency of higher order series to become unstable increases their sensitivity to errors in strain measurement data within the Monte Carlo trials, resulting in greater stress uncertainty. The darkest areas correspond to convergence of a number of orders where their stress uncertainties agree. The light grey regions illustrate the divergence in uncertainty for higher order series, or the inability of low order series (0^{th} - 3^{rd} order) to describe the actual stress distribution. The 6^{th} order series is selected as the best solution for this experimental data set as it has the lowest RMS uncertainty of the series orders that have converged. Some orders have lower uncertainty, but have not fully converged and so are not selected. Higher orders that have converged show the first signs of instability and greater uncertainty, and were subsequently not selected either.

The convergence in stress results in the x-direction of the 6^{th}, 7^{th} and 8^{th} order series is shown in Figure 7.8. The results for 14^{th} order are also shown, where the instability in the calculated stress distribution is evident.

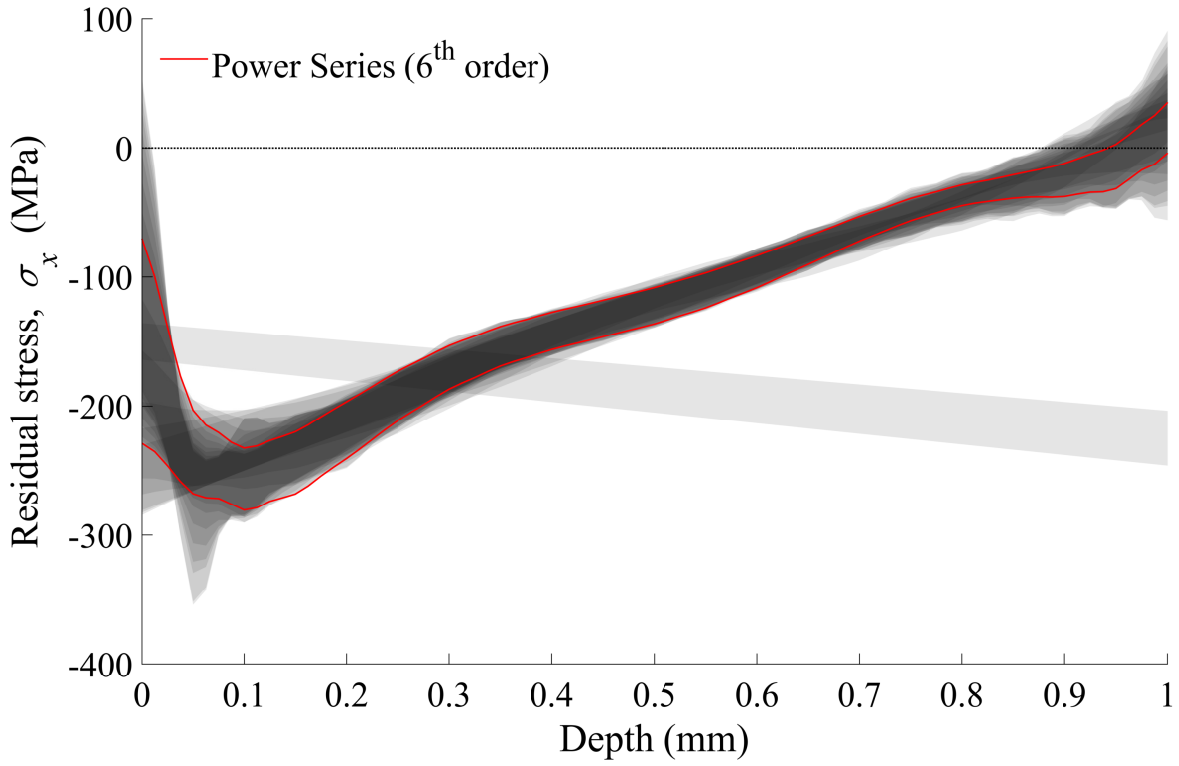


Figure 7.7: Overlap of the uncertainty bounds in σ_x for 0th to 14th order series

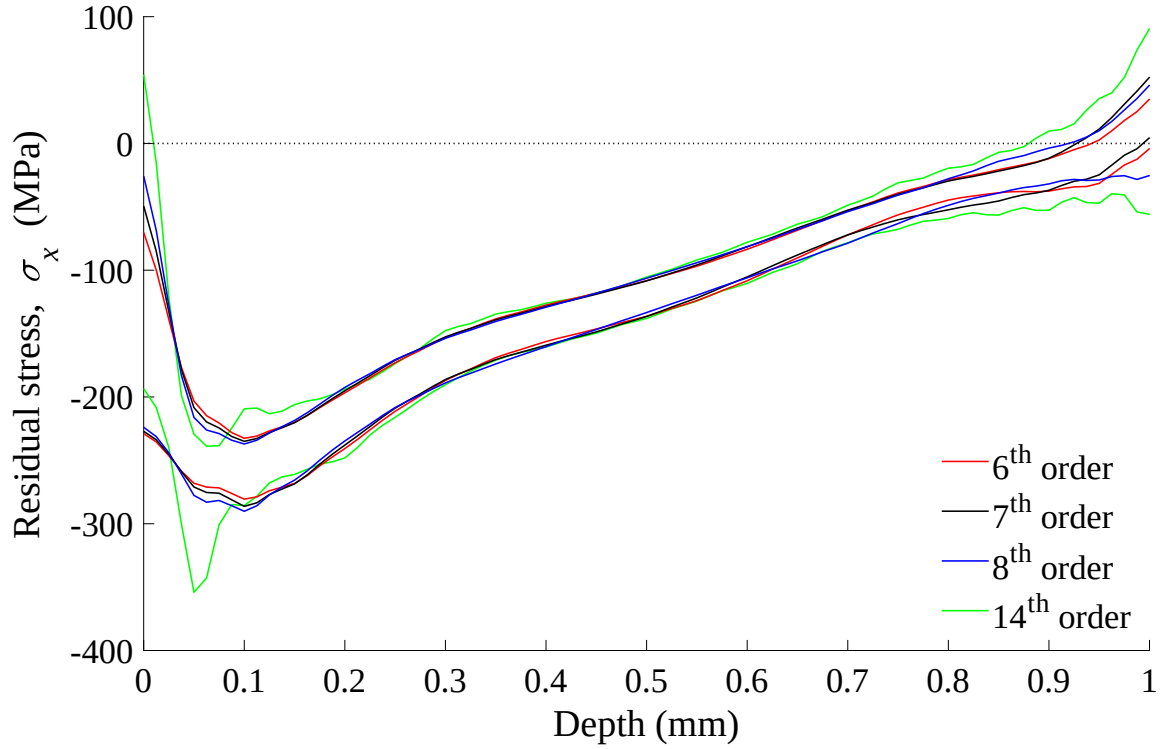


Figure 7.8: Overlap of the uncertainty bounds in σ_x for converged and 14th order series

7.4 Results and Discussion

The least-squares fits and associated uncertainties of the 6th order series to the strain measurements obtained from the x, y and $45°$ gauges are shown in Figure 7.9. The uncertainty associated with the inability of the 6th order power series expansion to exactly fit the measured strain data is included in Figure 7.9. The stress distributions and associated uncertainties obtained using the 6th order series are shown in Figure 7.10. The uncertainty in all three stress components is expected to increase with depth since the sensitivity of the measured strains on the upper surface to released stresses decreases. However, stress uncertainty remains stable up to a depth of 1 mm. The extension of the hole depth beyond 1 mm to provide additional strain data has helped improve the stability of higher order series at greater depths by providing additional data points to constrain the least-squares curve fit. The maximum stress uncertainty occurs near the surface since the least-squares fits are less constrained near their endpoints and tend to diverge from the mean, resulting in increased uncertainty. The residual stress distributions in the x and y directions are similar in magnitude and form, and the residual shear stress is close to zero, as expected. The results indicate that the raster pattern strategy used during LSP affected the relative magnitude of the induced compressive residual stresses in the x and y directions (aligned with the laser stepping and scanning directions, respectively). The magnitude of the induced compressive residual stress in the laser stepping direction is greater than in the laser scanning direction. Correa et al. [194] reported that samples peened using a LSP raster pattern strategy result in greater differences between residual stresses in the x and y directions than those induced by a random pattern strategy. Nobre et al. [76] also found that the magnitude of the compressive residual stress in the laser stepping direction is consistently greater than in the laser scanning direction. The rolling direction coincides with the laser stepping direction and could also have contributed to the difference in compressive residual stresses in the x and y directions. The peak stresses are only 55$\%$ of the bulk material yield stress and plasticity effects are therefore not included.

The residual stress distributions determined using the regularized integral and Zuccarello methods are overlaid on those determined using series expansion in Figures 7.11 and 7.12. Only x and y stresses are shown since the shear stress is close to zero. The residual stress distributions compare favourably and the uncertainty in stress is lower overall in the case of series expansion, especially at greater depths. Table 7.4 compares the RMS uncertainty in stress for each computational method and each uncertainty source, as well as the combined uncertainty, $u(Z)$.

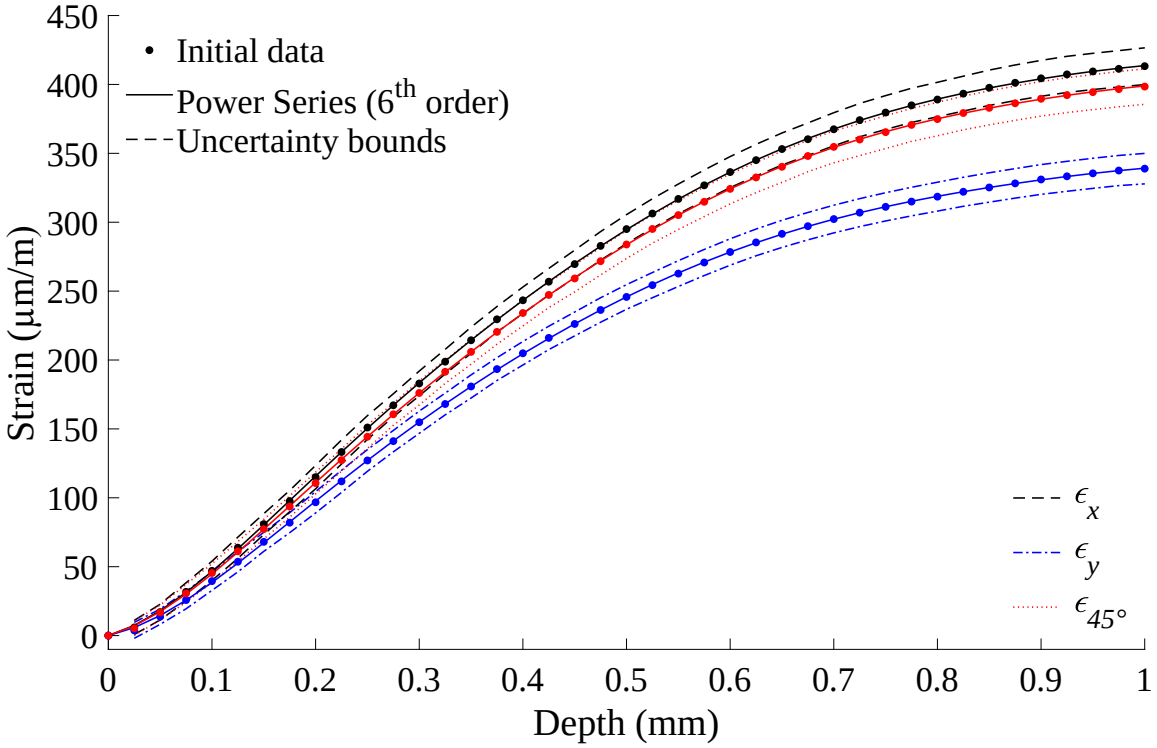


Figure 7.9: Least-squares curve fits to experimental strain data with associated uncertainties

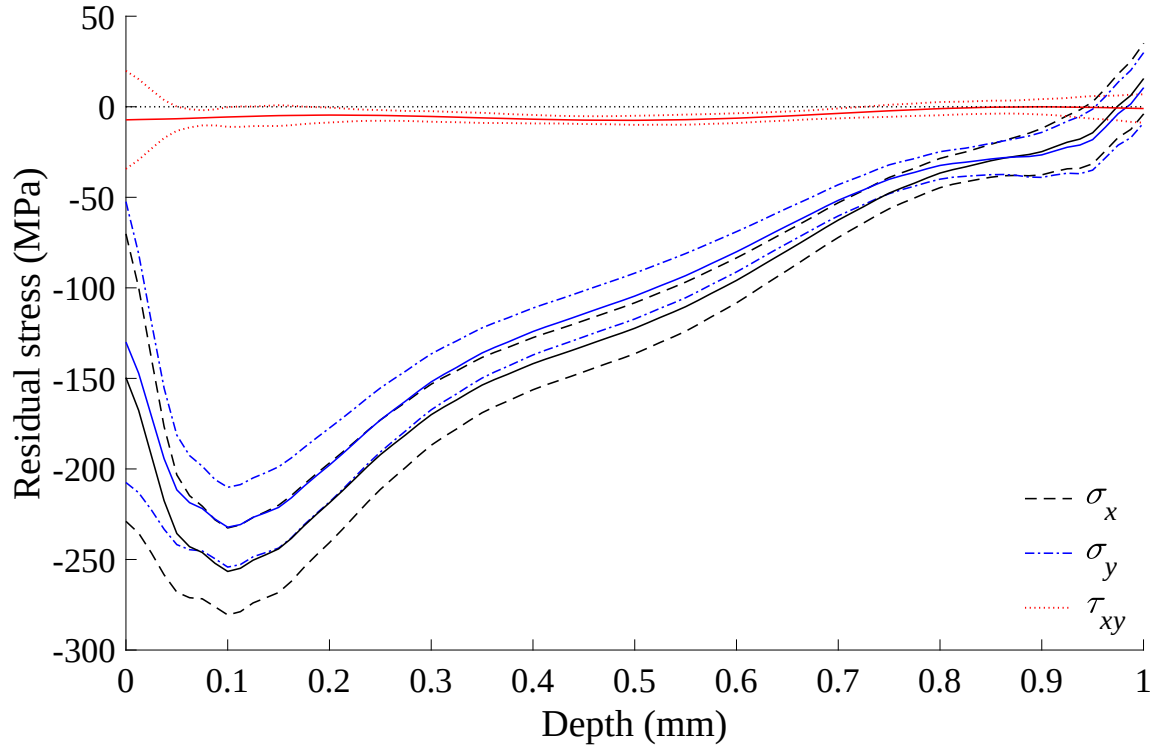


Figure 7.10: Stress distributions and associated uncertainties obtained using the 6th order series

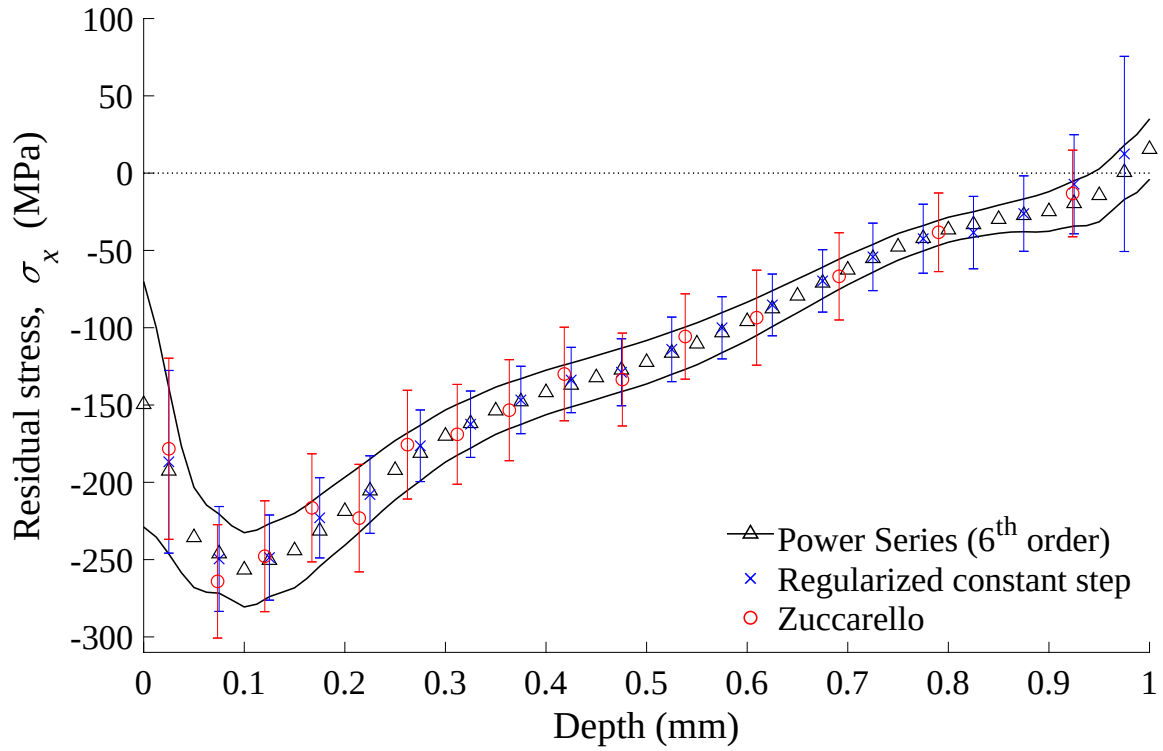


Figure 7.11: σ_x distributions and associated uncertainties of each method

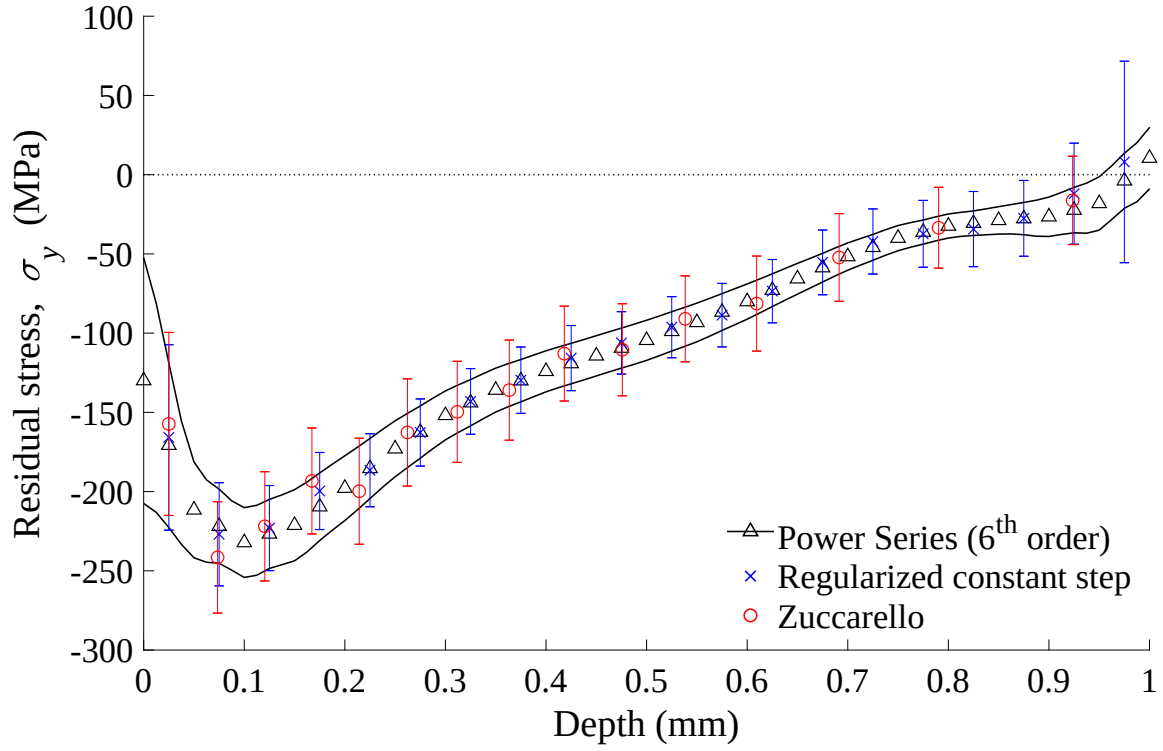


Figure 7.12: σ_y distributions and associated uncertainties of each method

Table 7.4: Breakdown of RMS uncertainty in stress arising from each uncertainty source, x_i

x_i	Contribution to $u(\sigma_x)$ [MPa]			Contribution to $u(\sigma_y)$ [MPa]			Contribution to $u(\tau_{xy})$ [MPa]		
	Series Expansion	Constant Step	Zuccarello	Series Expansion	Constant Step	Zuccarello	Series Expansion	Constant Step	Zuccarello
E	4.327	4.291	4.934	3.857	3.815	4.400	0.153	0.151	0.189
ν_{12}	1.267	1.010	1.163	1.301	1.010	1.163	0.024	0.000	0.000
z_i	0.421	0.905	2.394	0.390	0.872	2.172	0.031	0.020	0.080
z_0	5.023	6.453	7.263	4.786	6.184	7.039	0.147	0.199	0.843
HD	0.549	0.922	1.045	0.496	0.851	0.966	0.017	0.023	0.028
ϵ_m	2.302	2.296	2.625	2.052	2.044	2.341	0.082	0.080	0.101
ϵ_{noise}	3.088	11.522	13.685	3.103	11.501	13.707	2.014	9.922	10.554
K_t	0.037	0.039	0.045	0.037	0.039	0.045	0.029	0.001	0.002
ν_0	0.023	0.025	0.029	0.020	0.025	0.029	0.022	0.001	0.001
FE	4.119	2.868	3.298	3.672	2.550	2.941	0.146	0.101	0.126
Misfit	1.225	4.181	0.000	1.273	4.155	0.000	0.805	1.967	0.000
u(Z)	8.884	14.944	17.123	8.280	14.620	16.695	2.197	10.701	10.616

It is evident that the zero depth position and noise in the experimental strains are important contributors to the stress uncertainty. While the series expansion method has a slightly greater tolerance to uncertainty in the zero depth position than the other methods, its tolerance to noise in the strain data is far greater. The uncertainty in stress associated with noise is consequently far lower in the case of series expansion. The superior noise resistance characteristics of the series expansion method is complex and down to numerous factors that include the fundamental differences between the integral and series expansion methods, as well as the differences between least-squares curve fitting and regularization. Series expansion made use of double the number of hole depth increments than the integral method which enabled greater benefits to the least-squares curve fit. Another reason for the superior performance of series expansion is that regularization, as specified in the ASTM, applies a constant amount of regularization throughout the depth. It is clear from Figures 7.11 and 7.12 that the integral and series expansion methods perform similarly near the surface where the stress uncertainty is almost exactly the same. The majority of the difference in error comes from greater depths where the series expansion method performs much better. If regularization is increased with depth it may improve the behaviour of the integral method in this case.

Uncertainty due to hole diameter has negligible effect on the stress uncertainty compared to other, more dominant uncertainty sources considered. The misfit allowed by the use of Tikhonov regularization smooths the stress distribution and greatly reduces the overall uncertainty, but introduces its own considerable uncertainty into the stress results of the integral method. Regularization was not applied to the Zuccarello approach, and as a result it is the most adversely affected by noise in the experimental strain measurements.

7.5 Conclusions

A comprehensive study of three different computational methods for IHD in isotropic materials has been performed on an aluminium alloy 7075 specimen subjected to LSP surface treatment. The use of series expansion was investigated and compared to the widely used unit pulse integral method with regularization and the optimal depth distribution approach of Zuccarello. Contrary to previous research, it was found that series expansion orders greater than 1 can be successfully used with IHD to calculate the residual stress distribution in isotropic materials. The series expansion method was found to remain stable up to at least 8^{th} order in this investigation. The use of significantly more depth increments appears to be the main reason why the current approach is more stable than that presented by Schajer in 1981. Given the technology of the time, it is likely that it was not possible, either experimentally or computationally, to achieve the required number of increments to use orders above 1 such that the solution remained stable. Use of a finer FE mesh and eigenstrain distributions in the forward solution also allowed more accurate determination of the calibration coefficients for the higher order terms. This may have contributed somewhat to the improved numerical stability of the approach used in this chapter. Robust uncertainty estimation is incorporated into the analysis such that the uncertainty and convergence of stress solutions for increasing series expansion orders can be determined and used to find the most appropriate series order to approximate the true residual stress distribution, which greatly improves the results obtained.

There is a strong correlation in calculated stress between the series expansion and integral computational methods. The uncertainty associated with the series expansion method is lower than that associated with the regularized integral method and the Zuccarello approach, especially at greater depths, while providing greater depth resolution. The series expansion method is also more resilient to errors in zero depth detection and noise in the experimental strain measurements than the integral methods. It must be acknowledged, however, that at this stage in its development, the series expansion method requires more effort from practitioners than is required when using the integral method with ASTM E837-13a. For this reason it is important that work be undertaken to normalise the method so that it can be more widely adopted. In addition to normalising the effect of elastic properties, the effects of hole diameter and plate thickness also need to be fully investigated in the case of series expansion so that correction factors can be developed to aid normalisation of the method. This work must be performed with the view to developing a standard, or including this in the ASTM standard. This includes thickness limitations, hole diameter ranges and different types of strain gauges to make it truly applicable for use by other practitioners, in a similar manner to the ASTM standard. Effects such as plasticity, hole eccentricity and hole bottom fillet radius will also need to be addressed in future, just as the integral method was developed over time.

7.6 Contribution to Knowledge

– Although the approach presented in this chapter is based on the work of Schajer from 1981, the preliminary work of Schajer has been extended to demonstrate that series expansion with IHD in isotropic materials remains stable to much higher orders than previously concluded and convergence to a stress solution can be found before instability dominates.

– It is demonstrated that series expansion is a viable computational alternative for IHD in isotropic materials to measure rapidly varying residual stress distributions with reduced RMS uncertainty in stress compared to the regularized integral method and Zuccarello approach.

7.7 Acknowledgements

Thanks must be expressed to the Rental Pool Programme from the National Laser Centre (NLC) at the Council for Scientific and Industrial Research (CSIR), Pretoria, South Africa for the laser shock peening treatment.

8 Methods to Combine Residual Stress Measurements from XRD with IHD

This chapter presents and demonstrates a method to constrain IHD residual stress distributions of series expansion and the regularized integral method with XRD measurements, thereby obtaining full depth stress measurements with reduced uncertainty near the surface. While the integral method is simpler and more practical to use in most situations, incorporating near-surface XRD measurements is more easily achievable using series expansion since it makes use of mathematical functions to describe the stress distribution throughout the depth. This facilitates the constraint of the series to match the XRD data in a mathematically rigorous way. Constrained least-squares error minimisation is employed in the inverse solution to determine the amplitudes of each term in the eigenstrain series that results in a best fit to the measured data, while satisfying the near-surface stress conditions of the XRD measurements. These amplitudes are used with the far-field stress distributions generated by each contributing eigenstrain series to completely define the residual stress distribution. Since the integral method is the industry standard and preferred computational method among practitioners, a method to impose constraints using XRD measurements on the regularized integral method is also proposed. The methods are demonstrated on an aluminium alloy 7075 specimen of 10 mm thickness that underwent LSP treatment. Strong correlation in calculated residual stress distributions was found between the constrained series and regularized integral methods, and with the standard series expansion and regularized integral methods. The constrained methods allows near-surface XRD measurements to be rigorously incorporated into IHD results and as a consequence have reduced stress uncertainty near the surface when compared to both standard series expansion and integral methods. The effect of XRD uncertainty on the overall IHD stress distribution is localised to the near-surface measurements.

This section has been adapted and extended from: **T.C. Smit**, R.G. Reid. A Method to Combine Residual Stress Measurements from XRD and IHD using Series Expansion. *Experimental Mechanics*, 2021, Springer Nature. The published article is available at 10.1007/s11340-021-00719-4. Licensed permission to reuse this content can be found in Appendix I: Springer Nature License Agreements.

8.1 Introduction

It is common practice to use various residual stress measurement methods to complement each other and fully define a through-thickness stress distribution. In the case of improving LSP processing, residual stress at the surface and near the surface are both important to improve resistance to fatigue and crack initiation and propagation. The magnitude and distribution of the LSP-induced compressive stress depends on the combined effects of the laser system, material type, specimen geometry and numerous LSP processing parameters. It is, therefore, important to be able to accurately measure the resulting residual stress distribution so that the LSP processing parameters can be optimised for a particular application. IHD and XRD are two of the most commonly used methods to measure these residual stresses due to their ease of use, low cost and general availability to private entities, research institutions and universities.

While XRD can be used to determine the important surface stresses, it has the disadvantage of insufficient penetration depth to define the stress distribution below the surface. Measurement of the residual stress distribution beneath the surface requires successive layer removal and XRD measurements on each new surface which is cumbersome and expensive and fully destructive so it removes an advantage of the non-destructive XRD technique. This reduces the utility of the method in this situation. In contrast, IHD readily provides stress data to some depth but a physical characteristic of the IHD technique is that it is susceptible to large stress uncertainties near the surface, independent of the stress computation method used. This is primarily due to uncertainty in establishing the the zero depth datum of the measured strain data which similarly affects both series expansion and integral methods. Additionally, low magnitude strain measurement at small depth increments means that any noise error is a high percentage of the actual measurement. This is exacerbated by the hole bottom fillet radius that has and appreciable effect on the first few depth increments in particular. Small depth increments can be used with Tikhonov regularization to capture the LSP-induced residual stress profile that has a steep gradient beneath the surface. The continuity characteristics of the regularized integral solution also allow the interior data to be extrapolated to the surface and, with modern fine-increment drilling, the distance to be extrapolated is small. Series expansion can directly provide an estimate of the residual stress at or near the surface, however, the extrapolated stress distributions are susceptible to high uncertainty near the surface due to the series being less constrained at their ends. Additionally, since the first hole drilling increment accumulates the effects of the stresses within that depth, both integral and series expansion results are effectively slightly removed from the exact surface. To overcome this limitation of IHD, a method of incorporating near-surface XRD measurements into a set of IHD measurements is required.

Chapter 7 demonstrated that series expansion remains stable up to high orders when measuring a rapidly varying stress distribution provided that a sufficient number of depth increments are used

and convergence of the solution is found by comparing the stress distributions and associated uncertainties of a number of series orders. Series expansion achieved strong correlation, with reduced RMS uncertainty, to the regularized integral method. This chapter explores another benefit of series expansion that is more easily achievable than with the conventional approach. When using series expansion, mathematical functions describe the stress distribution throughout the depth of the specimen. This allows the imposition of magnitude and/or slope constraints on the stress solution to any known data at any depth through the thickness of the specimen, thereby allowing incorporation of other residual stress measurements into the least-squares inverse solution of IHD. While the published method of imposing constraints on the stress solution using series expansion forms the basis of this chapter, a novel means to impose constraints on the regularized solution of the integral method is also proposed and demonstrated. This is due to the integral method being the preferred computational method among practitioners and their familiarity with the integral method due to the ASTM standard. The proposed method will form the basis of a companion publication that will be submitted to *Experimental Mechanics* in the near future under the working title: *Imposition of Constraints on the Regularized Integral Method of IHD*.

8.2 Theoretical

8.2.1 Imposition of Constraints on the Series Expansion Method

The series expansion method allows for a constrained least-squares solution to determine the residual stress distribution subject to multiple magnitude and/or slope constraints. To constrain the series expansion stress solution to known stress magnitudes and/or slopes, $\mathbf{m}$ and $\mathbf{s}$ respectively, at any depth through the thickness and in any direction, the stress solution and gradient at these depths, $\boldsymbol{\sigma}_z$ and $\frac{d}{dz}\,\boldsymbol{\sigma}_z$, must be equal to the known stresses and slopes. In vector-matrix form:

$$\boldsymbol{\sigma}_z = \mathbf{m} \tag{8.1}$$

$$\frac{d}{dz}\,\boldsymbol{\sigma}_z = \mathbf{s} \tag{8.2}$$

Equations (8.1) and (8.2) can be combined and formulated in terms of the amplitude vector, $\mathbf{a}$, which contains the amplitudes of each applied eigenstrain function in the forward solution, and a constraint matrix $\mathbf{Q}$:

$$\mathbf{Q}\,\mathbf{a} = \mathbf{d} \tag{8.3}$$

Matrix $\mathbf{Q}$ is extracted from the stress matrix, $\mathbf{S}$, at depths where magnitude and slope constraints must be imposed. Rows representing constraint equations can simply be added to $\mathbf{Q}$ as required, with the corresponding imposed constraint added to vector $\mathbf{d}$. When considering all stress components, $\mathbf{Q}$ comprises rows representing each of the stress components:

$$\mathbf{Q} = \begin{bmatrix} S_{m_{x x_0}} & \cdots & S_{m_{x y_0}} & \cdots & S_{m_{x x y_0}} & \cdots & S_{m_{x_{j_n}}} \\ S_{m_{y x_0}} & \cdots & S_{m_{y y_0}} & \cdots & S_{m_{y x y_0}} & \cdots & S_{m_{y_{j_n}}} \\ S_{m_{x y x_0}} & \cdots & S_{m_{x y y_0}} & \cdots & S_{m_{x y x y_0}} & \cdots & S_{m_{x y_{j_n}}} \\ \vdots & \vdots & \vdots & \vdots & \vdots & \vdots & \vdots \\ \frac{d}{dz}\left(S_{m_{x x_0}}\right) & \cdots & \frac{d}{dz}\left(S_{m_{x y_0}}\right) & \cdots & \frac{d}{dz}\left(S_{m_{x x y_0}}\right) & \cdots & \frac{d}{dz}\left(S_{m_{x_{j_n}}}\right) \\ \frac{d}{dz}\left(S_{m_{y x_0}}\right) & \cdots & \frac{d}{dz}\left(S_{m_{y y_0}}\right) & \cdots & \frac{d}{dz}\left(S_{m_{y x y_0}}\right) & \cdots & \frac{d}{dz}\left(S_{m_{y_{j_n}}}\right) \\ \frac{d}{dz}\left(S_{m_{x y x_0}}\right) & \cdots & \frac{d}{dz}\left(S_{m_{x y y_0}}\right) & \cdots & \frac{d}{dz}\left(S_{m_{x y x y_0}}\right) & \cdots & \frac{d}{dz}\left(S_{m_{x y_{j_n}}}\right) \\ \vdots & \vdots & \vdots & \vdots & \vdots & \vdots & \vdots \end{bmatrix} \tag{8.4}$$

where m is the depth of an imposed constraint, j is the component of eigenstrain, and n is the order of the applied eigenstrain.

The imposition of constraints onto the series solution means that the coefficients of the amplitude vector are not all independent. It is necessary, therefore, to split the amplitude vector into independent and dependent terms. The amplitude vector, $\mathbf{a}$, and matrix $\mathbf{Q}$ are therefore decomposed into $\hat{\mathbf{a}}$ and $\bar{\mathbf{a}}$, and $\mathbf{Q}_A$ and $\mathbf{Q}_B$, respectively:

$$\mathbf{a} = \begin{Bmatrix} \hat{\mathbf{a}} \\ \bar{\mathbf{a}} \end{Bmatrix}, \quad \mathbf{Q} = [\mathbf{Q}_A \ : \ \mathbf{Q}_B] \tag{8.5}$$

where $\hat{\mathbf{a}}$ represents the vector of independent amplitude coefficients, $\bar{\mathbf{a}}$ represents the vector of dependent amplitude coefficients, and $\mathbf{Q}_B$ is a square invertible matrix. Equation (8.3) can now be rewritten as:

$$\begin{aligned} \mathbf{Q}_A\,\hat{\mathbf{a}} + \mathbf{Q}_B\,\bar{\mathbf{a}} &= \mathbf{d} \\ \mathbf{Q}_B\,\bar{\mathbf{a}} &= -\mathbf{Q}_A\,\hat{\mathbf{a}} + \mathbf{d} \\ \bar{\mathbf{a}} &= -{\mathbf{Q}_B}^{-1}\,\mathbf{Q}_A\,\hat{\mathbf{a}} + {\mathbf{Q}_B}^{-1}\,\mathbf{d} \end{aligned} \tag{8.6}$$

Therefore:

$$\begin{aligned} \mathbf{a} &= \begin{bmatrix} \mathbf{I} \\ -{\mathbf{Q}_B}^{-1}\,\mathbf{Q}_A \end{bmatrix} \hat{\mathbf{a}} + \begin{Bmatrix} \mathbf{0} \\ {\mathbf{Q}_B}^{-1}\,\mathbf{d} \end{Bmatrix} \\ &= \mathbf{G}\,\hat{\mathbf{a}} + \mathbf{h} \end{aligned} \tag{8.7}$$

The experimental strain vector, $\boldsymbol{\epsilon}_{meas}$, is used with the matrix of calibration coefficients in a constrained least-squares inverse solution to determine the vector of independent amplitude coefficients, $\hat{\mathbf{a}}$. In vector-matrix form:

$$\begin{aligned} \boldsymbol{\epsilon}_{meas} &= \mathbf{C}\,\mathbf{a} \\ \boldsymbol{\epsilon}_{meas} &= \mathbf{C}\,(\mathbf{G}\,\hat{\mathbf{a}} + \mathbf{h}) \\ \mathbf{G}^T\,\mathbf{C}^T\,(\boldsymbol{\epsilon}_{meas} - \mathbf{C}\,\mathbf{h}) &= \mathbf{G}^T\,\mathbf{C}^T\,\mathbf{C}\,\mathbf{G}\,\hat{\mathbf{a}} \end{aligned} \tag{8.8}$$

$$\hat{\mathbf{a}} = \left(\mathbf{G}^T\,\mathbf{C}^T\,\mathbf{C}\,\mathbf{G}\right)^{-1}\,\mathbf{G}^T\,\mathbf{C}^T\,(\boldsymbol{\epsilon}_{meas} - \mathbf{C}\,\mathbf{h}) \tag{8.9}$$

Finally, the amplitude vector, $\mathbf{a}$, containing the amplitudes of the applied eigenstrain distributions that best match the experimental strain response, while ensuring that the constraints imposed on the stress solution are satisfied can be found using equation (8.7)[ii]. The calculated amplitude vector is used with the stress matrix, $\mathbf{S}$, to determine the residual stress distributions using equation (5.12). As with standard series expansion, the use of a least-squares approach reduces sensitivity to strain measurement errors and subsequent uncertainty in calculated stress. To achieve a robust least-squares fit, the number of terms in $\boldsymbol{\epsilon}_{meas}$ must be significantly greater than in $\hat{\mathbf{a}}$. The most appropriate series order can be determined from the size and convergence of the associated uncertainties in the residual stress distributions as in section 5.3.5.

In the context of this chapter, to constrain the near-surface stress solution of series expansion with IHD to the measurements obtained from XRD, $\boldsymbol{\sigma}_{XRD}$, the approach above can be simplified to:

$$\mathbf{d} = \boldsymbol{\sigma}_{XRD} \tag{8.10}$$

and

$$\mathbf{Q} = \mathbf{S}_{XRD} = \begin{bmatrix} S_{1_{x x_0}} & \cdots & S_{1_{x y_0}} & \cdots & S_{1_{x x y_0}} & \cdots & S_{1_{x_{j_n}}} \\ S_{1_{y x_0}} & \cdots & S_{1_{y y_0}} & \cdots & S_{1_{y x y_0}} & \cdots & S_{1_{y_{j_n}}} \\ S_{1_{x y x_0}} & \cdots & S_{1_{x y y_0}} & \cdots & S_{1_{x y x y_0}} & \cdots & S_{1_{x y_{j_n}}} \end{bmatrix} \tag{8.11}$$

Equations (8.9) and (8.7) can then be used to enforce suitable relationships between the amplitude coefficients of series expansion such that the resultant stress distributions near the surface match the XRD measurements.

[ii] Imposing constraints on the stress solution is not limited to only a single application of series expansion. A similar approach to that described in this section has also been developed to imposed constraints on separate series, applied to different regions of a continuous material, to ensure magnitude and/or slope continuity at the interface between these regions. By this means, series expansions in separate regions are fully incorporated into a single least-squares solution and rigorously combined. Application of separate series within a continuous material may be necessary if the residual stress distribution, and accompanying IHD strain distribution, is too complex to describe by a single high order solution before instability dominates. Therefore, there is scope to use separate, lower order series to describe a complex residual stress distribution, and tie these separate series together by constraining both slope and magnitude at the interfaces between separate series. Separate series expansion may also be necessary if an isotropic material has distinct layers with a interface between them such as in SLM AM. In this case, the residual stress distribution may exhibit sharp turning points at the interfaces between layers that would not be well represented by a single series, even one of high order and instability could dominate. While the underlying mathematics for application of separate constrained series in SLM AM plates have been fully developed and tested, practical issues around the exact position and thickness of the weld interface between deposit layers, and plasticity effects due to the magnitude of residual stresses near the surface have prevented publication of this approach and inclusion in this thesis.

8.2.2 Imposition of Constraints on the Regularized Integral Method

To enable concise discussion, the method to impose constraints on the regularized solution is only shown for the isotropic (equi-biaxial) stress, $\boldsymbol{\sigma}_p$. The approach for the 45° shear stress, $\boldsymbol{\sigma}_q$, and the x-y shear stress, $\boldsymbol{\sigma}_t$, is the same. The standard regularized integral solution for $\boldsymbol{\sigma}_p$ is given by equation (8.12).

$$\left(\bar{\mathbf{A}}^T\,\bar{\mathbf{A}} + \alpha_p\,\mathbf{L}^T\,\mathbf{L}\right)\boldsymbol{\sigma}_p = \frac{E}{1+\nu}\,\bar{\mathbf{A}}^T\,\mathbf{p} \tag{8.12}$$

To impose multiple constraints on the regularized integral solution at any depth increments, the stress solution at these depths must be equal to the known stresses, $\mathbf{d}$. Vector $\mathbf{d}$ has the same length as $\boldsymbol{\sigma}_p$ and contains the known stresses at the relevant depth increments and zeros at the unconstrained increments. For example, if constraints are imposed on the 1st, 2nd and 4th depth increments, the constraint equations are given by:

$$\begin{aligned} \sigma_{p1} &= d_1 \\ \sigma_{p2} &= d_2 \\ \sigma_{p4} &= d_4 \end{aligned} \tag{8.13}$$

Which can be represented in vector-matrix form by:

$$\begin{bmatrix} 1 & 0 & 0 & 0 & \cdots & 0 \\ 0 & 1 & 0 & 0 & \cdots & 0 \\ 0 & 0 & 0 & 1 & \cdots & 0 \end{bmatrix} \begin{Bmatrix} \sigma_{p1} \\ \sigma_{p2} \\ \sigma_{p3} \\ \sigma_{p4} \\ \vdots \\ \sigma_{pn} \end{Bmatrix} = \begin{bmatrix} 1 & 0 & 0 & 0 & \cdots & 0 \\ 0 & 1 & 0 & 0 & \cdots & 0 \\ 0 & 0 & 0 & 1 & \cdots & 0 \end{bmatrix} \begin{Bmatrix} d_1 \\ d_2 \\ 0 \\ d_4 \\ \vdots \\ 0 \end{Bmatrix}$$

$$\mathbf{B}\,\boldsymbol{\sigma}_p = \mathbf{B}\,\mathbf{d} \tag{8.14}$$

where n is the number of depth increments.

The standard regularized solution is re-formulated as a constrained optimisation problem:

$$\begin{aligned} &\text{minimize} && f\left(\boldsymbol{\sigma}_p\right) = \left\|\mathbf{A}\boldsymbol{\sigma}_p - \mathbf{y}\right\|^2 \\ &\text{subject to} && \mathbf{b}_i\,\boldsymbol{\sigma}_p = \mathbf{b}_i\,\mathbf{d}, \qquad i = 1, \ldots, k \end{aligned} \tag{8.15}$$

where $\mathbf{b}_i$ is a vector containing the i^{th} row of the constraint matrix $\mathbf{B}$, k is the number of imposed constraints and:

$$\mathbf{A} = \left(\bar{\mathbf{A}}^T\bar{\mathbf{A}} + \alpha_P\mathbf{L}^T\mathbf{L}\right) \tag{8.16}$$

$$\mathbf{y} = \frac{E}{1+\nu}\,\bar{\mathbf{A}}^T\mathbf{p} \tag{8.17}$$

A Lagrangian function, $g\left(\boldsymbol{\sigma}_p, \lambda\right)$, with Lagrange multipliers, $\lambda_1, \ldots, \lambda_k$, can then be formed:

$$g\left(\boldsymbol{\sigma}_p, \lambda\right) = f\left(\boldsymbol{\sigma}_p\right) + \lambda_1 \left(\mathbf{b}_1\, \boldsymbol{\sigma}_p - \mathbf{b}_1\, \mathbf{d}\right) + \cdots + \lambda_k \left(\mathbf{b}_k\, \boldsymbol{\sigma}_p - \mathbf{b}_k\, \mathbf{d}\right) \tag{8.18}$$

Lagrange multipliers correspond to 'forces' needed to enforce the constraints. For an optimal solution of the Lagrangian function, $g\left(\hat{\boldsymbol{\sigma}}_p, \boldsymbol{\lambda}\right)$, the Karush-Kuhn-Tucker (KKT) conditions require that the gradient of $g\left(\hat{\boldsymbol{\sigma}}_p, \boldsymbol{\lambda}\right)$ be zero:

$$\begin{aligned}
&\frac{\partial g}{\partial \hat{\sigma}_{pi}}\left(\hat{\boldsymbol{\sigma}}_p, \boldsymbol{\lambda}\right) = 0, \quad i = 1, \ldots, n \\
&\frac{\partial g}{\partial \hat{\sigma}_{pi}}\left(\hat{\boldsymbol{\sigma}}_p, \boldsymbol{\lambda}\right) = 2 \sum_{j=1}^{n} \left(\mathbf{A}^T\, \mathbf{A}\right)_{ij} \hat{\sigma}_{pj} - 2\left(\mathbf{A}^T\, \mathbf{y}\right)_i + \sum_{j=1}^{k} \lambda_j\, \mathbf{b}_i = 0
\end{aligned} \tag{8.19}$$

$$\begin{aligned}
&\frac{\partial g}{\partial \lambda_i}\left(\hat{\boldsymbol{\sigma}}_p, \boldsymbol{\lambda}\right) = 0, \quad i = 1, \ldots, k \\
&\frac{\partial g}{\partial \lambda_i}\left(\hat{\boldsymbol{\sigma}}_p, \boldsymbol{\lambda}\right) = \mathbf{b}_i\, \hat{\boldsymbol{\sigma}}_p - \mathbf{b}_i\, \mathbf{d} = 0
\end{aligned} \tag{8.20}$$

where $\hat{\boldsymbol{\sigma}}_p$ is the regularized optimal solution that satisfies the imposed constraints and $\boldsymbol{\lambda}$ is a vector containing the Lagrange multipliers required to enforce the constraints.

Equation (8.20) is already satisfied by the constrained optimisation problem in equation (8.15). Equation (8.19) and (8.20) can be expressed in vector-matrix form by equation (8.21) and (8.22), respectively.

$$\begin{aligned}
&\frac{\partial g}{\partial \hat{\boldsymbol{\sigma}}_p}\left(\hat{\boldsymbol{\sigma}}_p, \boldsymbol{\lambda}\right) = 2\left(\mathbf{A}^T\, \mathbf{A}\right)\hat{\boldsymbol{\sigma}}_p - 2\left(\mathbf{A}^T\, \mathbf{y}\right) + \mathbf{B}\, \boldsymbol{\lambda} = 0 \\
&2\left(\mathbf{A}^T\, \mathbf{A}\right)\hat{\boldsymbol{\sigma}}_p + \mathbf{B}\, \boldsymbol{\lambda} = 2\left(\mathbf{A}^T\, \mathbf{y}\right)
\end{aligned} \tag{8.21}$$

$$\begin{aligned}
&\frac{\partial g}{\partial \boldsymbol{\lambda}}\left(\hat{\boldsymbol{\sigma}}_p, \boldsymbol{\lambda}\right) = \mathbf{B}\, \hat{\boldsymbol{\sigma}}_p - \mathbf{B}\, \mathbf{d} = 0 \\
&\mathbf{B}\, \hat{\boldsymbol{\sigma}}_p = \mathbf{B}\, \mathbf{d}
\end{aligned} \tag{8.22}$$

The KKT conditions are a set of non-linear equations in the original unknowns and the multipliers that characterise constrained stationary points. In matrix form, the KKT system (saddle point system) is given by equation (8.23) [iii].

$$\begin{bmatrix} 2\mathbf{A}^T\, \mathbf{A} & \mathbf{B}^T \\ \mathbf{B} & \mathbf{0} \end{bmatrix} \begin{Bmatrix} \hat{\boldsymbol{\sigma}}_p \\ \boldsymbol{\lambda} \end{Bmatrix} = \begin{Bmatrix} 2\mathbf{A}^T\, \mathbf{y} \\ \mathbf{B}\, \mathbf{d} \end{Bmatrix} \tag{8.23}$$

The simplest case is to constrain the stress in the first depth increment to a known value as is required in the context of this chapter. To constrain the regularized integral solution to near-surface XRD

[iii] The Lagrange multiplier and KKT approach presented in this section can also be applied to the constrained series expansion calculations presented in section 8.2.1. However, neither method is more or less complex in its application and there are no obvious benefits of one method over the other.

data, the XRD depth must be included in the calibration matrices, $\bar{\mathbf{A}}$ and $\bar{\mathbf{B}}$, with appropriate coefficients for this depth increment and stress application depth for all subsequent increments. A row for the depth increment and a column for the stress application depth corresponding to the XRD depth must be added to the calibration matrices. In this chapter, the first depth increment of the constant step calibration matrices is split into two smaller depths to ensure that the mid-step depth of the first increment aligns with the XRD depth. The coefficients corresponding to the two smaller depth increments and stress application depths can be obtained from the constant step cumulative calibration coefficients [93], similar to the Zuccarello approach. The XRD depth must also be included in the combination strain vectors ($\mathbf{p}$, $\mathbf{q}$ and $\mathbf{t}$).

Since the depth distribution used is no longer uniform, the tri-diagonal second derivative matrix, $\mathbf{L}$, must be modified [87]. In this case, only the second row of matrix $\mathbf{L}$ has to be modified to have the following tri-diagonal structure:

$$\frac{-2\,(W/n)^2}{(z_{i+1}-z_{i-1})\,(z_i-z_{i-1})} \qquad \frac{-2\,(W/n)^2}{(z_i-z_{i-1})\,(z_{i+1}-z_i)} \qquad \frac{-2\,(W/n)^2}{(z_{i+1}-z_i)\,(z_{i+1}-z_{i-1})} \tag{8.24}$$

where W is the final hole depth and z_i is the hole depth at increment i.

To constrain the first depth increment to XRD data, the constraint matrix, $\mathbf{B}$, simply becomes a row vector where all entries are zero except for the first entry of unity. All entries except for the first entry of the known stress vector, $\mathbf{d}$, are also zero and the first entry is the XRD stress measurement. Equation (8.23) is then used to find the optimal stress distribution that satisfies Tikhonov regularization and the imposed constraints. The amount of regularization that is applied can be optimised iteratively using the Morozov Discrepancy Principle [98].

8.3 Demonstration of Procedure

8.3.1 Experimental

8.3.1.1 Specimen and LSP

A rolled aluminium alloy 7075-T651 plate was reduced from 15 mm thickness to 10 mm by machining 1 mm from the top face of the plate and 4 mm from the bottom before preparing individual specimens of 60 mm $\times$ 60 mm. The mechanical properties and the chemical composition of aluminium alloy 7075-T651 are provided in Table 7.1. LSP treatment was applied to the upper face of the specimen as described in section 7.3.1. The specifications of the laser and the parameters used during LSP are provided in Table 7.2.

8.3.1.2 XRD

Laboratory XRD was used to obtain the near-surface residual stresses to constrain the IHD measurements. The $\sin^2\psi$ method [67] was performed using a Proto iXRD (Proto Manufacturing Inc.,Taylor, Michigan USA) instrument at the CSIR. Lattice spacing of the $\{311\}$ planes was measured for 7 angles between -27° and +27° using Cr-Kα radiation with a wavelength of 2.291 Å at a Bragg angle of approximately 139°. Measurements were taken using a 2 mm round aperture at 0°, 45°, and 90° with respect to the LSP raster pattern to obtain the in-plane stress-tensor. At each tilt angle, the sample was oscillated by $\pm 3°$ in ψ to improve counting statistics and reduce the effect of large grain sizes and texture in the aluminium specimen. The residual stresses were calculated for plane stress conditions using X-ray elastic constants of $^1/_2S_2$ = 19.54 $\times$ 10^{-6} MPa^{-1} and S_1 = -5.11 $\times$ 10^{-6} MPa^{-1} for the $\{311\}$ lattice plane. The XRD information depth was estimated to be 10.5 µm [195].

8.3.1.3 IHD

Incremental hole-drilling was conducted as per section 7.3.1. A total of 47 depth increments of 25 µm, including zero depth, up to a maximum depth of 1.15 mm is used in the analysis of the series expansion methods. The hole diameter was measured after IHD as 1.78 mm. The experimentally measured strain variations at the x, y and $45°$ strain gauge locations are presented in Figure 8.1.

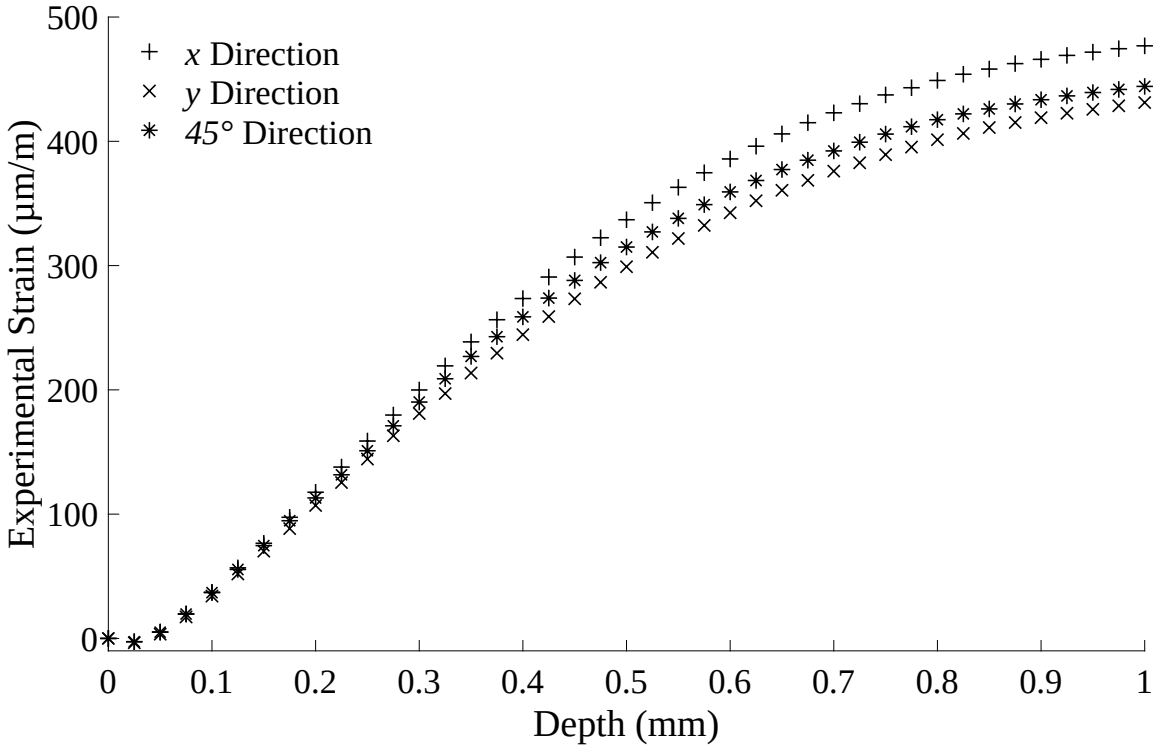


Figure 8.1: Strain variation with depth in the x, y and $45°$ strain gauge directions

8.3.2 Computational

FE calculations were conducted as per section 7.3.2. The specimen was modelled using 124 HEX8 type 3D elements through the thickness, 24 elements of 50 μm height through the first 1.2 mm from the surface and 100 elements through the remaining thickness with linearly increasing element height towards the bottom of the plate. For illustrative purposes, the stress distribution in the x-direction due to eigenstrain generated by a 2nd order temperature variation in the x-direction is presented in Figure 8.2. The mesh around the hole, on the top surface, and the position of the strain gauge grid locations (highlighted) are also presented. Spline interpolation was used, as in section 7.3.2, to double the number of coefficients in $\mathbf{C}$ to ensure that $\boldsymbol{\epsilon}_{meas}$ and $\mathbf{C}$ follow the same depth distribution as required by equation (5.10). FE models with hole diameters between 1.70 mm and 1.90 mm, with 0.05 mm spacing increments, were used such that calibration matrices for any experimental hole diameter within this range can be found by interpolation.

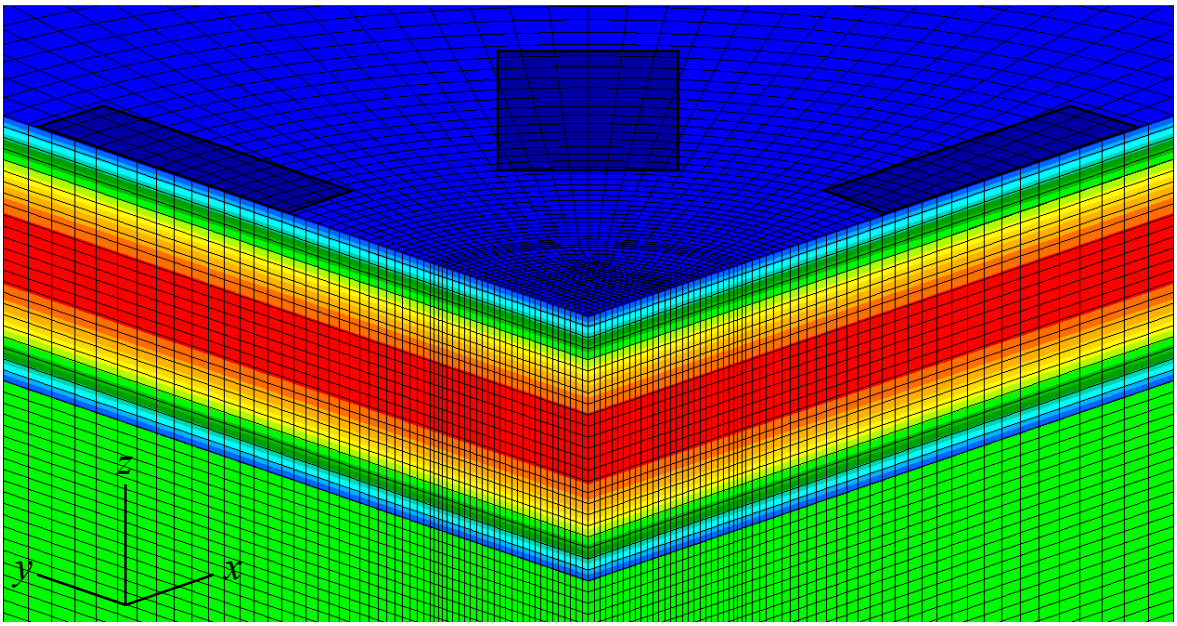


Figure 8.2: σ_x distribution generated by 2nd order eigenstrain in the x-direction, including the strain gauge grid locations

The FE model used for series expansion was also used to determine the calibration matrices for the integral method as per section 7.3.2. For the integral method, every second experimental strain datum was used such that the 50 μm depth increments correspond with the calculated $\bar{\mathbf{A}}$ and $\hat{\mathbf{B}}$ matrices from the FE model.

In the case of the constrained integral method, the first 50 μm depth increment of the constant step calibration matrices is split into two smaller depth increments of 21 μm and 29 μm, respectively. This ensures that the mid-step depth of the first increment aligns with the XRD depth. Spline interpolation was used to find the combination strains at the XRD depth.

8.3.3 Propagation of Uncertainties

Uncertainty propagation was conducted as described in section 5.3.3 and 7.3.3. Only the predominant experimental and computational uncertainty sources are considered in this chapter, provided in Table 8.1. Although other uncertainty sources such as the uncertainty in measured hole diameter and hole offset, for example, can be easily incorporated, it has been demonstrated in Chapter 6 and 7, respectively, that their effects on the stress uncertainty are negligible compared to the uncertainty sources considered here. Ten thousand Monte Carlo trials were simulated for each order of the constrained and standard series expansion and integral methods.

Table 8.1: Uncertainty sources and their assigned probability density functions

x_i	Description	$p(x_i)$	Type	Nominal value, uncertainty
$\sigma_{x_{XRD}}$	Stress in the x-direction from XRD measurements	Normal	B	60.4 MPa, 33.5 MPa
$\sigma_{y_{XRD}}$	Stress in the y-direction from XRD measurements	Normal	B	70.4 MPa, 15.4 MPa
$\tau_{xy_{XRD}}$	Shear stress from XRD measurements	Normal	B	-58.5 MPa, 38.7 MPa
E	Young's Modulus	Normal	B	71700 MPa, 3%
ν_{12}	Poisson's ratio	Normal	B	0.33, 3%
z_i	Incremental depths	Rectangular	B	25 µm, 0.5 µm
z_0	Zero depth	Rectangular	B	0 µm, 10 µm
ϵ_m	Indicated experimental strain	Normal	B	Figure 8.1, 1.6%
ϵ_{noise}	Experimental noise	Normal	A	Figure 8.1, 1 µm/m
FE	Finite element calculations	Normal	B	0, 2%

XRD measurement uncertainty reported by the Proto software only includes the estimated uncertainty associated with statistical errors and the elliptical least-squares fit of the $\sin^2\psi$ plot. The larger than usual uncertainty is due to the adverse effects of large grain sizes in aluminium alloy 7075-T651, and the texture and high stress gradient near the surface due to the effects of the LSP process on the aluminium material [66].

Uncertainty in IHD measurements were included in each Monte Carlo trial as per sections 5.3.3 and 7.3.3. The strain vector, $\boldsymbol{\epsilon}_{meas}$, calibration matrix, $\mathbf{C}$, stress matrix, $\mathbf{S}$ and XRD measurements of each Monte Carlo trial were used with equations (8.9), (8.7) and (5.12) for the constrained series method and equations (5.10) and (5.12) for standard series expansion to determine the stress distribution for that trial. The combination strains were calculated from the strain vector, $\boldsymbol{\epsilon}_{meas}$ of each Monte Carlo trial and used with calibration matrices, $\bar{\mathbf{A}}$ and $\bar{\mathbf{B}}$, and XRD measurements of that trial in equations (8.16), (8.17) and (8.23) to calculated the stress distributions of the constrained integral method. The combination strains and calibration matrices of each Monte Carlo trial were used with equations (2.6)-(2.8) in the case of the standard integral method.

8.3.4 Selection of Series Order

As the order of constrained series expansion is increased, the least-squares fit to the experimental strain data is improved as can be seen in Figure 8.3 for the x-direction strain gauge, where a 4^{th} order series expansion is not able to accurately fit the experimental strain data and a higher order series must be used. Although a 6^{th} order series is able to fit the experimental strain data fairly accurately, this alone does not guarantee convergence to a stress solution and higher order series may be required. In this instance, both 9^{th} and 10^{th} order series are able to accurately fit the experimental strain data and can be said to have converged. Since higher order series can become unstable, however, it is crucial that a series order that can fully describe the actual residual stress distribution is found before instabilities become apparent. The least-squares fit of standard series expansion to the experimental strain data is shown in Figure 8.4 for the x-direction strain gauge, where 4^{th} and 8^{th} order series expansions are applied, respectively. It is interesting to note that the 4^{th} order fit in Figure 8.3 is improved near the surface compared to Figure 8.4 due to the imposed constraints, but this adversely affects the fit to the strain data at greater depths.

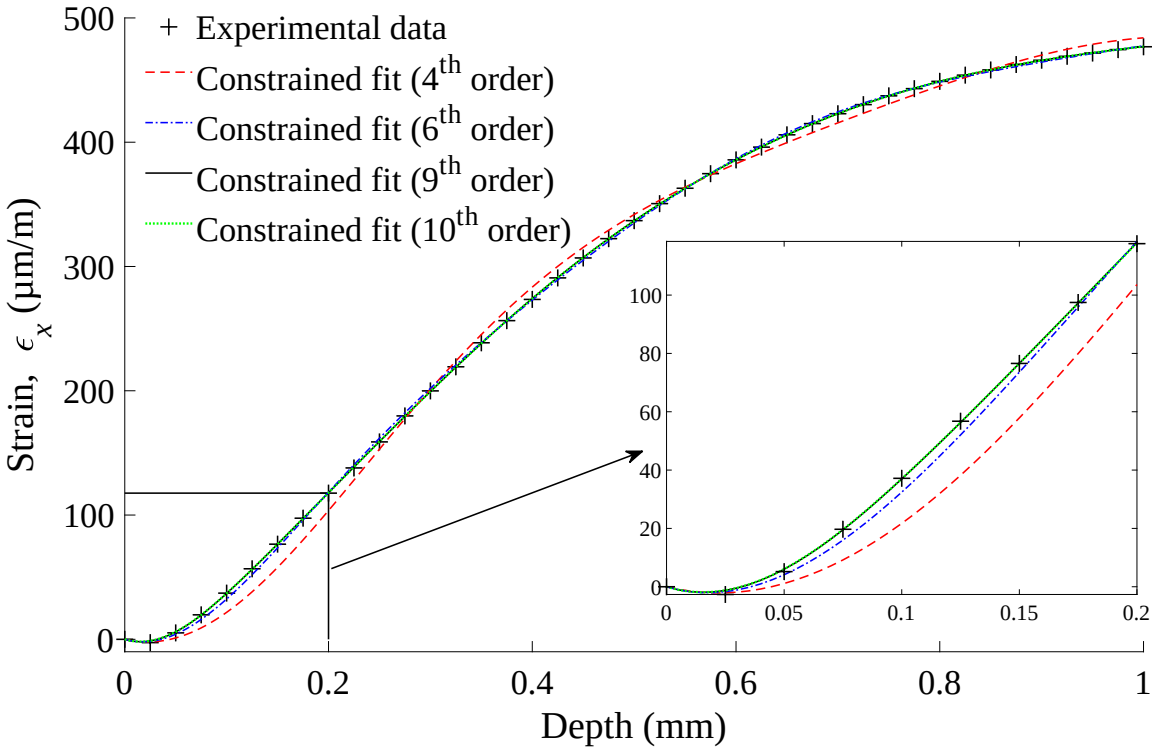


Figure 8.3: Constrained least-squares fits to strain data in the x-direction using 4^{th}, 6^{th}, 9^{th} and 10^{th} order series

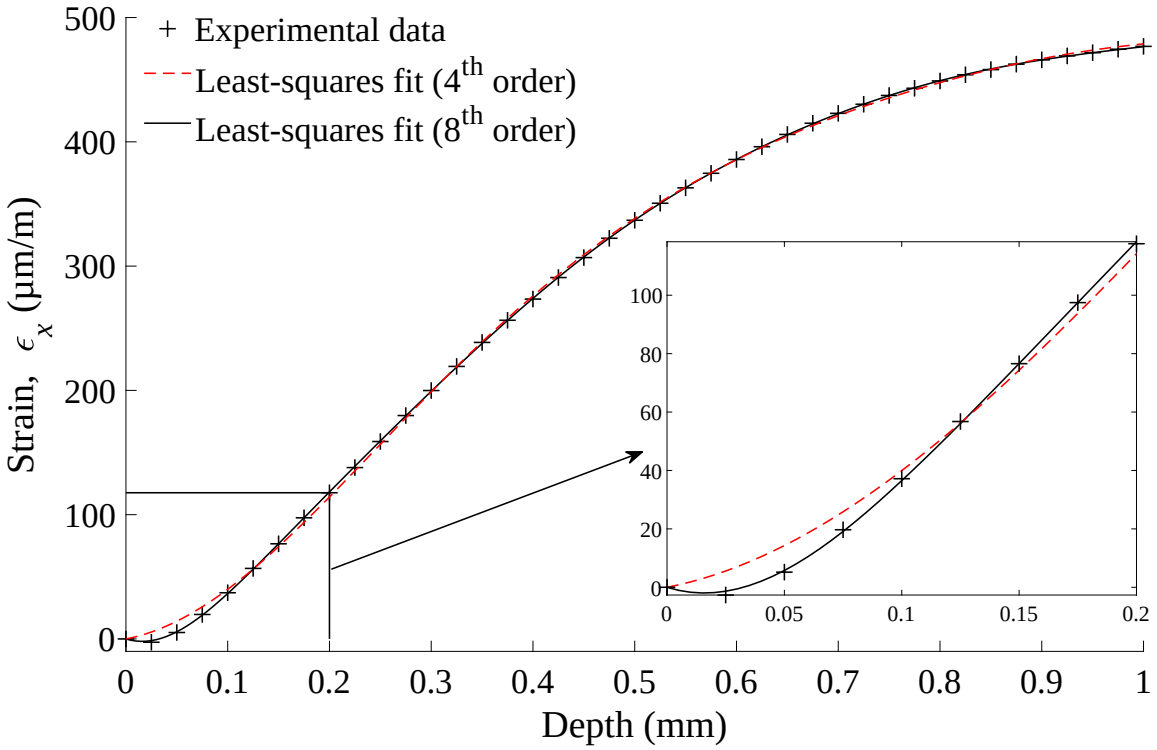


Figure 8.4: Least-squares fits to strain data in the x-direction using 4th and 8th order series

Series order selection is done as in section 5.3.5. The calculated stress distribution and associated uncertainty in the x-direction for orders 2 to 15 of the constrained series method are shown in Figure 8.5. The uncertainty bounds in the y-direction for orders 2 to 15 are similar to those in the x-direction and the corresponding figure is therefore omitted in the interest of brevity. All stress uncertainty bounds in Figure 8.5 are plotted using light grey such that convergence of a number of orders gives rise to darker areas. The remaining light grey areas correspond to low order series, 2nd to 5th order, that are unable to describe the actual stress distribution, and to higher order series where the uncertainty bounds start to diverge due to increasing instability. It is clear in Figure 8.5 that as the series order increases from 2 to 5, the series converge towards the actual residual stress distribution. The 6th order series has the lowest total uncertainty, as can be seen in Figure 8.6, but it has not converged and can therefore not be selected, similarly for the 7th and 8th order series. The orders 9 to 11 have converged and the 9th order series is selected as the best solution for this experimental data set as it has the lowest total RMS stress uncertainty of the series orders that have converged, as shown in Figure 8.6. The stress uncertainty of the integral method is also shown in Figure 8.6 for comparison purposes. Interestingly, the best series order for use in the standard series expansion method is one lower than that in the constrained solution. This difference arises because the imposition of constraints removes a degree of freedom from the solution in each stress direction and so an additional term is required in the constrained solution to get the same descriptive capability.

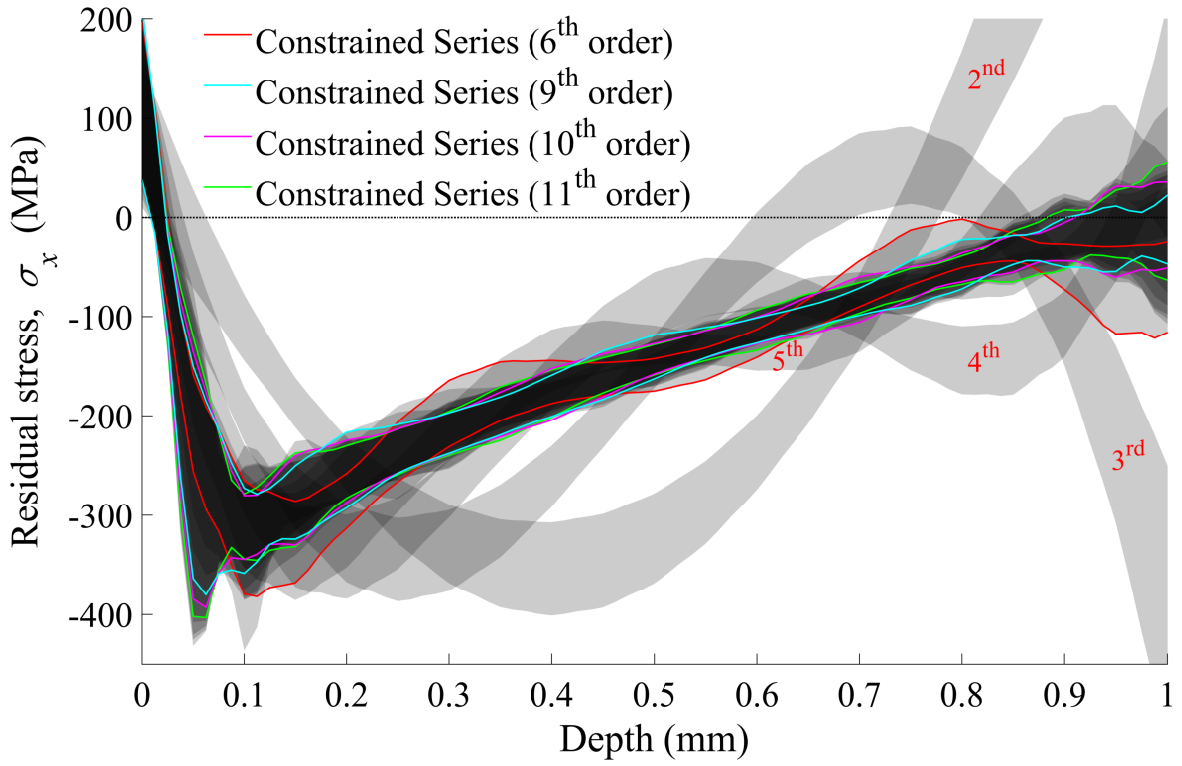


Figure 8.5: Overlap of the uncertainty bounds in σ_x for 2nd to 15th order series

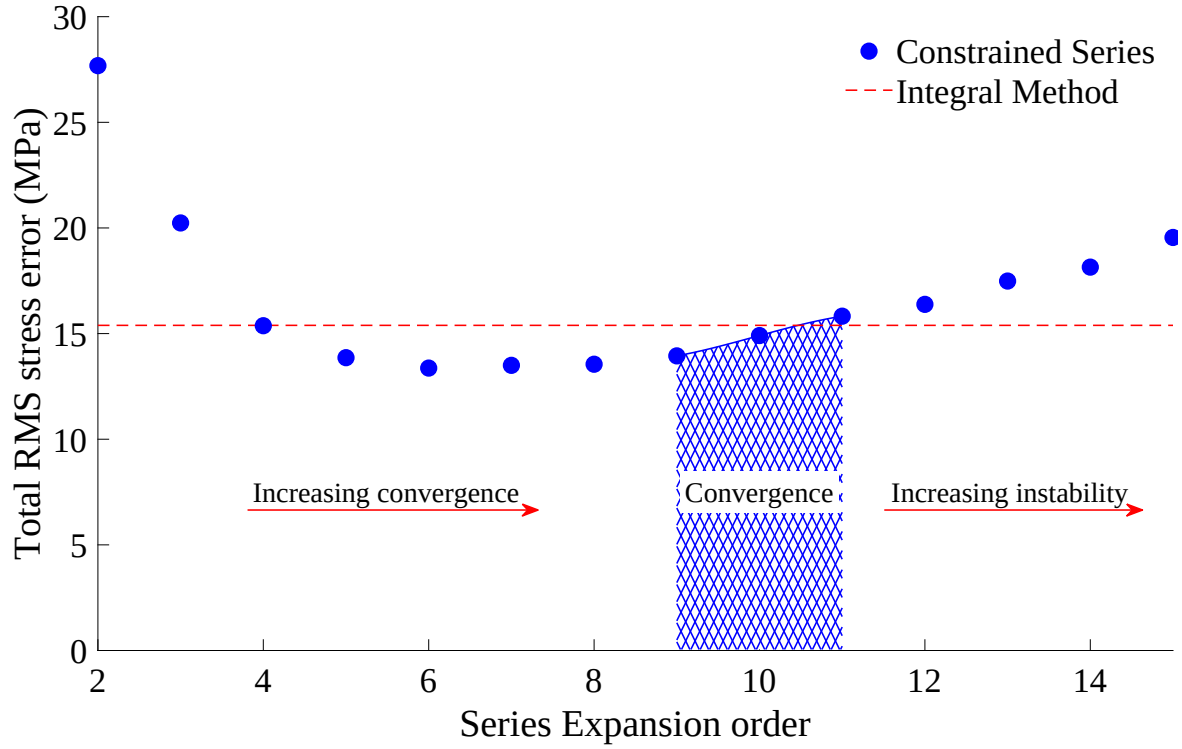


Figure 8.6: Variation and convergence of total RMS stress uncertainty for 2nd to 15th order series

8.4 Results and Discussion

Results of the published method to impose constraints using near-surface XRD data on series expansion are discussed first. Results of the proposed approach to impose constraints on the regularized integral method are discussed at the end of this section.

The least-squares fits of the constrained 9th order series to the experimental strain data are shown in Figure 8.7 with associated uncertainties. The strain uncertainty due to the inability of the constrained 9th order series to exactly match the measured strain data is included in this figure. The calculated stress distributions and associated uncertainties of the constrained 9th order series are shown in Figure 8.8. As expected, the LSP-induced residual stress distributions in the x and y directions are similar and the shear stress is close to zero. It is clear that a large tensile stress exists near the surface and that the combination of LSP parameters and specimen thickness used in this particular study did not result in the desired compressive stress on the surface.

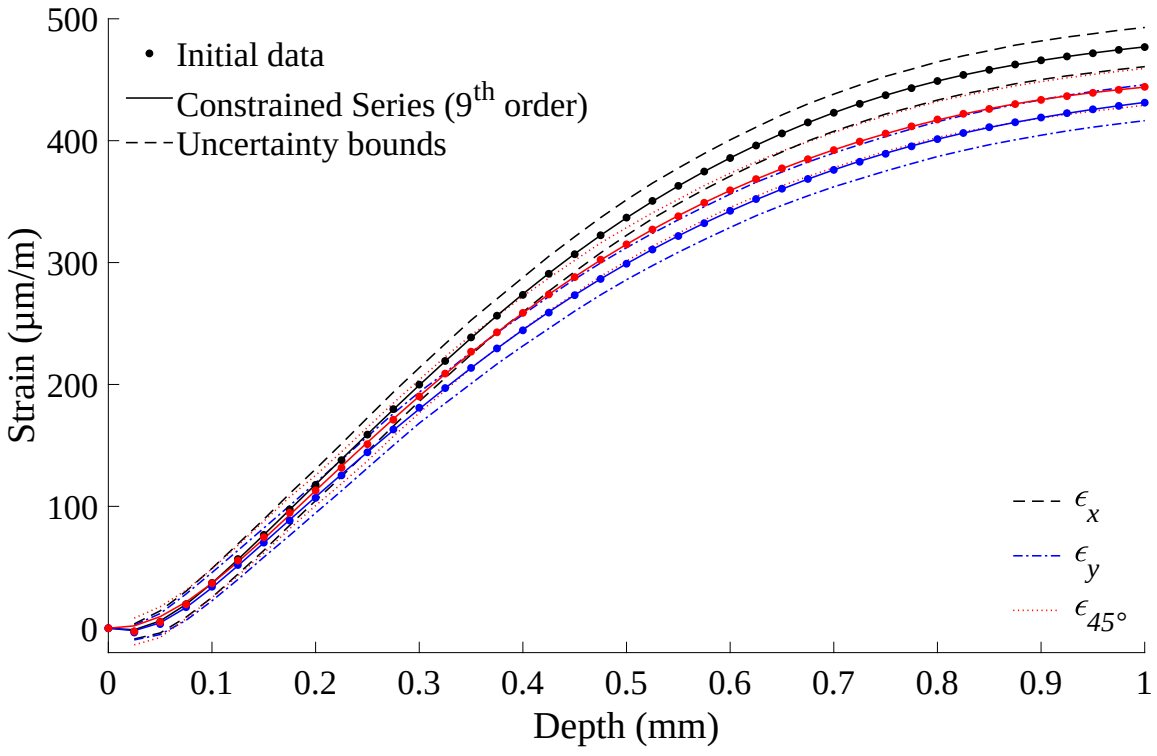


Figure 8.7: Least-squares fits to the experimental strain data using the constrained 9th order series

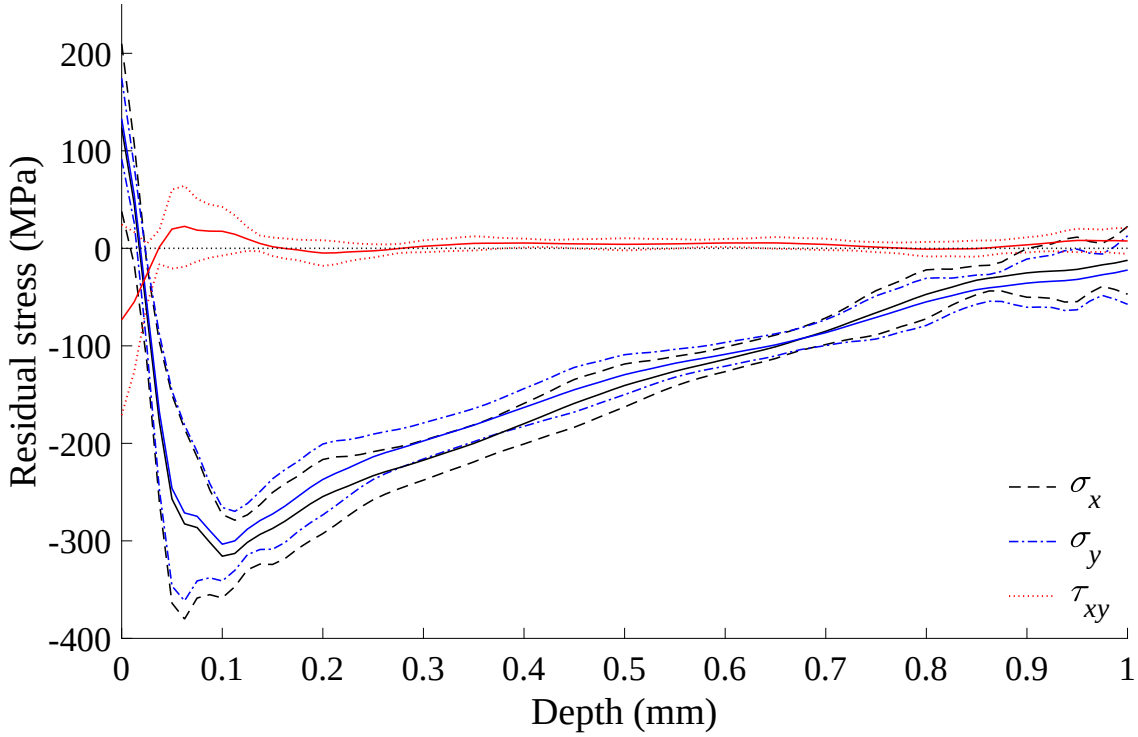


Figure 8.8: Stress distributions and associated uncertainties obtained using the constrained 9th order series

Plasticity effects were not included in the analysis since the maximum mean compressive stress is only 63% of the material yield strength. The FE model shown in Figure 8.2 revealed that the maximum von Mises stress during material removal was 505.5 MPa on the flat base of the hole when the hole depth was 0.25 mm, as shown in Figure 8.9. The variation of the maximum von Mises stress during material removal is shown in Figure 8.10. The maximum von Mises stress occurs in the flat base of the hole between 0.1-0.5 mm depth. Beyond this depth the maximum von Mises stress occurs on the hole surface in the region of the maximum compressive residual stress. The maximum von Mises stress, although some 0.4% above yield, will not have any meaningful impact on the results and, in fact, some small unmodelled hole-bottom fillet radius would have existed at this corner of the hole, reducing this stress concentration somewhat in practice.

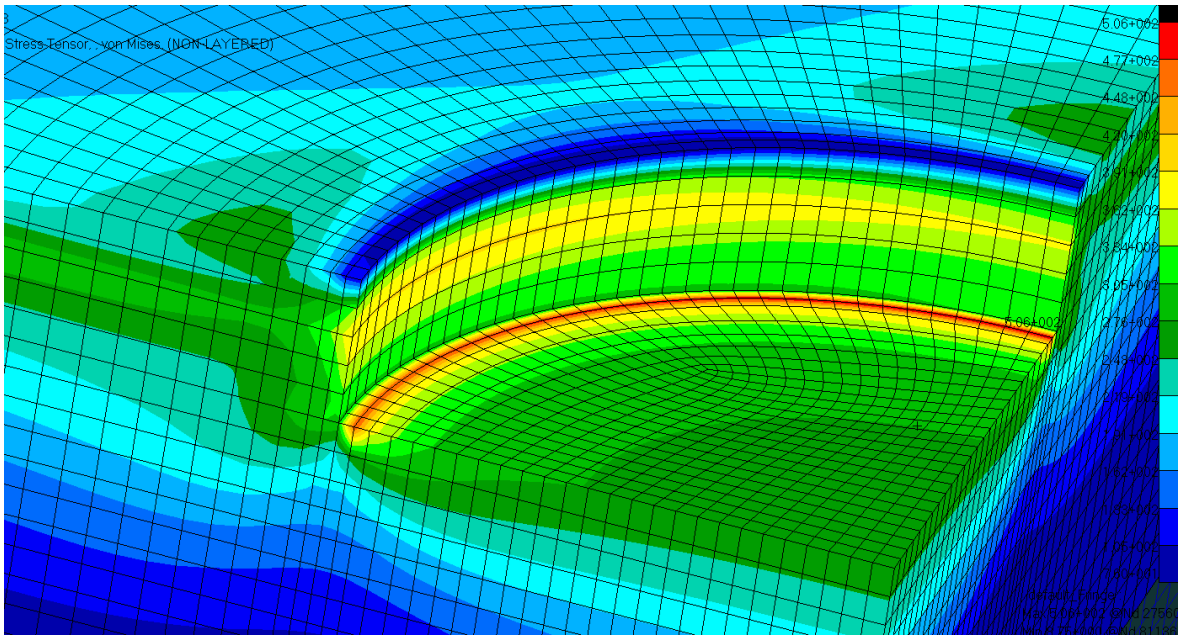


Figure 8.9: Location of maximum von Mises stress during material removal

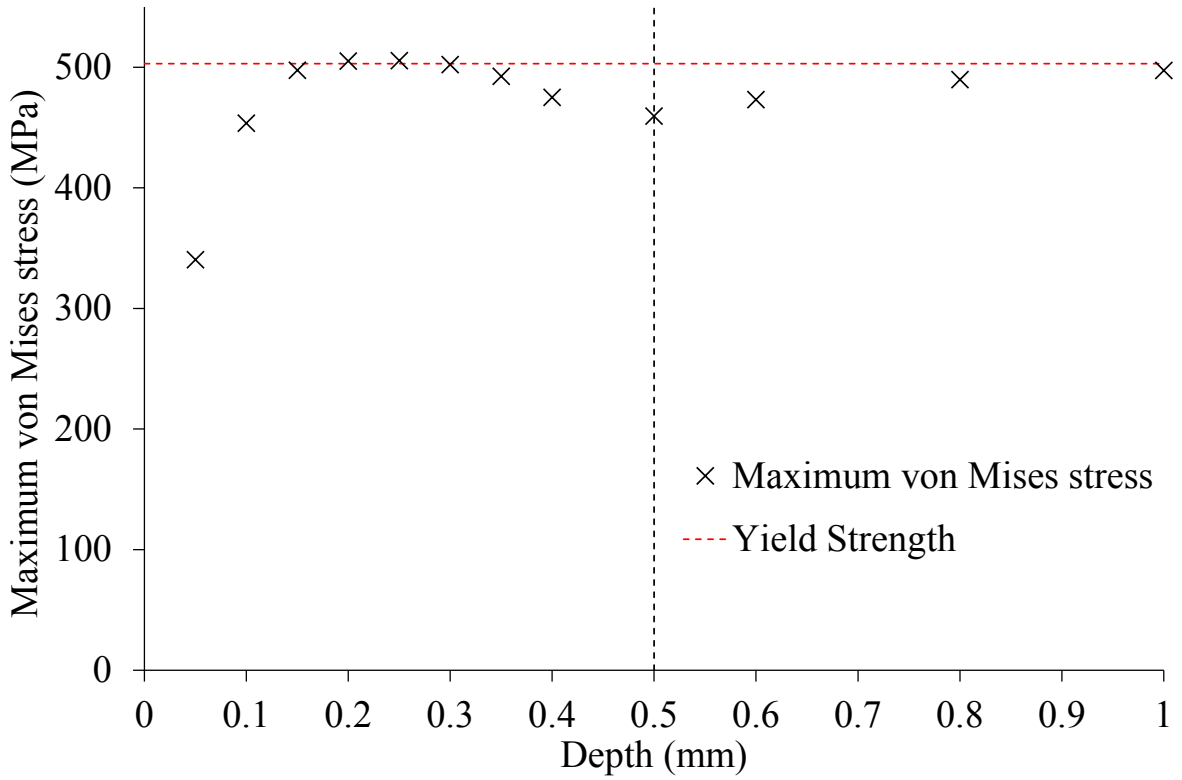


Figure 8.10: Variation of the maximum von Mises stress during material removal

The calculated stress distributions and associated uncertainties of the standard series expansion and regularized integral methods are shown with those obtained using the constrained series method in Figures 8.11 and 8.12. The magnitude and form of the residual stress distributions and uncertainties compare favourably. Standard series expansion defines the residual stress distribution well but exhibits high uncertainty in stress near the surface since curve fitting methods tend to give their least reliable results at their ends. It is evident from Figures 8.11 and 8.12 that standard series expansion does not offer any significant benefit over the integral method for near-surface stress measurement. It is clear that at the first stress datum of the integral method, the stress result and accompanying uncertainty of the standard series expansion and integral methods are the same. There is therefore no comparative advantage between the two methods on this front. In the case of the constrained series, the instability near the surface is reduced but at the expense of greater instability elsewhere, in particular the region of maximum compressive stress. The constrained series method significantly reduces the uncertainty in stress at the surface from 109.1±73.4 MPa to 123.8±43.0 MPa in the x-direction and 118.3±72.4 MPa to 133.0±20.8 MPa in the y-direction. Table 8.2 compares the RMS uncertainty in stress over 1 mm for each computational method arising from each uncertainty source as well as the combined uncertainty, $u(Z)$.

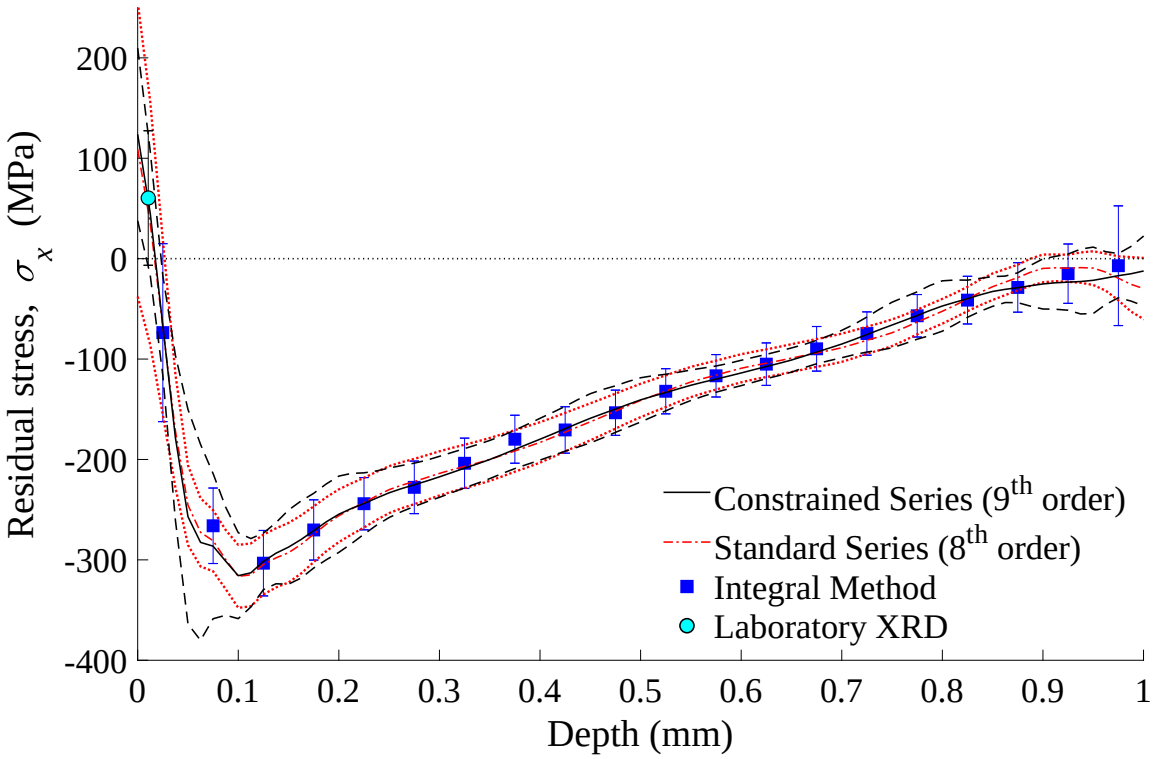


Figure 8.11: σ_x distributions and associated uncertainties of each method

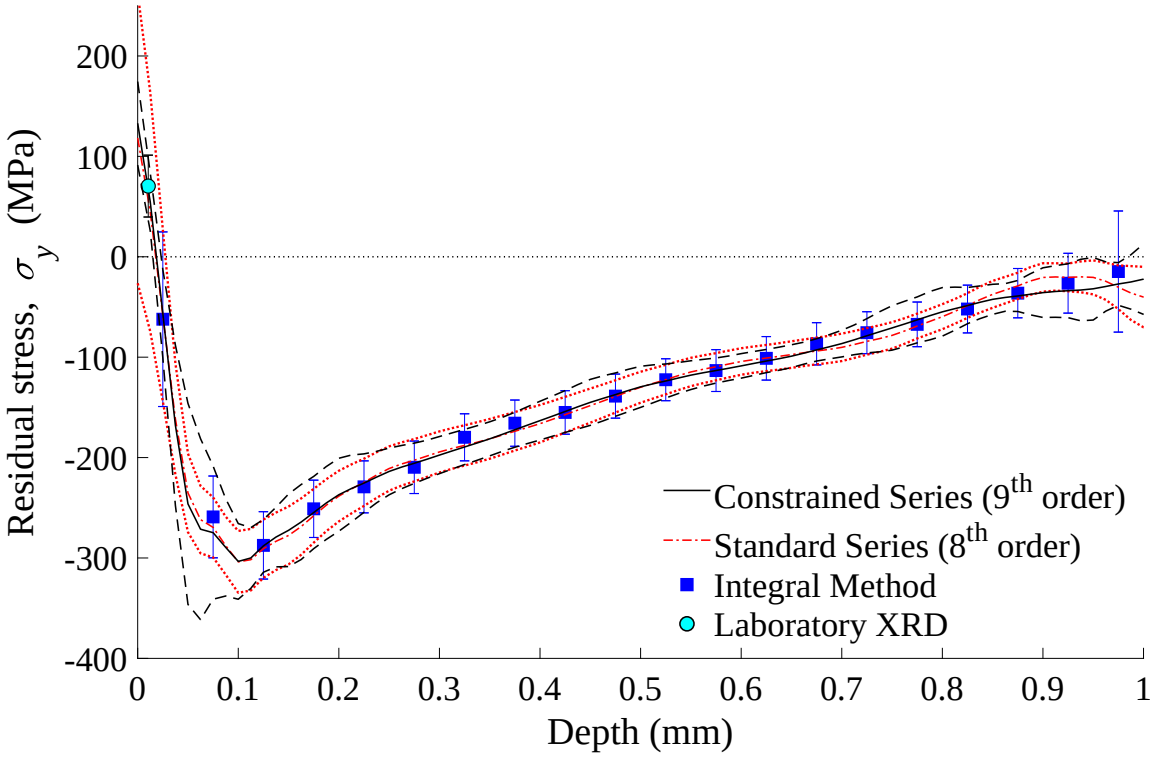


Figure 8.12: σ_y distributions and associated uncertainties of each method

Table 8.2: Breakdown of RMS uncertainty in stress arising from each uncertainty source, x_i

x_i	Contribution to $u(\sigma_x)$ [MPa]			Contribution to $u(\sigma_y)$ [MPa]			Contribution to $u(\tau_{xy})$ [MPa]		
	Constrained Series	Series Expansion	Integral Method	Constrained Series	Series Expansion	Integral Method	Constrained Series	Series Expansion	Integral Method
XRD	7.423	-	-	3.656	-	-	8.338	-	-
E	4.996	5.084	4.962	4.682	4.800	4.656	0.118	0.128	0.108
ν_{12}	1.499	1.539	1.194	1.522	1.551	1.194	0.065	0.054	0.000
z_i	0.652	0.734	1.338	0.630	0.704	1.314	0.050	0.051	0.001
z_0	11.827	12.240	10.214	11.551	11.936	9.892	0.458	0.568	0.278
ϵ_m	2.668	2.716	2.650	2.501	2.558	2.487	0.062	0.062	0.057
ϵ_{noise}	4.781	5.265	11.141	4.775	5.256	11.174	2.853	3.700	3.728
FE	4.703	4.788	3.261	4.409	4.509	3.058	0.110	0.109	0.072
Misfit	1.153	2.374	3.543	1.384	2.744	4.420	1.575	2.237	2.464
u(Z)	16.698	15.625	17.044	14.972	15.249	16.939	8.965	4.392	4.157

Table 8.2 demonstrates that zero depth position and noise in the experimental strains are some of the largest sources of uncertainty in stress. The series expansion methods are more tolerant of noise in the strain data due to least-squares curve fitting. Interestingly, the constrained series is less effected by noise in the experimental strains and zero depth position since it achieves a more stable fit to the strain data near the surface. However, the XRD measurements that help constrain the series near the surface introduce an additional stress uncertainty over the 1 mm depth which increases the total uncertainty of the constrained series to slightly above that of the unconstrained series. With more accurate XRD

results in less textured material such as steel, this additional uncertainty is reduced and the overall uncertainty for the constrained series is lower than that of the standard series expansion approach.

For illustrative purposes, Table 8.3 presents the breakdown of RMS stress uncertainty through the 1 mm depth and the respective surface stresses with their accompanying uncertainties resulting from varying only the uncertainty in XRD results of Table 8.1 across a broad range of magnitudes which include the typical value of ±20 MPa [69, 75]. As expected, the total uncertainty decreases with improved XRD accuracy until, at an XRD uncertainty of about ±20 MPa, the constrained series method outperforms standard series expansion. The uncertainty in surface stress also reduces with improved XRD accuracy, but cannot be eliminated entirely because of the inherent uncertainty in IHD results. As can be seen in Figure 8.13, the effect of XRD uncertainty on the stress distribution is localised to the near-surface measurements. The IHD uncertainty dominates as the hole depth increases so that the XRD uncertainty has little to no effect on the stress uncertainty below a depth of about 0.1 mm.

Table 8.3: Breakdown of RMS uncertainty in stress resulting from reducing only the uncertainty in XRD results

	Total uncertainties [MPa]			Surface stresses [MPa]		
	σ_x	σ_y	τ_{xy}	σ_x	σ_y	τ_{xy}
Series Expansion	15.625	15.249	4.392	109.1±73.4	118.3±72.4	-10.3±22.2
Constrained Series, *u(XRD)* = 40 MPa	17.452	17.078	9.194	124.1±51.7	133.4±51.8	-72.4±50.3
Constrained Series, *u(XRD)* = 30 MPa	16.231	15.928	7.218	123.1±38.0	133.5±38.5	-72.7±37.5
Constrained Series, *u(XRD)* = 20 MPa	15.553	15.153	5.488	123.5±26.3	133.5±26.6	-73.2±25.6
Constrained Series, *u(XRD)* = 10 MPa	15.142	14.704	3.941	123.3±14.8	133.3±14.6	-73.0±12.7
Constrained Series, *u(XRD)* = 0 MPa	14.950	14.541	3.315	123.4±7.5	133.2±7.3	-73.0±1.2

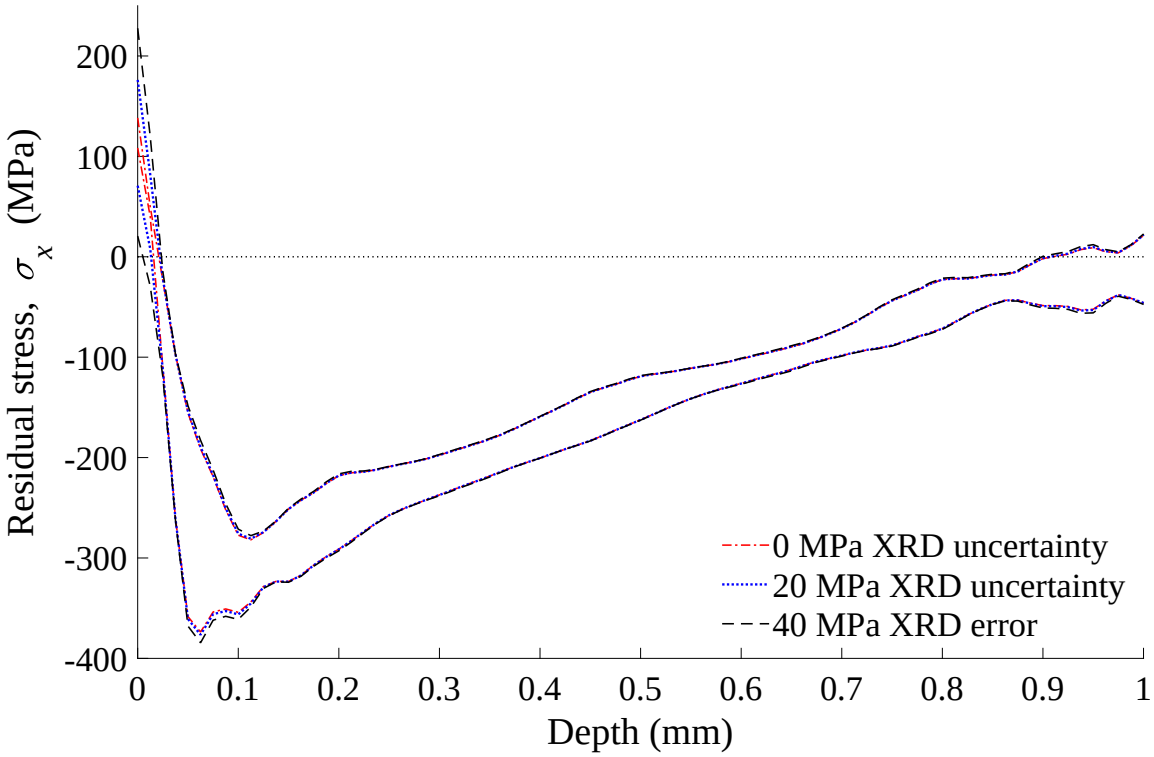


Figure 8.13: σ_x uncertainty distributions for varying magnitudes of XRD uncertainty

Imposition of constraints on the regularized integral method is also possible and yield similar results to those obtained using constrained series expansion. The calculated stress distributions and associated uncertainties of the constrained integral method are shown with those obtained using the standard regularized integral method and constrained series expansion in Figures 8.14 and 8.15. The magnitude and form of the residual stress distributions and uncertainties compare favourably. Additionally, the continuity condition of the regularized solution and the small depth between the surface and the XRD data can enable a good estimation of the surface stress, similar to series expansion. The constrained integral solution has slightly lower uncertainty than the standard method at greater depths since larger regularization factors could be employed without distortion of the stress solution than in the case of the standard method.

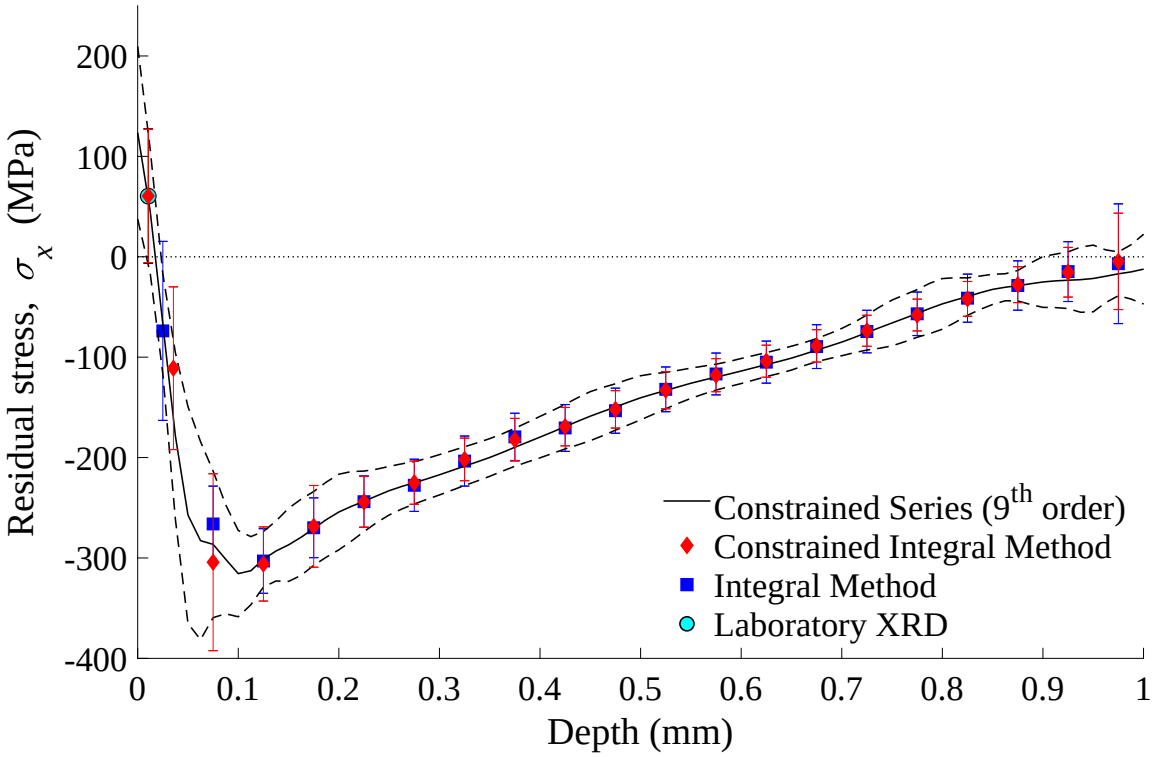


Figure 8.14: σ_x distributions and associated uncertainties of each method

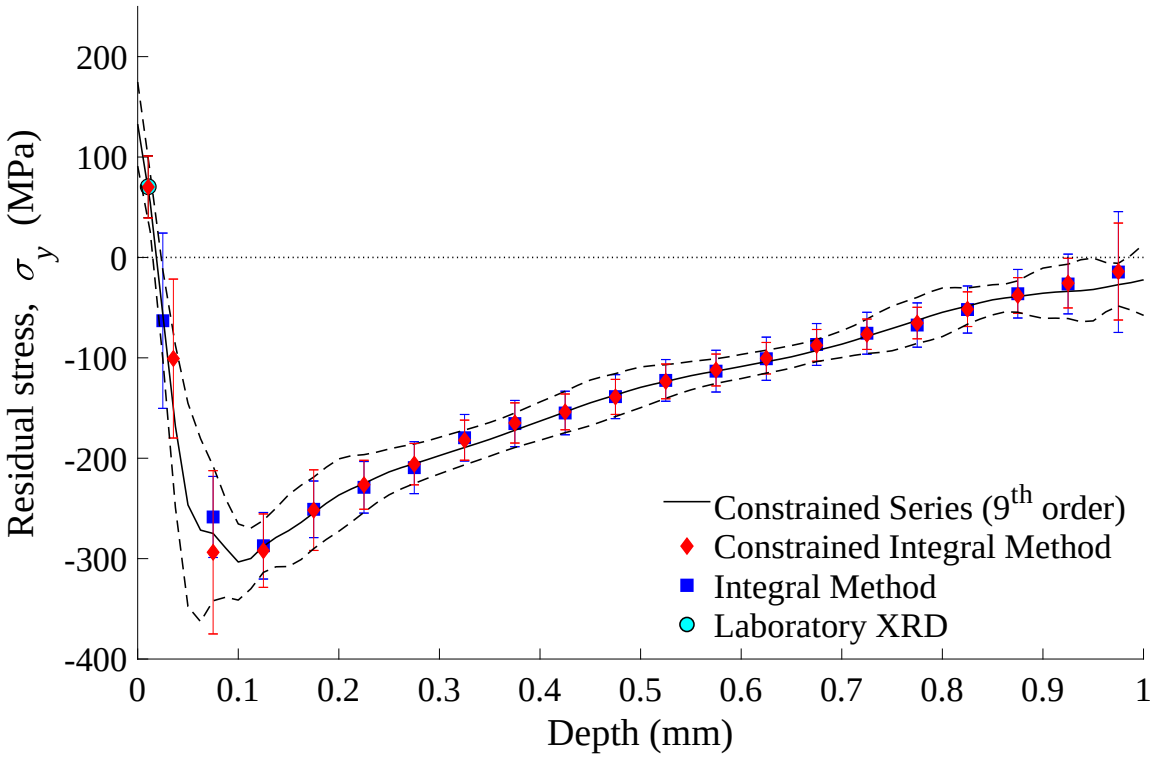


Figure 8.15: σ_y distributions and associated uncertainties of each method

Table 8.4 compares the RMS uncertainty in stress over 1 mm arising from each uncertainty source as well as the combined uncertainty, $u(Z)$ for the constrained integral and series expansion methods as well as the standard regularized integral method. The stress uncertainty for the constrained integral method compares well to the standard regularized integral method and constrained series expansion. The constrained integral method is less effected by noise in the experimental strains since larger regularization factors could be used without distorting the stress solution in this particular case. The stress uncertainty due to the misfit between regularized and experimental strain data is slightly smaller than the unconstrained method since the imposition of constraints near the surface improves the fit to the measured experimental data. However, stress uncertainty due to zero depth position is slightly increased due to the imposition of the constraint near the surface and the high stress gradient in the near-surface region. The additional stress uncertainty due to the imposition of constraints to XRD measurements over the 1 mm depth is slightly less than in the case of constrained series expansion in this particular case, but more investigation is required to access whether constrained integral or constrained series offers the best general solution. Series expansion still offers superior tolerance to noise in the experimental data, however.

Table 8.4: Breakdown of RMS uncertainty in stress arising from each uncertainty source, x_i

x_i	Contribution to $u(\sigma_x)$ [MPa]			Contribution to $u(\sigma_y)$ [MPa]			Contribution to $u(\tau_{xy})$ [MPa]		
	Constrained Integral Method	Constrained Series	Integral Method	Constrained Integral Method	Constrained Series	Integral Method	Constrained Integral Method	Constrained Series	Integral Method
XRD	6.000	7.423	-	3.236	3.656	-	8.464	8.338	-
E	4.780	4.996	4.962	4.475	4.682	4.656	0.100	0.118	0.108
ν_{12}	1.189	1.499	1.194	1.189	1.522	1.194	0.000	0.065	0.000
z_i	1.392	0.652	1.338	1.372	0.630	1.314	0.018	0.050	0.001
z_0	11.394	11.827	10.214	11.179	11.551	9.892	0.183	0.458	0.278
ϵ_m	2.643	2.668	2.650	2.475	2.501	2.487	0.055	0.062	0.057
ϵ_{noise}	8.040	4.781	11.141	8.100	4.775	11.174	3.632	2.853	3.728
FE	3.340	4.703	3.261	3.129	4.409	3.058	0.141	0.110	0.072
Misfit	2.483	1.153	3.543	2.593	1.384	4.420	4.782	1.575	2.464
u(Z)	17.336	16.698	17.044	16.148	14.972	16.939	9.546	8.965	4.157

8.5 Conclusions

The IHD method is prone to high uncertainty in near-surface residual stress measurements, irrespective of the computational method employed. A hybrid approach has been developed that makes use of near-surface XRD measurements to constrain the solution of IHD and thereby reduce the stress uncertainty near the surface. This allows the complete stress distribution up to 1 mm depth to be fully defined with increased accuracy using IHD. Constraints can be imposed on the least-squares solution of series expansion and the regularized solution of the integral method. A comprehensive demonstration of this approach for IHD has been performed on an aluminium alloy 7075 plate of 10 mm thickness that underwent LSP treatment. The use of constrained series expansion and regularized integral methods were compared to the standard unconstrained methods. While there is a strong correlation in the calculated stress distributions of all computational methods, the constrained methods significantly reduce the uncertainty in residual stress in the near-surface region because of its incorporation of XRD data from this region.

8.6 Contribution to Knowledge

- A method to impose constraints on series expansion is developed and demonstrated. The method is not limited in its use and a variation of the method can also be used to imposed constraints on separate series, applied to different regions of a continuous material, to ensure magnitude and/or slope continuity at the interface between these regions. Such an approach could be of use in niche applications in future.
- A method to impose magnitude constraints on the regularized integral method at any depth increment is also proposed and demonstrated.
- Two different residual stress measurement techniques, IHD and XRD, are combined to fully define a rapidly varying LSP-induced residual stress distribution with significantly reduced stress uncertainty in the near-surface region.

8.7 Acknowledgements

Thanks must be expressed to thank Dr Daniel Glaser of the National Laser Centre (NLC) at the Council for Scientific and Industrial Research (CSIR), Pretoria, South Africa, for conducting the XRD measurements used in this investigation through the Rental Pool Programme from the NLC at the CSIR.

9 Conclusions

IHD with the integral method is used extensively to measure residual stress distributions in almost any material type and has a standardised test procedure for isotropic materials. Tikhonov regularization should always be used with the integral method in isotropic materials to smooth the calculated stress distribution and remove noise artefacts from the experimental strain data, thereby reducing sensitivity to measurement errors. However, the use of Tikhonov regularization with the integral method has not been extended to composite materials such as FRP laminates. Therefore, existing integral methods for composite materials are sensitive to small measurement errors that can result in large stress uncertainties. The number of depth increments can be limited to reduce error sensitivity, but this approach greatly reduces the resolution of the calculated stress distribution which can adversely affect residual stress measurement in FRP laminates of arbitrary construction or where significant variation of residual stress within a single ply exists. Comprehensive uncertainty estimations are usually not conducted in IHD investigations, especially in composite materials, therefore the relative performance of existing methods are not always fully quantified.

To overcome the limitations of existing integral methods in composite materials, the use of separate series expansion has been extended to IHD for the first time to relate experimental strains to discontinuous stress distributions. The method is based on the approximation of the residual stress distribution by power series expansion of separate eigenstrain functions in each material type or ply orientation. The unknown amplitude coefficients of each series are simultaneously determined by least-squares error minimisation. The method is tolerant to measurement errors and allows all in-plane components of residual stress to be calculated. A comprehensive and robust uncertainty estimation methodology has been developed using Monte Carlo simulation. A wide variety of common experimental and computational uncertainty sources can be included in this approach. A methodology has been developed to resolve the issue of quantitatively selecting the series expansion orders that best approximates the true, or most probable, residual stress distribution from the experimental strain data, and to ensure that the series order is not increased to an extent that instabilities distort the stress solution or lead to large uncertainties. The uncertainty bounds and the convergence of every combination of series orders is investigated to find the combination of series orders with the lowest RMS stress uncertainty, selected only from those combinations that have converged to a stress solution. The separate series expansion method with IHD is not limited in its use, and allows the

analysis of any layered composite material or FRP laminate with any number of plies orientated in any direction, or any other material where discontinuous stress profiles could exist.

The use of Tikhonov regularization has been extended to measure discontinuous residual stress distributions in cross-ply FRP laminates using the unit pulse integral method with IHD for the first time. The inverse problem is decomposed and simplified for the sake of regularization only, after which the fully coupled inverse solution is considered using the regularized strain data. This approach smooths the resulting residual stress distribution and increases tolerance to measurement errors, thereby reducing stress uncertainties without the need to limit depth resolution. The degree of Tikhonov regularization applied can be optimised using Morozov Discrepancy Principle to reduce the stress uncertainty, while ensuring that the stress solution is not distorted. The uncertainty in stress associated with the regularized 16 increment integral method is similar in magnitude to that of the unregularized method with six depth increments, but with almost three times the resolution. The use of the integral method with Tikhonov regularization is computationally less expensive to implement than series expansion, requires fewer experimental depth increments and is more familiar to IHD practitioners. The method of incorporating Tikhonov regularization through simplifying approximations can be applied to any layered composite material where the incremental strain in a particular direction is predominantly due to the relaxation of residual stress in that direction. The extension of IHD with series expansion and the integral method with Tikhonov regularization to FRP laminates, along with robust uncertainty estimation can aid comparison and verification of existing and new analytical models for the prediction of residual stresses within these structures.

The use of series expansion with IHD in isotopic materials has rarely been used for the past 40 years since its inception due to suspected issues around instability at higher orders. The use of many small depth increments, fine FE meshing with eigenstrain loading to obtain calibration coefficients and a means to select an appropriate series order have resolved issues around instability. A study of series expansion with IHD has been performed on an aluminium alloy 7075 specimen subjected to LSP, and compared to the industry standard regularized integral method as well as the Zuccarello approach. Series expansion in isotropic materials is shown to be stable up to high orders and convergence to a stress solution can be found before instability dominates, with lower overall RMS uncertainty than the regularized integral method or Zuccarello approach. The effect of a wide range of uncertainty sources was investigated such that practitioners and other authors can make informed decisions on which method to use depending on their specific requirements, and their experimental and computational resources with their respective associated measurement uncertainties. Zero depth position and noise in the experimental strains are well known contributors to the residual stress uncertainty and the series expansion method has slightly greater tolerance to uncertainty in the zero depth position than the other methods, and far greater tolerance to noise in the strain data.

When measuring highly non-uniform residual stress distributions in isotropic materials, a physical characteristic of the IHD method is that it is susceptible to large stress uncertainties near the surface,

independent of the stress computation method used. This is primarily due to uncertainty in establishing the the zero depth datum of the measured strain data which similarly affects both series expansion and the integral method. A novel approach has been developed to combine near-surface XRD measurements with IHD to overcome this limitation. The approach rigorously incorporates XRD measurements by imposing constraints on the least-squares and regularized solutions of the series expansion and integral methods, respectively, thereby greatly reducing the stress uncertainty of IHD near the surface. This also reduces the need for successive XRD measurements after repeated layer removal since the complete stress distribution up to 1 mm depth can be fully defined with increased accuracy using IHD. The approach has been demonstrated on an aluminium alloy 7075 plate of 10 mm thickness that underwent LSP treatment where a strong correlation in the calculated stress distributions was found between the constrained approaches and the standard integral and series expansion methods.

This thesis extends the use of IHD to composite materials using both the regularized integral and series expansion methods. Demonstrates the use and advantages of series expansion with IHD to measure complex stress distributions in isotropic materials with reduced uncertainty. Provides and demonstrates a novel means to incorporate other residual stress measurements, such as XRD, into the inverse solution of IHD to reduce the effect of inherent characteristics that lead to large uncertainty in stress measurement.

10 Recommendations and Future Work

The following recommendations focus on future research avenues related to the topics of this thesis. Each recommendation has the potential for publication in its own right or in combination with another recommendation.

- Investigate the presence of transverse cracking in and around the hole when using IHD in FRP laminates.
- Further extend the use of Tikhonov regularization to FRP laminates with any number of plies, orientated in any direction, or any other composite material where discontinuous stress profiles could exist. This may be achievable through the use of multiple iterations of regularization until the experimental strains are regularized with respect to all in-plane stress and strain directions, including secondary contributions from other directions.
- Standardise the use of series expansion for general isotropic residual stress measurement with IHD, similar to ASTM E837-13a for the integral method. Currently the series expansion method requires more effort from practitioners than is required when using ASTM E837-13a, therefore it is important that work be undertaken to normalise the method so that it can be more widely adopted. In addition to normalising the effect of elastic properties, the effects of hole diameter, hole eccentricity and plate thickness also need to be fully investigated in the case of series expansion so that correction factors can be developed to aid standardisation of the method.
- Investigate the effect of hole bottom fillet radius on series expansion and integral methods in isotropic materials to compare the sensitivity of each method to real hole geometry. This investigation can also be extended to composite materials.
- Investigate the effect of plasticity on series expansion and integral methods in isotropic materials to compare the sensitivity of each method to residual stresses approaching the yield strength of the material. Since both the integral and series expansion methods use elasticity, there should not be an appreciable difference in sensitivity to plasticity effects. However, series expansion might help in this regard due to its reduced sensitivity to erroneous data points. If plasticity

errors occur near the surface, all the stresses beyond that point will be effected by the successive calculation procedure of the integral method. With series expansion, plasticity might only effect results in that region due to the use of least-squares curve fitting. Regularization may offer similar resistance, but these effects need to be investigated and quantified.

– Investigate the use of additional strain measurements beyond the maximum depth of interest for the regularized integral method in isotropic materials to help stabilise the residual stress distribution at greater depths, similar to series expansion. The investigations in Chapters 7 and 8 revealed that series expansion had reduced uncertainty at greater depths compared to the regularized integral method. It is suspected that this feature is due to the use of additional strain data points beyond the maximum stress depth rather than an inherent superiority of series expansion.

– Investigate the use of increasing regularization with increasing hole depth for the integral method in isotropic materials to improve resistance to noise and zero depth errors at greater depths.

– Investigate application of regularization with series expansion and the use of Morozov discrepancy principle for determination of the most appropriate series order and regularization parameters. Series expansion only allows a discrete set of choices for the order of the curve fit which can result in under or over fitting of the optimal series order. Regularization can solve this problem, however, as it adds a continuous range of complexity parameters to incorporate into the solution.

– Investigate the use of the Lagrange multiplier and KKT approach presented in section 8.2.2 for constrained series expansion calculations, and compare the computational cost of the Lagrange multiplier and KKT solution to the approach presented in section 8.2.1.

– Resolve issues around the use of a constrained separate series approach in SLM AM components. The exact position and thickness of the weld interface between deposit layers have to be accurately determined to aid imposition of constraints between specified regions within the material. Plasticity effects and potentially varying material properties such as modulus must also be accounted for.

– Perform IHD residual stress measurements with series expansion and the regularized integral method on fibre metal laminates and compare the measured stresses with non-destructive measurements from ND or synchrotron XRD. The aim of this investigation would be to evaluate the applicability of IHD in fibre metal laminates.

References

[1] Barnes JA and Byerly GE. The formation of residual stresses in laminated thermoplastic composites. *Composites Science and Technology*, 51(4):479–494, 1994. ISSN 02663538. doi: 10.1016/0266-3538(94)90081-7.

[2] Regester RF. Behavior of Fiber Reinforced Plastic Materials in Chemical Service. *Corrosion*, 25(4): 157–167, 1969. ISSN 0010-9312. doi: 10.5006/0010-9312-25.4.157.

[3] Garstka T, Ersoy N, Potter KD, and Wisnom MR. In situ measurements of through-the-thickness strains during processing of AS4/8552 composite. *Composites Part A: Applied Science and Manufacturing*, 38 (12):2517–2526, 2007. ISSN 1359-835X. doi: 10.1016/j.compositesa.2007.07.018.

[4] Shokrieh MM, Akbari S, and Daneshvar A. A comparison between the slitting method and the classical lamination theory in determination of macro-residual stresses in laminated composites. *Composite Structures*, 96:708–715, 2013. ISSN 02638223. doi: 10.1016/j.compstruct.2012.10.001.

[5] Parlevliet PP, Bersee HEN, and Beukers A. Residual stresses in thermoplastic composites – a study of the literature. Part III: Effects of thermal residual stresses. *Composites Part A: Applied Science and Manufacturing*, 38(6):1581–1596, 2007. ISSN 1359835X. doi: 10.1016/j.compositesa.2006.12.005.

[6] Safarabadi M and Shokrieh MM. *Residual stresses in composite materials*, chapter 8, pages 197–232. Woodhead Publishing Limited, 2014. ISBN 9780857092700. doi: 10.1533/9780857098597.2.197.

[7] Awaja F, Zhang S, Tripathi M, Nikiforov A, and Pugno N. Cracks, microcracks and fracture in polymer structures: Formation, detection, autonomic repair. *Progress in Materials Science*, 83:536 – 573, 2016. ISSN 0079-6425. doi: 10.1016/j.pmatsci.2016.07.007.

[8] Hiemstra DL and Sottos NR. Thermally induced interfacial microcracking in polymer matrix composites. *Journal of Composite Materials*, 27(10):1030–1051, 1993. doi: 10.1177/002199839302701005.

[9] Price JN and Hull D. Effect of matrix toughness on crack propagation during stress corrosion of glass reinforced composites. *Composites Science and Technology*, 28(3):193–210, 1987. ISSN 02663538. doi: 10.1016/0266-3538(87)90002-9.

[10] Hogg PJ. Factors affecting the stress corrosion of GRP in acid environments. *Composites*, 14(3):254–261, 1983. ISSN 0010-4361. doi: 10.1016/0010-4361(83)90013-7.

[11] Hogg PJ and Hull D. Micromechanisms of crack growth in composite materials under corrosive environments. *Metal Science*, 14(8-9):441–449, 1980. ISSN 0306-3453. doi: 10.1179/msc.1980.14.8-9.441.

[12] Jones FR, Rock JW, and Wheatley AR. Stress corrosion cracking and its implications for the long-term durability of E-glass fibre composites. *Composites*, 14(3):262–269, 1983. ISSN 00104361. doi: 10.1016/0010-4361(83)90014-9.

[13] Twigg G, Poursartip A, and Fernlund G. Tool-part interaction in composites processing. Part I: Experimental investigation and analytical model. *Composites Part A: Applied Science and Manufacturing*, 35 (1):121–133, 2004. ISSN 1359835X. doi: 10.1016/S1359-835X(03)00131-3.

[14] Hahn HT. Residual Stresses in Polymer Matrix Composite Laminates. *Journal of Composite Materials*, 10(4):266–278, 1976. ISSN 0021-9983. doi: 10.1177/002199837601000401.

[15] Seif MA, Khashaba UA, and Rojas-oviedo R. Residual stress measurements in CFRE and GFRE composite missile shells. *Composite Structures*, 79(2):261–269, 2007. ISSN 0263-8223. doi: 10.1016/j.compstruct.2006.01.002.

[16] Seif MA and Short SR. Determination of residual stresses in thin-walled composite cylinders. *Experimental Techniques*, 26(2):43–46, 2002.

[17] White SR and Hahn HT. Cure Cycle Optimization for the Reduction of Processing-Induced Residual Stresses in Composite Materials. *Journal of Composite Materials*, 27(14):1352–1378, 1993. ISSN 1530793X. doi: 10.1177/002199839302701402.

[18] Stone MA, Schwartz IF, and Chandler HD. Residual stresses associated with post-cure shrinkage in GRP tubes. *Composites Science and Technology*, 57(1):47–54, 1997. ISSN 02663538. doi: 10.1016/S0266-3538(96)00108-X.

[19] Mantell SC and Springer GS. Manufacturing Process Models for Thermoplastic Composites. *Journal of Composite Materials*, 26(16):2348–2377, 1992. ISSN 1530793X. doi: 10.1177/002199839202601602.

[20] Kim YK and White SR. Cure-dependent viscoelastic residual stress analysis of filament-wound composite cylinders. *Mechanics of Composite Materials and Structures*, 5(4):327–354, 1999. ISSN 10759417. doi: 10.1080/10759419808945905.

[21] White SR and Hahn HT. Process Modeling of Composite Materials: Residual Stress Development during Cure. Part I: Model Formulation. *Journal of Composite Materials*, 26(16):2402–2422, 1992. ISSN 0021-9983. doi: 10.1177/002199839202601604.

[22] Unger WJ and Hansen JS. The Effect of Thermal Processing on Residual Strain Development in Unidirectional Graphite Fibre Reinforced PEEK. *Journal of Composite Materials*, 27(1):59–82, 1993. ISSN 1530793X. doi: 10.1177/002199839302700105.

[23] Jeronimidis G and Parkyn AT. Residual Stresses in Carbon Fibre-Thermoplastic Matrix Laminates. *Journal of Composite Materials*, 22(5):401–415, 1988. ISSN 1530793X. doi: 10.1177/002199838802200502.

[24] Kim KS and Hahn HT. Residual stress development during processing of graphite/epoxy composites. *Composites Science and Technology*, 36(2):121–132, 1989. ISSN 02663538. doi: 10.1016/0266-3538(89)90083-3.

[25] Weitsman Y. Optimal Cool-Down in Linear Viscoelasticity. *Journal of Applied Mechanics*, 47(1):35, mar 1980. ISSN 00218936. doi: 10.1115/1.3153634.

[26] Lee K and Weitsman Y. Optimal Cool-Down in Nonlinear Thermoviscoelasticity with Application to Graphite Peek (Apc-2) Laminates. *Journal of Applied Mechanics-Transactions of the Asme*, 61(2):367–374, 1994. ISSN 00218936. doi: 10.1115/1.2901453.

[27] Wang TM, Daniel IM, and Gotro JT. Thermoviscoelastic Analysis of Residual Stresses and Warpage in Composite Laminates. *Journal of Composite Materials*, 26(6):883–899, 1992. ISSN 0021-9983. doi: 10.1177/002199839202600606.

[28] Ding K and Ye L. *Laser shock peening Performance and process simulation*. Woodhead Publishing in materials. Taylor & Francis, 2006. ISBN 9780849334443.

[29] Hammond DW and Meguid SA. Crack propagation in the presence of shot-peening residual stresses. *Engineering Fracture Mechanics*, 37(2):373 – 387, 1990. ISSN 0013-7944. doi: 10.1016/0013-7944(90)90048-L.

[30] Luo KY, Wang CY, Li YM, Luo M, Huang S, Hua XJ, and Lu JZ. Effects of laser shock peening and groove spacing on the wear behavior of non-smooth surface fabricated by laser surface texturing. *Applied Surface Science*, 313:600–606, 2014. ISSN 0169-4332. doi: 10.1016/j.apsusc.2014.06.029.

[31] Hong X, Wang S, Guo D, Wu H, Wang J, Dai Y, Xia X, and Xie Y. Confining medium and absorptive overlay: Their effects on a laser-induced shock wave. *Optics and Lasers in Engineering*, 29(6):447–455, 1998. ISSN 0143-8166. doi: 10.1016/S0143-8166(98)80012-2.

[32] Peyre P, Scherpereel X, Berthe L, Carboni C, Fabbro R, Béranger G, and Lemaitre C. Surface modifications induced in 316L steel by laser peening and shot-peening. influence on pitting corrosion resistance. *Materials Science and Engineering: A*, 280(2):294–302, 2000. ISSN 0921-5093. doi: 10.1016/S0921-5093(99)00698-X.

[33] Montross CS, Wei T, Ye L, Clark G, and Mai YW. Laser shock processing and its effects on microstructure and properties of metal alloys: A review. *International Journal of Fatigue*, 24(10):1021–1036, 2002. ISSN 0142-1123. doi: 10.1016/S0142-1123(02)00022-1.

[34] Peyre P and Fabbro R. Laser shock processing: A review of the physics and applications. *Optical and Quantum Electronics*, 27(12):1213–1229, 1995. ISSN 1572-817X. doi: 10.1007/BF00326477.

[35] Cellard C, Retraint D, François M, Rouhaud E, and Le Saunier D. Laser shock peening of Ti-17 titanium alloy: Influence of process parameters. *Materials Science and Engineering: A*, 532:362–372, 2012. ISSN 0921-5093. doi: 10.1016/j.msea.2011.10.104.

[36] Fairand AH and Clauer BP. Interaction of laser-induced stress waves with metals. In *Proceedings of the ASM Conference Applications of Lasers in Materials Processing, Washington, DC, USA, 18–20 April 1979*, Materials Park, OH, USA, 1979. ASM International.

[37] Hill MR, Dewald AT, Rankin JE, and Lee MJ. Measurement of laser peening residual stresses. *Materials Science and Technology*, 21(1):3–9, 2005. doi: 10.1179/174328405X14083.

[38] Ding K and Ye L. Simulation of multiple laser shock peening of a 35CD4 steel alloy. *Journal of Materials Processing Technology*, 178(1):162 – 169, 2006. ISSN 0924-0136. doi: 10.1016/j.jmatprotec.2006.03.170.

[39] Frija M, Hassine T, Fathallah R, Bouraoui C, and Dogui A. Finite element modelling of shot peening process: Prediction of the compressive residual stresses, the plastic deformations and the surface integrity. *Materials Science and Engineering A*, 426(1-2):173–180, 2006. doi: 10.1016/j.msea.2006.03.097.

[40] Peyre P, Fabbro R, Merrien P, and Lieurade HP. Laser shock processing of aluminium alloys. Application to high cycle fatigue behaviour. *Materials Science and Engineering: A*, 210(1):102–113, 1996. ISSN 0921-5093. doi: 10.1016/0921-5093(95)10084-9.

[41] Ruschau JJ, John R, Thompson SR, and Nicholas T. Fatigue crack nucleation and growth rate behavior of laser shock peened titanium. *International Journal of Fatigue*, 21:S199–S209, 1999. ISSN 0142-1123. doi: 10.1016/S0142-1123(99)00072-9.

[42] Sano Y, Obata M, Kubo T, Mukai N, Yoda M, Masaki K, and Ochi Y. Retardation of crack initiation and growth in austenitic stainless steels by laser peening without protective coating. *Materials Science and Engineering: A*, 417(1):334–340, 2006. ISSN 0921-5093. doi: 10.1016/j.msea.2005.11.017.

[43] Zhang Y, You J, Lu J, Cui C, Jiang Y, and Ren X. Effects of laser shock processing on stress corrosion cracking susceptibility of az31b magnesium alloy. *Surface and Coatings Technology*, 204(24):3947–3953, 2010. ISSN 0257-8972. doi: 10.1016/j.surfcoat.2010.03.015.

[44] Zhang XC, Zhang YK, Lu JZ, Xuan FZ, Wang ZD, and Tu ST. Improvement of fatigue life of Ti–6Al–4V alloy by laser shock peening. *Materials Science and Engineering: A*, 527(15):3411–3415, 2010. ISSN 0921-5093. doi: 10.1016/j.msea.2010.01.076.

[45] Chandrasekara KT. On the roughness dependence of wear of steels: A new approach. *Journal of Materials Science Letters*, 12(12):952–954, 1993. ISSN 1573-4811. doi: 10.1007/BF00455629.

[46] Kalainathan S, Sathyajith S, and Swaroop S. Effect of laser shot peening without coating on the surface properties and corrosion behavior of 316l steel. *Optics and Lasers in Engineering*, 50(12):1740–1745, 2012. ISSN 0143-8166. doi: 10.1016/j.optlaseng.2012.07.007.

[47] Peyre P, Sollier A, Chaieb I, Berthe L, Bartnicki E, Braham C, and Fabbro R. Fem simulation of residual stresses induced by laser peening. *Eur. Phys. J. AP*, 23(2):83–88, 2003. doi: 10.1051/epjap:2003037.

[48] Li K, Hu Y, and Yao Z. Experimental study of micro dimple fabrication based on laser shock processing. *Optics & Laser Technology*, 48:216–225, 2013. ISSN 0030-3992. doi: 10.1016/j.optlastec.2012.09.015.

[49] Clauer AH, Fairand BP, and Wilcox BA. Laser shock hardening of weld zones in aluminum alloys. *Metallurgical Transactions A*, 8(12):1871–1876, 1977. ISSN 1543-1940. doi: 10.1007/BF02646559.

[50] Srinivasan S, Garcia DB, Gean MC, Murthy H, and Farris TN. Fretting fatigue of laser shock peened Ti–6Al–4V. *Tribology International*, 42(9):1324–1329, 2009. ISSN 0301-679X. doi: 10.1016/j.triboint.2009.04.014. Special Issue: Fifth International Symposium on Fretting Fatigue.

[51] Scherpereel X, Peyre P, Fabbro R, Lederer G, and Celati N. Modifications of mechanical and electrochemical properties of stainless steel surfaces by laser shock processing. In Leo H. J. F. Beckmann, editor, *Lasers in Material Processing*, volume 3097, pages 546–557. International Society for Optics and Photonics, SPIE, 1997. doi: 10.1117/12.281115.

[52] Yilbas BS, Gondal MA, Arif AMF, and Shuja SZ. Laser shock processing of Ti-6Al-4V alloy. *Proceedings of the Institution of Mechanical Engineers, Part B: Journal of Engineering Manufacture*, 218(5): 473–482, 2004. doi: 10.1177/095440540421800501.

[53] Rozmus-Górnikowska M. Surface Modifications of a Ti-6Al-4V Alloy by a Laser Shock Processing. *Acta Physica Polonica A*, 117(5):808–811, 2010. doi: 10.12693/APhysPolA.117.808.

[54] Liu Q, Ding K, Ye L, Rey C, Barter SA, Sharp PK, and Clark G. Spallation-like phenomenon induced by laser shock peening surface treatment on 7050 aluminum alloy. In *Proceedings of Structural Integrity and Fracture International Conference (SIF'04), Brisbane, Australia, 26-29 September 2004*, pages 235–240. The University of Queensland: Brisbane, Australia, 2004.

[55] Rockstroh TJ, Bailey MS, and Ash CA. *Laser shock procesing of aircraft engine components*. General Electric Infrastructure-Avaition, Cincinnati, OH, USA, 2008.

[56] Gujba AK and Medraj M. Laser peening process and its impact on materials properties in comparison with shot peening and ultrasonic impact peening. *Materials*, 7(12):7925–7974, 2014. ISSN 1996-1944. doi: 10.3390/ma7127925.

[57] Zhou Z, Bhamare S, Ramakrishnan G, Mannava SR, Langer K, Wen Y, Qian D, and Vasudevan VK. Thermal relaxation of residual stress in laser shock peened Ti–6Al–4V alloy. *Surface and Coatings Technology*, 206(22):4619–4627, 2012. ISSN 0257-8972. doi: 10.1016/j.surfcoat.2012.05.022.

[58] Mannava S, McDaniel AE, Cowie WD, Halila H, Rhoda JE, and Ferrigno SJ. Laser shock peened gas turbine engine blade tip, U.S. Patent 5 620 307, Apr. 1997.

[59] Lin B, Lupton C, Spanrad S, Schofield J, and Tong J. Fatigue crack growth in laser-shock-peened ti–6al–4v aerofoil specimens due to foreign object damage. *International Journal of Fatigue*, 59:23–33, 2014. ISSN 0142-1123. doi: 10.1016/j.ijfatigue.2013.10.001.

[60] Clauer A. Laser shock processing: Past, present and future. In *Proceedings of the 4th International Conference on Laser Peening, Madrid, Spain, 6 May 2013*. Universidad Politécnica de Madrid: Madrid, Spain, 2013.

[61] Cao Zw, Che Zg, Zou Sk, and Fei Qx. Numerical simulation of residual stress field induced by laser shock processing with square spot. *Journal of Shanghai University (English Edition)*, 15(6):553–556, 2011. ISSN 1863-236X. doi: 10.1007/s11741-011-0785-1.

[62] Voothaluru R, Richard Liu C, and Cheng GJ. Finite element analysis of the variation in residual stress distribution in laser shock peening of steels. *Journal of Manufacturing Science and Engineering*, 134 (6), 11 2012. ISSN 1087-1357. doi: 10.1115/1.4007780.

[63] Hu Y, Yao Z, and Hu J. 3-d fem simulation of laser shock processing. *Surface and Coatings Technology*, 201(3):1426–1435, 2006. ISSN 0257-8972. doi: 10.1016/j.surfcoat.2006.02.018.

[64] Bragg W. The diffraction of short electromagnetic waves by a crystal. *Proceedings of the Cambridge Philosophical Society*, 17:43–57, 1913. ISSN 0567-7394. doi: 10.1107/S0567739472000609.

[65] Cullity BD and Stock SR. *Elements of X-ray Diffraction, Third Edition*. Prentice-Hall, 2001.

[66] Fitzpatrick ME, Fry AT, Holdway P, Kandil FA, Shackleton J, and Suominen L. Determination of residual stresses by X-ray diffraction, 2005. ISSN: 1368-6550.

[67] Macherauch E and Müller P. Das sin2y-verfahren der röntgenographischen spannungsmessung. *Zeitschrift für Angewandte Physik*, 13:305–312, 1961.

[68] Li A, Ji V, Lebrun JL, and Ingelbert G. Surface roughness effects on stress determination by the X-ray diffraction method. *Experimental Techniques*, 19(2):9–11, 1995. doi: 10.1111/j.1747-1567.1995.tb00840.x.

[69] Withers PJ and Bhadeshia HKDH. Residual stress. Part 1 - Measurement techniques. *Materials Science and Technology*, 17(4):355–365, 2001. doi: 10.1179/026708301101509980.

[70] Valentini E, Beghini M, Bertini L, Santus C, and Benedetti M. Procedure to perform a validated incremental hole drilling measurement: Application to shot peening residual stresses. *Strain*, 47(s1): e605–e618, 2011. doi: 10.1111/j.1475-1305.2009.00664.x.

[71] Correia D. *Investigation into the Friction Stir Welding of Aeronautical Grade Aluminium Alloys Using Standard and Innovative Tooling*. PhD thesis, The University of the Witwatersrand, 2014.

[72] Kandil F, Lord D, and Fry A. A review of residual stress measurement methods: A guide to technique selection. Technical report, National Physical Laboratory Materials Centre, Teddington, UK, 2001.

[73] Fry AT and Kandil FA. A study of parameters affecting the quality of residual stress measurements using XRD. In *Residual Stresses VI, ECRS6*, volume 404 of *Materials Science Forum*, pages 579–586. Trans Tech Publications Ltd, 8 2002. doi: 10.4028/www.scientific.net/MSF.404-407.579.

[74] François M, Convert F, and Branchu S. French round-robin test of X-ray stress determination on a shot-peened steel. *Experimental Mechanics*, 40(4):361–368, 2000. ISSN 1741-2765. doi: 10.1007/BF02326481.

[75] HS (Society of Automotive Engineers). *Residual Stress Measurement by X-ray Diffraction: HS-784*. SAE International, 2003. ISBN 9780768010695.

[76] Nobre JP, Polese C, and van Staden SN. Incremental hole drilling residual stress measurement in thin aluminum alloy plates subjected to laser shock peening. *Experimental Mechanics*, 60(1):553–564, 2020. doi: 10.1007/s11340-020-00586-5.

[77] Predecki P and Barrett CS. Stress Measurement in Graphite/Epoxy Composites By X-ray Diffraction from Fillers. *Journal of Composite Materials*, 13(1):61–71, 1979. ISSN 1530793x. doi: 10.1177/002199837901300105.

[78] Fenn RH, Jones AM, and Wells GM. X-ray Diffraction Investigation of Triaxial Residual Stresses in Composite Materials. *Journal of Composite Materials*, 27(14):1338–1351, 1993. ISSN 0021-9983. doi: 10.1177/002199839302701401.

[79] Benedikt B, Predecki PK, Kumosa L, Rupnowski P, and Kumosa M. Measurement of residual stresses in fibre reinforced composites based on X-ray diffraction. *Advances in X-ray Analysis*, 45(c):218–224, 2002.

[80] Fenn RH and Jones AM. Measurements of Residual Stress in Carbon Fibre Composite Materials Using X-ray Diffraction BT - International Conference on Residual Stresses: ICRS2. pages 160–165. Springer Netherlands, Dordrecht, 1989. ISBN 978-94-009-1143-7. doi: 10.1007/978-94-009-1143-7˙25.

[81] Meske R and Schnack E. A micromechanical model for X-ray stress analysis of fiber reinforced composites. *Journal of Composite Materials*, 35(11):972–998, 2001. ISSN 00219983. doi: 10.1177/002199801772662398.

[82] Schajer GS. Hole-Drilling Residual Stress Measurements at 75: Origins, Advances, Opportunities. *Experimental Mechanics*, 50(2):245–253, 2010. ISSN 1741-2765. doi: 10.1007/s11340-009-9285-y.

[83] Schajer GS. Residual stresses: Measurement by destructive testing. In *Encyclopedia of Materials: Science and Technology*, pages 8152 – 8158. Elsevier, Oxford, 2001. ISBN 978-0-08-043152-9. doi: 10.1016/B0-08-043152-6/01462-5.

[84] Treuting RG and Read WT. A mechanical determination of biaxial residual stress in sheet materials. *Journal of Applied Physics*, 22(2):130–134, 1951. ISSN 00218979. doi: 10.1063/1.1699913.

[85] Prime MB. Residual Stress Measurement by Successive Extension of a Slot: The Crack Compliance Method. *Applied Mechanics Reviews*, 52(2):75, 1999. ISSN 00036900. doi: 10.1115/1.3098926.

[86] ASTM E837-13a. *Standard test method for determining residual stresses by the hole-drilling strain-gage method*. ASTM International, West Conshohocken, PA, 2013.

[87] Schajer GS and Prime MB. Use of Inverse Solutions for Residual Stress Measurements. *Journal of Engineering Materials and Technology*, 128(3):375, 2006. ISSN 00944289. doi: 10.1115/1.2204952.

[88] Cheng W and Finnie I. *Residual Stress Measurement and the Slitting Method*. Mechanical Engineering Series. Springer US, 2007. ISBN 978-0-387-39030-7. doi: 10.1007/978-0-387-39030-7.

[89] Sicot O, Gong XL, Cherouat A, and Lu J. Influence of experimental parameters on determination of residual stress using the incremental hole-drilling method. *Composites Science and Technology*, 64(2): 171–180, 2004. ISSN 02663538. doi: 10.1016/S0266-3538(03)00278-1.

[90] Sicot O, Gong XL, Cherouat A, and Lu J. Determination of Residual Stress in Composite Laminates Using the Incremental Hole-drilling Method. *Journal of Composite Materials*, 37(9):831–844, 2003. ISSN 0021-9983. doi: 10.1177/0021998303031057.

[91] Shokrieh MM and Ghasemi ARK. Simulation of central hole drilling process for measurement of residual stresses in isotropic, orthotropic, and laminated composite plates. *Journal of Composite Materials*, 41(4), 2007. ISSN 00219983 1530793X. doi: 10.1177/0021998306063803.

[92] Schajer GS. Application of Finite Element Calculations to Residual Stress Measurements. *Journal of Engineering Materials and Technology*, 103(2):157, 1981. ISSN 00944289. doi: 10.1115/1.3224988.

[93] Schajer GS. Measurement of non-uniform residual stresses using the hole-drilling method. Part II. Practical application of the integral method. *Journal of Engineering Materials and Technology, Transactions of the ASME*, 110(4):344–349, 1988. ISSN 00944289. doi: 10.1115/1.3226059.

[94] Prime MB and Hill MR. Uncertainty, Model Error, and Order Selection for Series-Expanded, Residual-Stress Inverse Solutions. *Journal of Engineering Materials and Technology*, 128(2):175, 2006. ISSN 00944289. doi: 10.1115/1.2172278.

[95] Oettel R. The Determination of Uncertainties in Residual Stress Measurement (Using the hole drilling technique). *Code of Practice 15, Issue 1, EU Project No. SMT4-CT97-2165*, (1):18, 2000. ISSN 00392103. doi: 10.1007/bf02327502.

[96] Schajer GS and Altus E. Stress calculation error analysis for incremental hole-drilling residual stress measurements. *Journal of Engineering Materials and Technology-Transactions of the Asme*, 118(1): 120–126, 1996. ISSN 0094-4289. doi: 10.1115/1.2805924.

[97] Grant PV, Lord JD, and Whitehead P. The Measurement of Residual Stresses by the Incremental Hole Drilling Technique. *Measurement Good Practice Guide No. 53 - Issue 2*, (2):63, 2006. ISSN 1744-3911.

[98] Tikhonov AN, Goncharsky AV, Stepanov VV, and Yagola AG. *Numerical Methods for the Solution of Ill-Posed Problems*. Kluwer, Dordrecht, 1995.

[99] Akbari S, Taheri-Behrooz F, and Shokrieh MM. Slitting measurement of residual hoop stresses through the wall-thickness of a filament wound composite ring. *Experimental Mechanics*, 53:1509–1518, 11 2013. doi: 10.1007/s11340-013-9768-8.

[100] BIPM, IEC, IFCC, ILAC, IUPAC, IUPAP, ISO, and OIML. Evaluation of measurement data — Supplement 1 to the "Guide to the expression of uncertainty in measurement" — Propagation of distributions using a Monte Carlo method, JCGM 101: 2008. 2008.

[101] Cheng W and Finnie I. Measurement of Residual Hoop Stresses in Cylinders Using the Compliance Method. *Journal of Engineering Materials and Technology*, 108(April 1986):87–92, 1986. ISSN 00944289. doi: 10.1115/1.3225864.

[102] Cheng W and Finnie I. A Method for Measurement of Axisymmetric Axial Residual Stresses in Circumferentially Welded Thin-Walled Cylinders. *Journal of Engineering Materials and Technology*, 107 (3):181–185, 1985. ISSN 0094-4289.

[103] Cheng W and Finnie I. Measurement of residual stress distributions near the toe of an attachment welded on a plate using the crack compliance method. *Engineering Fracture Mechanics*, 46(1):79–91, 1993. ISSN 00137944. doi: 10.1016/0013-7944(93)90305-C.

[104] Fett T. Determination of Residual Stresses in Components Using the Fracture Mechanics Weight Function, 1996. ISSN 00137944.

[105] Prime MB and Hill MR. Residual stress, stress relief, and inhomogeneity in aluminum plate. *Scripta Materialia*, 46(1):77–82, 2002. ISSN 13596462. doi: 10.1016/S1359-6462(01)01201-5.

[106] Cheng W. Measurement of the Axial Residual Stresses Using the Initial Strain Approach . *Journal of Engineering Materials and Technology*, 122(1):135–140, 07 1999. ISSN 0094-4289. doi: 10.1115/1.482777.

[107] Qian X, Yao Z, Cao Y, and Lu J. An inverse approach for constructing residual stress using BEM. *Engineering Analysis with Boundary Elements*, 28(3):205–211, 2004. ISSN 09557997. doi: 10.1016/S0955-7997(03)00051-1.

[108] Beghini M, Bertini L, and Valentini R. Residual Stress Measurement and Modeling by the Initial Strain Distribution Method : Part II — Application to Cladded Plates with Different Heat Treatments. *Journal of Testing and Evaluation*, 32(3):1–7, 2004. ISSN 00903973.

[109] Prime MB and Hill MR. Measurement of Fiber-scale Residual Stress Variation in a Metal-matrix Composite. *Journal of Composite Materials*, 38(23):2079–2095, 2004. ISSN 0021-9983. doi: 10.1177/0021998304045584.

[110] Korsunsky AM, Regino G, and Nowell D. Residual stress analysis of welded joints by the variational eigenstrain approach. *Proceedings of SPIE - The International Society for Optical Engineering*, (July): 1–6, 2004. ISSN 0277786X. doi: 10.1117/12.621737.

[111] Smith DJ, Farrahi GH, Zhu WX, and McMahon CA. Obtaining multiaxial residual stress distributions from limited measurements. *Materials Science and Engineering A*, 303(1-2):281–291, 2001. ISSN 09215093. doi: 10.1016/S0921-5093(00)01837-2.

[112] Vaidyanathan S and Finnie I. Determination of Residual Stresses From Stress Intensity Factor Measurements. *Journal of Basic Engineering*, 93(2):242–246, 1971. ISSN 00219223. doi: 10.1115/1.3425220.

[113] Güngör S. Residual stress measurements in fibre reinforced titanium alloy composites. *Acta Materialia*, 50(8):2053–2073, 2002. ISSN 13596454. doi: 10.1016/S1359-6454(02)00050-2.

[114] Kang KJ, Darzens S, and Choi GS. Effect of Geometry and Materials on Residual Stress Measurement in Thin Films by Using the Focused Ion Beam. *Journal of Engineering Materials and Technology*, 126 (4):457–464, nov 2004. ISSN 0094-4289.

[115] Ersoy N and Vardar O. Measurement of residual stresses in layered composites by compliance method. *Journal of Composite Materials*, 34(7):575–598, 2000. doi: 10.1106/KK4W-0E04-ACU5-CKCN.

[116] Ganley JM, Maji AK, and Huybrechts S. Explaining spring-in in filament wound carbon fiber/epoxy composites. *Journal of Composite Materials*, 34(14):1216–1239, 2000. ISSN 00219983. doi: 10.1177/002199830003401404.

[117] Ritchie D and Leggatt RH. The measurement of the distribution of residual stresses through the thickness of a welded joint. *Strain*, 23(2):61–70, 1987. ISSN 14751305. doi: 10.1111/j.1475-1305.1987.tb00618.x.

[118] Hill MR, Dewald AT, Rankin JE, and Lee MJ. Measurement of laser peening residual stresses. *Materials Science and Technology*, 21(1):3–9, 2005. doi: 10.1179/174328405X14083.

[119] Chu J, Rigsbee J, Banas G, Lawrence F, and Elsayed-Ali H. Effects of laser-shock processing on the microstructure and surface mechanical properties of hadfield manganese steel. *Metallurgical and Materials Transactions A*, 26(6):1507–1517, 1995. ISSN 1543-1940. doi: 10.1007/BF02647602.

[120] Gagliardi MA, Sencer BH, Hunt AW, Maloy SA, and Gray GT. Relative Defect Density Measurements of Laser Shock Peened 316L Stainless Steel Using Positron Annihilation Spectroscopy. *Journal of Nondestructive Evaluation - J NONDESTRUCT EVAL*, 30:1–4, 12 2011. doi: 10.1007/s10921-011-0110-z.

[121] Strantza M, Vrancken B, Prime MB, Truman CE, Rombouts M, Brown DW, Guillaume P, and Van Hemelrijck D. Directional and oscillating residual stress on the mesoscale in additively manufactured Ti-6Al-4V. *Acta Materialia*, 168:299–308, 2019. ISSN 1359-6454. doi: 10.1016/j.actamat.2019.01.050.

[122] Prime MB and Finnie I. Surface Strains Due to Face Loading of a Slot in a Layered Half-Space. *Journal of Engineering Materials and Technology*, 118(3):410, 1996. ISSN 00944289. doi: 10.1115/1.2806828.

[123] Prime MB and Hellwig CH. Residual stresses in a bi-material laser clad measured using compliance. *Proc. of the 5th International Conference on Residual Stresses, Vol. 1*, 836:127–132, 1997. ISSN 1053-0894.

[124] Finnie S, Cheng W, Finnie I, Drezet JM, and Gremaud M. The Computation and Measurement of Residual Stresses in Laser Deposited Layers. *Journal of Engineering Materials and Technology*, 125 (3):302, 2003. ISSN 00944289. doi: 10.1115/1.1584493.

[125] Shokrieh MM and Akbari S. Effect of Residual Shear Stresses on Released Strains in Isotopic and Orthotropic Materials Measured by the Slitting Method. *Journal of Engineering Materials and Technology*, 134(1):011006, 2012. ISSN 00944289. doi: 10.1115/1.4005267.

[126] Ekbote B, Kwon P, and Prime MB. Micromechanics-based design and processing of efficient meso-scale heat exchanger. In *Proceedings of 21st Technical Conference of the American Society for Composites 2006*, volume 2, pages 978–992. American Society for Composites, 2006.

[127] Prime MB and Crane DL. Slitting method measurement of residual stress profiles, including stress discontinuities, in layered specimens. *Conference Proceedings of the Society for Experimental Mechanics Series*, 8:93–102, 2014. doi: 10.1007/978-3-319-00876-9˙12.

[128] Mathar J. Determination of initial stresses by measuring the deformation around drilled holes. *Transactions ASME*, 56(4):249–254, 1934.

[129] Soete W. Measurement and relaxation of residual stress. *Sheet Met. Ind.*, 26(266):1269–1281, 1949.

[130] Niku-Lari A, Lu J, and Flavenot JF. Measurement of residual-stress distribution by the incremental hole-drilling method. *Journal of Mechanical Working Technology*, 11(2):167–188, 1985. ISSN 03783804. doi: 10.1016/0378-3804(85)90023-3.

[131] Guo J, Fu H, Pan B, and Kang R. Recent progress of residual stress measurement methods: A review. *Chinese Journal of Aeronautics*, 2019. ISSN 1000-9361. doi: 10.1016/j.cja.2019.10.010.

[132] Scafidi M, Valentini E, and Zuccarello B. Error and uncertainty analysis of the residual stresses computed by using the hole drilling method. *Strain*, 47(4):301–312, 2011. ISSN 00392103. doi: 10.1111/j.1475-1305.2009.00688.x.

[133] Nicoletto G. Moiré interferometry determination of residual stresses in the presence of gradients. *Experimental Mechanics*, 31(3):252–256, 1991. ISSN 00144851. doi: 10.1007/BF02326068.

[134] Wu Z, Lu J, and Han B. Study of Residual Stress Distribution by a Combined Method of Moiré Interferometry and Incremental Hole Drilling, Part I: Theory. *Journal of Applied Mechanics*, 65(4):837, 1998. ISSN 00218936. doi: 10.1115/1.2791919.

[135] Min Y, Hong M, Xi Z, and Jian L. Determination of residual stress by use of phase shifting Moiré interferometry and hole-drilling method. *Optics and Lasers in Engineering*, 44(1):68–79, 2006. doi: 10.1016/j.optlaseng.2005.02.006.

[136] Furgiuele FM, Pagnotta L, and Poggialini A. Measuring Residual Stresses by Hole-Drilling and Coherent Optics Techniques: A Numerical Calibration. *J. Eng. Mat. and Tech. (Trans. ASME)*, 113(1):41–50, 1991. ISSN 15288889. doi: 10.1115/1.2903381.

[137] Ponslet E and Steinzig M. Residual stress measurement using the hole drilling method and laser speckle interferometry Part III: Analysis technique. *Experimental Techniques*, 27(December):45–48, 2003. ISSN 0732-8818. doi: 10.1111/j.1747-1567.2003.tb00130.x.

[138] Díaz FV, Kaufmann GH, and Möller O. Residual stress determination using blind-hole drilling and digital speckle pattern interferometry with automated data processing. *Experimental Mechanics*, 41(4): 319–323, 2001. ISSN 0014-4851. doi: 10.1007/BF02323925.

[139] Schmitt DR and Hunt RW. Inversion of speckle interferometer fringes for hole-drilling residual stress determinations. *Experimental Mechanics*, 40(2):129–137, 2000. ISSN 00144851. doi: 10.1007/BF02325038.

[140] McGinnis MJ. Application of Three-dimensional Digital Image Correlation to the Core-drilling Method. *Experimental Mechanics*, 45(4):359–367, 2005. ISSN 0014-4851. doi: 10.1177/0014485105055435.

[141] Lake BR, Appl FJ, and Bert CW. An investigation of the hole-drilling technique for measuring planar residual stress in rectangularly orthotropic materials, 1970. ISSN 0014-4851.

[142] Prasad CB, Prabhakaran R, and Tompkins S. Determination of calibration constants for the hole-drilling residual stress measurement technique applied to orthotropic composites—Part I: Theoretical considerations. *Composite Structures*, 8(2):105–118, 1987. ISSN 0263-8223. doi: 10.1016/0263-8223(87)90007-9.

[143] Shokrieh MM and Ghasemi K. AR. Determination of calibration factors of the hole drilling method for orthotropic composites using an exact solution. *Journal of Composite Materials*, 41(19):2293–2311, 2007. ISSN 00219983. doi: 10.1177/0021998307075443.

[144] Schajer GS and Yang L. Residual-stress measurement in orthotropic materials using the hole-drilling method. *Experimental Mechanics*, 34(4):324–333, 1994. ISSN 00144851. doi: 10.1007/BF02325147.

[145] Peral D, de Vicente J, Porro JA, and Ocaña JL. Uncertainty analysis for non-uniform residual stresses determined by the hole drilling strain gauge method. *Measurement: Journal of the International Measurement Confederation*, 97:51–63, 2017. ISSN 02632241. doi: 10.1016/j.measurement.2016.11.010.

[146] Richter R and Müller T. Measurement of Residual Stresses. *Experimental Techniques*, 41(1):79–85, 2017. ISSN 1747-1567. doi: 10.1007/s40799-016-0129-2.

[147] Nobre JP, Kornmeier M, and Scholtes B. Plasticity Effects in the Hole-Drilling Residual Stress Measurement in Peened Surfaces. *Experimental Mechanics*, 2018. ISSN 17412765. doi: 10.1007/s11340-017-0352-5.

[148] Vishay Precision Group. Measurement of Residual Stresses by the Hole-Drilling Strain Gage Method, Tech Note TN-503. Technical report, 2010.

[149] Nobre JP, Kornmeier M, Dias AM, and Scholtes B. Use of the hole-drilling method for measuring residual stresses in highly stressed shot-peened surfaces. *Experimental Mechanics*, 40:289–297, 2000. doi: 10.1007/BF02327502.

[150] Beghini M, Bertini L, and Santus C. A procedure for evaluating high residual stresses using the blind hole drilling method, including the effect of plasticity. *The Journal of Strain Analysis for Engineering Design*, 45(4):301–318, 2010. doi: 10.1243/03093247JSA5.

[151] Flaman MT. *Investigation of Ultra-high Speed Drilling for Residual Stress Measurement by the Centre Hole Method*. University of Toronto, 1979.

[152] Flaman MT and Herring JA. Comparison of Four Hole-Producing Techniques for the Center-Hole Residual-Stress Measurement Method. *Experimental Techniques*, 9(8):30–32, 1985. ISSN 1747-1567. doi: 10.1111/j.1747-1567.1985.tb02036.x.

[153] Schajer GS, Flaman MT, Roy G, and Lu J. Hole-drilling and ring core methods. In Lu J and Society for Experimental Mechanics, editors, *Handbook of Measurement of Residual Stresses*, chapter 2, pages 5–34. Fairmont Press, New York, 1996. ISBN 9780132557382.

[154] Schajer GS and Whitehead PS. Hole drilling and ring coring. In Schajer GS, editor, *Practical Residual Stress Measurement Methods*, chapter 2, pages 29–64. John Wiley & Sons, Ltd, 2013. ISBN 9781118402832. doi: 10.1002/9781118402832.ch2.

[155] Zuccarello B. Optimal calculation steps for the evaluation of residual stress by the incremental hole-drilling method. *Experimental Mechanics*, 39(2):117–124, 1999. ISSN 0014-4851. doi: 10.1007/BF02331114.

[156] Vangi D. Data Management for the Evaluation of Residual Stresses by the Incremental Hole-Drilling Method. *Journal of Engineering Materials and Technology*, 116(4):561–566, 1994. ISSN 0094-4289. doi: 10.1115/1.2904329.

[157] Akbari S, Taheri-Behrooz F, and Shokrieh MM. Characterization of residual stresses in a thin-walled filament wound carbon/epoxy ring using incremental hole drilling method. *Composites Science and Technology*, 94:8–15, 2014. ISSN 02663538. doi: 10.1016/j.compscitech.2014.01.008.

[158] Held E, Schuster S, and Gibmeier J. Incremental hole-drilling method vs. thin components: A simple correction approach. In *Residual Stresses IX*, volume 996 of *Advanced Materials Research*, pages 283–288. Trans Tech Publications Ltd, 10 2014. doi: 10.4028/www.scientific.net/AMR.996.283.

[159] Schajer GS. Compact Calibration Data for Hole-Drilling Residual Stress Measurements in Finite-Thickness Specimens. *Experimental Mechanics*, 60(5):665–678, 2020. ISSN 1741-2765. doi: 10.1007/s11340-020-00587-4.

[160] Blödorn R, Bonomo LA, Viotti MR, Schroeter RB, and Albertazzi A. Calibration Coefficients Determination Through Fem Simulations for the Hole-Drilling Method Considering the Real Hole Geometry. *Experimental Techniques*, 2017. ISSN 17471567. doi: 10.1007/s40799-016-0152-3.

[161] Beghini M, Bertini L, and Mori LF. Evaluating non-uniform residual stress by the hole-drilling method with concentric and eccentric holes. Part II: Application of the influence functions to the inverse problem. *Strain*, 46(4):337–346, 2010. ISSN 00392103. doi: 10.1111/j.1475-1305.2009.00684.x.

[162] Barsanti M, Beghini M, Bertini L, Monelli B, and Santus C. First-order correction to counter the effect of eccentricity on the hole-drilling integral method with strain-gage rosettes. *Journal of Strain Analysis for Engineering Design*, 2016. ISSN 20413130. doi: 10.1177/0309324716649529.

[163] Peral D, Correa C, Diaz M, Porro JA, de Vicente J, and Ocaña JL. Measured strains correction for eccentric holes in the determination of non-uniform residual stresses by the hole drilling strain gauge method. *Materials and Design*, 2017. ISSN 18734197. doi: 10.1016/j.matdes.2017.06.051.

[164] Santana YY, La Barbera-Sosa JG, Staia MH, Lesage J, Puchi-Cabrera ES, Chicot D, and Bemporad E. Measurement of residual stress in thermal spray coatings by the incremental hole drilling method. *Surface and Coatings Technology*, 201(5):2092–2098, 2006. ISSN 02578972. doi: 10.1016/j.surfcoat.2006.04.056.

[165] Lord JD, Penn D, and Whitehead P. The application of digital image correlation for measuring residual stress by incremental hole drilling. In *Advances in Experimental Mechanics VI*, volume 13 of *Applied Mechanics and Materials*, pages 65–73. Trans Tech Publications Ltd, 8 2008. doi: 10.4028/www.scientific.net/AMM.13-14.65.

[166] Robinson JS, Tanner DA, Truman CE, Paradowska AM, and Wimpory RC. The influence of quench sensitivity on residual stresses in the aluminium alloys 7010 and 7075. *Materials Characterization*, 65: 73–85, 2012. ISSN 10445803. doi: 10.1016/j.matchar.2012.01.005.

[167] Valentini E, Santus C, and Bandini M. Residual stress analysis of shot-peened aluminum alloy by fine increment hole-drilling and X-ray diffraction methods. *Procedia Engineering*, 10:3582 – 3587, 2011. ISSN 1877-7058. doi: 10.1016/j.proeng.2011.04.589. 11th International Conference on the Mechanical Behavior of Materials (ICM11).

[168] Petan L, Ocañ JL, and Grum J. Effects of laser shock peening on the surface integrity of 18 % Ni maraging steel. *Strojniski Vestnik/Journal of Mechanical Engineering*, 2016. ISSN 00392480. doi: 10.5545/sv-jme.2015.3305.

[169] Schajer GS. Measurement of Non-Uniform Residual Stresses Using the Hole-Drilling Method. Part I—Stress Calculation Procedures. *Journal of Engineering Materials and Technology*, 110(4):338–343, 10 1988. ISSN 0094-4289. doi: 10.1115/1.3226059.

[170] Bert CW and Thompson GL. A Method for Measuring Planar Residual Stresses in Rectangularly Orthotropic Materials. *Journal of Composite Materials*, 2(2):244–253, 1968. ISSN 0021-9983. doi: 10.1177/002199836800200209.

[171] Smith CB. Effect of elliptic or circular holes on the stress distribution in plates of wood or plywood considered as orthotropic materials. Technical report, Forest Products Laboratory (U.S.), Madison, WI, 1944.

[172] Pagliaro P and Zuccarello B. Residual stress analysis of orthotropic materials by the through-hole drilling method. *Experimental Mechanics*, 47(2):217–236, 2007. ISSN 00144851. doi: 10.1007/s11340-006-9019-3.

[173] Ghasemi AR, Taheri-Behrooz F, and Shokrieh MM. Determination of non-uniform residual stresses in laminated composites using integral hole drilling method: Experimental evaluation. *Journal of Composite Materials*, 48(4):415–425, 2014. ISSN 0021-9983. doi: 10.1177/0021998312473858.

[174] Gong XL, Wen Z, and Su Y. Experimental determination of residual stresses in composite laminates $[0_2/\theta_2]_s$. *Advanced Composite Materials*, 24(sup1):33–47, 2015. ISSN 0924-3046. doi: 10.1080/09243046.2014.937136.

[175] Valentini E, Bertelli L, and Benincasa A. Improvements in the hole-drilling test method for determining residual stresses in polymeric materials. *Materials Performance and Characterization*, 7(4):446–464, 2018. doi: 10.1520/MPC20170123.

[176] Nobre JP, Stiffel JH, Van Paepegem Van W, Nau A, Batista AC, Marques MJ, and Scholtes B. Quantifying the drilling effect during the application of incremental hole-drilling technique in laminate composites. In *Residual Stresses VIII*, volume 681 of *Materials Science Forum*, pages 510–515. Trans Tech Publications Ltd, 5 2011. doi: 10.4028/www.scientific.net/MSF.681.510.

[177] Nobre JP, Stiffel JH, Nau A, Outeiro JC, Batista AC, Van Paepegem W, and Scholtes B. Induced drilling strains in glass fibre reinforced epoxy composites. *CIRP Annals*, 62(1):87 – 90, 2013. ISSN 0007-8506. doi: 10.1016/j.cirp.2013.03.089.

[178] Vangi D. Residual Stress Evaluation by the Hole-Drilling Method With Off-Center Hole: An Extension of the Integral Method. *Journal of Engineering Materials and Technology*, 119(1):79, 1997. ISSN 00944289. doi: 10.1115/1.2805978.

[179] Rowlands RE. Strength(failure) theories and their experimental correlation. *Elsevier Science Publishers B. V., Handbook of Composites*, 3:71–125, 1985.

[180] Daniel IM. Failure mechanisms in fiber-reinforced composites. *Proceedings of the ARPA/AFML Review of Progress in Quantitative NDE*, 34:205–218, 1978.

[181] Herakovich CT. *Mechanics of Fibrous Composites*, chapter 9, pages 303–361. John Wiley & Sons, Inc., 1998. ISBN 978-0-471-10636-4.

[182] Soden PD, Hinton MJ, and Kaddour AS. Lamina properties, lay-up configurations and loading conditions for a range of fibre-reinforced composite laminates. *Composites Science and Technology*, 58(7): 1011–1022, 1998. ISSN 0266-3538. doi: 10.1016/S0266-3538(98)00078-5.

[183] Flaggs DL and Kural MH. Experimental determination of the in situ transverse lamina strength in graphite/epoxy laminates. *Journal of Composite Materials*, 16(2):103–116, 1982. doi: 10.1177/002199838201600203.

[184] Vishay Precision Group. Errors Due to Transverse Sensitivity in Strain Gages, Tech Note TN-509. Technical report, 2011.

[185] ASTM D3039/D3039M. *Standard Test Method for Tensile Properties of Polymer Matrix Composite Materials*. ASTM International, West Conshohocken, PA, 2014.

[186] ASTM D3518/D3518M. *Standard Test Method for In-Plane Shear Response of Polymer Matrix Composite Materials by Tensile Test of a 45° Laminate*. ASTM International, West Conshohocken, PA, 2013.

[187] Hill R. Theory of mechanical properties of fibre-strengthened materials: I. elastic behaviour. *Journal of the Mechanics and Physics of Solids*, 12(4):199 – 212, 1964. ISSN 0022-5096. doi: 10.1016/0022-5096(64)90019-5.

[188] Schajer GS. Use of displacement data to calculate strain gauge response in non-uniform strain fields. *Strain*, 29(1):9–13, 1993. doi: 10.1111/j.1475-1305.1993.tb00820.x.

[189] BIPM, IEC, IFCC, ILAC, IUPAC, IUPAP, ISO, and OIML. Evaluation of measurement data—Guide for the expression of uncertainty in measurement, JCGM 100: 2008. 2008.

[190] Scafidi M, Valentini E, and Zuccarello B. Effect of the hole-bottom fillet radius on the residual stress analysis by the hole drilling method. In *ICRS-8 The 8th International Conference on Residual Stress – Denver*, pages 263–270, 2008.

[191] Salehi SD and Shokrieh MM. Residual stress measurement using the slitting method via a combination of eigenstrain, regularization and series truncation techniques. *International Journal of Mechanical Sciences*, 152:558 – 567, 2019. ISSN 0020-7403. doi: 10.1016/j.ijmecsci.2019.01.011.

[192] ASM Handbook. *Volume 2: Properties and Selection: Nonferrous Alloys and Special-Purpose Materials*. ASM International, 1990. ISBN 978-0-87170-378-1.

[193] Alegre JM, Díaz A, Cuesta II, and Manso JM. Analysis of the Influence of the Thickness and the Hole Radius on the Calibration Coefficients in the Hole-Drilling Method for the Determination of Non-uniform Residual Stresses. *Experimental Mechanics*, 59(1):79–94, 2019. ISSN 1741-2765. doi: 10.1007/s11340-018-0433-0.

[194] Correa C, Peral D, Porro JA, Díaz M, Ruiz De Lara L, García-Beltrán A, and Ocaña JL. Random-type scanning patterns in laser shock peening without absorbing coating in 2024-T351 Al alloy: A solution to reduce residual stress anisotropy. *Optics and Laser Technology*, 2015. ISSN 00303992. doi: 10.1016/j.optlastec.2015.04.027.

[195] Noyan IC and Cohen JB. *Residual Stress: Measurement by Diffraction and Interpretation*. Springer-Verlag New York, 1987. ISBN 978-1-4613-9570-6. doi: 10.1007/978-1-4613-9570-6.

Appendix I: Springer Nature License Agreements

SPRINGER NATURE LICENSE
TERMS AND CONDITIONS

Aug 18, 2020

This Agreement between Teubes Smit ("You") and Springer Nature ("Springer Nature") consists of your license details and the terms and conditions provided by Springer Nature and Copyright Clearance Center.

License Number	4884840150239
License date	Aug 09, 2020
Licensed Content Title	Residual Stress Measurement in Composite Laminates Using Incremental Hole-Drilling with Power Series
Licensed Content Author	T. C. Smit et al
	Jun 4, 2018
Type of Use	Thesis/Dissertation
Requestor type	academic/university or research institute
Format	electronic
Portion	full article/chapter
Will you be translating?	no
Circulation/distribution	30 - 99

SPRINGER NATURE LICENSE
TERMS AND CONDITIONS

Sep 01, 2020

This Agreement between Teubes Smit ("You") and Springer Nature ("Springer Nature") consists of your license details and the terms and conditions provided by Springer Nature and Copyright Clearance Center.

License Number	4900200395562
License date	Sep 01, 2020
Licensed Content Publisher	Springer Nature
Licensed Content Publication	Experimental Mechanics
Licensed Content Title	Tikhonov regularization with Incremental Hole-Drilling and the Integral Method in Cross-Ply Composite Laminates
Licensed Content Author	T.C. Smit et al
Licensed Content Date	Jul 27, 2020
Type of Use	Thesis/Dissertation
Requestor type	academic/university or research institute
Format	electronic
Portion	full article/chapter
Will you be translating?	no

SPRINGER NATURE LICENSE
TERMS AND CONDITIONS

Sep 01, 2020

This Agreement between Teubes Smit ("You") and Springer Nature ("Springer Nature") consists of your license details and the terms and conditions provided by Springer Nature and Copyright Clearance Center.

License Number	4900200202945
License date	Sep 01, 2020
Licensed Content Publisher	Springer Nature
Licensed Content Publication	Experimental Mechanics
Licensed Content Title	Use of Power Series Expansion for Residual Stress Determination by the Incremental Hole-Drilling Technique
Licensed Content Author	T.C. Smit et al
Licensed Content Date	Aug 31, 2020
Type of Use	Thesis/Dissertation
Requestor type	academic/university or research institute
Format	electronic
Portion	full article/chapter
Will you be translating?	no

SPRINGER NATURE LICENSE
TERMS AND CONDITIONS

Apr 18, 2021

This Agreement between Teubes Smit ("You") and Springer Nature ("Springer Nature") consists of your license details and the terms and conditions provided by Springer Nature and Copyright Clearance Center.

License Number	5051900234729
License date	Apr 18, 2021
Licensed Content Publisher	Springer Nature
Licensed Content Publication	Experimental Mechanics
Licensed Content Title	A Method to Combine Residual Stress Measurements from XRD and IHD using Series Expansion
Licensed Content Author	T. C. Smit et al
Licensed Content Date	Apr 17, 2021
Type of Use	Thesis/Dissertation
Requestor type	academic/university or research institute
Format	electronic
Portion	full article/chapter
Will you be translating?	no

Author of this Springer Nature content	yes
Title	Extension of the Incremental Hole-Drilling Technique for Residual Stress Measurement
Requestor Location	Teubes Smit 52 van Vuuren Street Roodepoort, 1709 South Africa Attn: University of the Witwatersrand
Total	0.00 USD

Terms and Conditions

Springer Nature Customer Service Centre GmbH
Terms and Conditions

This agreement sets out the terms and conditions of the licence (the **Licence**) between you and **Springer Nature Customer Service Centre GmbH** (the **Licensor**). By clicking 'accept' and completing the transaction for the material (**Licensed Material**), you also confirm your acceptance of these terms and conditions.

1. Grant of License

1. 1. The Licensor grants you a personal, non-exclusive, non-transferable, world-wide licence to reproduce the Licensed Material for the purpose specified in your order only. Licences are granted for the specific use requested in the order and for no other use, subject to the conditions below.

1. 2. The Licensor warrants that it has, to the best of its knowledge, the rights to license reuse of the Licensed Material. However, you should ensure that the material you are requesting is original to the Licensor and does not carry the copyright of another entity (as credited in the published version).

1. 3. If the credit line on any part of the material you have requested indicates that it was reprinted or adapted with permission from another source, then you should also seek permission from that source to reuse the material.

2. Scope of Licence

2. 1. You may only use the Licensed Content in the manner and to the extent permitted

by these Ts&Cs and any applicable laws.

2. 2. A separate licence may be required for any additional use of the Licensed Material, e.g. where a licence has been purchased for print only use, separate permission must be obtained for electronic re-use. Similarly, a licence is only valid in the language selected and does not apply for editions in other languages unless additional translation rights have been granted separately in the licence. Any content owned by third parties are expressly excluded from the licence.

2. 3. Similarly, rights for additional components such as custom editions and derivatives require additional permission and may be subject to an additional fee. Please apply to Journalpermissions@springernature.com/bookpermissions@springernature.com for these rights.

2. 4. Where permission has been granted **free of charge** for material in print, permission may also be granted for any electronic version of that work, provided that the material is incidental to your work as a whole and that the electronic version is essentially equivalent to, or substitutes for, the print version.

2. 5. An alternative scope of licence may apply to signatories of the STM Permissions Guidelines, as amended from time to time.

3. Duration of Licence

3. 1. A licence for is valid from the date of purchase ('Licence Date') at the end of the relevant period in the below table:

Scope of Licence	**Duration of Licence**
Post on a website	12 months
Presentations	12 months
Books and journals	Lifetime of the edition in the language purchased

4. Acknowledgement

4. 1. The Licensor's permission must be acknowledged next to the Licenced Material in print. In electronic form, this acknowledgement must be visible at the same time as the figures/tables/illustrations or abstract, and must be hyperlinked to the journal/book's homepage. Our required acknowledgement format is in the Appendix below.

5. Restrictions on use

5. 1. Use of the Licensed Material may be permitted for incidental promotional use and minor editing privileges e.g. minor adaptations of single figures, changes of format, colour and/or style where the adaptation is credited as set out in Appendix 1 below. Any other changes including but not limited to, cropping, adapting, omitting material that

affect the meaning, intention or moral rights of the author are strictly prohibited.

5. 2. You must not use any Licensed Material as part of any design or trademark.

5. 3. Licensed Material may be used in Open Access Publications (OAP) before publication by Springer Nature, but any Licensed Material must be removed from OAP sites prior to final publication.

6. Ownership of Rights

6. 1. Licensed Material remains the property of either Licensor or the relevant third party and any rights not explicitly granted herein are expressly reserved.

7. Warranty

IN NO EVENT SHALL LICENSOR BE LIABLE TO YOU OR ANY OTHER PARTY OR ANY OTHER PERSON OR FOR ANY SPECIAL, CONSEQUENTIAL, INCIDENTAL OR INDIRECT DAMAGES, HOWEVER CAUSED, ARISING OUT OF OR IN CONNECTION WITH THE DOWNLOADING, VIEWING OR USE OF THE MATERIALS REGARDLESS OF THE FORM OF ACTION, WHETHER FOR BREACH OF CONTRACT, BREACH OF WARRANTY, TORT, NEGLIGENCE, INFRINGEMENT OR OTHERWISE (INCLUDING, WITHOUT LIMITATION, DAMAGES BASED ON LOSS OF PROFITS, DATA, FILES, USE, BUSINESS OPPORTUNITY OR CLAIMS OF THIRD PARTIES), AND
WHETHER OR NOT THE PARTY HAS BEEN ADVISED OF THE POSSIBILITY OF SUCH DAMAGES. THIS LIMITATION SHALL APPLY NOTWITHSTANDING ANY FAILURE OF ESSENTIAL PURPOSE OF ANY LIMITED REMEDY PROVIDED HEREIN.

8. Limitations

8. 1. ***BOOKS ONLY:***Where **'reuse in a dissertation/thesis'** has been selected the following terms apply: Print rights of the final author's accepted manuscript (for clarity, NOT the published version) for up to 100 copies, electronic rights for use only on a personal website or institutional repository as defined by the Sherpa guideline (www.sherpa.ac.uk/romeo/).

9. Termination and Cancellation

9. 1. Licences will expire after the period shown in Clause 3 (above).

9. 2. Licensee reserves the right to terminate the Licence in the event that payment is not received in full or if there has been a breach of this agreement by you.

Appendix 1 — Acknowledgements:

For Journal Content:
Reprinted by permission from [**the Licensor**]: [**Journal Publisher** (e.g. Nature/Springer/Palgrave)] [**JOURNAL NAME**] [**REFERENCE CITATION** (Article name, Author(s) Name), [**COPYRIGHT**] (year of publication)

For **Advance Online Publication papers:**
Reprinted by permission from [**the Licensor**]: [**Journal Publisher** (e.g. Nature/Springer/Palgrave)] [**JOURNAL NAME**] [**REFERENCE CITATION** (Article name, Author(s) Name), [**COPYRIGHT**] (year of publication), advance online publication, day month year (doi: 10.1038/sj.[JOURNAL ACRONYM].)

For Adaptations/Translations:
Adapted/Translated by permission from [**the Licensor**]: [**Journal Publisher** (e.g. Nature/Springer/Palgrave)] [**JOURNAL NAME**] [**REFERENCE CITATION** (Article name, Author(s) Name), [**COPYRIGHT**] (year of publication)

Note: For any republication from the British Journal of Cancer, the following credit line style applies:

Reprinted/adapted/translated by permission from [**the Licensor**]: on behalf of Cancer Research UK: : [**Journal Publisher** (e.g. Nature/Springer/Palgrave)] [**JOURNAL NAME**] [**REFERENCE CITATION** (Article name, Author(s) Name), [**COPYRIGHT]** (year of publication)

For **Advance Online Publication** papers:
Reprinted by permission from The [**the Licensor**]: on behalf of Cancer Research UK: [**Journal Publisher** (e.g. Nature/Springer/Palgrave)] [**JOURNAL NAME**] [**REFERENCE CITATION** (Article name, Author(s) Name), [**COPYRIGHT**] (year of publication), advance online publication, day month year (doi: 10.1038/sj.[JOURNAL ACRONYM])

For Book content:
Reprinted/adapted by permission from [**the Licensor**]: [**Book Publisher** (e.g. Palgrave Macmillan, Springer etc) [**Book Title**] by [**Book author**(s)] [**COPYRIGHT**] (year of publication)

Other Conditions:

Version 1.2

Questions? customercare@copyright.com or +1-855-239-3415 (toll free in the US) or +1-978-646-2777.